^{3}Neutral Current Detectors for the Sudbury Neutrino Observatory

Peter Michael Thornewell
Lincoln College, Oxford

Thesis submitted in partial fulfillment of the requirements
for the degree of Doctor of Philosophy
at the University of Oxford

Trinity Term 1997

Detectors for the Sudbury Neutrino Observatory

Peter Michael Thornewell
Lincoln College, Oxford

Thesis submitted for the degree of Doctor of Philosophy

Trinity Term 1997

Abstract

Current solar neutrino experiments indicate the possibility of neutrino oscillations. These flavour oscillations can be confirmed or refuted by the Sudbury Neutrino Observatory (SNO), a 1,000 tonne heavy water Čerenkov detector presently under construction. This detector will measure the ^{8}B ν_e flux and energy spectrum via a pure charge current reaction, and *independently* the ^{8}B *total* ν flux via a pure neutral current reaction. The experiment is thus self-normalizing and does not rely on the predictions of solar models to search for neutrino oscillations.

The default method suggested for observing the neutron produced in the neutral current reaction proposed by the SNO collaboration is to dope the heavy water with ^{35}Cl in the form of dissolved salt and observe the γ shower produced by neutron capture. Presented here is an alternative method for observing the neutral current neutron by using ^{3}He proportional counters, distributed throughout the detector. The total length of detectors will approach half a mile.

The pulse shape analysis techniques developed through the course of this thesis are used to differentiate the neutron signal from the inherent α backgrounds present in the walls of the detector and also as a method of assaying the radiopurity of the counters.

As proof of principle, experiments have been running at the Waste Isolation Pilot Plant in Carlsbad, New Mexico, using prototype detectors. The results of these experiments show that the use of ^{3}He proportional counters inside the SNO detector is feasible and will not cause an appreciable increase in backgrounds. In addition, discrete neutral current detectors have the particular advantage over the default method of being able to identify neutral current events on an event by event basis.

Acknowledgments

Thanks must go to both the SNO groups at LANL and Oxford for their help and suggestions and participation in this thesis. Particular thanks to my innumerable supervisors and especially to Nick Jelley for his extreme patience, to Andrew Hime who worked with me on this project during its many years and to Hamish Robertson whose skill and knowledge of both physics and preamplifiers will always amaze me. Thanks must also go to both Mel Anaya and Tom Burritt for their construction efforts both at WIPP and LANL in building the many detectors and other apparatus which were used as part of this thesis. I am indebted to John Wilkerson for showing me the light on various computing and programming matters, and even more so to Frank McGirt, who then had to show me how to do it properly.

During the course of the thesis I have had chance to work with many post-docs and summer students at Los Alamos. My thanks to them for both making my time in Los Alamos interesting and informative and for performing some of the simulations used in this thesis.

I would also like to thank the various heads of the Sub-Department of Nuclear and Particle Physics not only for their interest in, and support of, the SNO project.

And finally I would like to thank my wife for putting up with me for all these years. This thesis is dedicated to you.

Contents

1 Solar Neutrinos **1**
- 1.1 The Neutrino, the Sun and the Solar Neutrino Problem . . . 1
- 1.2 Solar Models and Solar Neutrinos . . . 2
  - 1.2.1 Stellar Evolution . . . 3
  - 1.2.2 Helioseismology . . . 6
- 1.3 Current Solar Neutrino Experiments . . . 8
  - 1.3.1 Chlorine . . . 10
  - 1.3.2 Kamiokande . . . 11
  - 1.3.3 SAGE & GALLEX . . . 13
- 1.4 The Solar Neutrino Problem . . . 15
- 1.5 Resolving the Solar Neutrino Problem . . . 16
  - 1.5.1 Non-Standard Solar Models . . . 16
  - 1.5.2 Vacuum Oscillations . . . 17
  - 1.5.3 MSW Effect . . . 19
  - 1.5.4 Other Explanations . . . 20
- 1.6 Prospects for Further Experimental Results . . . 22

2 The Sudbury Neutrino Observatory **25**
- 2.1 Detector Description . . . 25
- 2.2 Neutrino Interactions . . . 27
  - 2.2.1 Charged Current $\nu_e + d \rightarrow p + p + e^-$ . . . 27
  - 2.2.2 Elastic Scattering $\nu_x + e^- \rightarrow \nu_x + e^-$ . . . 28
  - 2.2.3 Neutral Current $\nu_x + d \rightarrow n + p + \nu_x$ . . . 28
  - 2.2.4 Other Reactions . . . 28
  - 2.2.5 Discussion . . . 29
- 2.3 Detector Calibration . . . 31
- 2.4 Purity Requirements . . . 31
- 2.5 Neutral Current Detection in SNO . . . 35
- 2.6 The Dissolved Salt Option . . . 36
  - 2.6.1 Dissolved Salt II . . . 37
- 2.7 ^{3}He Proportional Counters . . . 37

3 ^{3}He Proportional Counters **40**
- 3.1 Pulse Shape Analysis . . . 40
  - 3.1.1 The Proportional Counter . . . 40
  - 3.1.2 Pulse Formation . . . 42
  - 3.1.3 Extended Tracks . . . 44
  - 3.1.4 The Space Charge Effect . . . 47
- 3.2 Ionizing Radiation . . . 48
  - 3.2.1 Neutrons . . . 48

3.2.2 Alpha Particles . . . 54
3.2.3 Betas & Gammas . . . 58
3.3 Noise and Spurious Pulses . . . 60
3.3.1 HV Discharge . . . 60
3.3.2 Sound Pickup . . . 62
3.3.3 Unidentified Pulses . . . 62
3.4 Neutron Signal Separation . . . 62
3.5 Optimization of Counter Parameters . . . 63
3.5.1 Purity Requirements . . . 63
3.5.2 Choice of Gas Mixture and Operating Parameters . . . 65

4 The WIPP Facility 68
4.1 Description of WIPP and Purpose . . . 68
4.2 LANL Experimental Setup . . . 69
4.3 History of LANL Experiments at WIPP . . . 74
4.3.1 Stage 1 . . . 74
4.3.2 Stage 2a . . . 77
4.3.3 Stage 2b . . . 82

5 Physics Results from WIPP 84
5.1 Stage 1 2 m Stainless Steel Detectors . . . 84
5.1.1 End Effects . . . 86
5.1.2 Introduction of the δ parameter . . . 90
5.1.3 Surface ^{210}Po Contamination . . . 92
5.1.4 Detector Longevity . . . 94
5.2 Stage 2 Double-Ended Readout . . . 94
5.2.1 An explanation of the electronics . . . 96
5.2.2 Multiple Series . . . 97
5.3 Stage 2 Analysis . . . 97
5.3.1 Anomalous Pulses . . . 98
5.4 Short Stainless Steel Detector #2 . . . 99
5.5 Nickel CVD Detector #1 . . . 100
5.5.1 Effects of Etching . . . 102
5.5.2 Lead Shielding . . . 104
5.6 Nickel CVD Detectors #2 & #3 . . . 104
5.6.1 Elimination of Radon . . . 109
5.6.2 The Effects of Etching . . . 112
5.6.3 Surface and Bulk Contamination . . . 117
5.6.4 Neutron Window . . . 118
5.6.5 High Energy Neutron Irradiation . . . 120

6 Extraction of Physics from the NCD Array 122
6.1 Neutral Current Detectors in SNO . . . 122
6.1.1 NCD Electronics . . . 125
6.2 Neutron Signal Separation . . . 127
6.2.1 Neutron Distributions in SNO . . . 130
6.2.2 NCD Geometries . . . 131
6.2.3 Neutron Transport and Detection . . . 134
6.2.4 Binning of Neutron Data . . . 135
6.2.5 Neutron Signal Separation Efficiencies . . . 136
6.3 Separation of Non-uniform Signals . . . 139

6.3.1 The Effects of Hot Spots on Signal Extraction . . . 141
6.3.2 Identification of Unknown Hot Spots . . . 142
6.3.3 Analysis of Simulated Data . . . 146
6.4 Identification of Dead Counters . . . 158

7 Conclusions **160**
7.1 Final Conclusions . . . 160
7.2 Current State of the NCD Project . . . 161
7.3 CHIME . . . 163

A The MSW Effect **165**

B Standard Analysis Techniques **166**
B.1 Charge Pulses . . . 166
B.1.1 Charge Pulse Analysis . . . 166
B.1.2 Charge Pulse Analysis with Position . . . 167
B.2 Parameter Choices . . . 169

C Maximum Likelihood Fitters **170**
C.1 The Maximum Likelihood Fitter . . . 170
C.2 Comparison To χ^2 Fit . . . 171

D Cosmogenic Production of Radio-Isotopes in Nickel **172**
D.1 Introduction . . . 172
D.2 Cosmogenic Probabilities . . . 172
D.3 Photodisintegration of the Deuteron . . . 172
D.4 Levels of ^{56}Co Produced by Cosmic Rays . . . 176
D.5 Conclusions . . . 177

E Monte Carlo Techniques **179**
E.1 Production of Distributions . . . 179
E.2 Probability Distributions . . . 179
E.3 Neutron Capture Distributions . . . 180
E.3.1 Multiple Monte Carlo Simulations . . . 180
E.3.2 Single Monte Carlo Simulations . . . 180

F WIPP Stage 2 Data Reduction **182**
F.1 Series Numbers and Their Meaning . . . 187

G ^{232}Th and ^{238}U decay schemes **197**

Chapter 1

Solar Neutrinos

1.1 The Neutrino, the Sun and the Solar Neutrino Problem

The existence of the neutrino was originally suggested by Pauli in 1930 to solve simultaneously the problems of energy conservation and spin statistics in β-decay. He proposed in his 'desperate remedy', that a new and light fermion, which had a very small interaction cross-section, was emitted along with the β-particle. Indeed, the neutrino remained a theoretical particle until its existence was experimentally demonstrated in 1956 by Reines and Cowan [1]. They measured the cross-section for the inverse β-decay of the proton, using the then new reactor at Savannah River, South Carolina as a source of anti-neutrinos. Since then, the neutrino has played a critical role in understanding the weak interaction. Indeed, several decades of experiments have made clear the V-A structure of the weak interaction, and have shown the existence of three distinct generations of light ($m_\nu < 45\,\mathrm{GeV}$) neutrinos. (Strictly 2.991 ± 0.016 from the Particle Data Group's fit to LEP 95 data.)

What, however, links this small, difficult to detect and seemingly massless particle with the Sun, which is its exact opposite in all respects? Why should particle physics and astrophysics be related at such extremes, and what is the problem with solar neutrinos? The answer to all of these questions lies with the method of energy production in the Sun and other stars. Given stellar lifetimes and the considerable amount of energy that is liberated, the only feasible conclusion is that the energy is generated by nuclear fusion, a process which produces not only the star's energy, but also copious quantities of neutrinos.

Given sufficient knowledge of the physical processes occurring in a star's interior, the appropriate input parameters, and a suitably powerful computer, it is possible to construct a mathematical model of the Sun. This model should then be able to reproduce the observable parameters of not only our own Sun but also of any other main sequence star. Various models have been constructed and when applied to the Sun, they correctly predict its size, luminosity and chemical composition as well as accounting for helio-seismological observations. However, after several decades of measurement, there is a significant discrepancy between the theoretical

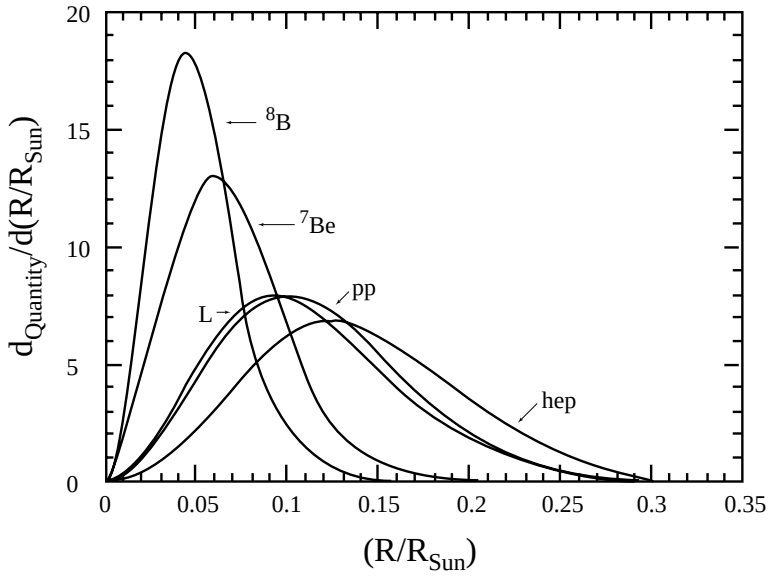

Figure 1.1: Neutrino and energy production as a function of solar radius, $R_\odot$. (Taken from Bahcall [4])

and measured solar neutrino flux. This is referred to as the Solar Neutrino Problem.

There appear to be several solutions to this discrepancy. First, it is possible that the experiments are incorrect. As is discussed further in section 1.3, with four different detectors using three different detection methods, this seems somewhat unlikely. Second, it is possible that the solar models are incorrect. The majority of solar neutrinos are produced within the first 20% of the solar radius, (see Figure 1.1), whilst the majority of solar observations (made using electromagnetic radiation) are of the outermost 0.05%. Finally, and of greatest interest to the particle physics community, is the possibility that something is happening to solar neutrinos during their almost eight minute transit from their creation in the central regions of the Sun to their final detection on Earth. This would be an indication of physics beyond the Standard Model of elementary particles.

The remaining sections of this Chapter discuss these Standard Solar Models (SSM's), the experiments which attempt to measure the solar neutrino flux, possible solutions to the solar neutrino problem and future solar neutrino experiments.

1.2 Solar Models and Solar Neutrinos

Solar models are designed to simulate the processes of energy production and transportation which occur inside a star, throughout the star's lifetime, using a number of assumptions of the physics involved and the initial starting conditions. Indeed, accurate solar models are not only able to reproduce the required observables for the Sun but also for other stars. They

correctly predict the sparse nature of the Hertzsprung-Russell diagram (log Luminosity vs colour/temperature) and the Mass-Luminosity relationship. Indeed, any model which treats the Sun as a special case should be regarded suspiciously. Fortunately, a much simpler calculation can be made to obtain a prediction for the solar neutrino flux.

The fusion process, much simplified, can be viewed as:

$$4p + 2e^- \longrightarrow {}^4\mathrm{He} + 2\nu_e + 26.731\,\mathrm{MeV} \tag{1.1}$$

Given that two neutrinos are produced for every 26.731 MeV of energy it is possible to obtain the total integrated flux of neutrinos at the Earth's surface. It must be assumed that all other sources of energy are negligible and that the dominant neutrino carries away little of the energy produced (Figure 1.2 shows that the *p-p* chain neutrino carries away very little of the energy). Given the energy output of the Sun ($L_\odot$) is 3.9×10^{26}W and the average Earth-Sun distance (D) is 1.496×10^{13} cm then,

$$\text{flux} = \frac{2L_\odot}{4\pi D^2 \times 26.7\,\mathrm{MeV}} = 6.48 \times 10^{10}\,\nu/\mathrm{cm}^2/\mathrm{s} \tag{1.2}$$

which is in good agreement with the much more detailed model of Bahcall and Pinsonneault [4] of $6.6 \times 10^{10}\,\nu/\mathrm{cm}^2/\mathrm{s}$. However, this simple calculation does not reveal the ν_e energy spectrum resulting from the many different reactions believed to occur in the solar interior. For spectral information, the detailed mathematical models of the Sun, which include the physics of energy transport, nuclear reactions and thermodynamic stability, must be used.

1.2.1 Stellar Evolution

The Sun is a stable, main sequence star and it is therefore safe to assume that it has evolved quasistatically over the last 4.6 billion years; the age of the Sun being estimated from isotopic dating of meteorite samples. A number of assumptions of the physics involved and stellar conditions must be made to build a self-consistent model of the stellar interior.

- Spherical symmetry along with no rotational effects. The Sun is spherical to within 5 parts in 10^5 and this initially appears to be a good assumption. However, the solar rotation is of the order of 25 days, with not all latitudes of the Sun rotating with the same angular frequency.

- Hydrostatic equilibrium - the radiative and particle pressures must match the gravitational forces exactly:

$$\frac{\partial P(r)}{\partial r} = -\frac{GM(r)\rho(r)}{r^2} \tag{1.3}$$

  This must be true as any gross violation would causes the Sun to collapse in less than an hour.

- Energy transport is due to photons and convective motion. The equation concerning energy transport relies on two components: the photon opacity and the electron conduction opacity. In the core, which is the most important region for solar neutrinos, the photon or radiative opacity dominates. The equation describing energy transport then becomes

$$L_r = -4\pi r^2 \frac{1}{\kappa\rho} \frac{ac}{3} \frac{\partial T^4}{\partial r} \tag{1.4}$$

  where L_r is the energy passing through a sphere of radius r at temperature T, and the opacity and density are given by κ and ρ respectively. The value of a is given by $\frac{8\pi^5 k^4}{15h^3c^3}$. The accuracy of these calculations is of extreme importance. The flux of various neutrino branches can be shown to be highly dependent on the temperature of the plasma, because of the large Coloumb barriers which exist in the reactions which produce them.

- Energy is generated almost entirely by nuclear reactions. These nuclear reaction cycles are shown in Figure 1.3 and Table 1.2. In most models nuclear energy is the only energy source, but some [4] also include the effects of gravitational expansion and collapse.

- Chemical composition changes only as a result of nuclear reactions. The solar interior is assumed to be initially chemically homogeneous and no convective mixing is allowed. This is a reasonable assumption given that there is essentially no overlap between the convective zone and the radiative core where the neutrinos are produced. The exception is the model of Bahcall and Pinsonneault[4] which includes the effects of helium diffusion in the core. Figure 1.4 shows a comparison of sound speeds predicted by different standard solar models with the sound speeds measured by helioseismology indicating the the effects of diffusion must be considered in the SSM. Section 1.2.2 discusses helioseismology further.

- There is no unknown physics which plays any significant role in the mechanics of the Sun.

With these assumptions about the mechanism of solar evolution, all that remains is to define the input parameters. Indeed, the major difference between authors is in the value of these input parameters. The two most widely reported models of Bahcall *et al.* and Turck-Chièze *et al.*, using these assumptions, agree at the 1% level when using the same value for these parameters. These input parameters can be separated into two distinct groups: the initial conditions (*e.g.* mass and elemental abundances) and the other physical values which must either be experimentally determined or calculated theoretically (*e.g.* nuclear cross-sections and opacities). The values for these parameters have come from a variety of sources [3].

The abundances of elements heavier than ^{4}He can be determined by examining the solar electromagnetic spectrum. By inference, this represents the initial abundance of elements because changes due to nuclear processes are assumed to be negligible in this region. The ratio of hydrogen and helium is more difficult to determine. Accordingly, most models determine this ratio by requiring that the measured and calculated solar luminosities agree at the current epoch. The resulting values are consistent with the current H/He values obtained from interstellar observations.

The nuclear cross-sections are taken from a variety of sources. One of the difficulties associated with solar models is in obtaining accurate values for these cross-sections. Even at stellar temperatures, the energies of individual particles are too low for nuclear reactions to proceed at an observable rate. These low energy cross-sections are impossible to measure in the laboratory and must be extrapolated from higher energies. The only exception to this general rule is ^{3}He(^{3}He,α)2p. At thermal energies, with two like charged particles, the cross section is dominated by the quantum mechanical tunnelling through the Coulomb barrier,

$$\sigma(E) \sim \frac{S(E)}{E} \exp(-2\pi\eta) \tag{1.5}$$

where $\eta = Z_1 Z_2 (e^2/4\pi\hbar v)$ is the Gamow penetration factor, $S(E)$ is a smoothly varying function of energy in the absence of resonances and the $1/E$ term is due to the overlap of the particle wavefunctions. The value of $S(E)$ at zero energy is referred to as the cross-section factor, S_0. Of most importance are the measurement of S_{34} and S_{17} which govern the rate of production of ^{7}Be and ^{8}B neutrinos. Measurement of these parameters is difficult and errors will result in a significant change in the neutrino flux. The radiative opacity values are taken from OPAL calculations.

Having established reasonable values for these parameters, the solar model calculations start with an initially homogeneous chemical mix. The model is evolved in steps of order 10^7 - 10^8 years (the step size has been shown to have very little effect on the final result). At each point the model is iterated to a self-consistent solution. Nuclear processes are then simulated to change the chemical and physical states of the model. There are two reaction schemes which are considered. The first, and for the Sun, the more important, is the 'pp' chain (Figure 1.3). This chain accounts for about 98.4% of the solar luminosity. The second chain, the CNO cycle, achieves the same fusion of four protons to produce one helium nucleus by catalysis with ^{12}C. Only the major neutrino producing reactions are shown in Table 1.2. After 4.6 billion years, the final result must match the solar observables such as luminosity, radius and mass.

The final result is the flux and energy spectrum of solar neutrinos. Figure 1.2 shows the solar neutrino spectrum, whilst Figure 1.1 shows the production as a function of solar radius. Both Figures are taken from Bahcall [3].

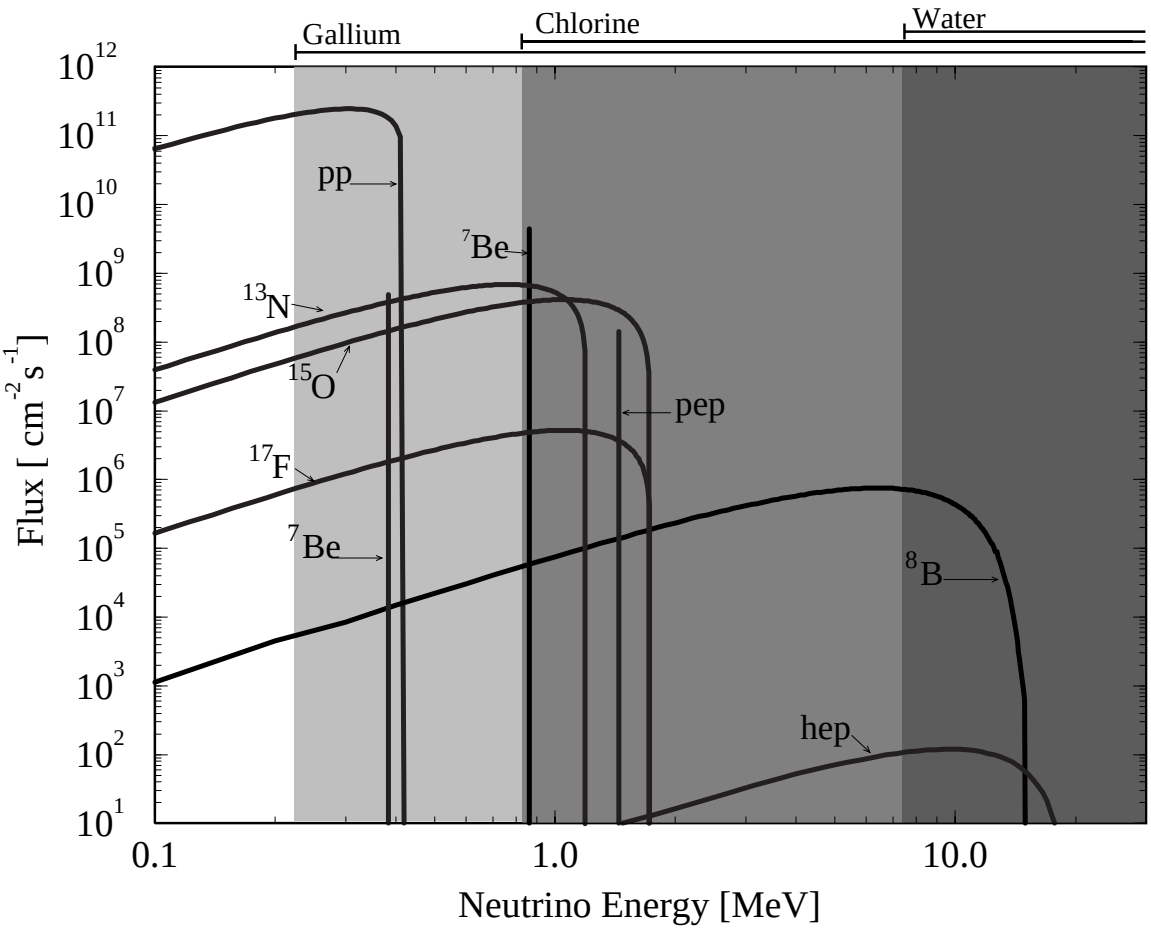

Figure 1.2: The Solar Neutrino Spectrum from Bahcall and Pinsonneault. Continuum sources are in units of number per cm^2/s/MeV, whilst line sources are shown as number per cm^2/s.

All that now remains is to measure the spectrum directly or determine the integrated flux over some region of the spectrum. The cross-sections for the neutrino interactions with various targets can be calculated and used to estimate the total number of counts expected for a particular experiment. Table 1.1 shows the threshold levels, reactions and locations of the four current solar neutrino experiments [3]. As can be seen, the existing experiments have provided a coarse spectroscopy of the solar ν spectrum.

1.2.2 Helioseismology

Any discussion of solar modeling would be incomplete without a brief mention of helioseismology. This is analogous to terrestrial seismology and provides information on the interior of the Sun by observing slight motions of its surface. The Sun acts as a resonant cavity whose oscillations can be observed by the Doppler shift in its spectral (absorption) lines. This was first observed by Leighton *et al.* [19] in 1962 but an explanation for these oscillations was

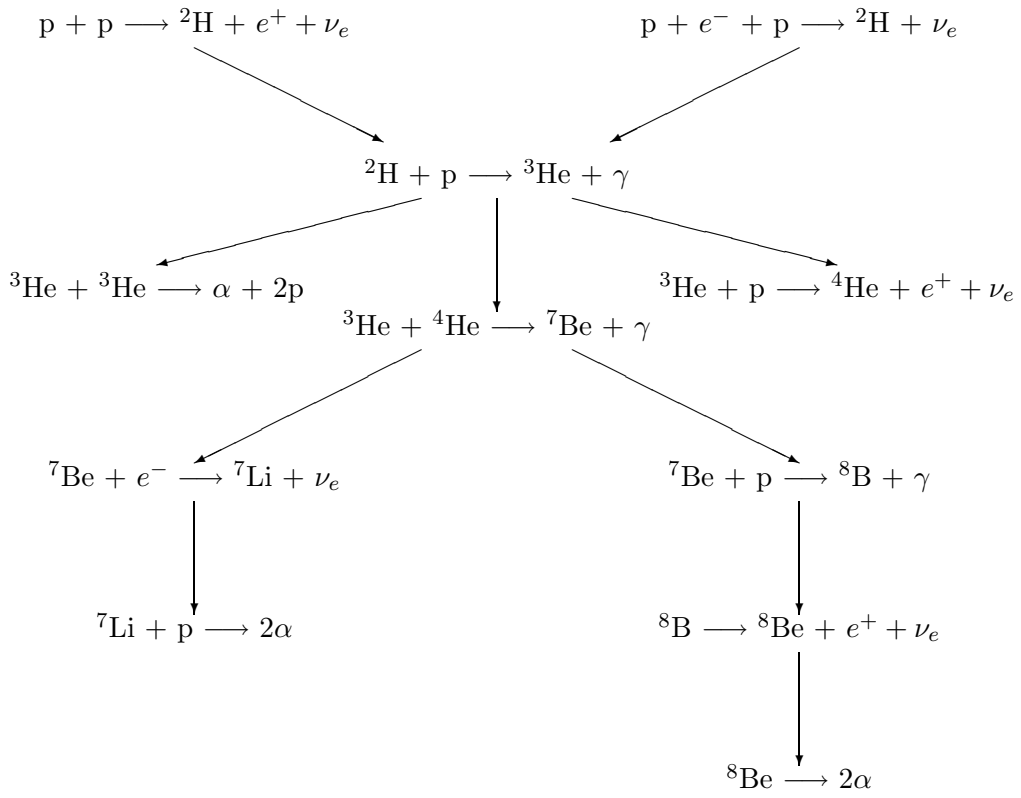

No.	Reaction	Termination (%)	τ (yr)	E_ν (MeV)	Abbrev.
1	$p + p \longrightarrow {}^2H + e^+ + \nu_e$	100	10^{10}	≤ 0.420	pp
2	$p + e^- + p \longrightarrow {}^2H + \nu_e$	0.4	10^{12}	1.442	pep
3	${}^2H + p \longrightarrow {}^3He + \gamma$	100	10^8		
4	${}^3He + {}^3He \longrightarrow \alpha + 2p$	85	10^5		
5	${}^3He + {}^4He \longrightarrow {}^7Be + \gamma$	15	10^6		
6	${}^7Be + e^- \longrightarrow {}^7Li + \nu_e$	15	10^{-1}	0.861 or 0.383	^{7}Be
7	${}^7Li + p \longrightarrow 2\alpha$	15	10^{-5}		
8	${}^7Be + p \longrightarrow {}^8B + \gamma$	0.02	10^2		
9	${}^8B \longrightarrow {}^8Be + e^+ + \nu_e$	0.02	10^{-8}	≤ 15	^{8}B
10	${}^8Be \longrightarrow 2\alpha$	0.02			
11	${}^3He + p \longrightarrow {}^4He + e^+ + \nu_e$	0.00002	10^{12}	≤ 18.77	hep

Figure 1.3: The 'pp' cycle. The termination percentage is the fraction of terminations that include the particular reaction.

Experiment	Reaction	Threshold	Location
Homestake	$\nu_e + {}^{37}\mathrm{Cl} \rightarrow e^- + {}^{37}\mathrm{Ar}$	0.8 MeV	United States
Kamiokande	$\nu + e^- \rightarrow \nu + e^-$	7.3 MeV	Japan
SAGE	$\nu_e + {}^{71}\mathrm{Ga} \rightarrow e^- + {}^{71}\mathrm{Ge}$	0.233 MeV	Russia
GALLEX	$\nu_e + {}^{71}\mathrm{Ga} \rightarrow e^- + {}^{71}\mathrm{Ge}$	0.233 MeV	Italy

Table 1.1: The energy thresholds for the four solar neutrino experiments.

Reaction			E_ν
${}^{12}\mathrm{C} + \mathrm{p}$	$\longrightarrow$	${}^{13}\mathrm{N} + \gamma$	
${}^{13}\mathrm{N}$	$\longrightarrow$	${}^{13}\mathrm{C} + e^+ + \nu_e$	≤ 1.199
${}^{13}\mathrm{C} + \mathrm{p}$	$\longrightarrow$	${}^{14}\mathrm{N} + \gamma$	
${}^{14}\mathrm{N} + \mathrm{p}$	$\longrightarrow$	${}^{15}\mathrm{O} + \gamma$	
${}^{15}\mathrm{O}$	$\longrightarrow$	${}^{15}\mathrm{N} + e^+ + \nu_e$	≤ 1.732
${}^{15}\mathrm{N} + \mathrm{p}$	$\longrightarrow$	${}^{12}\mathrm{C} + \alpha$	

Table 1.2: The CNO cycle. Only the main reactions are shown.

not provided until the early 1970's. Using Fourier techniques, it is possible to separate the component frequencies. Two modes of oscillation are involved: those which are caused by pressure or acoustic waves (known as p-modes) and those which are due to buoyancy fluctuations (g-modes). The p-mode oscillations are largely confined to the convective region and can not provide information on the density of the core where neutrino production occurs. It is still possible to determine the radial temperature and density distributions of the Sun from these measurements for comparison with distributions predicted by solar models. The g-mode oscillations are thought to penetrate much further into the core. Their measurement is much more difficult as their amplitudes decrease rapidly through the convective zone. The measurements made by helioseismology are in good agreement with the those predicted by SSMs (Figure 1.4 is taken from [5]). The most important aspect to consider is that this is another consistency check for SSMs.

1.3 Current Solar Neutrino Experiments

The neutrino's greatest asset in probing the stellar interior, its small reaction cross-section, also makes its detection on Earth difficult. In order to detect even a small fraction of the 65 billion solar neutrinos which pass through each square centimetre of the Earth every second, massive detectors must be used featuring many tonnes of target material. Currently, four experiments have reported results of solar neutrino detection. Three of them are radiochemical experiments whilst the other is a water Čerenkov detector. As the expected signal is so small,

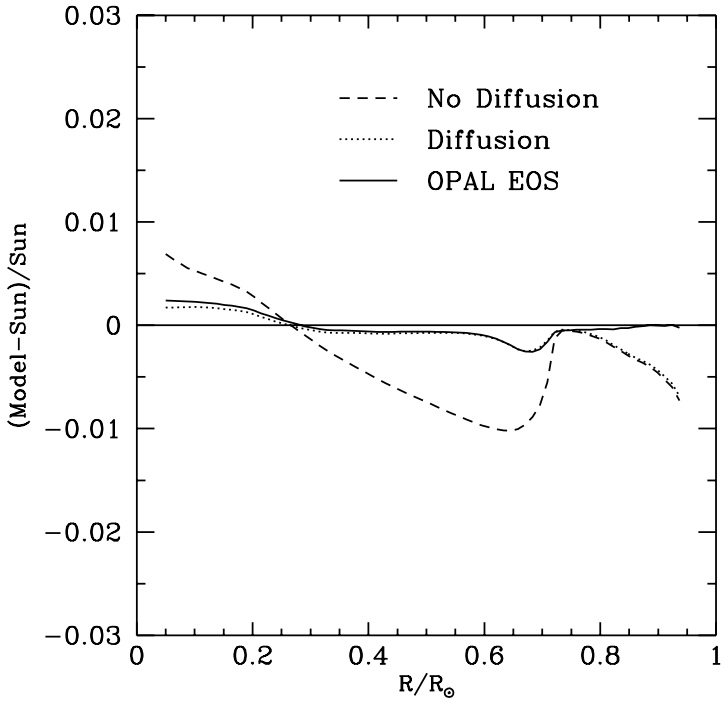

Figure 1.4: Comparison of sound speeds predicted by different standard solar models with the sound speeds measured by helioseismology.

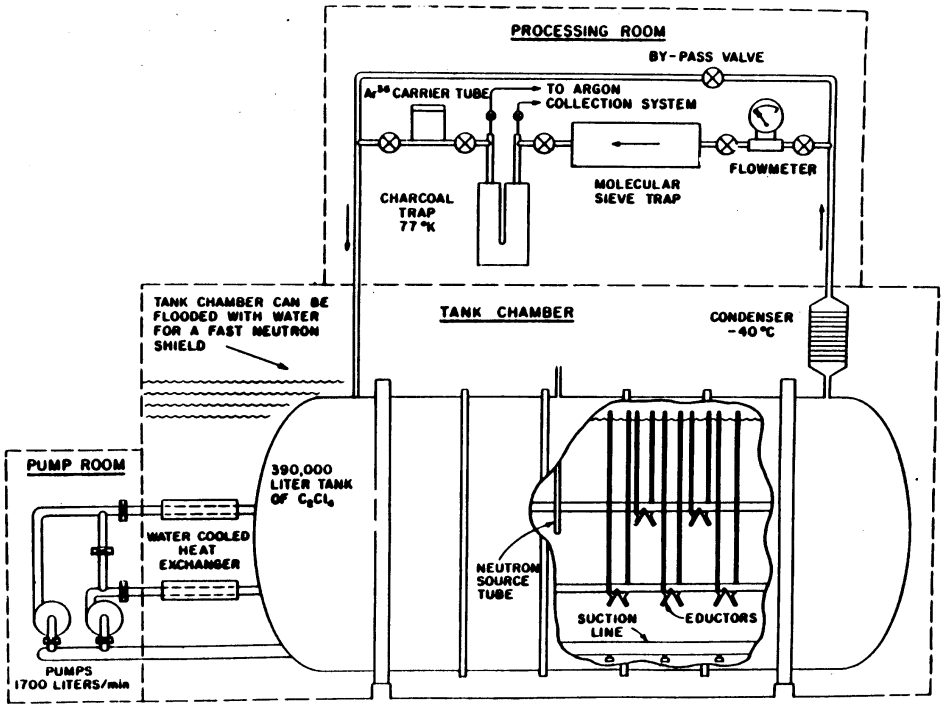

Figure 1.5: A schematic diagram of the Chlorine experiment.

all the experiments are deep underground to reduce backgrounds produced by cosmic rays. The experimental designs and results are discussed below.

1.3.1 Chlorine

The Chlorine experiment was the first and, for nearly 25 years, the only solar neutrino experiment. It is still in operation at the Homestake mine, in Lead, South Dakota at a depth of 4850 feet (equivalent to 4900 m of water as a shield, 4900 m.w.e.). The sensitive volume is 615 tonnes of liquid perchlorethylene (C_2Cl_4), a common dry cleaning fluid. This mass of fluid represents a target of 2.2×10^{30} atoms of ^{37}Cl. The neutrino-chlorine interaction is,

$$^{37}\mathrm{Cl} + \nu_e \longrightarrow {}^{37}\mathrm{Ar} + e^-, \tag{1.6}$$

and has a Q-value of -0.814 MeV. The Q-value is sufficiently low that the experiment is sensitive to neutrinos from all but the *pp* chain. Additionally, there is a large matrix element for the transition to the excited isobaric analogue state ($\mathrm{J^P} = \frac{3}{2}^+$, $\mathrm{T} = \frac{3}{2}$) at about 5 MeV, which enhances the sensitivity to ^{8}B neutrinos. The resulting ^{37}Ar, in either case, is unstable and decays with a half-life of 35 days back to ^{37}Cl by electron capture. This decay is characterised by the emission of 2.82 keV X-rays.

As only of the order of one ^{37}Ar atoms is produced every two days, the extraction of the few atoms of ^{37}Ar from the many tonnes of C_2Cl_4 is achieved by a complex chemical procedure.

Following this extraction, a known amount (of the order of a few tenths of a cc) of inert ^{36}Ar or ^{38}Ar is added to the tank. After 60 days of exposure, the argon is removed by sweeping the detector with helium. Any argon in the mixture is recovered using a charcoal trap cooled to liquid nitrogen temperature. The fraction of original carrier gas recovered provides an estimate of the extraction efficiency, which is typically 94%. The charcoal trap is heated and the trapped gas is swept out with helium. The resulting gas is passed over heated titanium metal to remove any non-noble gases and then through a gas chromatograph to separate other noble gases. The resulting Ar is then mixed with methane to produce a suitable gas for a small proportional counter. The counter is placed inside a sodium iodide detector, which acts to veto background events associated with external gamma activity. Additionally, the NaI itself is inside a large passive shield. The gas is then counted for at least 8 months (several half-lives).

The extraction efficiency for ^{37}Ar and the neutral carrier were shown to be equivalent using a small amount of tetrachloroethylene labeled with ^{36}Cl. This decayed to produce $^{36}Ar^{+}$. Activation analysis was then used to determine the quantity of ^{36}Ar recovered with a relative efficiency of $100 \pm 3\%$.

The main backgrounds in the Chlorine experiment arise from two sources: cosmic ray muons with their associated products and fast neutrons from the rock walls. The cosmic ray component was estimated at 0.4 ± 0.16 SNU by measuring the production rate of ^{37}Ar in small tanks placed at different levels in the mine, and then extrapolating to the depth of the main tank. The fast neutron flux can interfere via the reaction ^{37}Cl(n,p)^{37}Ar. The threshold for this reaction is of the order of 1 MeV. It was planned to flood the cavity with water to eliminate this background as the water would act as a neutron moderator. However, to date, this has yet to happened. A maximum likelihood analysis method was then used to separate the exponentially decaying signal from a time-independent background. The latest result, accumulated from twenty years of operation, is

$$\begin{aligned} \text{Observed Capture Rate} &= 2.55 \pm 0.14(\text{stat}) \pm 0.14(\text{syst}) \text{ SNU[11]} \\ \text{Theoretical Capture Rate} &= 9.3 \pm 1.4 \text{ SNU[4]} \\ \text{Ratio Observed/Theoretical} &= 0.28 \pm 0.02 \pm 0.04 \end{aligned}$$

The SNU is an acronym for solar neutrino unit, defined as 10^{-36} captures/target atom/sec. The theoretical rate is due mainly to the flux of ^{8}B neutrinos with approximately 1.3 SNU resulting from ^{7}Be.

1.3.2 Kamiokande

The Kamiokande experiment is a water Čerenkov detector originally designed to search for

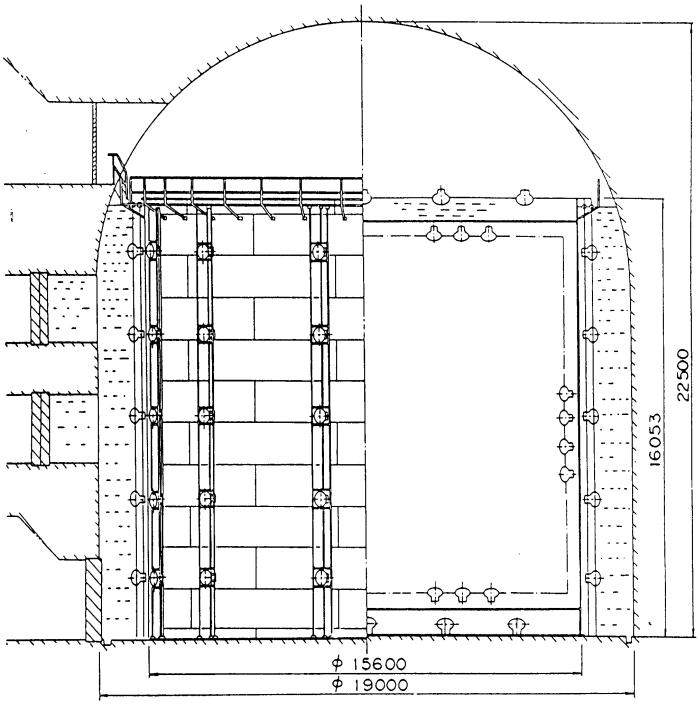

Figure 1.6: A schematic diagram of the Kamiokande experiment.

proton decay. It was then subsequently upgraded to be sensitive to ^{8}B neutrinos. This upgrade was performed in two stages. Firstly, the original Kamiokande detector was upgraded to Kamiokande II by reducing the trigger threshold to 9 MeV, to become sensitive to ^{8}B neutrinos. In order to achieve this lower trigger level, the water was purged of natural radioactivity by: recirculating it through ion-exchange columns, adding a degasification system to remove radon and hermetically sealing the detector using a radon free cover gas. However, the main advance was the use of fast electronics which resulted in a better fiducial volume. Still the trigger rate for the entire detector was 0.7 Hz a factor of 10^5 higher than the expected signal. Secondly, in 1990, the threshold was lowered to 7.0 MeV by: doubling the gain of the PMTs, replacing some 100 of the tubes that had failed, upgrading the fast electronics and placing wavelength-shifting plates in front of the PMTs to increase the amount of light collected. This upgrade was known as Kamiokande III.

Neutrino interactions with the water were observable because of the characteristic Čerenkov radiation emitted by the scattered high energy electron.

$$\nu_x + e^- \longrightarrow \nu'_x + e^{-\prime} \qquad \sigma_e \sim 6 \times \sigma_{\mu,\tau}$$

It was situated 1 km underground (2700 m.w.e) in the Kamioka mine, in the Japanese Alps. The detector contained 3 ktonnes of ultrapure water, although only the central 680 tonnes are

used for solar neutrino detection. The water was contained in a large cylindrical steel tank, 15.6 m in diameter and 16 m high, the inside of which had been painted black with a specially prepared epoxy. The inner volume of 2140 tonnes was viewed by 948 20-inch phototubes whilst the outer region was viewed by 123 PMT's. This outer volume acted both as a veto for cosmic ray muons and as passive shielding for natural radioactivity from the rock walls.

The solar neutrino signal could only be measured by accurately subtracting all the backgrounds.

1. This involved enforcing a fiducial volume cut to include only the inner 680 tonnes of the water target.

2. Selecting events between the trigger threshold and 20 MeV only. The lower level removes most of the γ backgrounds, whilst the upper removes electrons from the decay of stopped muons.

3. Through going muons are removed using the anti-coincidence detectors.

4. Decays from the spallation products of through going muons are removed by applying spatial and temporal cuts correlated to the previous muon track.

5. An additional γ ray cut is applied to low energy events where $\cos\theta_{wall} > 0.67$. This removes gamma rays which have reached the inner fudical volume by traveling almost perpendicular to the wall.

6. Finally a fit was performed on the remaining data assuming an excess of electrons pointing away from the Sun, consistent with the physics of neutrino electron scattering, superimposed on a flat, isotropic background. Thus, this is the only experiment to confirm the Sun as the source of the neutrinos detected.

The results of Kamiokande II and III were combined to give

$$\frac{\phi(^8\mathrm{B})_{\mathrm{obs}}}{\phi(^8\mathrm{B})_{\mathrm{SSM}}} = 0.423 \pm 0.03(\mathrm{stat}) \pm 0.05(\mathrm{syst})[12]$$

The result is given as a fraction of the expected flux rather than as a SNU value as the threshold for the experiment was not fixed. As the trigger level for the experiment was so high, Kamiokande II/III is only sensitive to the ^{8}Be neutrino and hence provides an absolute measure of that flux. This becomes important when trying to understand the results of all four experiments.

1.3.3 SAGE & GALLEX

Both gallium experiments, SAGE and GALLEX, rely on the reaction

$$\nu_e + ^{71}\mathrm{Ga} \longrightarrow e^- + ^{71}\mathrm{Ge} \tag{1.7}$$

which has a Q-value of 0.2332 MeV and, as such, is sensitive to all thermonuclear sources of neutrinos. Most importantly, this reaction is sensitive to neutrinos from the *p*-*p* chain which dominates the solar neutrino flux. The ^{71}Ge produced is unstable and decays by electron capture back to ^{71}Ga with a half-life of 11.43 days. The decay can be detected by observing the characteristic X-rays (K shell – 10.37 keV, and L shell – 1.17 keV). The great advantage of these experiments is that they are relatively insensitive to the solar model used. Assuming that the Sun is in hydrostatic equilibrium then to be consistent with the observed solar luminosity the minimum observed rate is 80 SNU.

The experiments differ in their methods of storing the gallium and separating the germanium. The SAGE experiment is based in the Baksan Neutrino Observatory, in the Northern Caucasus mountains, with an overburden of 4700 m.w.e. SAGE exploits the low melting point of gallium (29.8°) and uses 60 tonnes (initially 30 tonnes) of liquid gallium metal contained in eight reactor vessels, lined with Teflon. Initially, 70 mg of natural Ge carrier is added in the form of a Ga-Ge alloy to the reactors. After a typical four week exposure period, the Ge carrier and any neutrino induced ^{71}Ge atoms are extracted. A solution of HCl, H_2O_2 and H_2O is added to each reactor and the mixture is agitated intensively by teflon coated paddles and vanes inside each reactor. This method results in an aqueous solution of $GeCl_4$ and solutions from separate reactors are then vacuum siphoned off, combined and then concentrated by vacuum evaporation. The solution is then acidified with HCl and an argon purge is used to sweep the solution into a 1 litre volume of water. Multiple pass solvent extraction is used to purify the $GeCl_4$ which is subsequently converted into germane gas and then further purified by gas chromatography. The overall efficiency is typically $80 \pm 6\%$. The germane gas is then mixed with Xe and counted inside a sealed proportional counter. The counters are placed inside a sodium iodide veto chamber and calibrated at monthly intervals using an ^{55}Fe source, (5.9 keV). The SAGE collaboration's current result is

$$\text{Observed Capture Rate SAGE} = 69 \pm 10^{+5}_{-7} \text{ SNU[14]} \tag{1.8}$$

The GALLEX collaboration, based in the Gran Sasso laboratory, with an overburden of 3300 m.w.e., uses 30.3 tonnes of gallium in the form of acidified gallium chloride solution. The acidic nature of the solution (HCl is used) ensures that any Ge atoms produced are in the form of $GeCl_4$. Initially, 1 mg of germanium is added to the tank as a carrier. After 3 weeks of exposure the tank is purged with 1900 m^3 of nitrogen as the chloride form of germanium is extremely volatile. The nitrogen gas is then scrubbed with 50 litres of counter-flowing water. The extraction takes typically about 20 hours and results in an extraction efficiency of 99%. The solution is then extracted into carbon tetrachloride and then back-extracted into tritium-free water. Germane gas (GeH_4) is then synthesized and purified through gas

chromatography. The germane is then mixed with xenon (70% by volume) and placed inside a miniature proportional counter which has been specially designed to maximize the counting efficiency and reduce background levels. The detectors are then counted over a typical period of 6 months, whilst being calibrated, using three lines at 1.03, 5.09 and 9.75 keV, every 6 weeks. To reduce backgrounds further, the counters are inserted into a form fitting copper/lead housing to reduce space for radon and operated inside a Faraday cage which is itself inside a low activity lead shield of 8.6 tonnes. Inside this shield the counters are placed inside a sodium iodide detector (the 'active' position), to veto external backgrounds, or inside a copper shield, (the 'passive' position) to range out external backgrounds. The sodium iodide has a greater intrinsic background, but provides more diagnostic information. The GALLEX collaboration's current result is

$$\text{Observed Capture Rate GALLEX} = 69.7 \pm 6.7^{+3.9}_{-4.5}\ \text{SNU[15]} \tag{1.9}$$

It is noteworthy that the two experiments, relying on two separate extraction techniques, are consistent with each other. The results of the two experiments may then be combined yielding a result of

$$\text{Combined SAGE \& GALLEX results } 69.5 \pm 6.7\ \text{SNU} \tag{1.10}$$

which should be compared with the theoretical value of Bahcall [4] of 137 ± 8 SNU.

Recently both SAGE and GALLEX have performed calibration experiments using ^{51}Cr as a source of neutrinos. GALLEX used a $\sim$1.52 MCi source which was placed inside their tank for a period of approximately 4 months. The result expressed as a fraction of the total number of expected ^{71}Ge atoms is

$$\text{GALLEX} \qquad R = 0.97 \pm 0.11 \quad (1\sigma \text{ stat. \& syst.})$$

The SAGE collaboration used a smaller source of $\sim$0.509 MCi.

$$\text{SAGE} \qquad R = 0.93^{+0.25}_{-0.17} \quad (1\sigma \text{ stat. \& syst.})$$

Both these numbers are clearly consistent with unity and lead to the conclusion that the radiochemical experiments are operating as expected.

1.4 The Solar Neutrino Problem

All four solar neutrino experiments observe a deficit of solar neutrinos compared to the predictions of the standard solar model. This is not, however, the only problem with solar neutrinos. The results of the four experiments also indicate an energy dependent suppression of the solar neutrino spectrum [9][8]. As shown in Table 1.3, an analysis of three classes of experiments

Experiment	Homestake	SAGE & GALLEX	Kamiokande
Target	^{37}Cl	^{71}Ga	H_2O
Threshold	0.814 MeV	0.233 MeV	7.0 MeV (cut)
Observed	2.5 ± 0.2 SNU	74 ± 8 SNU	$\phi(\mathrm{B}) = 2.9 \pm 0.4$
Predicted	9 ± 1 SNU	132 ± 7 SNU	$\phi(\mathrm{B}) = 5.7 \pm 0.8$
pp	0	70	0
pep	0.2	3	0
^{7}Be	1.2	38	0
^{8}B	7.4	16	5.7
CNO	0.5	10	0

Table 1.3: Results from the three classes of solar neutrino experiments.

which are sensitive to different regions of the solar neutrino spectrum indicate that the largest suppression is in the middle of the spectrum (the ^{7}Be line and the lower energy part of the ^{8}B spectrum). In order to satisfy all of the results it is necessary to suppress the flux of ^{7}Be neutrinos with respect to the ^{8}B flux. In fact, the lastest model independent analysis of Heeger and Robertson [7] indicates that the best fit to all the experiments requires that the flux of ^{7}Be must be made *negative*. This is the modern solar neutrino problem. The following section details some of the possible solutions.

1.5 Resolving the Solar Neutrino Problem

1.5.1 Non-Standard Solar Models

There are many suggestions of possible modifications to the Standard Solar Model, with the aim of bringing the experimental and theoretical results into agreement. The general concept is to provide some mechanism of lowering the central core temperature T_c as the flux of ^{8}B and to a lesser extent ^{7}Be are particularly sensitive to this value ($\sim T_c^{25}$ and $\sim T_c^{11}$ respectively[6]). Indeed, the Chlorine data can be made consistent with the SSM if the central temperature of the sun, T_c, is lowered by about 7-8%. However, the results of the other neutrino experiments can not be explained away in this manner, and an article by Hata *et al.* [30] and Heeger and Robertson [7] shows that astrophysical solutions are excluded at the 96% C.L. assuming that none of the experiments are grossly incorrect (See Figure 1.7). The basic gist of this argument is as follows. As the Kamiokande experiment is only sensitive to ^{8}B neutrinos, it directly determines the flux of this branch. Using this as a constraint in the solar model, the central temperature is reduced by 4% and the resulting model can then be used to estimate the rate for the Chlorine experiment. This is then reduced to 4.4 SNU, compared to the observed value of 2.56 ± 0.21 SNU. As the Chlorine experiment is sensitive to ^{7}Be neutrinos which have a much

weaker temperature dependence it is therefore almost impossible to reconcile the experiments merely by altering T_c. The non-standard solar models are further rejected when the results from the gallium experiments are included as they are primarily sensitive to the *p*-*p* flux which is largely model independent.

Astrophysical and/or nuclear physical explanations generally predict that the largest suppression should be of the ^{8}B neutrinos (since they are made after and from ^{7}Be) and that the ^{8}B spectrum is not significantly distorted. Thus, unless most of the experiments are wrong or exhibit very large statistical fluctuations, a solution based on neutrino properties is favored.

1.5.2 Vacuum Oscillations

The Standard Model of particle physics (SM) *states* that neutrinos are both massless and left-handed. In comparison, the photon is *required* to be massless due to the global $U(1)$ symmetry of the electromagnetic field, a symmetry which guarantees charge conservation. However, massive neutrinos are common in many extensions of the SM, though none of the current experiments have provided evidence of a massive neutrino, but have only placed upper limits on their mass:

$$\begin{aligned} m_{\nu_e} &< 5.1\,\text{eV},\ \text{tritium } \beta \text{ decay} \\ m_{\nu_\mu} &< 160\,\text{keV},\ \pi \to \mu\nu_\mu \\ m_{\nu_\tau} &< 24\,\text{MeV},\ \tau \to \nu_\tau + 5\pi(\pi^0) \end{aligned}$$

All of the above radiochemical experiments are sensitive *only* to the flux of electron type neutrinos. Similarly, Kamiokande is sensitive mainly to electron type neutrinos as the cross-section for ν_μ and ν_τ is lower by a factor of 6-7. If the neutrinos were able to change flavour during flight then this could provide a solution of the SNP.

For oscillations to occur, neutrinos *must* be massive and the mass eigenstates (ν_1, ν_2, ν_3) *must not* be the same as the eigenstates of the weak interaction $(\nu_e, \nu_\mu, \nu_\tau)$. This is analogous to the mixing between states in the quark sector.

To demonstrate, a two component model with a single mixing angle θ will be used. The two sets of eigenstates are related by the expression

$$\begin{pmatrix} \nu_e \\ \nu_f \end{pmatrix} = \begin{pmatrix} \cos\theta & \sin\theta \\ -\sin\theta & \cos\theta \end{pmatrix} \begin{pmatrix} \nu_1 \\ \nu_2 \end{pmatrix} \tag{1.11}$$

where $\nu_f = \nu_\mu$, ν_τ or a sterile neutrino ν_s. The mass eigenstates are represented by ν_1 and ν_2, whilst ν_e and ν_f are weak eigenstates. Neutrinos produced by the Weak Interaction must be

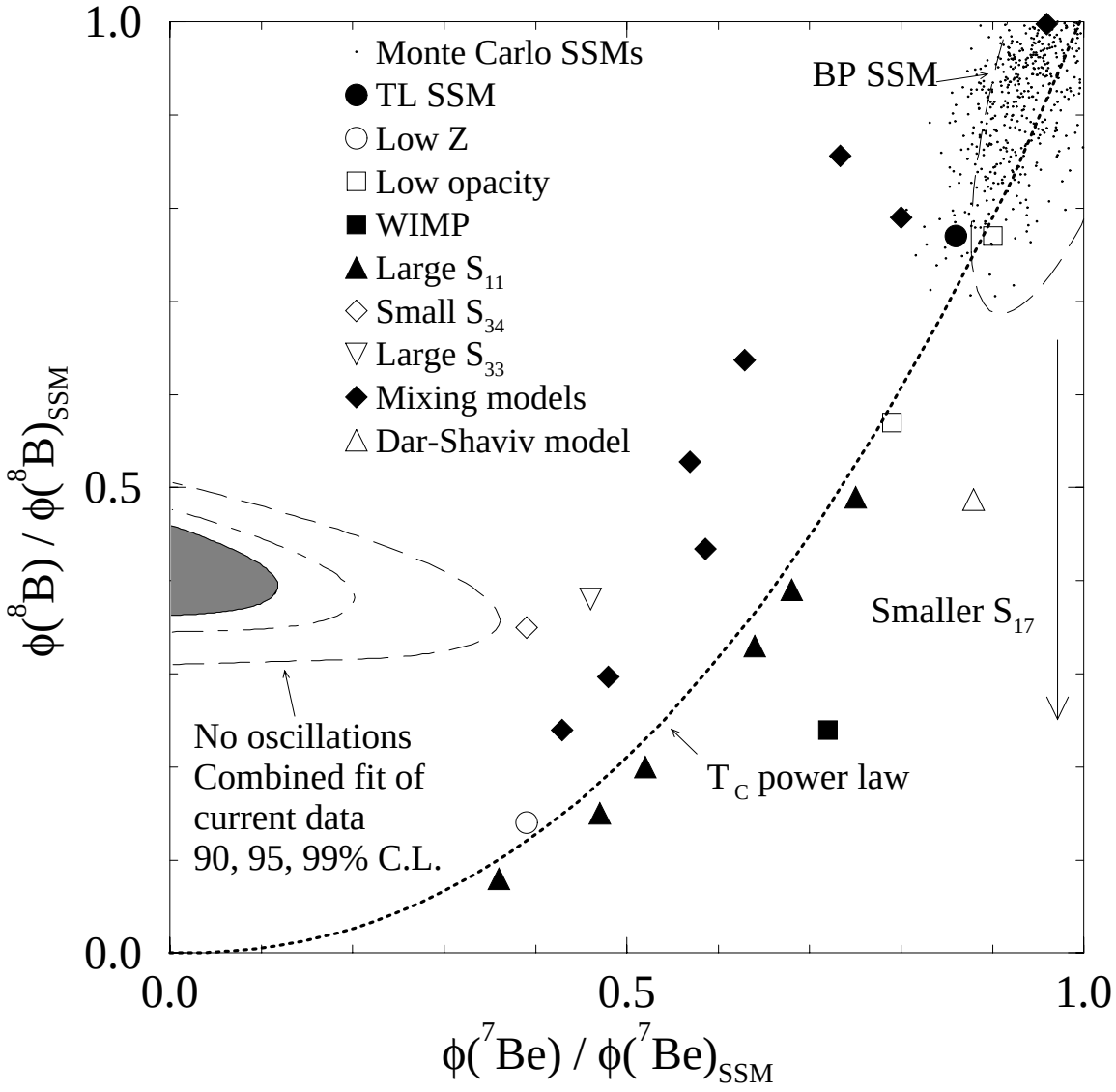

Figure 1.7: Chi Squared Fits to various SSMs from Hata*et al.* The T_c power law curve is from Bahcall 1992.

in a weak eigenstate. For example, consider an electron type neutrino produced at time $t = 0$,

$$|\nu(0)\rangle = |\nu_e\rangle \tag{1.12}$$

The general wavefunction for the propagation of this state can then be written as ($\hbar = c = 1$),

$$|\nu(t)\rangle = \cos\theta e^{-iE_1 t}|\nu_1\rangle + \sin\theta e^{-iE_2 t}|\nu_2\rangle, \tag{1.13}$$

since it is the states of definite momentum (the mass eigenstates) that propagate in space and time. The probability of the neutrino still being of type ν_e at time t under the assumption that $p \gg m$, and hence $x \sim t$, is then given by

$$|\langle\nu_e|\nu(t)\rangle|^2 = 1 - \sin^2 2\theta \sin^2 \frac{\Delta m^2 t}{2E} \tag{1.14}$$

where E is the average energy and $\Delta m^2 = |m_1^2 - m_2^2|$. The vacuum oscillation length L_{osc}, the distance required to change the phase by 2π is then given by

$$L_{osc} = \frac{4\pi E}{\Delta m^2} \tag{1.15}$$

The value of t can then be related to L, the Earth-Sun distance. Glashow and Krauss[16] have shown that a mixing angle of 45° (maximal mixing) and Δm^2 of order 10^{-12} is required to achieve a suppression factor of 2.5 for the Chlorine experiment. The vacuum oscillation is a valid solution to the SNP.

1.5.3 MSW Effect

Vacuum solutions must rely on near maximal mixing to explain the observed solar neutrino deficit. Another solution, proposed by Mikheev and Smirnov [21] based on earlier work by Wolfenstein[17], predict large oscillations, even for the case of small mixing angles. Because electron type neutrinos are able to interact with matter via both the charged and neutral current reactions, whereas other flavours can interact only by the neutral current, it is possible for the phase of the electron type neutrino to evolve differently from the others. These matter enhanced oscillations can lead to a large resonance if the density of matter during part of the neutrino's flight is correct. Appendix A contains the detailed mathematics of the MSW effect. The condition for resonance can be expressed in terms of the particle density n (electron density for oscillations to another weak eigenstate, electron density - 1/2 neutron density for oscillations to a sterile state.)

$$n = \frac{\Delta m^2 \cos 2\theta}{2\sqrt{2} G_F E} \tag{1.16}$$

If the density were constant from the neutrino's creation in the Sun to its detection on Earth then the resonance condition would again require fine-tuning. However, the conditions where the neutrinos are created are extremely dense ($\sim 150\text{g/cm}^3$) but as they move outwards the

density decreases. Over a range of energies (for a particular value of Δm^2 and θ) the neutrino traverses some region of just the right density for the MSW resonance to occur. The allowed regions of the (Δm^2, θ) phase space, using the limits of solar density, radius and the results of the four experiments and all of the nuclear and astrophysical uncertainties are shown in Figure 1.8. Therefore, measurements of the neutrino energy spectrum could decide which of the possible solutions is correct.

For the two possible solutions, it should be noted that the oscillation probability is energy dependent. This is extremely attractive for solving the modern SNP. This implies that the two solutions should be differentiable if an accurate measurement of the solar neutrino spectrum could be made, as different regions of the spectrum would be suppressed (see Figure 1.9).

1.5.4 Other Explanations

One suggestion which could simultaneously solve the Dark Matter problem, required not only for the closure of the universe but also to explain in particular the rotation rates of the outer rim of galaxies, is the existence of WIMP's (Weakly Interacting Massive Particles). If they were present in the Sun in sufficient numbers, then it would be possible for them to modify the energy transport in the solar core to sufficiently reduce the neutrino levels to those observed in the Kamiokande and Chlorine experiments. However, this would require the mass and scattering cross-sections to lie in an appropriate range. For the WIMP's to satisfy this their mass must lie in the range 2–10 GeV. However, there is no evidence to date for any WIMPs. Figure 1.7 shows that using the data from all the experiments the WIMP solution is ruled out well beyond the 99% confidence level.

Another suggestion is that some of the neutrinos may be transformed into some sterile state, which is unable to interact with the matter of the detectors. Similarly, if the neutrino were to possess a large magnetic moment it could undergo a transition through an interaction with the Sun's magnetic field. For the case of the Dirac neutrino this would lead to a right-handed neutrino, which would be unable to interact with matter and would appear to be 'sterile'. It was at one time thought that this might be a solution to the SNP as there appeared to be an anticorrelation between the flux of neutrinos measured by the Chlorine experiment and the number of sun spots. However, no such change was observed by the Kamiokande experiment and further analysis of the Chlorine data is not consistent with any correlation.

If however, there exists a sterile neutrino which is undetectable, the theories of vacuum oscillations and MSW effects may be applied. The only conceivable difference would be a reduction in the total neutrino flux observed. However, none of the current generation of solar neutrino detectors is able to observe the total neutrino flux at such a level that it can be extracted from the electron-type flux.

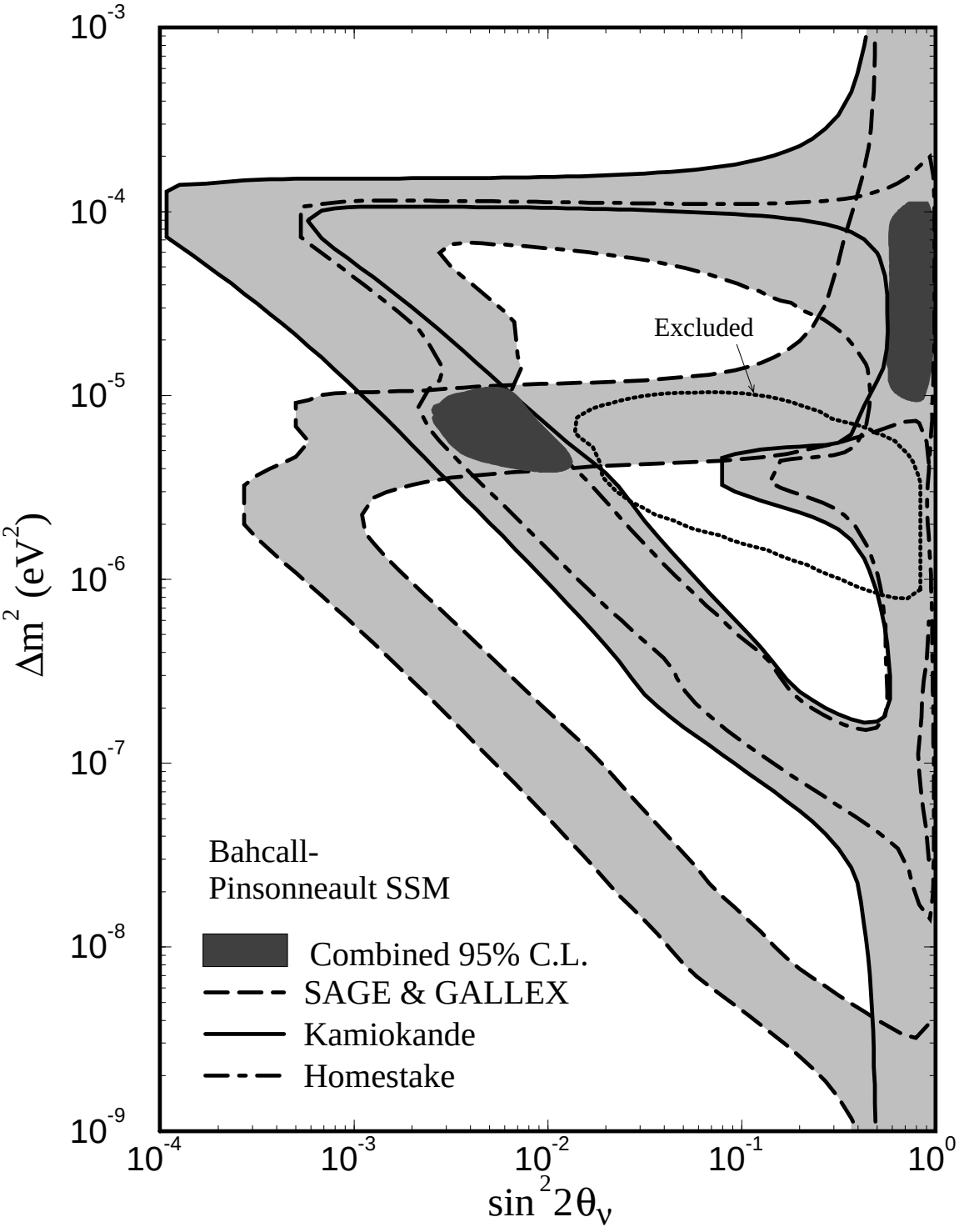

Figure 1.8: The allowed phase space using the BP SSM.

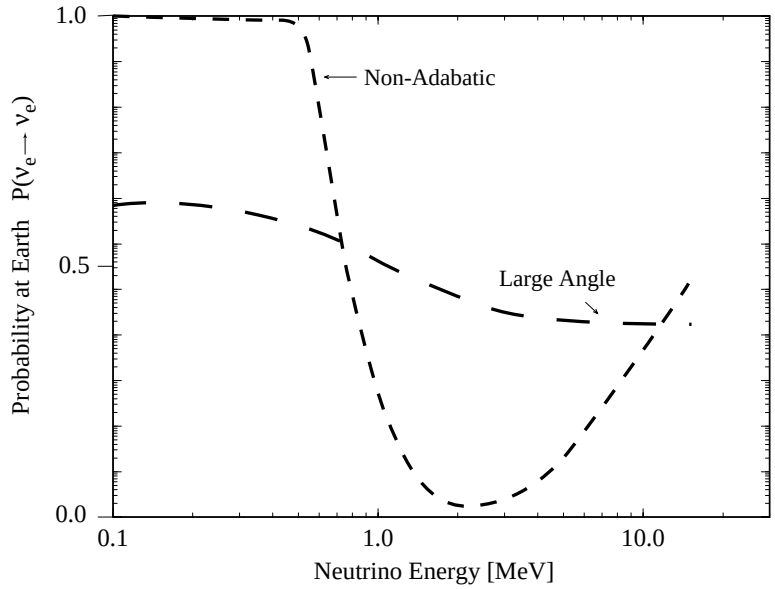

Figure 1.9: Survival probability for non-adiabatic and large angle solutions.

A further possibility would be if neutrinos were able to decay during their transit from the Sun to the Earth. However, the detection of neutrinos from SN1987A in both the IMB and Kamiokande detectors rules this out, for if neutrinos were able to decay on the order of the Sun-Earth timescales ($\sim$ 8 minutes) then no neutrinos would have survived from the supernova. In addition this solution does not provide for the energy dependent suppression of the solar neutrino flux necessary for solving the modern SNP.

In conclusion, other explanations of the SNP have been raised but do not seem to have the simple elegance of the MSW solution which supplies both suppression of the ν flux and the energy dependence while requiring only a minimal extension to the successful electro-weak theory. In addition, the application of the MSW effect to the neutrino spectrum resulting from the SSM's agrees well with the current experimental values and results in a value for the central temperature of the Sun which is consistent with the predictions of SSMs.

1.6 Prospects for Further Experimental Results

Although the existing solar neutrino experiments have provided valuable and intriguing data, the next generation of neutrino detectors will allow a higher precision measurement of the solar neutrino flux and its spectrum. In addition, these experiments will focus on physics directly manifest as neutrino oscillations and independent of SSM calculations.

Superkamiokande (SK) is a larger version of the Kamiokande experiment. It features 50,000 tonnes of ultrapure water as its target although the fiducial cuts, to remove events due

∼60 events/day	standard solar model
∼35 events/day	vacuum oscillation
∼38 events/day	MSW solution at high angle
∼18 events/day	MSW solution at small angle

Table 1.4: The theoretical number of electron neutrino interactions observed above 250 keV in counts per day for Borexino.

to activity in the wall of the detector and the photo-tubesreduce this value to 22,000 tonnes. It uses 11,146 20-inch PMTs for its inner counter and 1,857 8-inch PMTs in its outer counter. The outer counter is designed to act as a veto for through going particles. Assuming the SSM, the detector should record 8,400 neutrino-electron scattering events per year, above the 5 MeV threshold. This is extremely large and data from 27 days of operation have yielded the same number of events as 1000 days of data from Kamimokande III. Because of its large mass and high count rate, SuperK may be able to differentiate between the different possible ν oscillation solutions within two years of running by gaining adequate statistics on the ^{8}B neutrino spectrum shape.

Borexino will be a real time solar neutrino experiment. It consists of an 8.5 m diameter transparent nylon inner vessel filled with 300 tons of liquid scintillator and viewed by about 2000 photomultipliers coupled to light concentrators. The PMTs are mounted on a 13.7 m diameter sealed stainless steel sphere. The sphere is immersed in an 18 m diameter by 18 m high cylindrical tank containing ultra pure water. The liquid buffer between the nylon inner vessel (IV) and the sphere will be either pure pseudocumene or pure water at a level of 10^{-14} g/g with respect to U. A software fiducial volume of 6 m diameter corresponding to 100 tons of scintillator will be defined as a final shielding for the external background.

The scintillator is made of an aromatic solvent (pseudocumene or PXE) and a fluor (PPO or terphenil) with a wavelength light shifter added (bis-MSB) to reduce adsorption reemission light effects. As with SK, the reaction observed will be the neutrino electron scattering but with a threshold of 250 keV.

Their main physics goal is a measurement of the ^{7}Be neutrino flux, the part of the spectrun which must be surpressed by MSW for fluxes measured by current experiments to agree with the Standard Solar Model. As the light collected is scintillation and not Čerenkov light there is no possibility of measuring an absolute spectrum. Instead the resulting spectrum is convolved with the response of the scintillator, which acts to smear the energy to lower values. The expected theoretical rates are shown in Table 1.4

To allow the low energy threshold of 250 keV Borexino requires a very low background, and as such the very highest purity component material. The required purity for the materials

Material	Limit of U
stainless steel	10^{-9} g/g
water in the external tank	10^{-10} g/g
Photomultiplier	10^{-10} g/g
liquid buffer	10^{-14} g/g
inner vessel	10^{-12} g/g
scintillator	10^{-16} g/g

Table 1.5: The upper limits of U activity in Borexino.

are shown in Table 1.5

The purity requirements are stringent not only because of this low energy threshold but also because the scattered electron will produce scintillation light which is isotropic instead of the characteristic Čerenkov cone in SK. This destroys any directional information and does not allow for neutrino signal separation based on the angle of events towards the Sun.

The third experiment under development is the Sudbury Neutrino Observatory (SNO),a heavy water Čerenkov water detector. The advantage of heavy water is that the neutrino is able to interact with it in two different ways. The charge current reaction produces an electron from an interaction of a ν_e with a deuteron nucleus. However, a second reaction, the neutral current reaction, produces a free neutron from the interaction of any active neutrino flavour with the heavy water. With these reactions it is possible to measure both the electron and total neutrino fluxes simultaneously. As this experiment forms the backbone of this thesis, a fuller description is given in the following Chapter.

Chapter 2

The Sudbury Neutrino Observatory

2.1 Detector Description

The Sudbury Neutrino Observatory (SNO) is currently under construction in an INCO nickel mine near Sudbury, Ontario. Shaft number nine, where the detector is being constructed is the second deepest continuous shaft in the western world and affords a large rock overburden of 6800 feet (5900 $m.w.e$) which reduces the through going cosmic ray component to only four muons per hour, with only one per day stopping in the detector. The barrel shaped cavity for the experiment (33 m high and 22 m in diameter) is large enough to contain a 10 storey building and is approximately 1200 m from the shaft. This shape is the strongest configuration for an excavated room. A schematic of the detector is shown in Figure 2.1.

The most important aspect of the detector is its use of 1 ktonne of 99.92% enriched heavy water (D_2O) as the active target, which allows a measurement, not only of the electron type neutrino flux, but also of the total neutrino flux. The physics of the neutrino's interaction with heavy water is discussed in Section 2.2. The heavy water is contained in a specially designed, low activity acrylic sphere of radius 6 m and thickness 5 cm, although an equatorial 'belly-band' is twice as thick. Acrylic was chosen for two reasons; it is optically transparent at the wavelengths required for observing Čerenkov radiation, and it is capable of being manufactured at the level of 1 ppt (1 part in 10^{12} by weight) with respect to U and Th. The need for such low levels of natural radioactivity is covered in Section 2.4.

The central volume is observed by 9500 Hamamatsu 8-inch diameter phototubes at a distance of 2.5 m from the acrylic wall. Each phototube has mounted upon it a concentrator which increases the photocathode coverage by 75% whilst reducing the effective angle that the tube can observe. This helps to reduce the number of false triggers caused by light originating in neighboring tubes (due to radioactivity in the glass). This restriction is chosen such that all tubes are able to view a central sphere of radius 7 m. The tubes and their reflectors are mounted in a phototube support structure, constructed of four inch stainless steel tubing which forms a three frequency icosohedron. The rest of the cavity is filled with 7300 tonnes

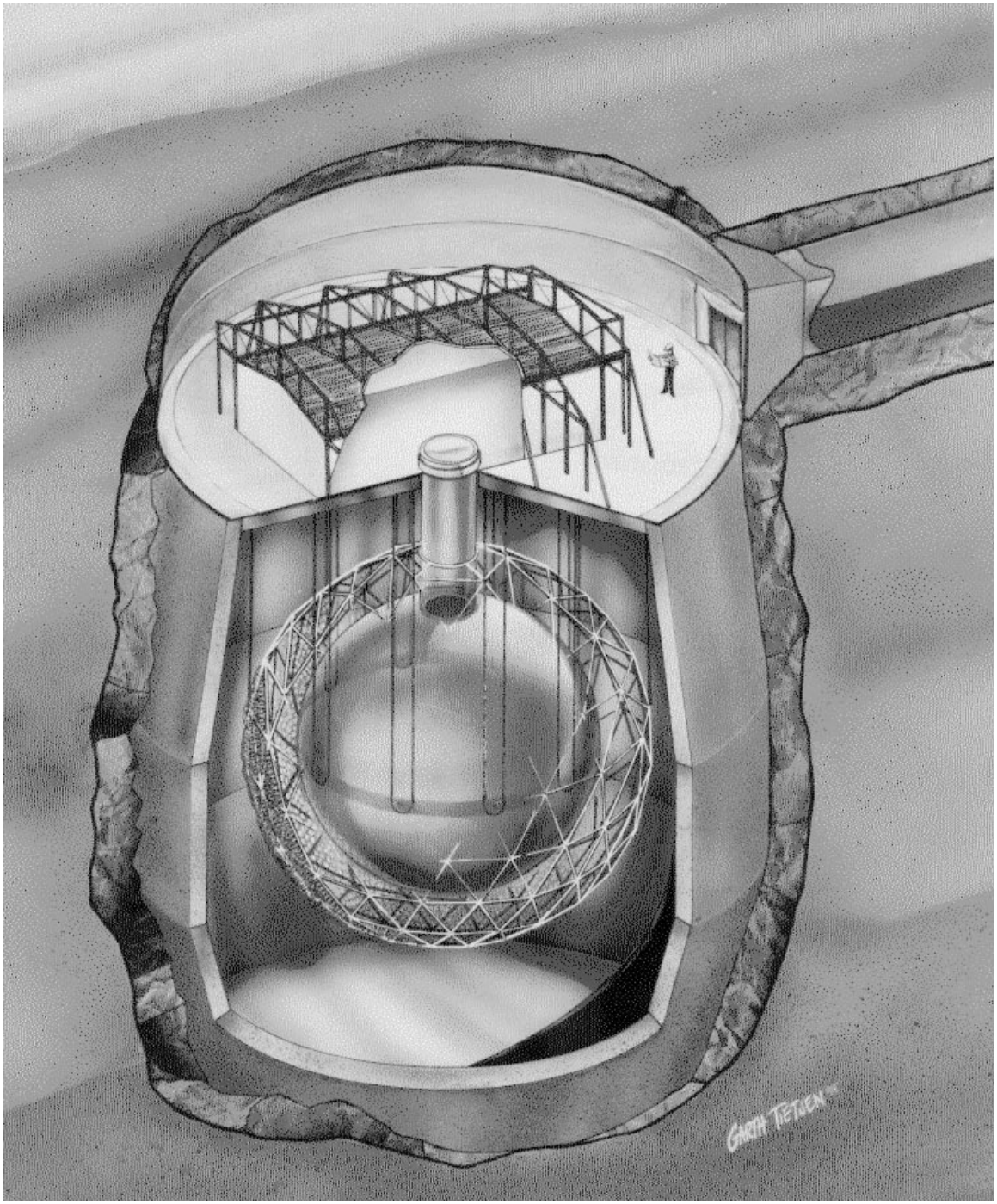

Figure 2.1: The SNO Detector.

Case	Charged Current	Electron Scattering	Neutral Current
SSM	9750	1100	5000
Vacuum Oscillations	3260	480	5000
MSW (Adiabatic)	3750	645	5000
MSW (Non Adiabatic)	3750	488	5000
SSM/3	3250	366	1667

Table 2.1: The predicted event rate in SNO per ktonne-year for an energy threshold of 5 MeV, using the Bahcall 1992 SSM. The Neutral Current rates are for the total number of neutrons produced.

of ultra pure light water to provide shielding from γ-rays and fast neutrons originating in the cavity walls. It also provides a target for electron-neutrino scattering and $\bar{\nu}_e p$ (important for super-novae), which are covered in more detail in Section 2.2.

Magnetic field coils have been built into the detector walls (Helmholtz coils) to reduce the effect of the vertical component of the Earth's magnetic field to less than 2 mT. This minimizes the dependence of the photomultiplier's response to its orientation in the cavity. This is important as all the interactions taking place inside the detector (with the exception of the neutral current process in the presence of ^{3}He detectors) produce Čerenkov radiation which is then detected by the photomultiplier tubes. The temperature of the entire experiment is kept at $\sim 10^\circ$C (compared to the rock wall temperature of $\sim 40^\circ$C) to reduce the noise levels in the phototubes. This reduction in noise levels will enable the reconstruction of an event, using timing, location and number of hits, to within 30 cm at 5 MeV, and to determine the direction and energy of the radiating electron. The position information is extremely important as it used to reject background events which occur outside of the heavy water.

2.2 Neutrino Interactions

For solar neutrino detection, SNO has three expected reaction mechanisms. Each reaction mechanism and its detection method are outlined below. Table 2.1 lists the expected number of events per ktonne-year using the Bahcall (1992) standard solar model.

2.2.1 Charged Current $\nu_e + d \rightarrow p + p + e^-$

This reaction, referred to as the 'inverse β-decay of the deuteron', is unique to SNO. It is sensitive only to the electron type neutrino and has a Q value of 1.44 MeV. Because of kinematic constraints, the majority of the neutrino's energy is transferred to the electron, with $E_e \simeq E_\nu - 1.44$ MeV, whilst the angular distribution is given by $W(\theta) = 1 - \frac{1}{3}\frac{v}{c}\cos\theta$. The interaction

is detected by the Čerenkov radiation emitted by the high energy electron. The electron's energy is recorded by the number of photon hits on the PMTs, 9.6 hits per MeV[22], though an *insitu* calibration must be performed to confirm this number and the response of the detector.

2.2.2 Elastic Scattering $\nu_x + e^- \rightarrow \nu_x + e^-$

This reaction is flavour blind as any of the neutrino species may scatter by Z^0 exchange. However, there is an enhancement by a factor of 6–7 in the cross-section for the electron neutrino as it may also scatter by $W^{\pm}$ exchange. Again the reaction is detected via the Čerenkov radiation from the scattered electron, and the resulting electron energy spectrum may be related to the original solar neutrino spectrum as in the Kamiokande experiment. The final state is strongly forward peaked with 90% of electrons with greater than 5 MeV of energy being contained in a cone of half-angle 18°. Although the expected rate of 1100 counts per year [Table 2.1] is only of order 10% of the charge current signal, the directional information allows the separation of the two. Studies by the Oxford group [31] have shown that by using neural network analysis and other analysis techniques of the hit pattern on the PMT it is possible, in a statistical manner, to separate the two interactions.

2.2.3 Neutral Current $\nu_x + d \rightarrow n + p + \nu_x$

Similarly, the neutral current reaction is flavour blind, but in this case there is no enhancement of the electron type neutrino. The cross section is the same for all active species above 2.223 MeV (the binding energy of the deuteron). Unlike the other two reactions, no particle capable of producing Čerenkov radiation is released. The measurement of this reaction relies on the detection of the free neutron produced. All the detection methods discussed in Section 2.5 required that the neutron be thermalised as the capture cross sections are much higher at thermal energies. Fortunately heavy water is an excellent moderator, but the thermalisation process results in the loss of all energy and directional information. The creation position of the neutron is preserved at the order of one metre which corresponds to the mean neutron thermalisation distance in heavy water. As the detection of this particular reaction is the basis for this thesis, the detection methods are covered more completely later in this Chapter.

2.2.4 Other Reactions

$$\bar{\nu}_e + d \rightarrow n + n + e^+$$
$$\bar{\nu}_e + p \rightarrow n + e^+$$

The detection of the final two reactions from the Čerenkov light of the positrons and the detection of the free neutrons, would be a rare event. They are of little concern to the solar

Reaction	Target	Burst Phase	Cooling Phase
$\nu_e + d \longrightarrow p + p + e^-$	D_2O	10	33
$\nu_x + e^- \longrightarrow e^- + \nu_x$	D_2O/H_2O	1	16
$\nu_x + d \longrightarrow n + p + \nu_x$	D_2O	6	760
$\bar{\nu}_e + d \longrightarrow n + n + e^+$	D_2O	0	20
$\bar{\nu}_e + p \longrightarrow n + e^+$	H_2O	0	120

Table 2.2: Total number of events per ktonne-year of target from a SuperNova at 10 kpc.

neutrino problem as the Sun is not expected to produce significant numbers of anti-neutrinos (a small number are produced in solar flares). However, should the gravitational collapse of a nearby star (Type II SuperNova) happen during the lifetime (∼10 years) of the SNO detector (optimistically estimated at 10%), then it should be possible to measure the resulting neutrinos and anti-neutrinos from the explosion. The expected number of events for each reaction from a supernova 10 kpc from the Earth is shown in Table 2.2.

2.2.5 Discussion

SNO's greatest asset is that it is, in the words of John Bahcall, an 'equal opportunity' detector. It has the ability to measure both the flux of ν_e (charged current, CC) and the *total* ν flux (neutral current, NC). The experiment is therefore self-normalising, to the extent that both cross-sections are understood, and the ratio of CC events to NC events in comparison to the calculated ratio will differentiate the two possible solutions to the SNP; if the ratio is less than the calculated value then neutrino flavour oscillations must be occurring, if the ratios are equal then either too few neutrinos are being produced or they are oscillating into a sterile state. However, it has the great advantage that the result is independent of any solar model. For completeness, it should be noted that its is not strictly the neutrino interaction cross sections that must be known accurately but rather the ratio of these cross sections, which is simple to calculate.

In addition to this, SNO like Kamiokande, is a real-time experiment, allowing the measurement of changes in the neutrino flux in a matter of hours rather than the weeks associated with the radio-chemical experiments. SNO is superior to the original Kamiokande experiment as its will have a much larger event rate allowing low statistical errors over a short period of running. In fact, a measurement of the secular variation of the Earth's orbit should just be possible within two years of running as a check on the solar origin of signals[20].

SNO's lower threshold and higher energy resolution should also allow it, via the charge current interaction, to measure the shape of the ^8B neutrino spectrum. This may allow discrimination between the two possible MSW solutions as well as the vacuum oscillation solutions

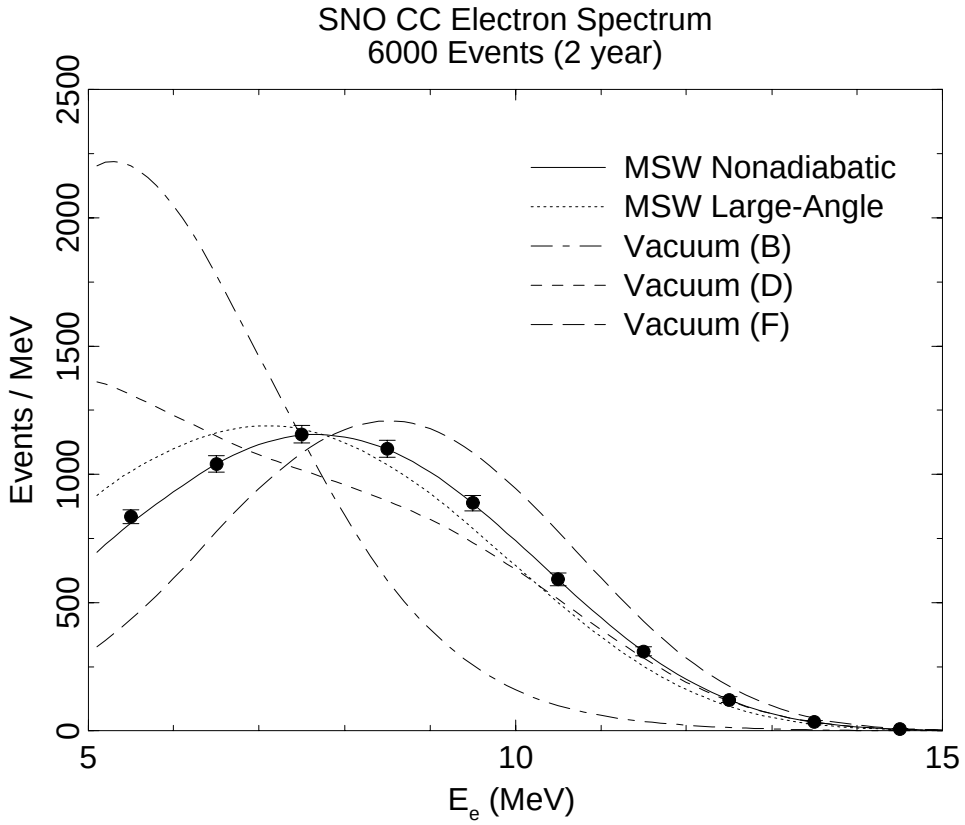

Figure 2.2: The resulting neutrino spectrum from the two possible MSW solutions and the vacuum oscillation solution. From top to bottom they are the MSW adiabatic solution, the MSW large angle solution and the vacuum oscillation solutions. It should be noted that the shape of the large angle solution is the same as the undistorted ^{8}B spectrum.

as the conversion probabilities are a strong function of neutrino's energy. Figure 2.2 demonstrates the difference between the two spectra. It should be noted that the resolution of these two possibilities is highly dependent on the knowledge of the background levels in SNO. Figure 2.3 shows the energy spectrum for signals and backgrounds along with the total sum. This should be compared with the spectral distortion induced by the two possible MSW oscillation solutions. The difference between the two solutions is most pronounced in the 5 to 8 MeV region implying that backgrounds in this region should be reduced and well understood.

Finally SNO's ability to measure the flux of (anti-)neutrinos from a possible supernova would set a limit on the mass of other neutrino species from the time distribution of events. A mass difference between the electron type neutrino and any other flavour will result in the second flavour arriving slightly later. It is estimated that a limit of the order of 30-50 eV on the mass of the neutrino could be made in this manner.

2.3 Detector Calibration

Detector calibration is required to understand the response of the detector in both the background and ^{8}B regions of the spectrum. The calibration is then used to cross check and define some of the parameters in the Monte Carlo simulation of SNO. Other experiments which have used water Čerenkov detectors have found discrepancies between their experiments and Monte Carlos. The IMB detector, designed to look for proton decay, required an overall factor of 0.53 to reconcile their prediction of phototube hits with measurements made of through going muons. Similarly, Kamiokande required a factor of 0.85 to correct its Monte Carlo simulation. A variety of reasons have been suggested for this loss of efficiency; the counting efficiency of single photoelectrons in the photomultipliers, optical attenuation in the water are all possibilities, but the fact remains that an *insitu* measurement of the detector's response must be made. The SNO collaboration's initial work on the small scale test detector required a factor of 0.82 to reconcile their measurements. These discrepancies may be attributed to difficulties in understanding the response of the detectors. In comparison, SNO has made a substantial effort to model and measure the performance of its components to remove these discrepancies. However, an insitu calibration is essential to give confidence in the accuracy of the modeling. To show the importance of the calibration it should be noted that in Figure 2.3 the energy spectrum from one year of running for the various expected backgrounds and signals along with the cumulative spectrum *i.e.* the spectrum which will be measured by SNO. To distinguish the possible solutions of the SNP it is most important to examine the shape of the ^{8}B spectrum. If the response of the detector is not exactly known for all possible sources of radiation then this determination becomes near impossible.

To this end a variety of sources have been suggested to calibrate SNO over a sufficiently large energy range using both γ rays and β particles. Table 2.3 lists these sources and their respective energies. SNO must also be calibrated for its efficiency for neutral currents/neutron captures. (Neutron transport is also modeled in SNOMAN (SNO Monte carlo and ANalysis code) using the MCNP (Monte Carlo N-Particles) libraries.) The current suggestion is to use a tagged ^{252}Cf source. This emits four neutrons per decay along with several γ-rays. The scintillator surrounding the source emits a short burst of light with every decay, allowing the neutron emitted to be tagged.

2.4 Purity Requirements

To measure the small number of neutrino interactions expected per day, excessive care must be taken with the materials used to make the detector to reduce the number of background events. In addition the level of any contaminants must also be verifiable. There are three

Reaction	Energy	Comments
^{2}H(n,γ)^{3}H	Eγ = 6.25 MeV	
^{3}He(n,γ)^{4}He	Eγ = 21 MeV	Requires fast neutrons
^{3}H(p,γ)^{4}He	Eγ = 20 MeV	Requires accelerated protons
^{35}Cl(n,γ)^{36}Cl	Eγ = 8.6 MeV	Multiplicity of γ's
^{11}B(p,γ)^{12}C	Eγ = 11.7, 4.4 MeV	Requires accelerated protons
Decay	β End point	Comments
$^{16}\mathrm{N} \rightarrow {}^{16}\mathrm{O} + e^- + \bar{\nu}_e$	Q = 10.4 MeV	26% τ = 7.13 s
	Q = 4.3 MeV, Eγ = 6.1 MeV	68%
$^{8}\mathrm{Li} \rightarrow {}^{8}\mathrm{Be} + e^- + \bar{\nu}_e$	Q = 13.1 MeV	τ = 0.84 s
Source	Energy	Comments
^{252}Cf $\rightarrow$ fission	Maxwellian distribution of neutron energies	Fission releases four neutrons with associated γ-rays per decay

Table 2.3: Proposed list of calibration sources for SNO.

principal sources of background radiation; cosmogenic, direct Čerenkov production and photodisintegration. For the latter two, the main sources are members of the long lived ^{232}Th and ^{238}U series (shown in Appendix D), and ^{40}K.

Cosmogenic is, at first glance, the least problematic of the three. The only cosmic ray component, besides neutrinos, which are able to penetrate to the depth of the SNO detector are muons. The calculated rate is only $\sim$ 100 muons per day passing through the detector with only one of these stopping inside the detector. Experience with the Kamiokande experiment has shown that it is possible to remove the through going muon and any induced spallation products by applying a spatial and temporal cut on the data as the resulting products have short lifetimes ($t_{1/2} < 1$ s). However, this estimate is based only on the production of spallation *insitu*. The effects of cosmic radiation on additives, such as those required for measuring the neutral current signal, must also be taken into consideration, and these are discussed more thoroughly later in this Chapter. The effects of cosmic rays on the light water, heavy water and acrylic used to build the vessel are negligible as no long lived isotopes are capable of being produced. The only isotopes likely to be produced are ^{7}Be, ^{10}Be and ^{14}C but all are below the Čerenkov threshold.

The direct Čerenkov radiation arises from the production of electrons with energies above threshold, either directly or by Compton scattering, from radioactive decays *insitu*. Although this may not seem problematic at first, as there are few decays from the U and Th chains above the threshold limit of 5 MeV, the effect of phototube noise, multiplicity, coincidences of decays and the intrinsic resolution of the detector make it possible to erroneously reconstruct an event with greater energy than it truly possesses. Figure 2.3 shows the effect of these decays

	^{232}Th	^{238}U
D_2O	4×10^{-15}	5×10^{-14}
H_2O	1×10^{-13}	1×10^{-12}
Acrylic	2×10^{-12}	4×10^{-12}

Table 2.4: Limits on the U and Th contaminants in the acrylic vessel and light and heavy water. The units are grams of contaminant per gram of material.

on the expected spectrum. The majority of the low energy background 'wall' is due to β's and γ's from the PMTs which are incorrectly reconstructed in the D_2O. However, even given the purity of the D_2O there will still be sufficient activity to produce a secondary low energy wall. It is the level of this internal β-γ background which is most relevant to the charge current threshold. Should the threshold rise much higher than 5 MeV it will be difficult to distinguish between the two possible MSW solutions to the SNP as it is over this region that the spectra differ most.

The photodisintegration of the deuteron can be caused by any photon above the threshold level of 2.223 MeV. Any neutron produced by photodisintegration is indistinguishable from one produced by the neutral current interaction. The most important isotopes are ^{208}Tl and ^{214}Bi which produce γ-rays above this threshold. The full decay scheme of the U and Th chains is contained in Appendix D. However, in pure D_2O, the probability of photodisintegration is only of the order of 0.2% due to the photon primarily Compton scattering. Even given this low probability, special care has been taken to limit the radioactivity of the components used in the detector. As the phototubes have been made using low activity glass, coupled with the 2.5 m of light water shielding, the dominant source of these neutrons is from the acrylic vessel and any material in the heavy and light water. To achieve a photodisintegration signal of the order of 1 neutron produced per day, there are strict limits on the levels of U and Th for each material. These levels are shown in Table 2.4. The total limit for any objects/substances placed in the heavy water are set so they should not produce more events than the total volume of the D_2O. Given the quality of the heavy water, this corresponds to less than 3.7 μg Th and 45μg U for any additives.

Measurements taken from samples of the acrylic to be used in the construction of the vessel are encouragingly below the levels required. Currently, both the heavy and light water are above these levels. Should the level of the light water not be reduced the resulting increase in γ-rays will require that the tirgger threshold of the detector as a whole be increased (to reduce the data rate). For the heavy water, an increased background level will make the separation of NC and CC signal more problematic. However, it is also known that ultrapure water is an extremely strong solvent and they are both expected to leach contaminants from

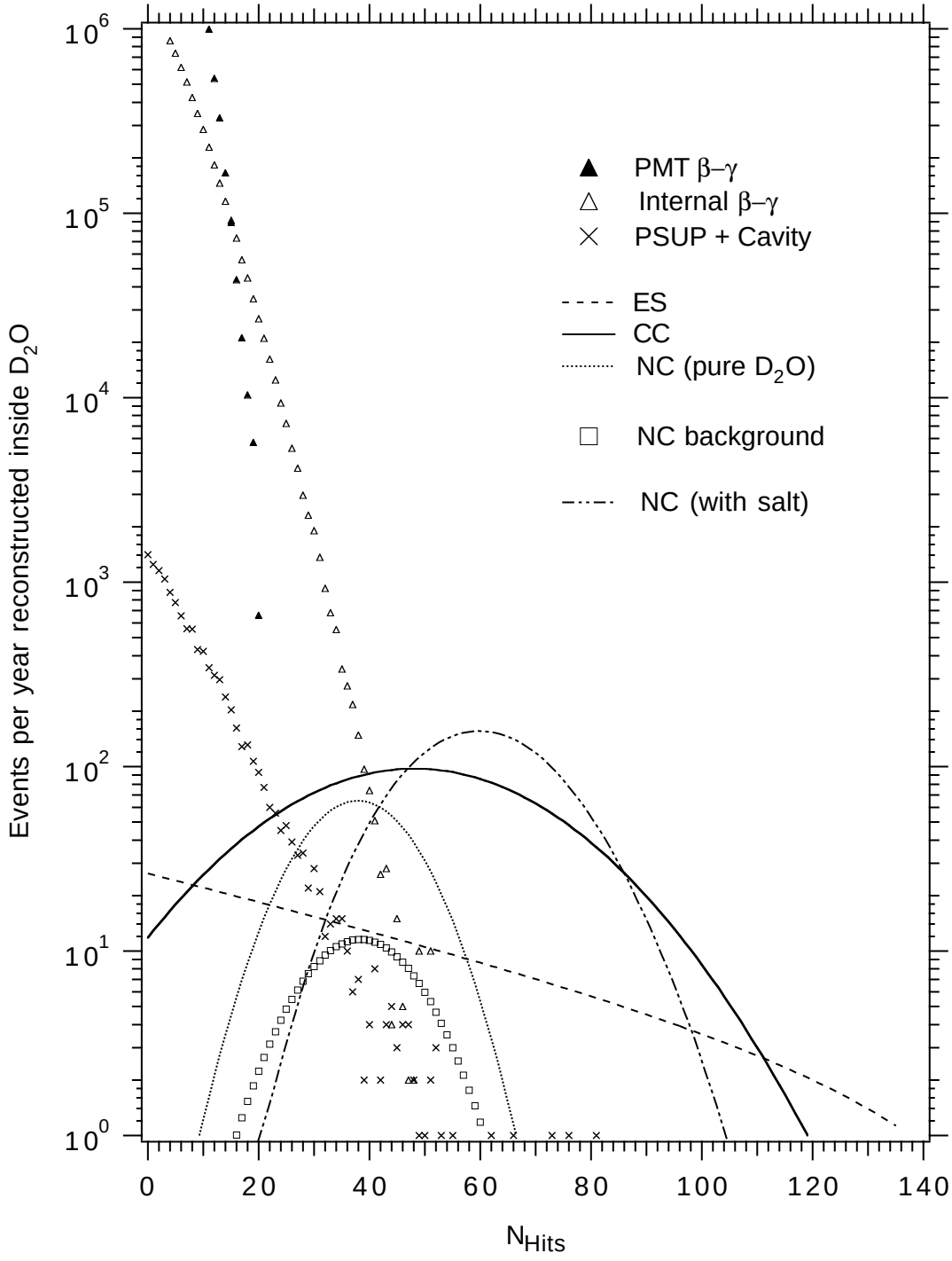

Figure 2.3: Energy distribution from one year of data either with only D_2O or with D_2O and dissolved salt inside the acrylic vessel. The neutral current signal results both from neutron capture on deuterium and capture of ^{35}Cl. The resulting γ-rays shower inside the vessel and the electrons so produced are detected by the PMT array.

their surroundings. This problem will require a continuous recirculation and cleaning of both volumes of water, requiring two separate ultrafiltration systems. In addition, any material placed inside the detector must also be assayed for radioactivity. The final problem of checking any material placed inside the heavy water is covered in more detail in in following sections, where the different methods of neutron detection in SNO are discussed.

2.5 Neutral Current Detection in SNO

The detection of the neutral current interaction with deuterium reduces to the detection of a free neutron moving in the heavy water. There have been several methods considered, all of which rely on measuring either the emission of charged particles or the Čerenkov light produced by γ rays after the neutron has been captured. All methods must meet the same basic criteria, that the final result of the total flux of left-handed neutrinos determined by the NC interaction must be unambiguous. In addition it is highly desirable that SNO should also be able to produce this same information in other situations, such as supernovae, as well as for solar neutrinos.

These basic criteria can then be separated into more specific ones:

- Unambiguous identification of charge-current and neutral-current interactions. The signal produced by neutral current detection should be separable from the Čerenkov radiation produced by CC and ES reactions.
- Adequate statistical accuracy over a reasonable period of time. The efficiency of the detection and separation methods should not degrade over the expected lifetime of SNO.
- Independent insitu measurements, or limits, on all known backgrounds.
- Simultaneous measurements of backgrounds with signal. It is desirable to measure the NC and CC spectra at the same time rather than perform the subtraction of two data sets, one with NC and one without, taken at different times.
- Confirmation of the results by an alternative method with different systematics. It is highly desirable to have two different methods for detecting the neutral current interaction in which the origins of systematic errors are different.

In addition, several other factors must be taken into consideration, in order to safeguard the physics productivity of SNO:

- Acceptable interference with the charged-current and elastic scattering signals.
- A good duty factor. *i.e.* The detector should be able to determine both charge and neutral current signal for as much time as possible.

- Stable, low maintenance operation.

In addition to the above other factors must also be taken into consideration:

- There should be no significant risk to personnel.
- There should be no significant risk to the heavy water.
- The method must be viable from an engineering stand point.
- The cost of the method must be realistic.

Outlined below are the two methods currently anticipated for the SNO detector.

2.6 The Dissolved Salt Option

Since the original SNO proposal [18] the default method for detecting the free neutrons produced by the neutral current interaction has been to add ^{35}Cl, in the form of either $MgCl_2$ or NaCl, to the heavy water. This is more commonly referred to as the dissolved salt option. Any neutron produced is thermalised in the heavy water and is captured, with a 83% probability, on ^{35}Cl. The reaction produces 8.6 MeV of γ rays (the decay scheme allows for 1, 2 or 3 photons) which are then detected as Čerenkov radiation by the electromagnetic shower they produce. The overall efficiency, including capture efficiency and the detection of the shower produced above threshold (60 PMT hits) is of the order of 50%. This low detection efficiency is related to the high trigger threshold of the SNO detector, ~ 5 MeV, and the multiplicity of photons involved.

$$n + {}^{35}\mathrm{Cl} \longrightarrow {}^{36}\mathrm{Cl} + \gamma'\mathrm{s}$$

This method has the following characteristics:

1. The signal produced, Čerenkov radiation from the showering γ rays, is indistinguishable from the signal produced by a charge-current or elastic scattering event, on an event by event basis. Initially it was proposed that the neutral current signal be obtained by operating the detector both with and without salt and subtracting the two resulting spectra. This assumes that there is no (unknown) time dependence in both the signal and the background. However, recent studies by the Oxford Monte Carlo group[31] using correlations in the hit pattern of PMT in SNO have performed further analysis of the dissolved salt option. A brief summary of their work is covered in Section 2.6.1.

2. The salt must be pure at the level of 1.0 pg/g with respect to U and Th to reduce the background of neutrons produced by photodisintegration

$$d + \gamma \longrightarrow n + p \qquad (\mathrm{Q} = 2.224\,\mathrm{MeV})$$

to less than 10% of the SSM NC signal. It must also contain few of any other isotopes which are able to decay with the emission of a γ ray above 2.224 MeV. These isotopes may be produced by the action of cosmic rays on the pure salt. Appendix D covers this in more detail for the specific case of nickel, though a similar analysis can be applied to magnesium.

3. The heavy water must be returned to AECL to specified purity limits. This raises two issues,

   i The salt must be removed to these limits and,

   ii No light water must be added. This implies the use of anhydrous $MgCl_2$ which circumvents the problem of adding a salt which contains water molecules as part of its crystal structure.

2.6.1 Dissolved Salt II

Since the original idea of dissolving salt in the heavy water, a significant amount of time has been spent simulating the response of the detector to the various signals and backgrounds expected in SNO. As a result of these detailed simulations it has been shown that there is a significant difference between the hit pattern (the pattern of PMTs registering at least one photo-electron from an event) resulting from a charge current interaction and the γ cascade from an excited ^{36}Cl nucleus. Using, for example, a neural network, it is possible to separate these interactions in a statistical manner. However, it is not possible to separate them on an event by event basis. Figure 2.4 shows the histogram depicting the value of a single output node network trained on the two classes of events. This allows for running the detector without the need for salt cycling. For further information see references [32] and [31].

2.7 ^{3}He Proportional Counters

The dissolved salt option is not the only possible method of determining the neutral current rate. It was proposed by Los Alamos [20] to use a discrete method of detecting neutrons which would provide a signal which would be separable from the charge current signal on an event by event basis as opposed to the statistical separation required by the dissolved salt option. The Los Alamos proposal [20] discusses other discrete methods that were investigated and the reasons for their dismissal. The preferred design was a proportional counter utilising ^{3}He (the choice of ^{3}He as one of the proportional counter gases is documented in the following Chapter). The thermal neutron capture reaction with ^{3}He reults in the production of a proton and a triton with 191 and 573 keV respecitvely, $n + {}^3\mathrm{He} \rightarrow p + t + 764\,\mathrm{keV}$.

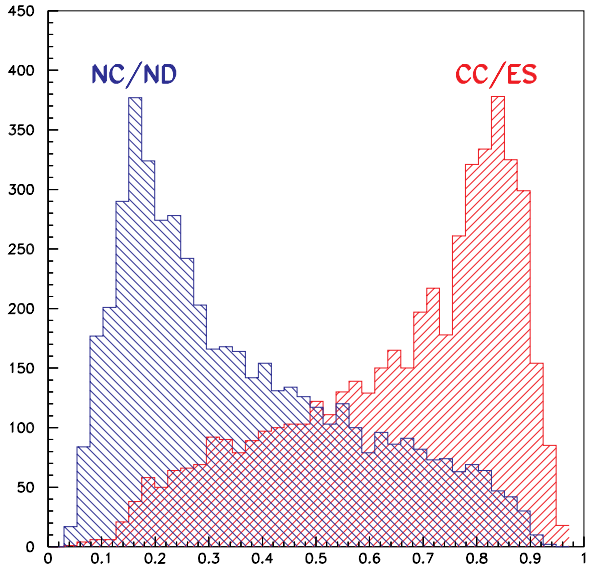

Figure 2.4: A histogram of the testing set output values of a network with one output node trained to distinguish between charge current and γ cascade events. The two hashed histograms show the output for the 500 events of each type.

The major advantage of discrete neutral current detectors is their ability to unambiguously separate CC and NC signals on an event by event basis. However the deployment of discrete counters is complicated in several ways:

1. Any discrete counter should have minimal interference with the Čerenkov light produced in CC and ES reactions. This effectively places an upper limit on the size and number of detectors which can be used inside SNO.

2. The efficiency for detecting neutrons must be acceptable. This effectively establishes a lower bound on the number and size of detectors. These limitations are discussed more fully in Chapter 6.

3. The detector must be stable over the lifetime of SNO. This implies that any detectors made must not degrade over the period of ten years. For the case of ^{3}He proportional counters the main concern is degradation of any 'wet' components as the detectors once placed inside SNO will be extremely difficult to remove.

4. Again, no significant activity can be introduced into the heavy water. This places a limit in the possible materials that could be used to construct the detectors.

Nonetheless, discrete ^{3}He counters offer a solution to all the criteria stated for any neutral

current option. This does not imply that this solution is by any means easy. There are great difficulties in satisfying the constraints from backgrounds and mechanical strength to name but two. The next Chapter deals more thoroughly with the design and implementation of these counters.

Chapter 3

^{3}He Proportional Counters

3.1 Pulse Shape Analysis

3.1.1 The Proportional Counter

The proportional counter is in comparison to most modern experimental equipment, old and well known technology. Similarly, the use of ^{3}He proportional counters for detecting neutrons is not new, they are even produced commercially. However, commercial detectors are not able to meet the strict purity requirements stipulated for SNO, nor the mechanical and electrical constraints placed on the detectors.

A typical proportional counter, shown in Figure 3.1, consists of a cylindrical tube, with a thin central wire maintained at a positive high voltage. The tube is filled with a mixture of gases, typically with low electronegativity. The gas may be flowed through the detector or the detector may be sealed depending on the operating conditions. The type, pressure and proportions of gases and the operating voltage affect the characteristics of the counter and the optimization of these parameters is dealt with in Section 3.5.

A charged particle traveling though the detector will cause ionization in the gas, the total number of electron-ion pairs being proportional to the initial energy of the particle. Typically it takes 30 eV to produce an ion pair, so a 5.5 MeV α particle will produce 1.83×10^5 ion pairs. The rate of production of ion pairs is dependent on the energy, charge and mass of the particle and, as demonstrated later in Section 3.2, is an important way of distinguishing between events caused by neutron capture and any other signals from the counter.

The electric field causes the charges to separate and accelerates the electrons towards the central wire whilst the positive ions drift more slowly towards the counter wall. The motion of the ions and electrons produce a signal, the shape of which is covered later in this Chapter. However, the signal amplitude is related to the number of initial ion pairs produced and the multiplication of charge in the avalanche region.

If the voltage on the central wire is increased above a threshold voltage, V_T, and the gas inside the detector has a low electron affinity, then the electrons can be accelerated to energies

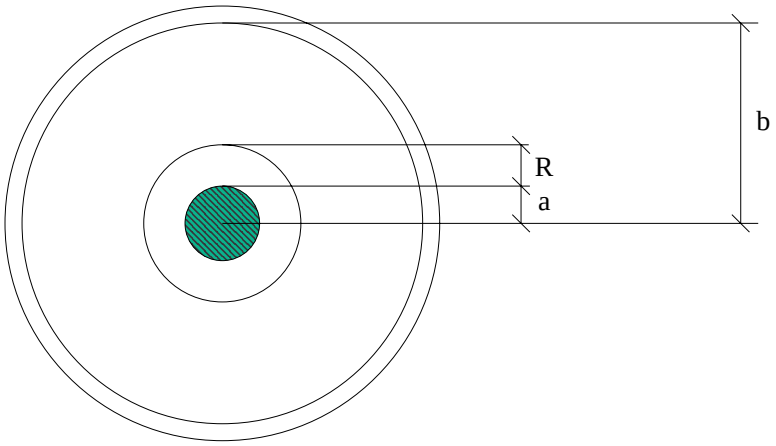

Figure 3.1: The cross section of a typical cylindrical proportional counter (not to scale). The parameters listed are: a the wire radius, b the counter radius (internal) and R the multiplication region.

high enough to cause further ionization in the gas. This occurs only in regions where the fields are extremely high, *i.e.* within a few radii of the central wire. The effect is to increase the number of ion pairs formed by a factor A, the gas gain, thereby boosting the signal. Unfortunately, if there is a component of the gas with a high electron affinity, some of the electrons can be captured to form anions, which can not be accelerated in the same manner to produce avalanches at the wire. These electronegative gases, such as water vapour and oxygen, must be excluded from the system at the level of parts in 10^6. Although gas gains of the order of 10^4 are not unknown, for SNO NCD's the gain is much more moderate due the the self-induced space charge effect, and $A \sim 10^2$ [38].

While operating in proportional mode the gas gain obeys the following relation [33]

$$\log(A) = \frac{\log 2}{(b/a)} \frac{V}{\Delta V} \log\left\{ \frac{V}{paK \log(b/a)} \right\} \tag{3.1}$$

where K and ΔV are parameters of the particular gas used, a and b are the wire and tube radii respectively, V is the operating voltage and p is the gas pressure. Hence, the gas gain is a function both of the gas and the physical parameters of the detector. If the voltage is increased, the resolution for extended tracks (as opposed to the point ionization of low energy X-rays) eventually worsens due to a self-screening space charge effect which is explained further in Section 3.1.4. At still higher voltages the proportionality between ionization particle energy and output charge breaks down. This is the proportional limit. Above this, the counter is operating in GM or Geiger-Müller mode and any energy input gives the same output. The difference between ionization chambers, proportional counters and Geiger counters is covered in detail by Wilkinson [25].

3.1.2 Pulse Formation

The signal from a proportional counter is from the collection of electrons drifting to the central wire and the associated positive ions that drift towards the cathode wall. The ensuing pulse can be formulated by considering the evolution of charge across a cylindrical capacitor [24]. For an electron-ion pair created at a distance r' from the central wire, the total induced voltages from the electron and ion are

$$V^- = \frac{-q}{lCV_0}\int_{a+r'}^{a}\frac{d\phi(r)}{dr}dr = \frac{-q}{2\pi\epsilon l}\log(\frac{a+r'}{a}) \tag{3.2}$$

$$V^+ = \frac{q}{lCV_0}\int_{a+r'}^{b}\frac{d\phi(r)}{dr}dr = \frac{-q}{2\pi\epsilon l}\log(\frac{b}{a+r'}) \tag{3.3}$$

where l is the length of the detector, C is the capacitance per unit length, V_0 is the operating voltage, a is the wire radius and b is the inner radius of the detector. The total contribution of which is

$$V^+ + V^- = \frac{-q}{2\pi\epsilon l}\log(\frac{b}{a}) = \frac{-q}{lC} \tag{3.4}$$

and the relative contributions are

$$\frac{V^-}{V^+} = \frac{\frac{-q}{2\pi\epsilon l}\log(\frac{a+r'}{a})}{\frac{-q}{2\pi\epsilon l}\log(\frac{b}{a+r'})} = \frac{\log(\frac{a+r'}{a})}{\log(\frac{b}{a+r'})} \tag{3.5}$$

The pulse shape is determined by the drift of both the electrons and the positive ions. The pulse shape is defined by the voltage change, $V(t)$, and can be related to the charge by the relation $Q(t) = lCV(t)$ and to the current by $I(t) = dQ(t)/dt = lCdV(t)/dt$. Charge and current are the measured parameters as charge and current sensitive preamplifiers are used in the data acquisition system.

$$V(t) = \int_{r(0)}^{r(t)}\frac{dV}{dr}dr = \frac{-q}{2\pi\epsilon l}[\log r(t) - \log r(0)] \tag{3.6}$$

$$V(t) = \frac{-q}{2\pi\epsilon l}\log\left(\frac{r(t)}{r'}\right) \tag{3.7}$$

Positive Ion Component

For the positive ions, $r(t)$ can be calculated as the positive ion velocity is a linear function of the field

$$\frac{dr(t)}{dt} = \mu E(r) = \frac{\mu CV_0}{2\pi\epsilon}\frac{1}{r} \tag{3.8}$$

where μ is the positive ion mobility. And hence

$$V(t) = \frac{-q}{2\pi\epsilon l}\frac{1}{2}\log\left(1 + \frac{\mu CV_0}{\pi\epsilon(r')^2}t\right) = \frac{-q}{4\pi\epsilon l}\log\left(1 + \frac{t}{\tau}\right) \tag{3.9}$$

$$\tau = \frac{\pi\epsilon(r')^2}{\mu CV_0} \tag{3.10}$$

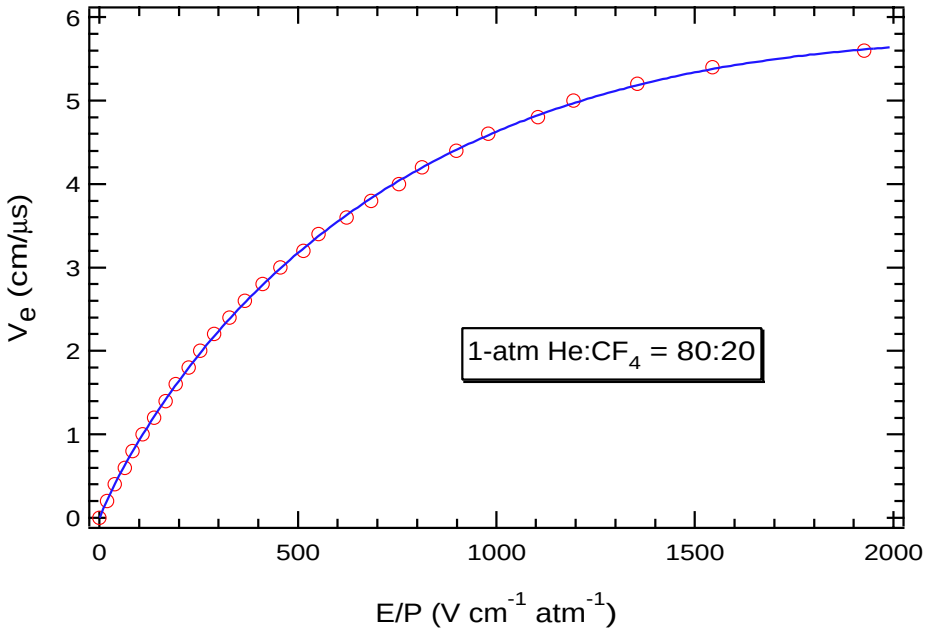

Figure 3.2: The electron drift velocity for 1 atm. of a 80% He 20% CF_4 gas mixture as a function of the electric field.

Electronic Component

For the electronic component of the pulse, the electron drift velocity is not a linear function of the field, but for the gas mixture used in NCD's it may be approximated by the expression

$$-\frac{dr(t)}{dt} = \mu_e E^{1/2} = \mu_e \left(\frac{CV_0}{2\pi\epsilon}\right)^{1/2} \frac{1}{r^{1/2}} \tag{3.11}$$

where μ_e is the electron mobility. This leads to the final result for the electronic component

$$\begin{aligned} V(t) &= \frac{-q}{2\pi\epsilon l}\left[\log r' - \log\left\{(r')^{3/2} - \frac{3}{2}\mu_e(\frac{CV_0}{2\pi\epsilon})^{1/2}t\right\}^{2/3}\right] \\ &= \frac{q}{2\pi\epsilon l}\frac{2}{3}\log\left(1 - \frac{3}{2}\frac{\mu_e}{(r')^{3/2}}\left(\frac{CV_0}{2\pi\epsilon}\right)^{1/2}t\right) \end{aligned}$$

However, the validity of this expression decreases as the field increases. At higher fields it is necessary to approximate the drift velocity by a polynomial in $E^{\frac{1}{2}}$. Figure 3.2 shows a electron drift velocity curve and the parameters used in the fit.

When examining the total signal from a proportional counter, it is relevant to consider three possible cases:

No Gas Gain The only components which matter are the drift of the electron and ion from their initial starting position. The resulting pulse is a combination of $V(t)^-$ and $V(t)^+$. The contribution from each component is related to the initial starting position, r'.

Intermediate Gas Gain At intermediate gas gains, the pulse is the combination of the initial drift of ion and electron towards the wall and wire followed by the outward drift of the ions after multiplication and the rapid motion of the electrons into the wire. The contribution of the multiplication electrons to the signal is usually taken to be negligible, as they are created so close to the wire [24]. However, from the equations in Section 3.1.2, in a counter with $(b/a) \sim 2000$, the electronic component is of order 10% of the signal.

$$\frac{V^-}{V^+} = \frac{\log 2}{\log(\frac{b}{2a})} \tag{3.12}$$

The approximation is still valid as the time taken for the electrons to be collected is so very small compared to the drift of the positive ions, that this fraction of the signal is collected almost immediately.

This results in an initial slow rise before the main multiplication pulse. For SNO NCD's this initial rise is only a percent of the total signal and the large gas gain approximation is generally used. However, in certain situations, the initial ionization rise can still be seen and its usefulness will be demonstrated later in the Chapter.

Large Gas Gain At large gas gains ($A \geq 100$) the majority of the charge is created within a few radii of the wire, with $r' \sim a$, and the original ionization comprises such a small fraction that its effects may safely be ignored. This approximation leads to the "text book" equation shown below and illustrated in Figure 3.3 for the pulse shape of a single ion pair.

$$Q(t) = -\frac{q}{2\log(b/a)} \log\left(1 + \frac{t}{\tau}\right) \tag{3.13}$$

$$I(t) = \frac{dQ(t)}{dt} = -\frac{q}{2\log(b/a)} \frac{1}{t+\tau} \tag{3.14}$$

$$\tau = \frac{\pi \epsilon a^2}{\mu C V_0} \tag{3.15}$$

3.1.3 Extended Tracks

So far the discussion has been based on the charge evolution of a single electron-ion pair. The situation is changed for an extended track. A charged particle passing through the gas leaves behind a trail of electron-ion pairs along its track. The radial distribution of ion pairs, $q(r)$, is determined by the track's orientation and the particle's rate of loss of energy (dE/dx). Figure 3.4 shows this result for three simulated events. The first pulse is a track parallel to the wire, and behaves like a single ion-pair whilst the second and third are 'square waves' of widths 2 and 4μs respectively. It should be noted that these are very simple simulations and

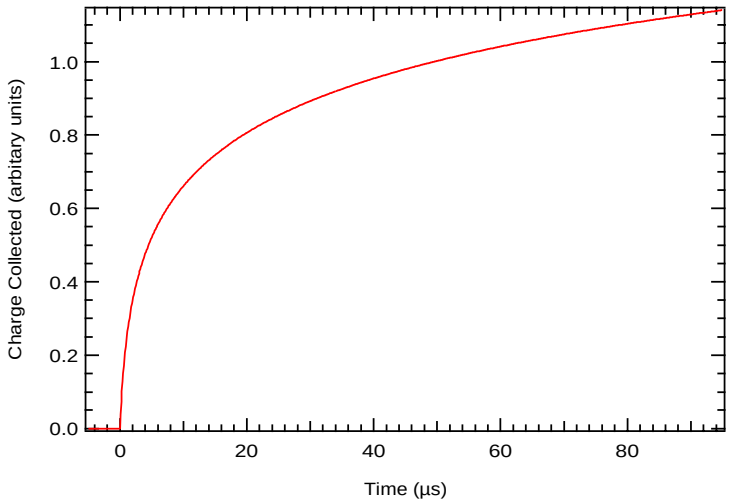

Figure 3.3: The charge signal from a single ion pair ignoring the initial ionization. The value of τ used was 1 ns.

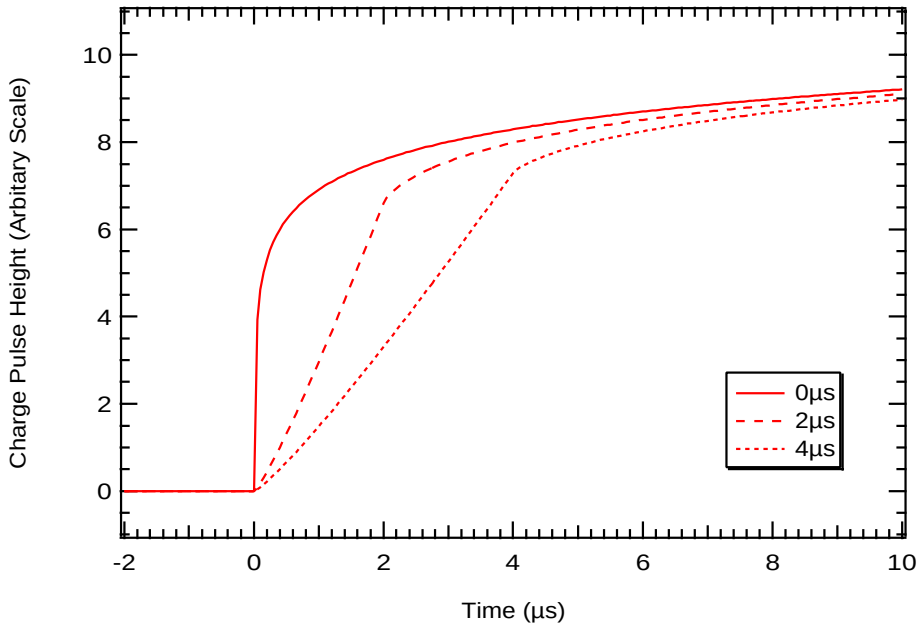

Figure 3.4: Simulated pulses with varying widths.

do not take into account the radially dependent electron drift velocities or the diffusion of electrons on route to the central wire.

The resulting charge and current signals may be viewed as a convolution of the individual pairs as they drift from the various radii.

$$Q(t) = \int \left[q(t_0) \frac{1}{2\log(b/a)} \log\Big(1 + \frac{(t-t_0)}{\tau}\Big) \right] dt_0 \tag{3.16}$$

$$I(t) = \int \left[q(t_0) \frac{1}{2\log(b/a)} \frac{1}{(t-t_0)+\tau} \right] dt_0 \tag{3.17}$$

However, the electron drift velocity depends on the local field and hence the position of the electron, r. This implies that it is not possible to just view the pulse as the time projection of its charged particle track. The effect of the drift velocity curve is to disperse the charge that arrives later, distorting some of the pulse's features.

The time taken for an electron at radius, r', to drift into the wire, assuming again that $v_e \propto E^{\frac{1}{2}}$ is

$$t(r') = \frac{2}{3\mu_e} \left(\frac{\log(b/a)}{V_0} \right)^{1/2} \left[r'^{3/2} - a^{3/2} \right] \tag{3.18}$$

The spread in time between two electrons, one at r and the other at $r + \delta r$ is dependent on r.

$$\delta t(r) = \frac{1}{\mu_e} \left(\frac{\log(b/a)}{V_0} \right)^{\frac{1}{2}} r^{\frac{1}{2}} \delta r \tag{3.19}$$

and the spread in a group of electrons close to the wall and an equivalent group, three quarters of the way to the wire, is a factor of two.

This is an important consideration when looking for particular pulse features and its effect must be taken into consideration when considering pulse features.

However, some measure of the radial distribution of the initial ionization can be made by measuring the time for a pulse to reach a certain percentage of its total energy. It is impractical to measure the total energy of the particle as this would require approximately $\tau(b/a)^2$ for all the charge to arrive at the wall. For typical values of $\tau \sim 1ns$ and $b/a \sim 2000$, the time for total charge collection is 4 ms. Instead the total energy is taken to be the pulse height 10μs after the start of the pulse. This leads to two problems:

1. The full charge is not collected. Typically, as 10% of the signal is collected immediately from the electrons, and only 60% of the ionic component (the remaining 90% of the total signal) is collected, the total charge collected is then only 64% of the maximum possible.

2. The limit leads to an error in the energy called the ballistic deficit. The deficit arise because of the different orientations of the extended tracks. For a track parallel to the wire all the electrons arrive at the wire in a time dependent on their straggling whilst

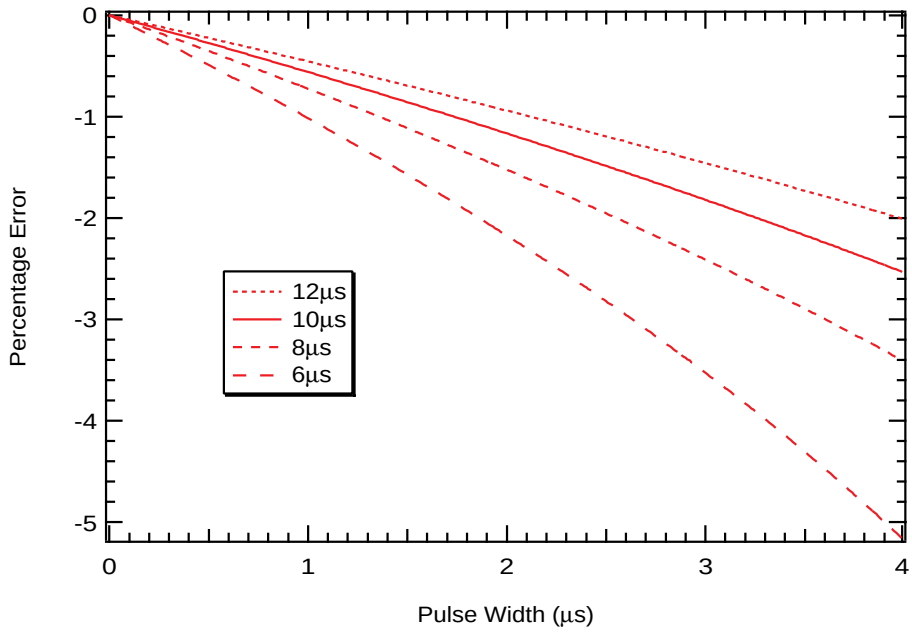

Figure 3.5: A graph showing the relationship between pulse width and measured energy.

for a track perpendicular to the wire the last electron arrives on the order of μs later. In the examples in Figure 3.4 the deficit is of the order of 3%, whilst Figure 3.5 shows the relation between a pulse's 'width' and its measured energy as a function of the time at which the energy is measured.

Further details of pulse shape analysis and the parameters derived from charge pulses in given in Appendix B. In particular two parameters are used extensively, the pulse's energy and t_f, the time to achieve a fraction, f, of that energy. Their importance is demonstrated in Section 3.2.

3.1.4 The Space Charge Effect

The self screening space charge effect can be seen when large densities of positive ions collect around the anode wire and effectively screen it from other electrons. It is most noticeable when the extended track is perpendicular to the wire and less noticeable when the track is parallel to the wire. The explanation is as follows.

For an extended track perpendicular to the wire: When the first part of the electrons from the extended track reaches the wire, multiplication occurs and a large number of positive ions are created within a few radii of the wire in the area where the electrons arrived. They provide a positive ion sheath around the wire which slowly disperses towards the cathode wall. This sheath, however, effectively screens the positive potential of the wire to other electrons arriving slightly later, at the same position along the wire. These electrons feel a slightly reduced field

and accordingly have a lower gas gain.

For an extended track parallel to the wire: In this case all electrons arrive approximately simultaneously at the wire, along a length of the wire. As there are no trailing electrons to be effected by the reduced field there is no reduction in the gas gain.

Therefore any track perpendicular to the wire has a reduced gas gain when compared to a track parallel to the wire. This effect is more prevalent at higher gas gains and densities (as this reduces the tracks length and hence increases the charge density). Figures 3.6, 3.7 and 3.8 demonstrates this principle using the neutron spectrum from a commercial neutron detector at increasing gas gains (increasing operating voltages).

If the above simple explanation of the space charge effect were indeed true then it would be possible to reconstruct the true energy of an event by using the information contained in the rise time parameter, which is an indication of the pulses width or orientation. However, from the data shown in Figure 3.8 there is still energy reduction in the pulses with shorter rise times. This does initially appear to inconsistent with the earlier explanation of the space charge effect. It can be reconciled by considering the source of the ion pairs in the proportional counter. For neutron capture events the reaction can occur anywhere within the volume of the gas resulting in tracks being produced with the same orientation but at different radial positions. The rise time of these tracks is different as the appropriate time for the electrons to drift into the wire is a function of the electric field and hence the radius. In addition is it possible for events of differing orientation to have the same rise time due to the tracks crossing the wire.

For α particles the situation is simplified as the only source is the wall of the detector. However ongoing analysis[39] has shown that the rise time parameter may not provide enough information to correct the energy but instead an analysis of the entire pulse shape may have to be used.

3.2 Ionizing Radiation

3.2.1 Neutrons

The purpose of the NCD is to capture a neutron and produce some characteristic signal which could be separated, with good efficiency, from any background. Thermal neutron capture on ^{3}He leads to the production of a proton and triton with 764 keV of energy. The cross-section for thermal neutron capture on ^{3}He is 5327 ± 10 barns. Conservation of momentum and energy dictates that the two particles are ejected back-to-back with 573 keV and 191 keV for the p and t respectively. Figure 3.9 illustrates the specific energy loss curves for the proton and triton.

$$n + {}^3\mathrm{He} \rightarrow p_{(191\,\mathrm{keV})} + t_{(573\,\mathrm{keV})} + 764\,\mathrm{keV} \tag{3.20}$$

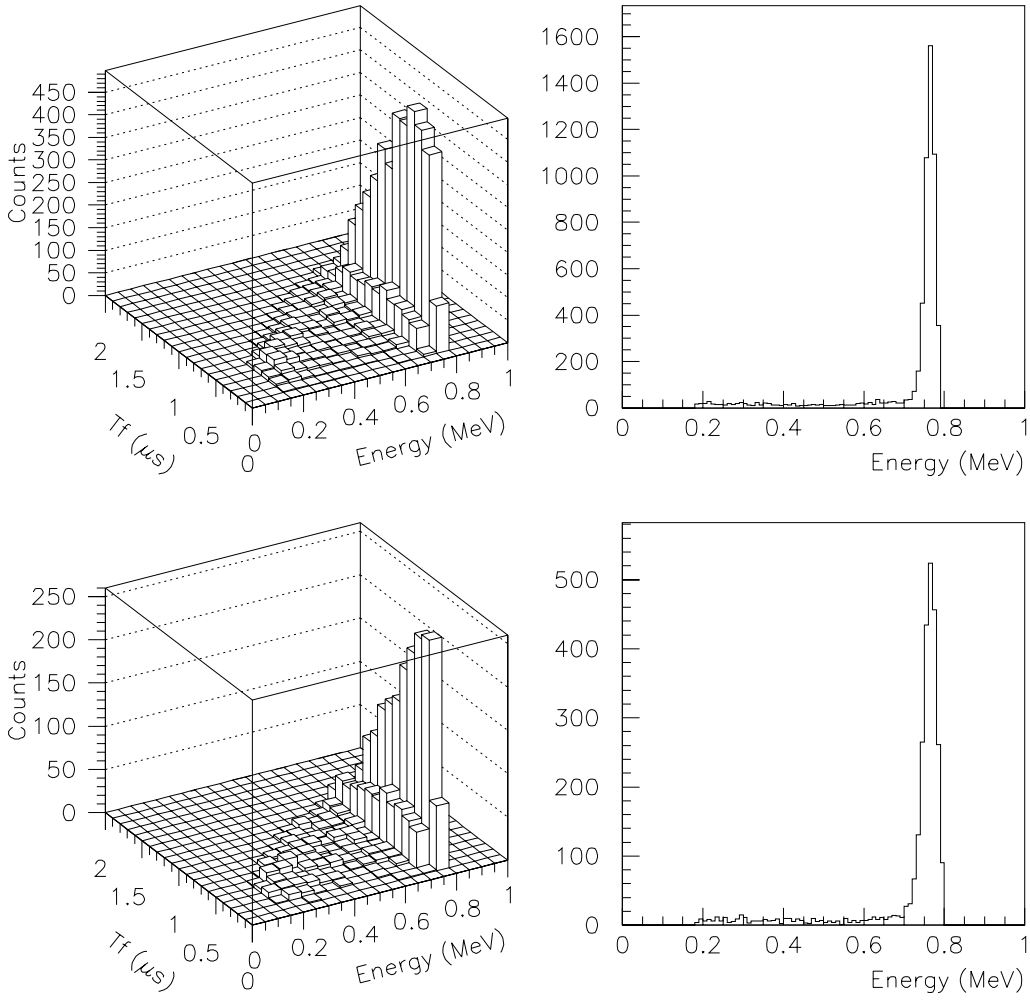

Figure 3.6: Rise time vs. energy and energy histogram plots for a commercial ^{3}He proportional counter at gas gains of 10 and 29 respectively.

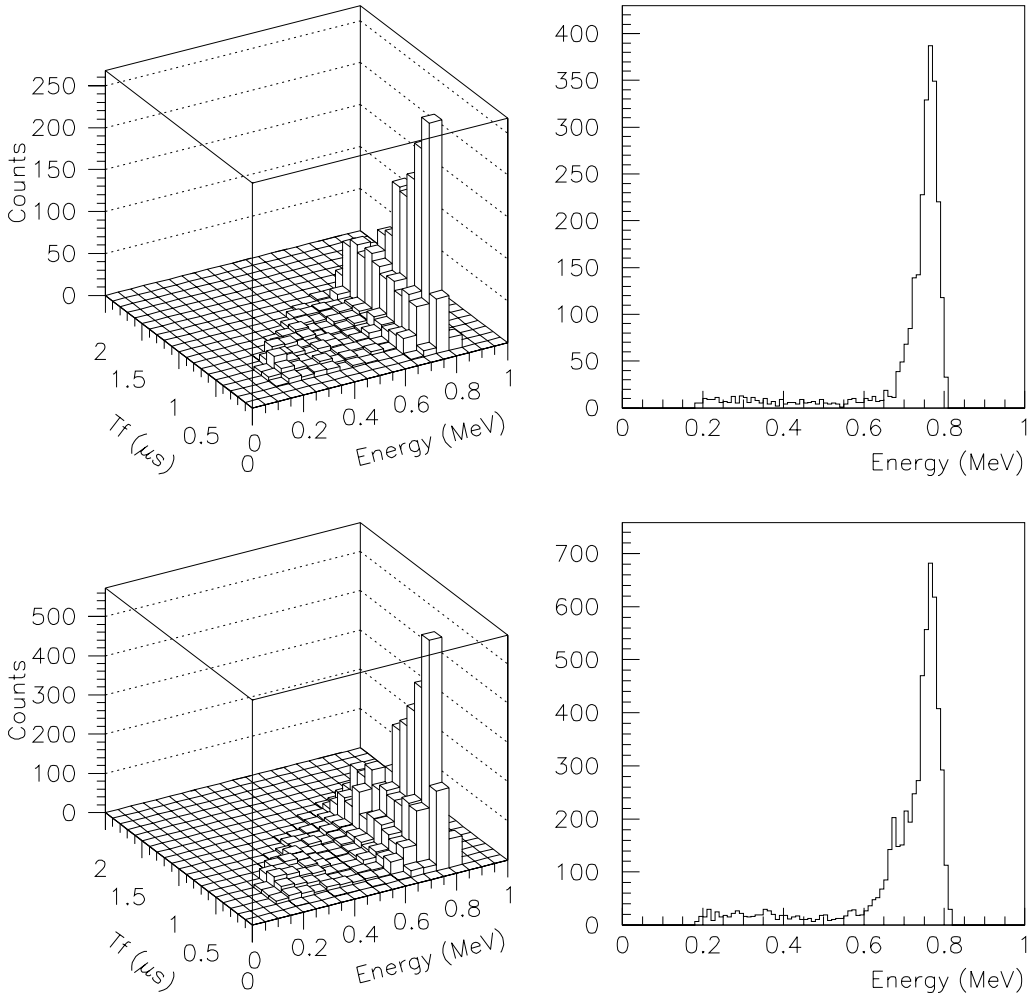

Figure 3.7: Rise time vs. energy and energy histogram plots for a commercial ^{3}He proportional counter at gas gains of 50 and 91 respectively.

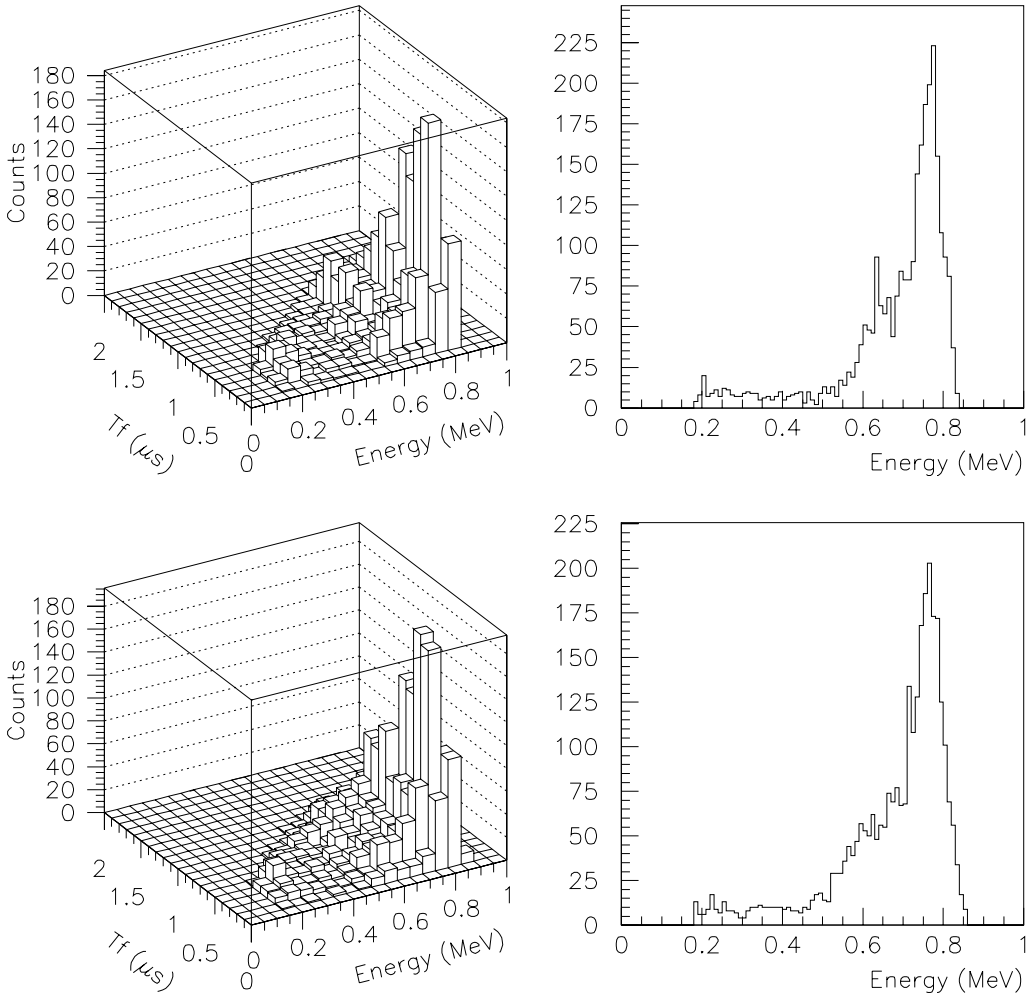

Figure 3.8: Rise time vs. energy and energy histogram plots for a commercial ^{3}He proportional counter at gas gains of 161 and 215 respectively.

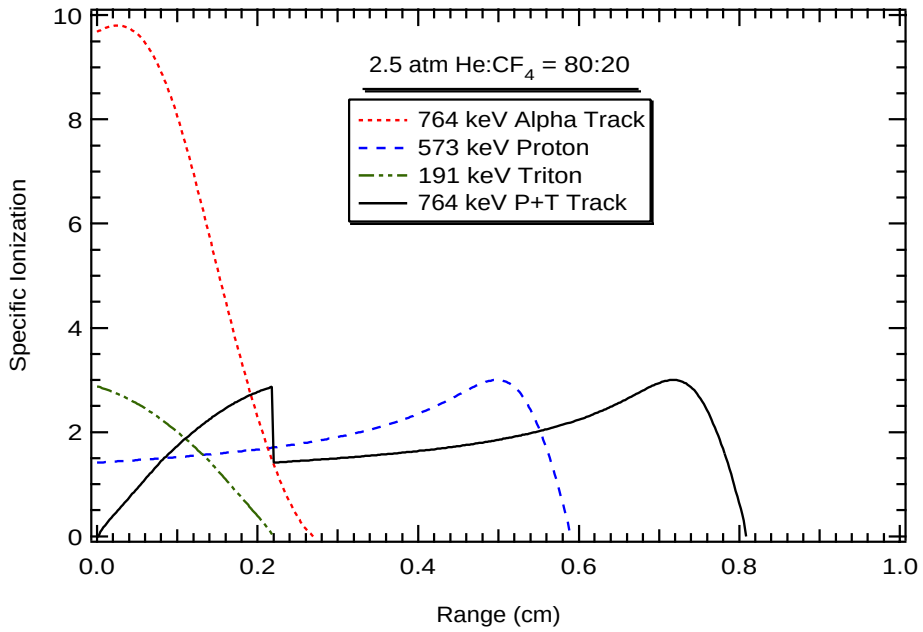

Figure 3.9: The dE/dx curves for the proton and triton resulting from neutron capture. In addition the specific ionization is also shown for the triton, the proton and a 764 keV α particle.

As explained in Section 3.1.3 the specific ionization along with the orientation of the track determines the radial distribution of charge and hence the final signal. Previous analysis by the SAGE collaboration has shown that there is much improved analysis and a greater ability to separate true signals from background 'noise' by using a digitizer which records the entire signal from the proportional counter. For SNO NCD the entire pulse is also digitized so that the topology of the pulses can be exploited as a means of event discrimination. Figures 3.10 and 3.11 show these effects for events in which the tracks are parallel and perpendicular to the wire respectively. As the entire pulse is digitized, the time to reach a faction, f, of their energy can be measured. This is the t_f parameter where a typical value for $f \sim 50\%$. Appendix B covers the details of a typical pulse analysis and the parameters that are measured. These parameters are then used in discrimination rather than the entire pulse shape and correspond to the range of t_f for the neutron capture spectrum.

The energy from neutron capture is not always 764 keV. It can be less than this due to the wall effect, in which one of the tracks intercepts the wall of the counter, effectively removing some of the 764 keV from the gas. This produces a lower energy continuum, shown in Figure 3.12. There are two features corresponding to the proton and triton edges, where one of the particles is lost to the wall. This reduction in the total energy reduces the maximum value of t_f. By using a time-energy plot it is then possible to define a neutron window. For simplicity a cut off at 191 keV is used which results in a loss in efficiency of less than 0.1%

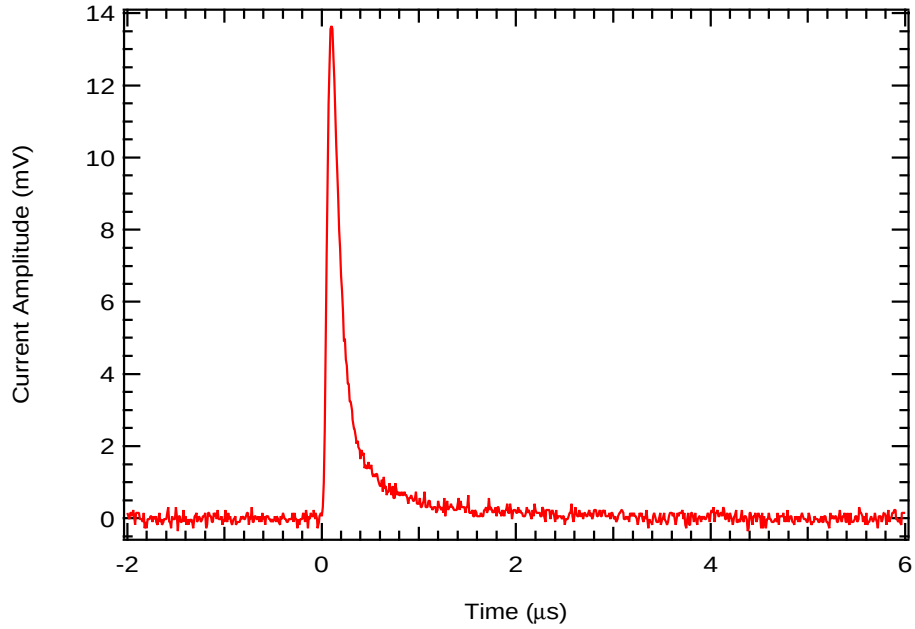

Figure 3.10: A current pulse from a neutron capture event where the proton and triton tracks are parallel to the wire.

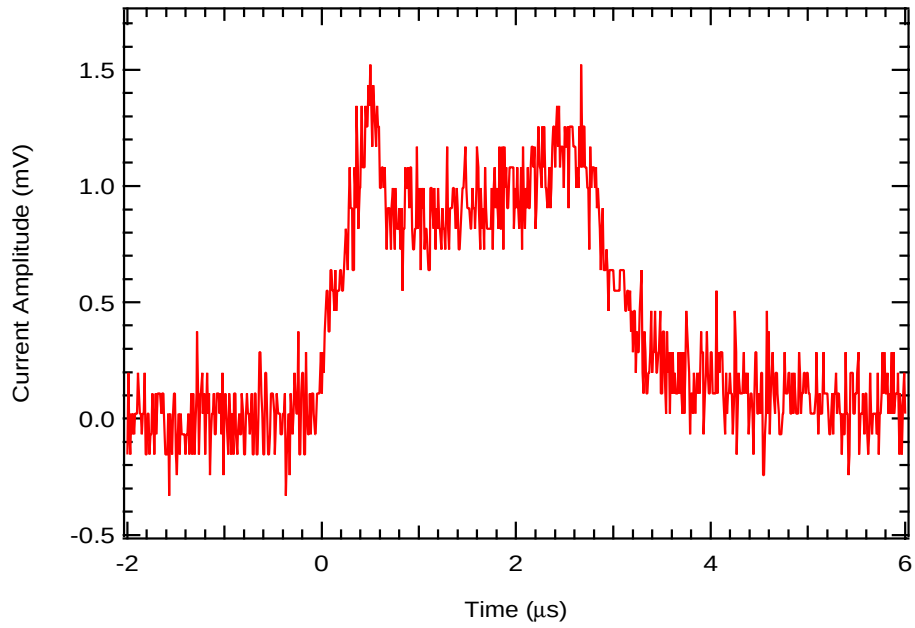

Figure 3.11: A current pulse from a neutron capture event where the proton and triton tracks are perpendicular to the wire.

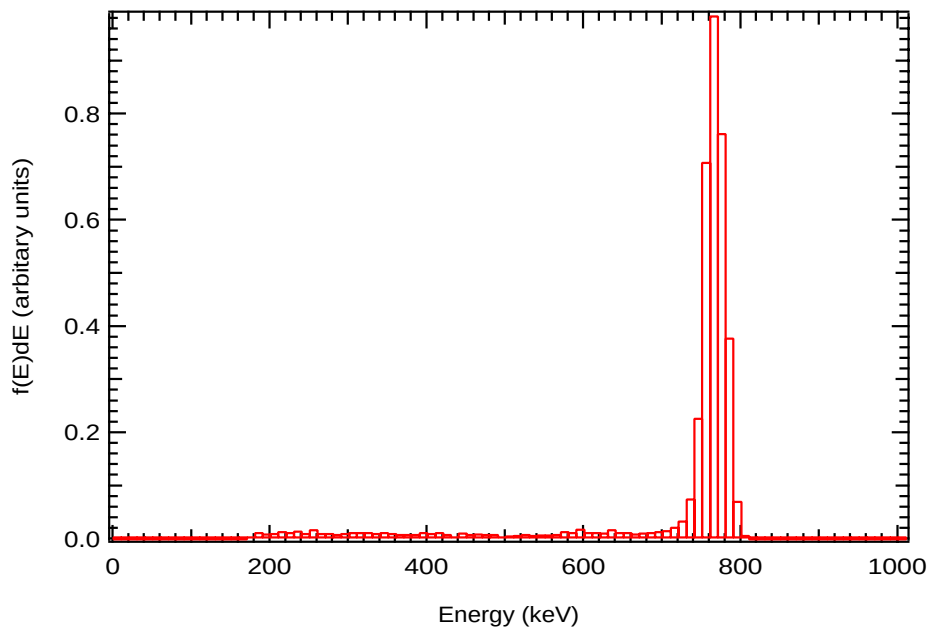

Figure 3.12: A neutron calibration energy spectrum.

(though this is gas dependent). All neutron capture events with more than 191 keV must occur inside this window. More importantly, anything which lies outside the window can not be regarded as neutron capture. Figure 3.13 shows data taken using a thermalized neutron source and the neutron window.

3.2.2 Alpha Particles

Alpha particles are the main background to the neutron signal. Although there are few reactions in which α particles are emitted with less than 1 MeV, either the wall effect, where the track of the α intersects the wall of the detector, or the transport of the particle through the material of the wall, can sufficiently reduce their energy. Figure 3.14 shows the dE/dx curve for an α particle.

There are two main sources of α contamination; bulk and surface. Bulk contamination is due to radio-nuclides distributed throughout the material of the wall and is associated with the fabrication process. Surface contamination results from exposure after fabrication and the nuclides are only on the surface of the detector, though they can subsequently be removed by etching the surface with an acid. Of the two, bulk contamination is the more serious, both for SNO and for the separation of neutron and α events.

Like the neutron pulses the α pulses are produced with a variable width corresponding to the orientation of the track and the energy of the particle. The effect is to produce a 'triangular' window similar to that from neutrons but extending to much higher energies.

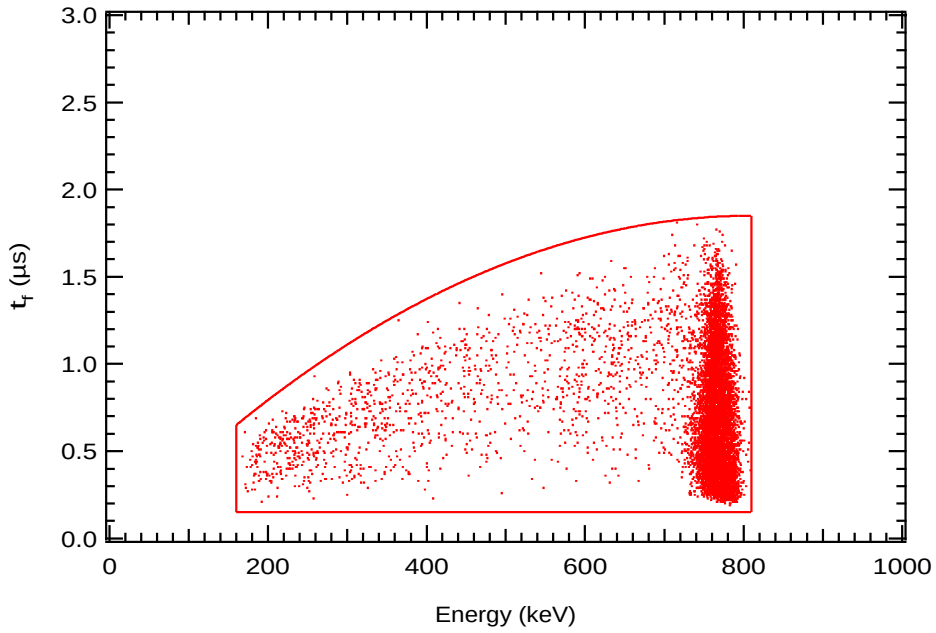

Figure 3.13: A t_F *vs* Energy plot from a thermal neutron calibration.

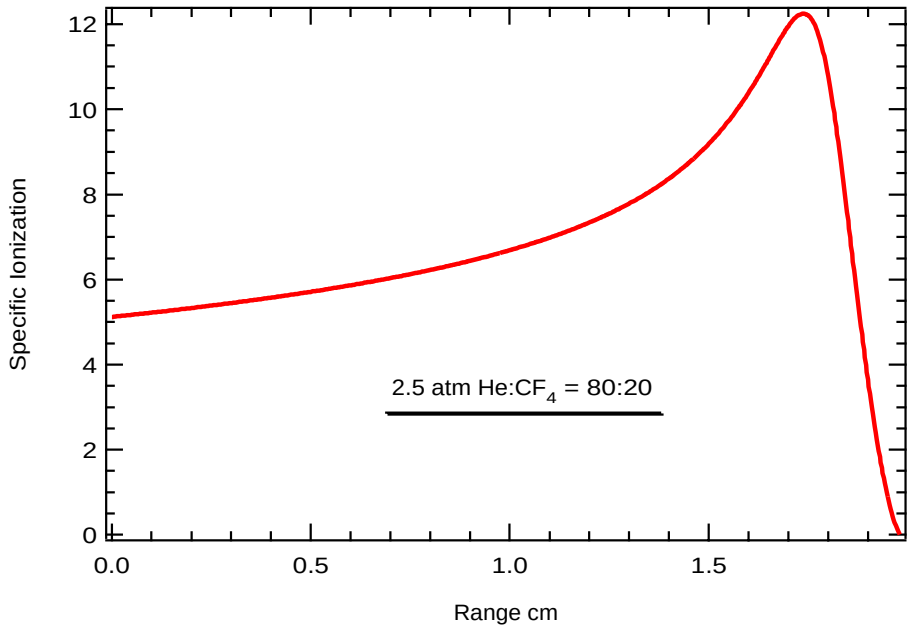

Figure 3.14: The dE/dx curve for an α particle. The shaded areas correspond to $764keV$ deposition by wall effect and by energy loss through the material of the wall.

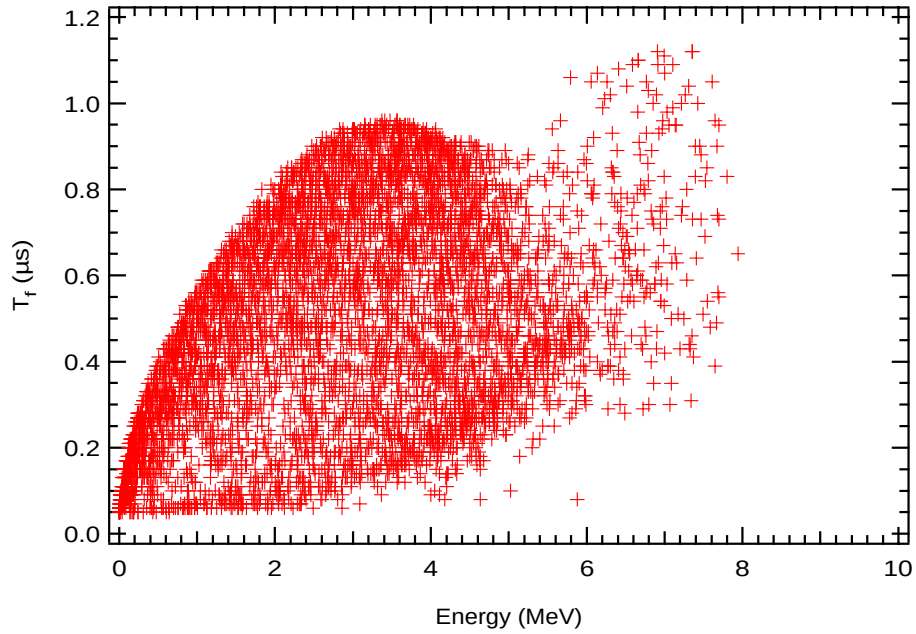

Figure 3.15: A monte Carlo simulation of the α particle observed from U chain isotopes in equilibrium uniformly distributed throughout the bulk of the detector wall as a typical rise time *vs* energy plot.

Bulk contamination is the more problematic, as the degraded α particles may be emitted at all angles from the wall and, as such, will spread out to fill the total α section inside the neutron window.

In contrast, surface contamination leads predominantly to the production of a peak (as a large number of particles deposit their full energy in the gas, their range being insufficient to reach the opposing counter wall). For surface α's to enter the neutron window they must deposit between 191 and 764 keV of energy. This can only be achieved if the α particle strikes the wall of the detector, and implies that the 'width' of the pulse should be lower than the maximum possible. As a result only a small number of α particles enter the neutron window and possess smaller t_f's than α's from bulk contamination.

These bulk contamination can be seen in Figure 3.15 whilst Figure 3.16 illustrates the surface contamination. The final Figure 3.17 shows the result from a single isotope (5.3 MeV ^{210}Po) on the surface of the detector [36]. Figure 3.18 illustrates how α particles affect the neutron window. It must be noted that the α particles are unable to affect the upper part of the neutron window as therefore this region may be referred to as the background free region.

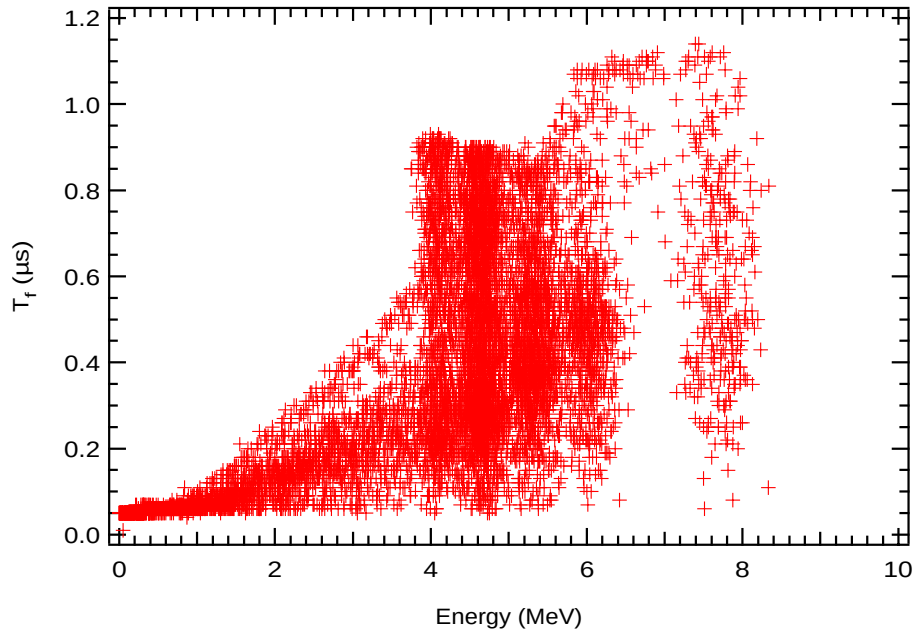

Figure 3.16: A Monte Carlo simulation of the α particle observed from the decay of U chain isotopes in equilibrium on the walls of the detector as a typical rise time *vs* energy plot.

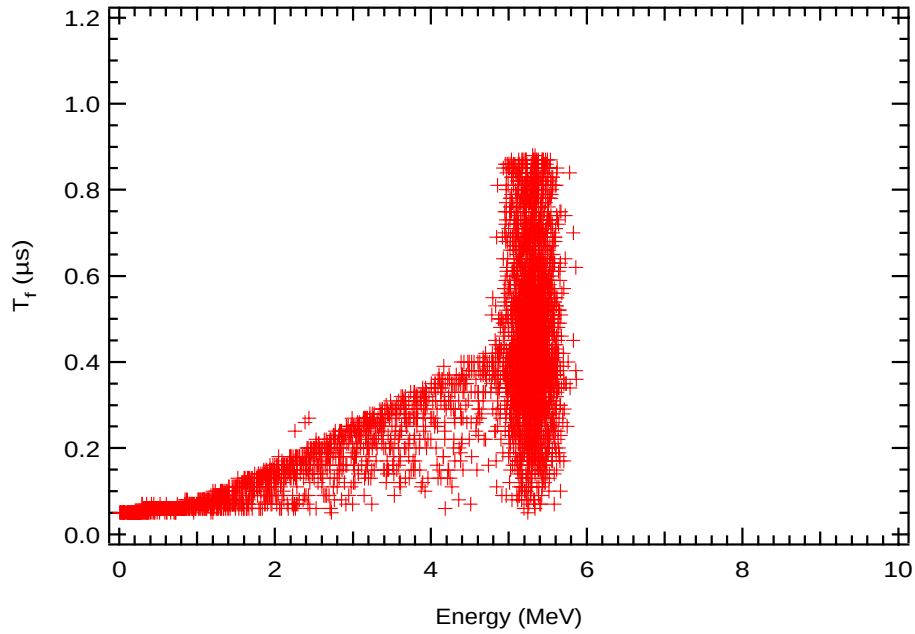

Figure 3.17: A Monte Carlo simulation of the α particle observed from the decay of ^{210}Po on the walls of the detector as a typical rise time *vs* energy plot.

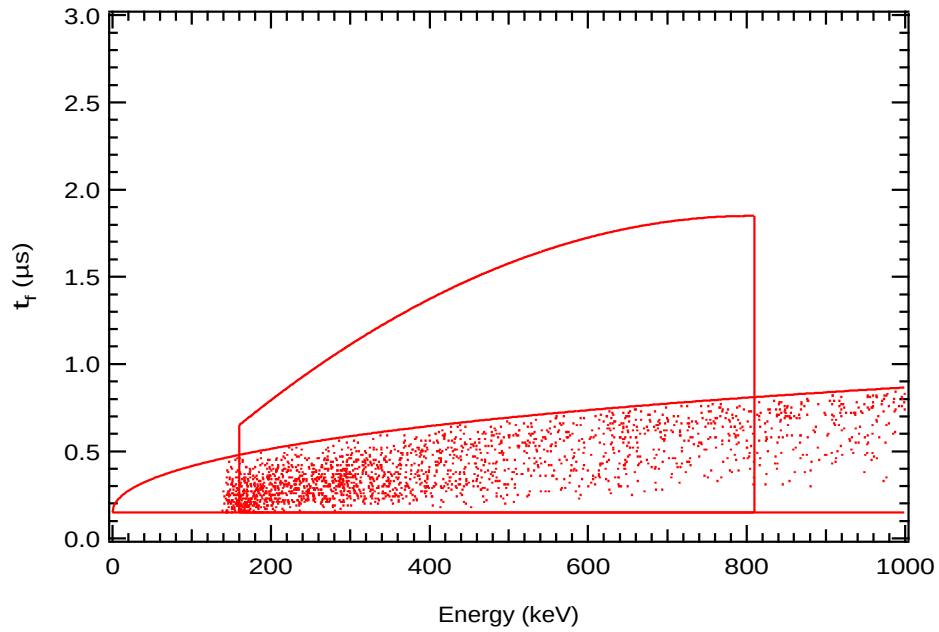

Figure 3.18: A t_F *vs* Energy plot from a bulk α source. The neutron window is also shown for reference, as is the α window. It should be noted that there is a region of the neutron window which can not be affected by α particles.

Wire Alpha's

The central wire of the counter will also contain some natural radioactivity. Although the total mass is much smaller, it may be possible for an α particle to be emitted from the wire. An α particle coming from the wire heading towards the wall of the detector should be easily distinguishable from an α particle from the wall, heading towards the wire. This is because the former has a Bragg peak at the end of the pulse whilst the latter has a peak at the beginning. This is normally, very easy to distinguish. Figure 3.19 is an example of both wall and wire alpha particles. It should be noted that this technique requires α particles with energies greater than 1 MeV for the production of the Bragg peak and hence is of little interest for the purpose of separating neutron and capture and α events in the detector.

3.2.3 Betas & Gammas

The detection of β and γ rays is identical as Compton scattering of a photon inside a proportional counter produces a recoil electron. The energy deposited by one of these processes is generally low (given the range of the electron and photon in the gas), though multiple scatters may increase it above the lower cut off of the neutron energy window. However, multiple scatterings lead to a much larger value of t_f than is achievable with a single extended track. Compton electrons from γ rays are a natural background from the ^{40}K in the salt at WIPP

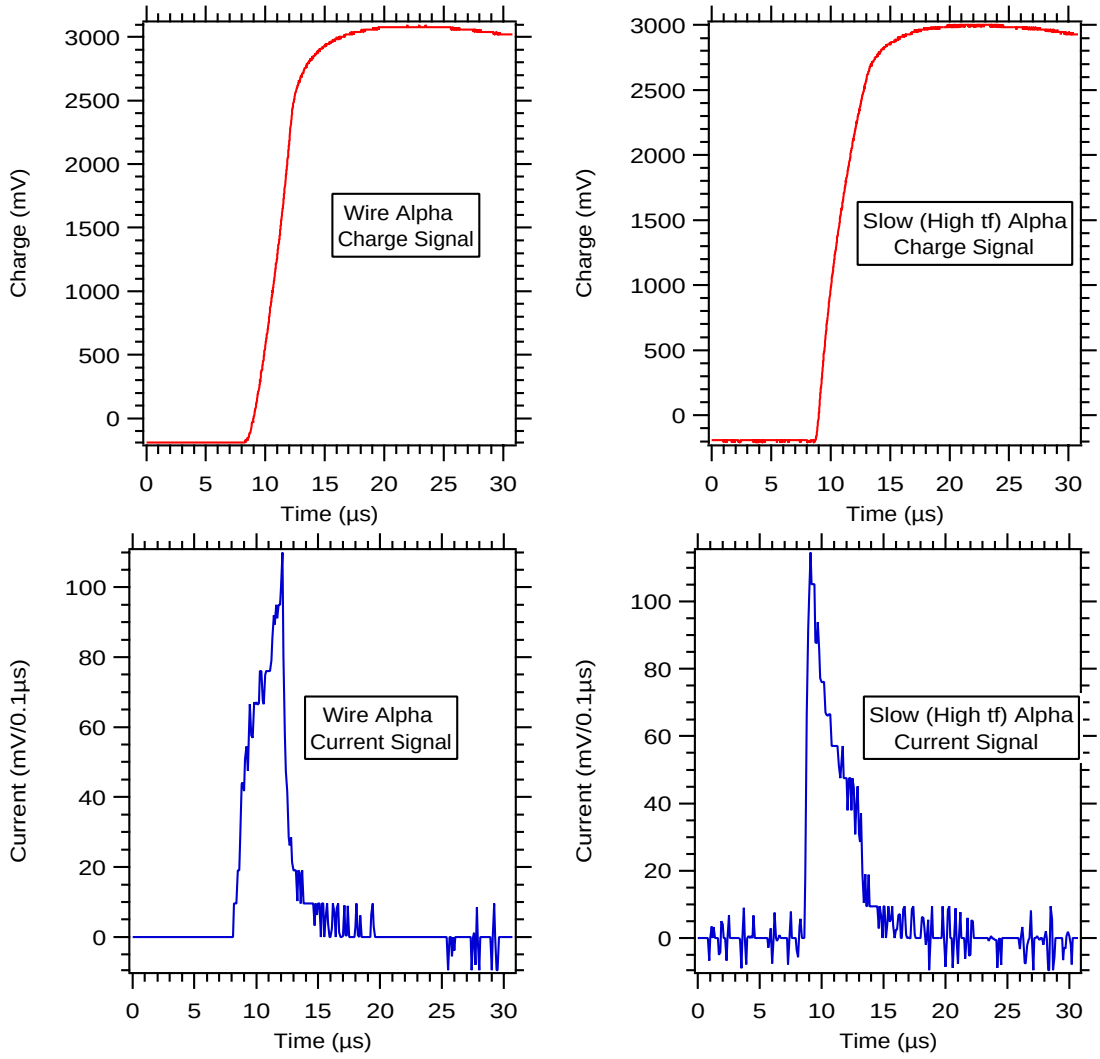

Figure 3.19: Pulses produced by α particles from the wire and the wall of the detector respectively. The pulses were originally taken using a charge sensitive preamplifier, the current pulses, which better illustrate the Bragg peak, were created by software differentiation.

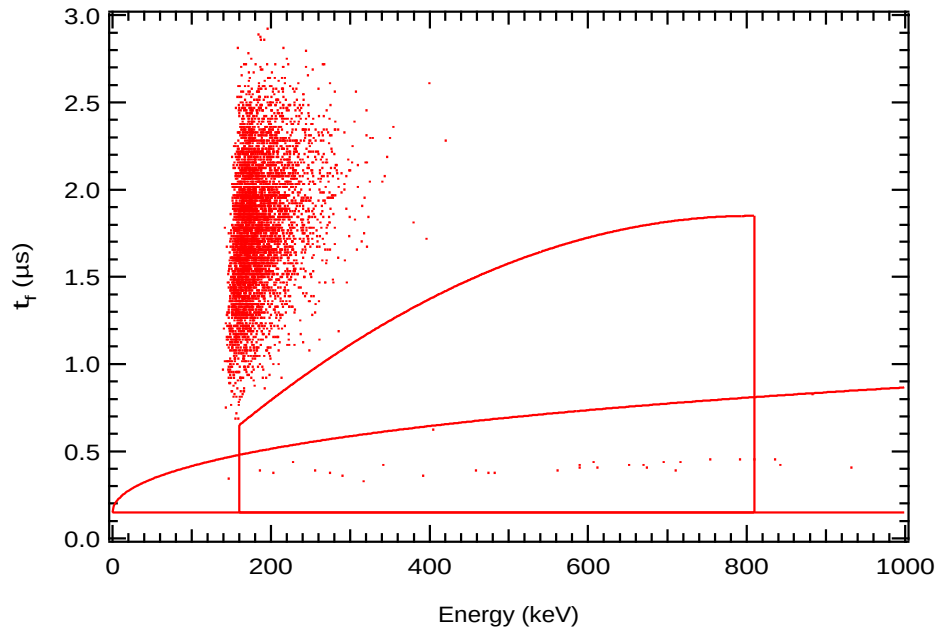

Figure 3.20: A t_F *vs* Energy plot from a ^{60}Co source. Some residual α activity from the walls of the counter can be seen in the lower part of the plot and is bounded by the α window.

(the test site for the fist generation of low background proportional counters) and will also be present, though at a greatly reduced level, in the SNO detector. A typical t_f *vs* energy plot from a ^{60}Co source is shown in Figure 3.20 along with the neutron and α windows. As can be seen none of the $\sim$ 5000 events lie inside the neutron window (with the exception of some surface α activity from the detectors walls). Discrimination is complete and β's and γ's are easily distinguished from events in the He(n,p)t window.

Finally Figure 3.21 combines the neutron capture, α and Compton spectra. The most important feature is the background free region of the neutron window which can not be contaminated by any α or β/γ activity.

3.3 Noise and Spurious Pulses

3.3.1 HV Discharge

High voltage discharge does not occur by the same methods of charge collection as outlined in Section 3.1.2. The output pulse has none of the evolution associated with a gas pulse. It has a very fast rise time with a decay characteristic of the decay time of the pre-amplifier. Figure 3.22 show one of these pulses.

High voltage discharge was frequently a contaminant of pulses seen from the proportional counter. They originated from both the pre-amplifiers and the feed-thru's in the detectors endcaps. As the pulse is fast and does not exhibit any of the features characteristic of ionization

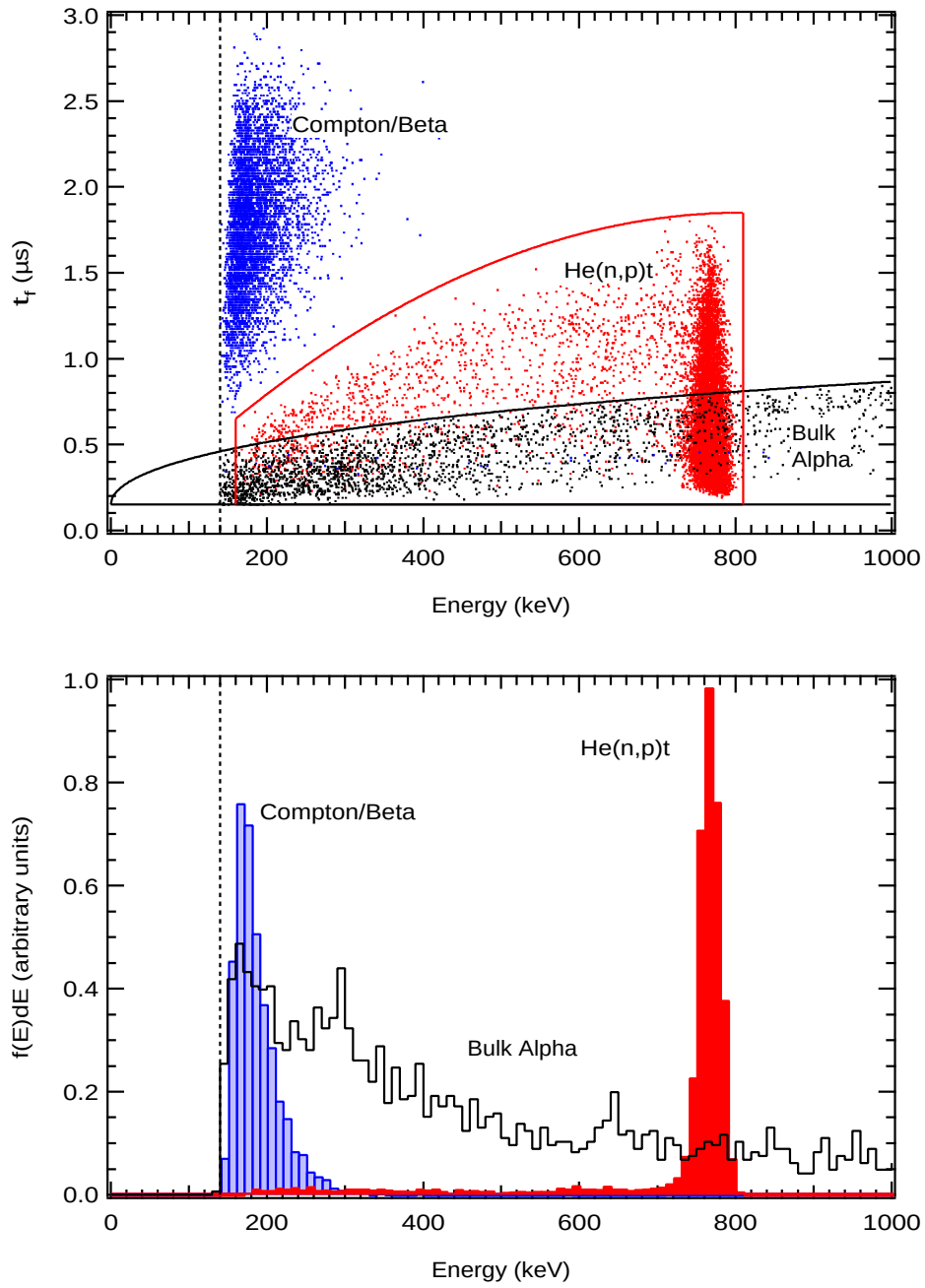

Figure 3.21: The upper diagram is t_F *vs* Energy plot where neutron, α and Compton distributions have been combined. The most important feature is the background free region of the neutron window. The lower diagram shows the same data as just an energy histogram to illustrate the nescessity of pulse shape analysis in separating all the distributions.

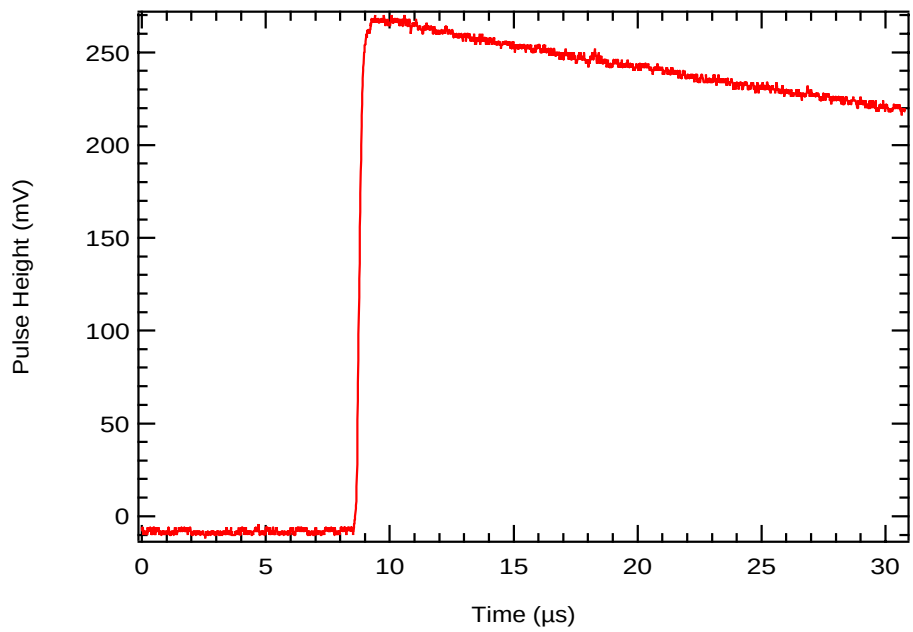

Figure 3.22: A high voltage discharge. Note that the pulses does not exhibit the characteristic $\log(1 + t/\tau)$ time dependence of an ionization event.

it can be easily discriminated. The very fast rise and decay of the pulse produces a value of t_f which is unphysical for gas pulses, whilst its sharp decay, produces a value of δ which is untypical of a gas pulse.

3.3.2 Sound Pickup

Though this has not appeared to be a major contaminant of the pulses from a proportional counter, it's effect has occasionally been seen. However, it is easily identified by its ringing shape and can easily be discriminated from a gas pulse.

3.3.3 Unidentified Pulses

Throughout the WIPP experiments there have always occurred pulses whose origins were initially puzzling. They can be removed, as with HV discharge, by cuts using the t_f and δ parameters. Their numbers have been radically reduced by changing the design of detector endcaps and the design of the electronic trigger. Chapters 4 and 5 deal with these issues as part of the various stages of the WIPP experiment.

3.4 Neutron Signal Separation

As has been described the only contaminant of the neutron window comes from α particles. However, their shorter range means that these events can only affect the lower half of the

neutron window, leaving 50% of the window background free. Although this implies a loss in efficiency, it removes any systematic uncertainties from attempting to fit neutron spectra to the data as events may be defined as absolutely coming from a neutron capture. However, using only 50% of the data is wasteful. Although the lower half of the neutron window is contaminated with α events it is possible to extract the total neutron rate by fitting the expected neutron spectrum from a two dimensional t_f, energy distribution with those from surface and bulk α, as the α distributions are radically different. As shown in the lower diagram of Figure 3.21 there is a great deal of information in the peak at 764 keV. However, the efficiency of extracting the signal is dependent on the number of α particles in the lower neutron window. This sets a purity standard in addition to the standard required by SNO. Even if the region is heavily contaminated a consistency check can always be performed using the counts in the background free region and dividing by 50%.

This analysis depends on knowing the shape of the underlying spectra. This is easily measured for the case of the neutron capture distribution as calibrations taken at LANL are thought to be no different than the neutron signal from SNO, but, it is more difficult for the α backgrounds. As was explained in Section 3.2.2 there is a difference between surface and bulk contamination. It is planned to approximate these distribution by using a ^{235}U foil inside a proportional counter for the bulk contamination, whilst the surface contamination will be measured using an ^{241}Am source. Appendix C deals with the Maximum Likelihood technique which was one of the possible methods of separating the signals.

3.5 Optimization of Counter Parameters

Optimization of parameters is by definition the changing of the design and components to produce the best possible instrument under the applied constraints. However, the term also implies that the change in one parameter will affect the characteristics of the detector but will require the change of another parameter to counteract the side-effect of the first. The process of describing the parameters of the detector system becomes difficult as one parameter will depend on some other described later. Nonetheless, the parameters have been separated into two sections. The first deals with the mechanical and purity requirements whilst the second deals with the optimization of generating and retrieving a signal from the counter[38].

3.5.1 Purity Requirements

In addition to being efficient at capturing free neutrons, the proportional counters must satisfy the strict purity requirements with respect to U and Th contamination that any material inside the SNO detector must meet. This is especially relevant for NCD's, which reside in the active volume of the D_2O.

The purity requirements of SNO state that the entire NCD array can contain no more than 3.7μg of Th or 45μg of U and that the measurement of these levels must be done in situ or before the counters are placed inside the vessel. These levels correspond to the production of one neutron per day by photodisintegration from the U and Th daughters. Not only does this limit the total mass of material that can be used, as there are only finite levels to which U and Th can be removed, but it also implies that the measurement of activity from each counter using self α counting is not satisfactory. There are two reasons for this. Firstly, each counter has a dead region associated with the endcap and feed-thru's where the fields are not sufficient to cause multiplication and any activity will remain unmeasured. Secondly, the outside surface of the detector can not be measured. A separate detector has been designed for screening the outside of individual detectors. It should be noted that although the self α counting measures activity in the first few microns of the detector wall there is no reason to expect that the interior of the wall has identical levels of contamination due to the process by which the detectors are fabricated. However, the majority of contamination is expected to come from surface contamination which can be removed by etching.

Other factors also enter into the purity specifications. If the material is subjected to cosmic rays then the spallation products may produce γ rays capable of causing photodisintegration. This puts limits on the materials, their exposure time and the location where they are made[1].

The limitation is then on the total mass and the material which should be used. As the length of tubing used is of the order of 800 m this implies varying the wall thickness and the material.

However, the detectors must be mechanically stable when subjected to the varied hydrostatic pressures in the vessel and also to the torque associated with motion of each string as it is moved to its location at the bottom of the vessel. This mechanical constraint places limits on the material used, the wall thickness and maximum length of a single sealed cylinder that can be used.

Other considerations are that the counter be made out of a material that conducts, will not react with the heavy water, is non-porous, to both water and the gas contained inside the counter, and is relatively transparent to the neutrons which the counter is designed to detect.

The first prototype was to be a polycarbonate cylinder with electroplated copper on the inside. Polycarbonate is an intrinsically clean material and, while electroplated copper tends to carry lead along with it, the total mass, 32 kg, was so small that this would not present a problem. However, polycarbonate contains many hydrogen atoms and so would not be transparent to neutrons and electoplating resulted in a material which is porous. The plated copper would then allow the helium gas inside the counter to escape and the counter would

[1]Higher altitudes have a higher flux of cosmic rays.

not last the required ten years. Attempting to make a counter from solid electoplated copper would again fail for several reasons; the mass of copper involved would introduce large amounts of radioactive lead, the softness of the copper would lead to structural problems, and concerns were raised with respect to attack by the ultra pure water.

The second design was based on a counter made from chemical vapour deposited nickel. At high temperatures nickel carbonyl, $Ni(CO)_4$, can be decomposed to give elemental nickel and carbon monoxide. For nickel carbonyl this occurs at a temperature where no other carbonyls can undergo this reaction and the resulting material is extremely low in contaminants. Etching the internal surface of the counter with acid to a depth of $20\,\mu$m removes any impurities left on the surface by the mandrel on which the tube was made.

Unfortunately, the action of high energy neutrons and protons on the nickel causes spallation products, the most serious of which, because of its relatively long half-life, 78.8 days, and its emission of γ rays above 2.2 MeV is ^{56}Co. Calculations, based on a program by Lewin and Martoff, show that the equilibrium rate for ^{56}Co production in nickel is 24.22 decays/day/kg. The total amount of cobalt present in the nickel is governed by the exposure time, t_e, the 'decay time' or the time underground away from cosmic rays, t_u, and the half-life of the isotope, $t_{1/2}$.

$$R = R_0\left(1 - \exp\Big(\frac{t_e \log 2}{t_{1/2}}\Big)\right)\exp\Big(-\frac{t_u \log 2}{t_{1/2}}\Big) \tag{3.21}$$

Comparisons of this code with experimental measurements of cosmogenic activity by Brodzinski *et al.* agree within a factor of two. Further details are available in Appendix D. The final conclusion being that should nickel dectectors should be stored underground for a period of approximately six months before being installed in SNO to allow the cosmogenic component sufficient time to decay away.

3.5.2 Choice of Gas Mixture and Operating Parameters

It is impossible to do justice to the extremely complex problem of optimizing the parameters for the neutral current detectors. The list of possible options is not only limited to; gas mixture, total gas pressure, wall thickness of the counter, radius of the counter, anode wire diameter, anode wire tension, anode wire composition, operating voltage,.... The choice of gas mixture is detailed below, but more comprehensive details of the gas mixture and other parameters may be found in reference [38].

Figure 3.23 illustrates the contraints applied to the total gas pressure and the fraction of CF_4 when considering; the efficiency for capturing neutrons, the pressure required to stop the detector collapsing from the hydrostatic pressure at the bottom of SNO, the ability to extract neutron capture events from backgrounds (further dependent on the wall fraction and the 'speed' of the gas) and the maximum voltage/maximum gas gain that can be tolerated

Parameter	Considerations	Ref.
Gas Mixture	Fraction of wall events Drift speed of the electrons Quenching of U.V. photons Stable over the lifetime of SNO	[38]
Total Gas Pressure	Must be sufficient to stop detectors from collapsing Affects the wall thickness of the detectors Fraction of wall events Neutron capture efficiency Operating voltage	[38]
Wall Thickness	Limits of U and Th allowed	
Radius of Detector	Interference with Čerenkov light Neutron capture efficiency	
Anode Wire Diameter	Operating Voltage to obtain suitable gas gain Transmission of signals due to skin effect	
Anode Wire Tension	Stability over ten years without breaking Stability during transportation Minimal droop during horizontally testing	
Operating Voltage	Large enough for good signal to noise for small pulses Small enough to reduce the Space charge effect Small enough that no significant discharge occurs in components	

Table 3.1: A list of some of the parameters that must be optimised for neutral current detectors.

by the detector (too little leads to problems with signal to noise, too much results in high voltage breakdowns and problems with the space charge effect). The Figure is taken from reference [38].

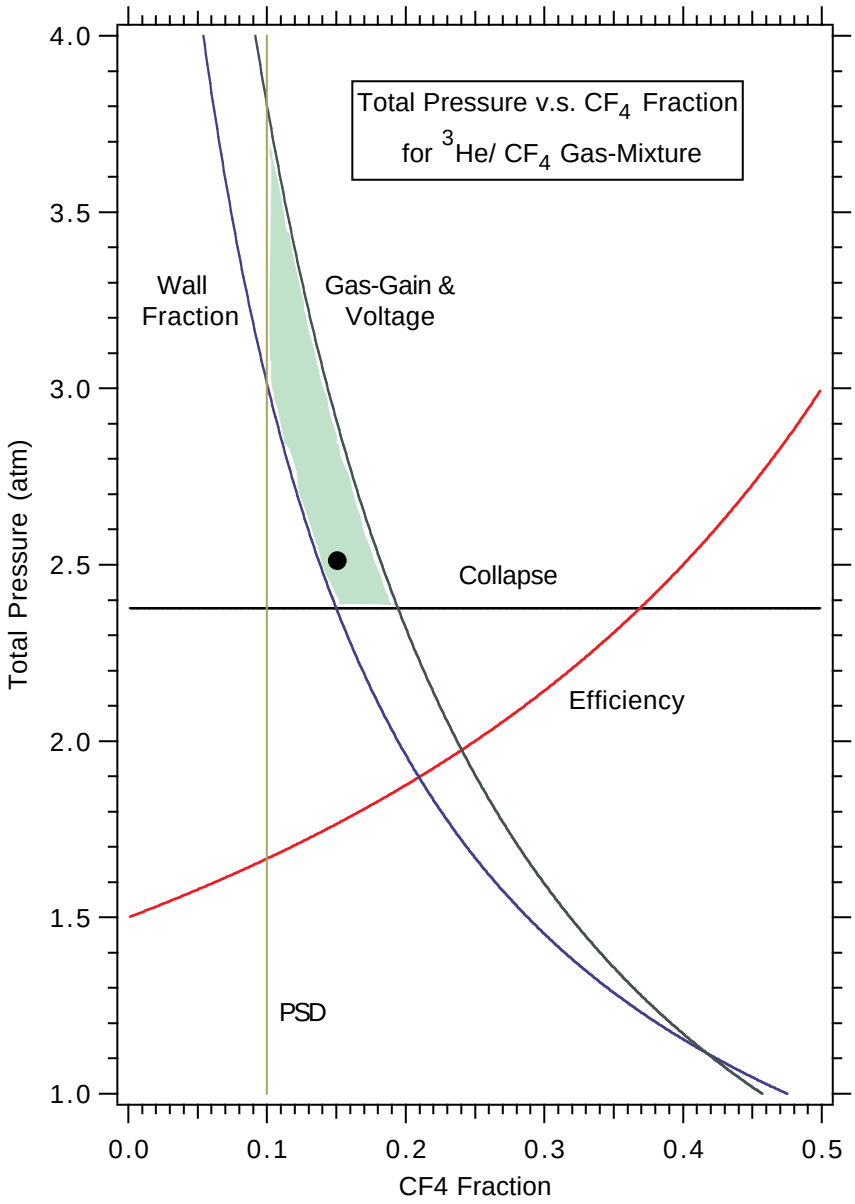

Figure 3.23: Some of the constraints placed upon the total gas pressure and the fraction of CF_4. This figure illustrates the limits provided by the neutron capture efficiency, the collapse pressure, pulse shape discrimination and the maximum voltage/gas gain.

Chapter 4

The WIPP Facility

4.1 Description of WIPP and Purpose

The Waste Isolation Pilot Plant (WIPP), is a research and development facility designed to demonstrate the safe disposal of low level radioactive waste. It is located near Carlsbad, SE New Mexico approximately 325 miles from Los Alamos. The facility is owned by the United States Department of Energy (DoE) and operated by the Westinghouse Electric Corporation, with scientific support provided by the Sandia National Laboratory. The waste in question is low activity transuranic waste, typically clothes, tools and equipment, which have become slightly contaminated with uranium. These items are sealed inside 55 gallon drums and placed inside large excavated rooms in the salt. After the room has been filled with drums it is back filled by blowing in salt dust. Over time the salt plastically deforms around the barrels, sealing them into the rock.

WIPP was designed to be both a test facility and the site for disposal. Currently, the site is not storing waste. As WIPP is in an experimental phase they have been willing to help with outside experiments. Currently, two outside experiments are in operation at the WIPP, the Los Alamos Low Background Experiment and the development experiment for the Super Nova Burst Observatory (SNBO).

For us, the mine has several advantages, besides its relatively close proximity to Los Alamos.

- WIPP, Sandia National Laboratory (SNL), who supply the scientific support for WIPP and Los Alamos are all DoE prime contractors. This allows Los Alamos to work under the wing of Sandia reducing some of the potential beaurocratic problems.

- The mine is 2150 feet deep and this radically reduces the through going cosmic muon rate down to only $200/m^2/day$. It totally eliminates the hadronic component. Figure 4.1 shows the depth of WIPP in comparison to other underground sites.

- WIPP is a salt mine and the salt is, radioactively, relatively clean with respect to U and Th, although it does have a high concentration of potassium and inevitably, radioactive

^{40}K.

- Sandia National Laboratory is already conducting experiments underground for determining the suitability of the site. As such, there is considerable experimental support available as well as ample power and telecommunications.

4.2 LANL Experimental Setup

The only way to measure the activity of the nickel detector in an environment free from the hadronic component of cosmic rays was to construct an experimental area underground. Although pulse shape discrimination would be able to remove the majority of events it would be impossible to distinguish between an α particle produced by cosmic ray spallation and an α particle resulting from the decay of U/Th and their daughters. Additionally hadrons and Ni(n,p)γ would mimic He(n,p)t. In addition, the high cosmic ray flux at Los Alamos results in a much higher trigger rate. Figure 4.2 shows two data sets, one taken at Los Alamos and the other at the WIPP. Also, it should be noted that the aim of the WIPP series of experiments was to measure α activity to the level of $2\,\alpha$'s/m^2/day a level which would be impossible at Los Alamos, given the hadronic component and without sophisticated cosmic ray veto techniques.

The LANL experiment was initially located in an equipment shed (G shed) in a rarely used portion of the mine, approximately half a mile from the main area of the mine. Los Alamos shared this shed with another Sandia experiment which was measuring the deformation of the salt over time. The shed's location is shown in Figure 4.3.

The experiment was split into two parts, one outside the shed consists of a large Faraday shielded, waterproof tank, which contained the detectors and the preamplifiers. Inside the shed was the data acquisition system, which comprised HV power supplies, digitizers and the associated electronics of amplifiers and discriminators. A computer was also placed inside the shed to record the data and to relay it back to Los Alamos. Figure 4.4 shows the exact layout. At the end of January 1996 the area of G-shed was decommissioned by the WIPP and the experiment was moved to an alternative site, Q-shed, also shown in Figure 4.3. Currently measurements of the latest full-scale prototypes are in progress at Q-shed.

Access to the mine was limited, due both to physical working hours and its remote location from Los Alamos. The WIPP site has strict safety rules which limit the hours that an individual is able to work underground and, although WIPP is described as close to Los Alamos, it takes over four hours to drive there. As a result, remote access of the experiment was achieved via commercial software and a phone connection in G shed. This enabled remote monitoring and some control over the experiment from Los Alamos (or indeed from hotel rooms in Carlsbad when time underground was limited). Although most of the experimental monitoring could

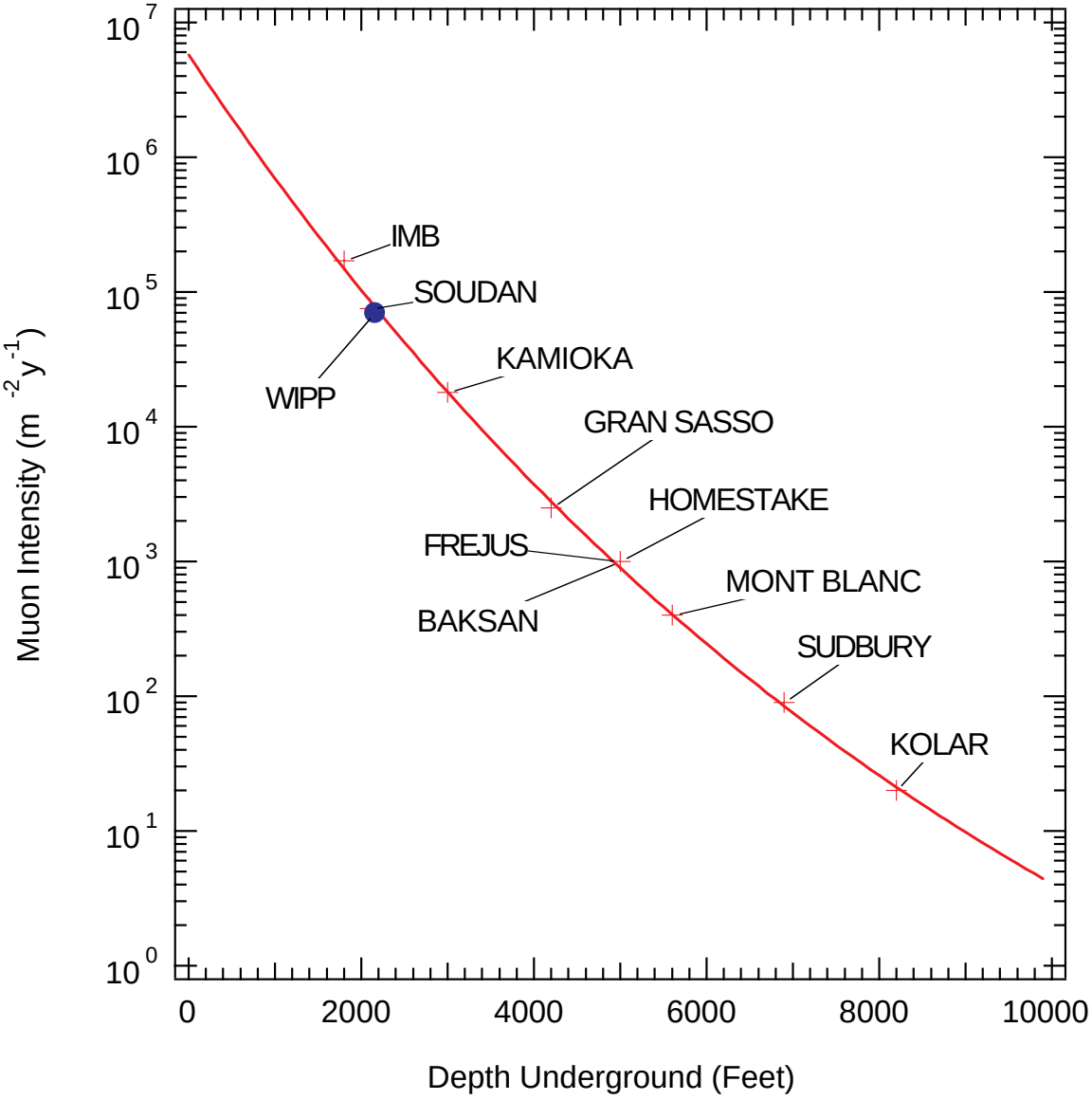

Figure 4.1: The depth of underground experimental areas.

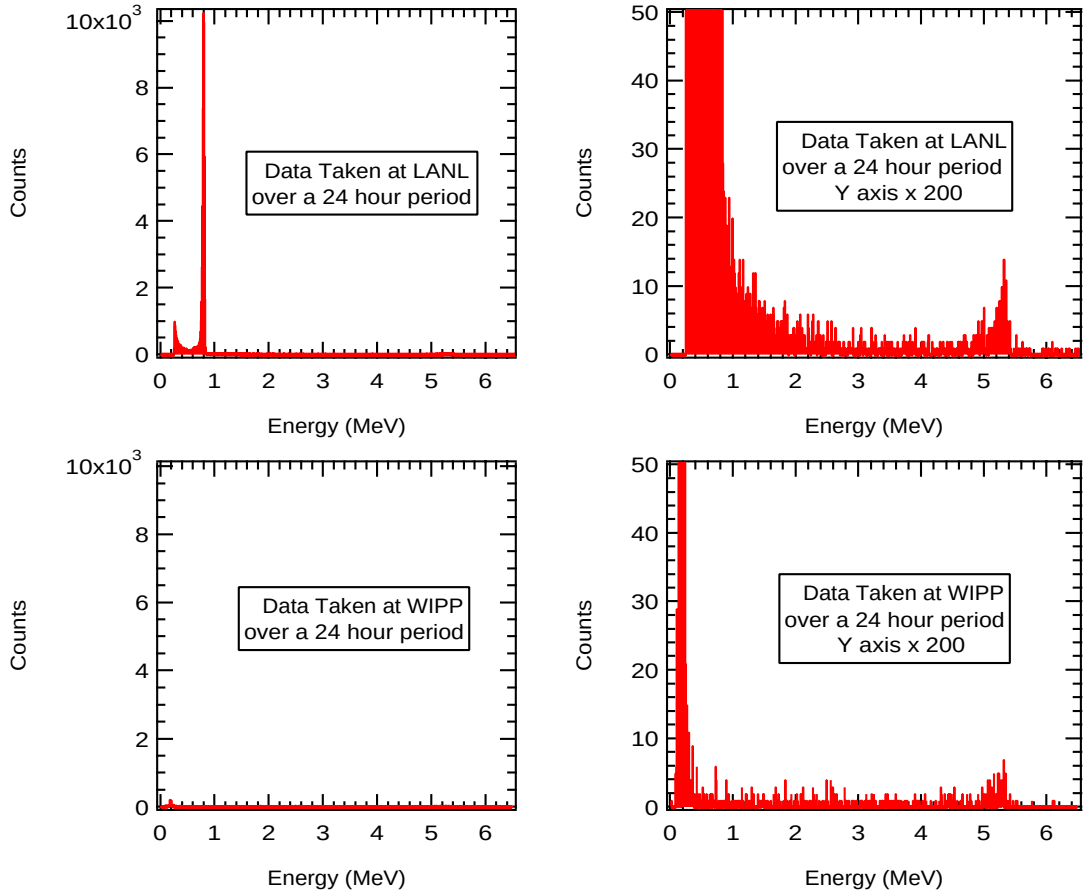

Figure 4.2: Two energy spectra. The top graphs were taken at Los Alamos whilst the others were taken at WIPP. The data rates correspond to 63462 and 1874 counts per day respectively.

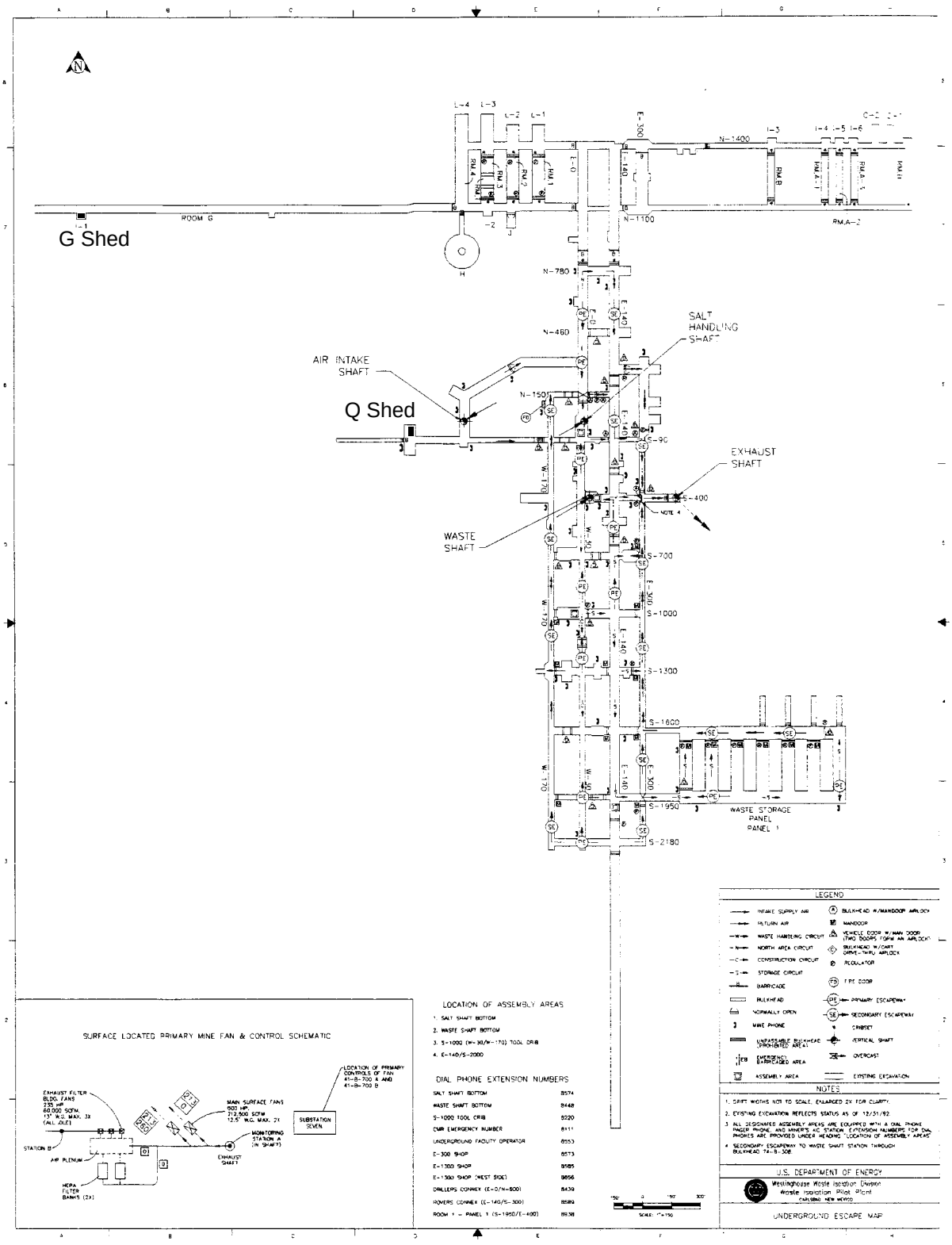

Figure 4.3: Overview of the WIPP site mine.

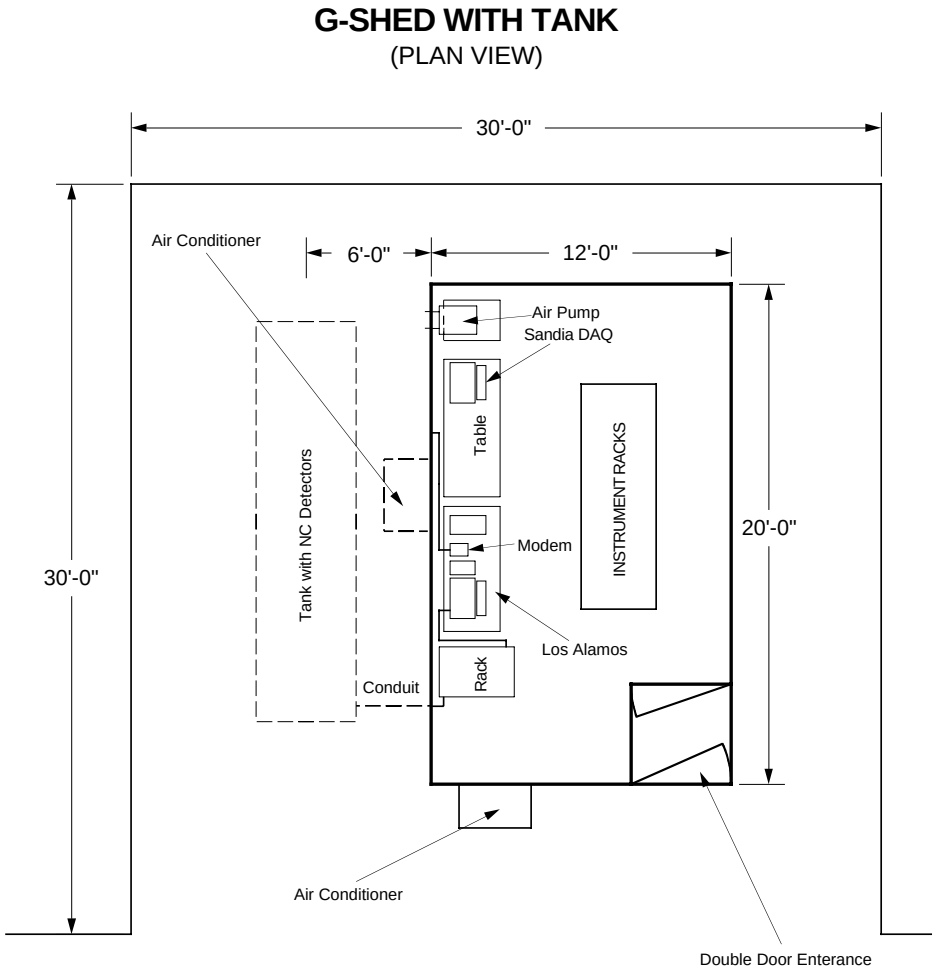

Figure 4.4: The layout of both the electronics and Faraday shielded tank for the WIPP series of experiments.

be carried out remotely from Los Alamos, problems which require the restarting of the crates or the computer had to be carried out by WIPP employees. Eventually the majority of these problems were found to be caused by brown outs and short duration power outages and these were solved by connecting the entire system to a large computer controlled UPS (Uninterruptable Power Supply).

Data retrieval from the site was done in two ways; either by downloading the data over a phone line, which proved to be expensive, or by transferring the data to a magneto-optical disk which would then be mailed back to Los Alamos. The second method was cheaper but did not allow access to the data for periods of up to three weeks. The more recent experiments involving the full-scale test detectors have significantly lower data rates and the data can be retrieved via modem on a daily basis in a matter of minutes.

4.3 History of LANL Experiments at WIPP

There were several detectors measured at the WIPP site though for convenience of labeling there were three distinct stages. The results of these stages are covered in more detail in Chapter 5.

4.3.1 Stage 1

Stage 1 is defined as the set-up and shake down period. The detectors used were two metre thin walled stainless steel tubes with standard conflat end-caps and feed-thru's. They resembled the SNO NCD detectors only in length and gas mixture. The experiment was started in May 1993, but no useful data was retrieved until after a neutron source had been shipped to the WIPP and the detectors calibrated underground. This stage was completed mid-January 1994. The detectors were filled with 2.5 atm. of ^{3}He, ^{4}He and CF_4 in the ratio 0.04:0.76:0.20.

Although the following Chapter discusses the physics results from this stage in detail, many aspects of operating a remote experiment underground were learnt, the most important of which were:

Identification of electronic problems not normally seen when operating an experiment at LANL. The initial electronics and data acquisition design was assembled quickly to meet the shipping window and as a result no analysis software was available to examine the resulting pulses. It was not until after the experiment had been assembled that problems were noticed in two areas. Firstly, the P/S 777 (Philips Scientific) fast amplifier was saturating with pulses above 4 MeV. This was undesirable as the largest α particles from the Th chain have an energy of 9 MeV. Secondly, the data sets showed a large number of slowly rising pulses with anomalously high baselines. These were deduced to have come from events with energies close

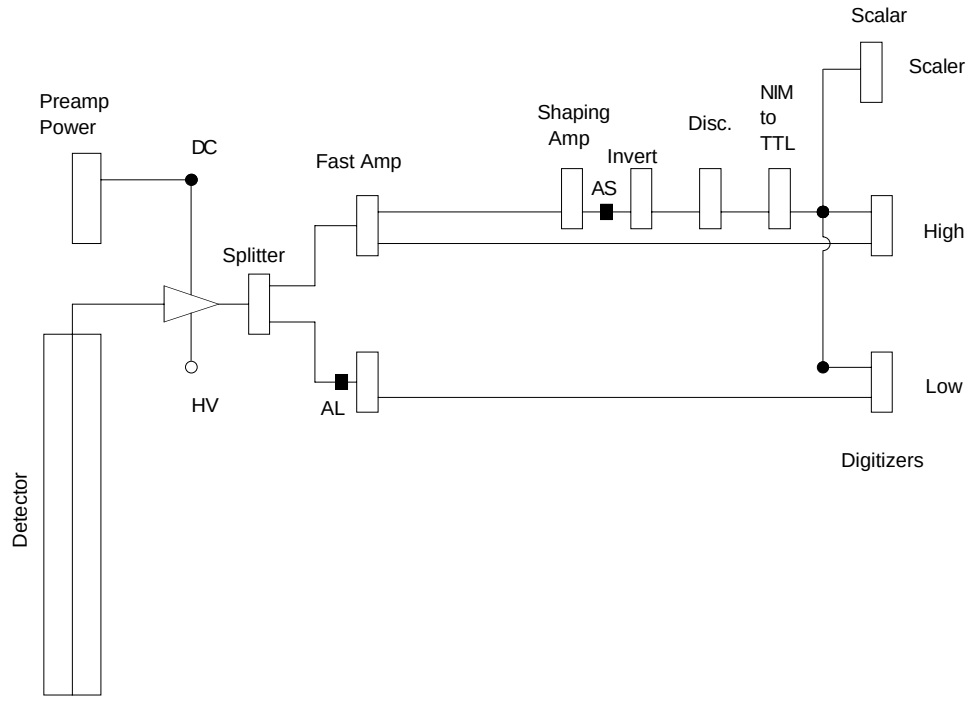

Figure 4.5: A schematic of the electronics used in WIPP Stage 1.

to that of the trigger. Figure 4.6 shows how one of these could be formed. These two problems were solved by splitting the signal into high and low gain parts and designing a new method of triggering based on shaped signals. Figure 4.5 shows the electronic layout used. The signal from the pre-amplifier is split into high and low gain channels corresponding to 0.1–1 and 0.1–10 MeV respectively. This produced detailed information over the neutron window as well as the full range of U and Th alphas. In addition a neutron source was shipped to WIPP to calibrate the new electronics system in August 1993.

A large number of pulses which were not normally present at LANL. Due to the problems of DAQ rate at LANL, digitized data sets were normally taken over a short period of time, typically less than an hour and usually with a source present. As a result the only pulses analysed were those from the source or from cosmic rays. The data from Stage 1 provided a large number of unexpected pulses which led to a great deal of R&D in pulse shape analysis, and recognition of spurious events.

Gas contamination as a result of outgassing. During Stage 1 it was noticed that the resolution of the fourth stainless steel detector had worsened significantly. Analysis of the data in the neutron window concluded that the change was due to the presence of a small amount of an electonegative gas in the detector. As the detector was at a positive pressure with respect

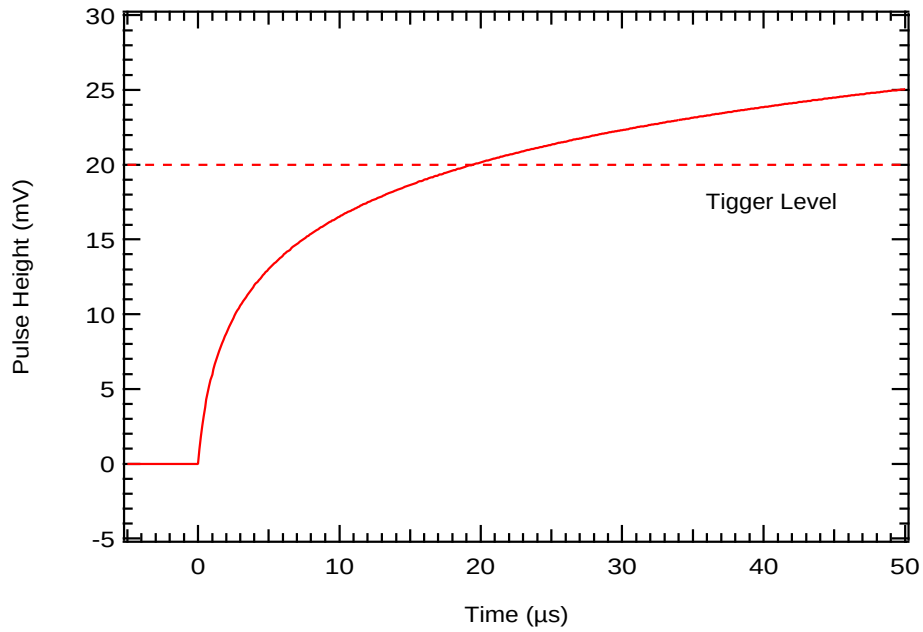

Figure 4.6: A simulation of how an anomalously high baseline pulse could occur. If the maximum height of the pulse is close to the trigger level, then only part of the pulse which is recorded is this slow rising section with an apparently high baseline as the transient digitizers only record 10 μs before the trigger.

to its surroundings, the only possibility was that the gas had been released from the walls of the detector. As a result the next series of experiments took great care in cleaning counter surfaces prior to assembly and baking of the complete counters after assembly.

Ideas for the next series of experiments. Examination of Stage 1 data showed that a large number of events originated from the end-caps of the detector, where the electric fields were non-uniform and the resulting pulses somewhat distorted. Given the activity associated with the end-caps, it was decided that position information was vital if any statistically valid statements were to be made about the levels of U and Th in the next series of detectors. In addition it would be desirable to avoid production of these type of pulses. This lead to further R&D in field shaping in the endcap regions which was further refined after the first short Ni CVD detector.

Observation of ^{210}Po. Analysis of the data showed a significant contribution from an α emitter at 5.3 MeV. Examination of the time-energy plot showed that there was a significant amount of ^{210}Po on the surface of the detector which decayed away with half-life of the order of 138 days. This implied that the Po was not in equilibrium with its parent isotope, ^{210}Pb, a somewhat surprising result in view of its likely origin as a ^{222}Rn daughter.

4.3.2 Stage 2a

Stage 2a is defined as primarily the shakedown period for position encoding of proportional counters using the double-ended charge-division method. From the lessons learnt in Stage 1, a new electronics system was designed such that the event position along the length of the detector could be recorded along with the pulse shape. Figure 4.7 shows the electronics used for both Stages 2a and 2b. Two charge sensitive preamplifiers were used in conjunction with a high resistivity (nichrome) wire. Any signal produced would undergo charge division, a fraction collected by pre-amplifier A and the remainder collected by B. The signals A and B were then summed using a P/S 744 to form $A + B$ for two reasons. Firstly, $A + B$ contained the full energy of the pulse and could be used, via the shaping amplifier, to produce an energy dependent trigger. Secondly, summing the two pulses canceled the noise generated by the resistive wire (a series noise generator). The ratio of B to $A + B$ at a particular time after the trigger was then used to provide position information, where the ratio is linearly dependent on the event position. Figure 4.8 shows the results of this for neutron slit experiments performed in Los Alamos [39]. Appendix B provides further information of the pulse analysis techniques.

The initial detectors were again made from stainless steel as the prototype nickel CVD detectors had not yet been completed. Additionally, the steel tube were radioactively dirty and again provided a large sample of pulses which were used to identify possible problems with the system. They were intended to be replaced by the first set of short nickel CVD counters, the first of which was installed on March 23$^{\text{rd}}$ 1994. This detector was constructed from two 15 inch slightly tapered tubes (minimum/maximum diameter 2.00/1.93 inches) which were laser welded together. The tapering was intentional as it made removal of the Ni CVD tubes from the stainless steel mandrel easier. However, full production tubes are straight, the problems of removing thin walled nickel tubes from their mandrels having been solved during the course of this thesis. The two halves were cleaned differently. The left hand side of the detector was chemically etched to a depth of approximately 0.15 μm. The right hand side was cleaned with acetone and alcohol to remove any surface grease or dust. At this stage ultra-clean endcaps were not available for this detector; endcaps that had been produced via electroplating had to be used instead. These were expected to have a high concentration of U and Th in comparison to the CVD nickel. Therefore it was necessary to remove the endcaps entirely from the data sets using a position dependent cut. In addition a longer length of insulator was used to reduce the field in the endcaps region so that few α particles from the endcaps would enter into the data set. All three detectors were initially run with a mixture of ^{3}He, ^{4}He and CF_4. During Stage 2a it was decided that the Ni CVD detector should be refilled without ^{3}He as calibration was no longer the major issue. Instead it was desirable to obtain data on just the α particles in the neutron window for verification of the neutron only region. This stage lasted

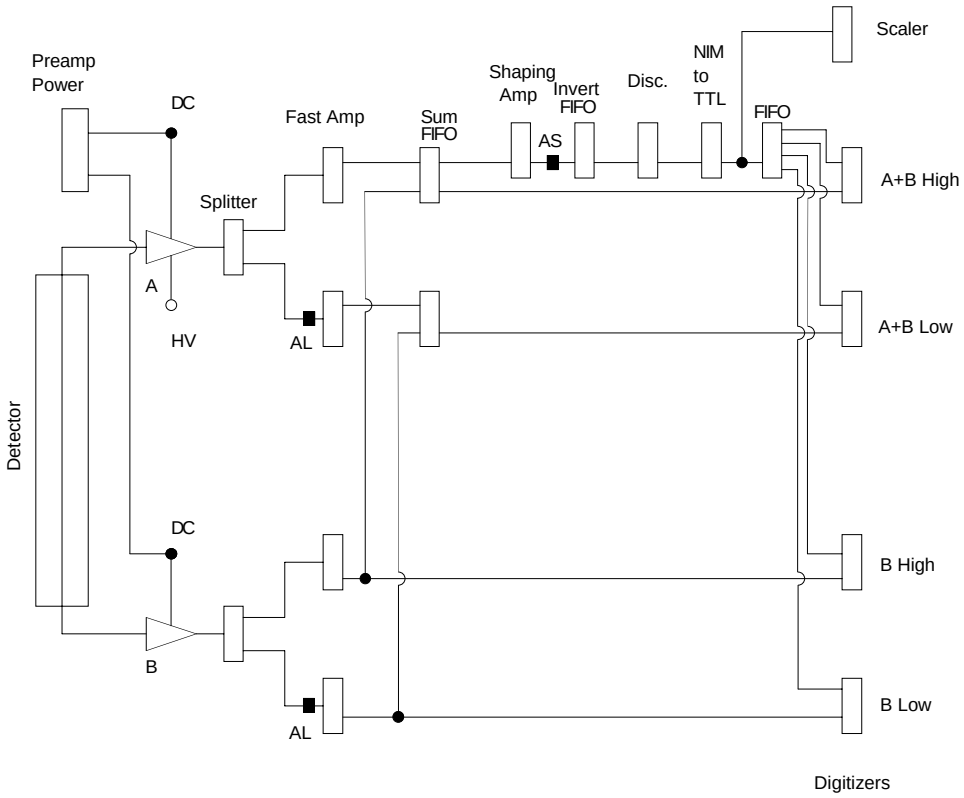

Figure 4.7: The electronics used for double ended position encoding with charge sensitive preamps used in WIPP Stages 2a and 2b. The abbreviation FIFO is used for the Fan In Fan Out modules used. The AL and AS refer to the attenuators used to adjust the gain for 0.1–10 MeV signals and for the shaped pulses respectively.

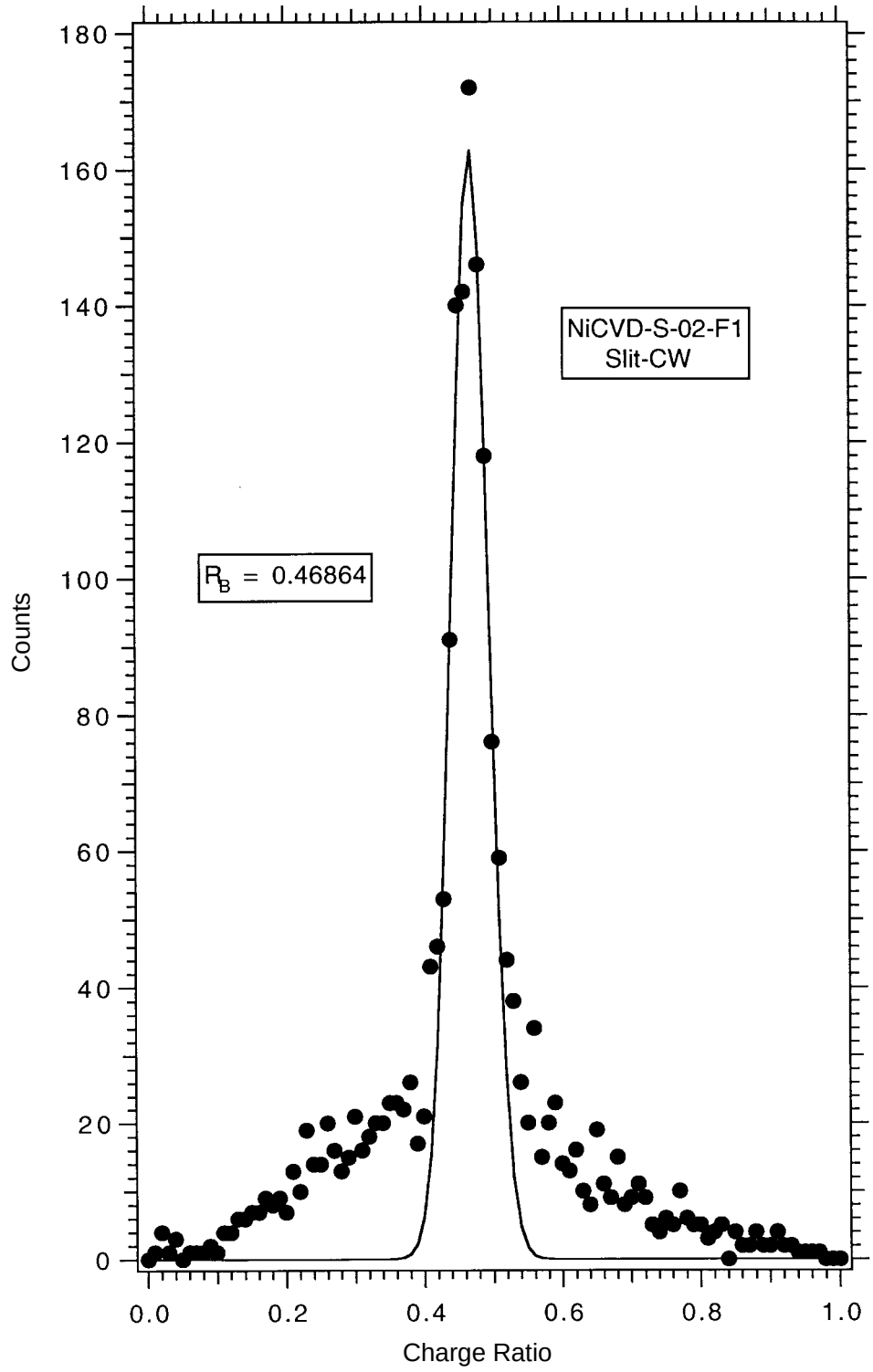

Figure 4.8: Position information obtained by using a collimated ^{252}Cf source at Los Alamos. The peak is not truly Gaussian, due to the Lorentzian profile of the collumated neutron source.

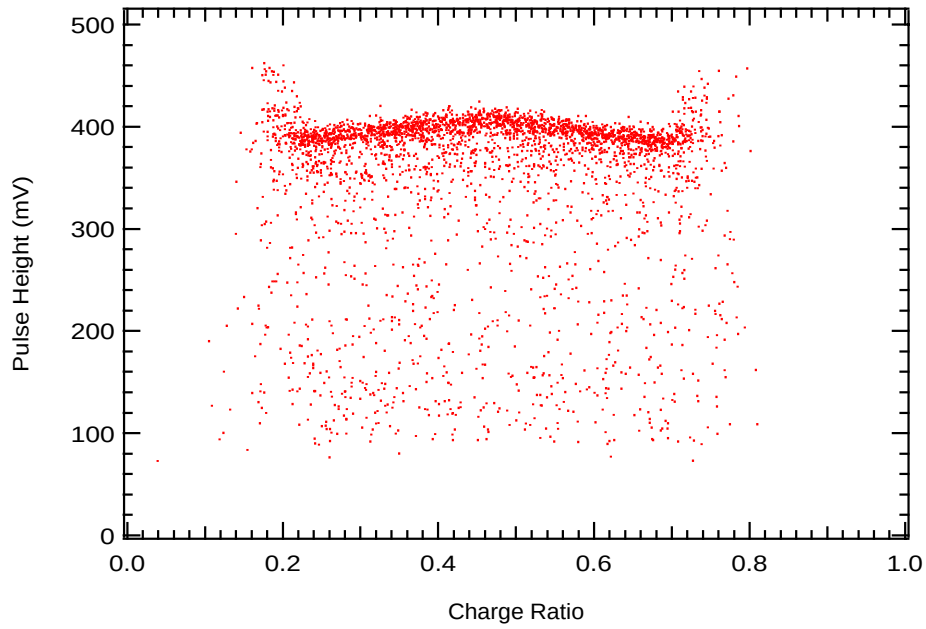

Figure 4.9: A neutron calibration spectrum of NiCVD 1 taken at the WIPP. The data has not been cut to remove either the endcap events or remove the position dependence of the gas gain. The charge ratio is used to determine the event's position along the axis of the detector.

until September 6^{th} 1994, when two further nickel detectors were produced.

During this period various problems were identified:

Field Shaping. The length of penetration of the quartz feed-thru was insufficient to remove distorted pulses due to activity in the endcap region. Figure 4.9 shows a neutron calibration spectrum from the short nickel CVD detector. Two features require explanation in the figure. Firstly, as the tube is tapered towards its centre there is a corresponding increase in gas gain (Equation 3.1). Secondly, towards each end of the detector the gas gain rises sharply. This rise in gas gain is attributed to the smaller radius associated with the end caps. Figure 6.2 shows the design of a detector and the shape of the endcap. This feature was undesirable and the second set of short CVD detectors extended the quartz feed-thru further into the detector to remove this effect.

The different halves of the detector contained differing amounts of activity. Both parts of the detector were produced in the same manner but one was etched while the other was only cleaned. As some surface activity remained even after etching, it was decided that the next series of detectors should be etched to different levels to determine the effectiveness of the etching procedure. However, this simple test demonstrated the importance of chemical etching. It should also be noted that the effect radically reduced the measured levels of surface

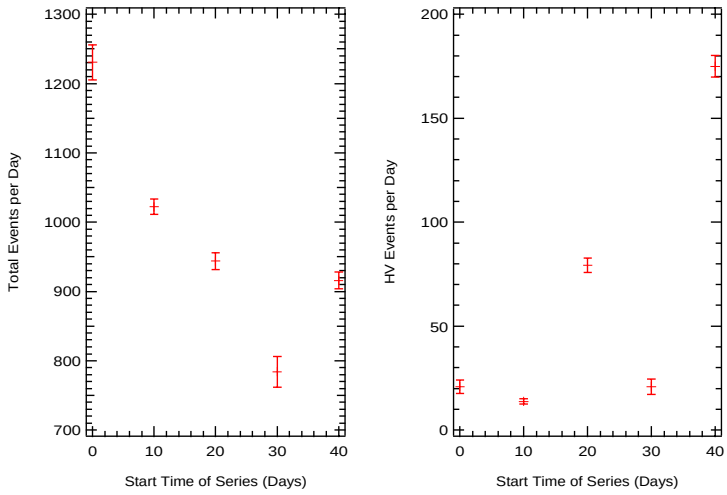

Figure 4.10: The data rates during the first part of Stage 2a for Ni CVD 1. The left hand graph depicts the total event rate (in events per day) for the first five 10 day periods whilst the right hand graph depicts the number of events per day which can be attributed to high voltage discharges.

U and Th rather than reducing the levels of bulk U and Th.

The data showed a peak of α activity at 5.3 MeV. U and Th were expected to be present in the bulk of the material (albeit in very small amounts) and hence any α activity should have produced a continuum rather than a peak spectrum. A peak represents surface contamination (most of the particles enter the gas with their full energy in comparison to a bulk source where many of the α's are degraded in energy as they traverse the material of the wall). In addition lifetime fits from earlier data from Stage 1 showed that the peak was consistent with ^{210}Po ($Q = 5.3$ MeV, $t_{1/2} = 138.8$ days). It is difficult to imagine where this contamination originated from especially when considering it was decaying with a half life of 138 days and not in equilibrium with its parent ^{210}Pb, $t_{1/2} = 22$ years.

HV discharge became a significant problem. Occasionally, a large number of spurious events, which were identified as originating from the pre-amplifier, appeared in the data. These were determined to result from HV discharge within the pre-amps and feed-thru's and though they were completely separable from normal proportional counter pulses the rates were sufficiently high as to swamp the data. Figure 4.10 shows a prolonged series of discharge events. For this reason three different pairs of pre-amps were used with Ni CVD 1 during Stage 2a. This led to a serious R&D effort to eliminate HV discharge in the preamplifier capacitors and current pre-amps produce less than 1 spurious count per day.

Det 1	LHS	Etched $\sim 0.15\mu$m	Lead based solder
Det 1	RHS	Cleaned with acetone	Lead based solder
Det 2	LHS	Etched $\sim 1\mu$m	Tin/Silver solder
Det 2	RHS	Etched $\sim 2\mu$m	Tin/Silver solder
Det 3	LHS	Etched $\sim 1\mu$m	Tin/Silver solder
Det 3	RHS	Etched $\sim 1\mu$m	Tin/Silver solder

Table 4.1: The levels of etching performed on the various halves of the two new short nickel CVD detectors and the solder used for attaching the central wire. After etching the segment Det 3 RHS was exposed to 0.9 pCi/litre radon loaded air for 48 hours.

There were frequent breaks in the data sets corresponding to the CAMAC crates reporting an error. Although these errors were reported during Stage 1 there was insufficient time to solve this particular problem. During Stage 2a this became more problematic. The system was designed such that should a power outage occur, then the CAMAC crates would go offline and hence report an error when queried by the computer. The computer would then check the UPS and if a power outage existed then the computer would stop acquisition and turn both itself and the UPS off. The UPS would then restart only when power was restored. Unfortunately if the cause of the problem was either a short duration power outage or a 'brown out' then full power would be provided to the UPS before it was turned off by the computer. The UPS would then not turn itself (and hence the computer) back on until the next outage. This problem was not solved until February 1996 (during Stage 2b) when the entire electronics system (computer and electronics rack) was placed on a large 10 kVA UPS. Since then, the computer has polled the UPS every 60 seconds to ensure that power was still available. Should the UPS come close to being exhausted then the system would shutdown, but this corresponds to several hours without power.

4.3.3 Stage 2b

Stage 2b is defined as the measurement phase for two more nickel CVD detectors in addition to the first detector. Again the new detectors were produced by welding together two 15 inch tapered Ni CVD tubes. Due to a pin hole leak in the middle of one of the segments detector number 3 was shorter than the other two. As a result of the discoveries in Stage 2a, the tube segments were cleaned/etched differently. Table 4.1 shows the different levels of etching and exposure. Also as a result of Stage 2a, the length of the quartz feed-thru was extended.

The motivation for the different levels of etching and air exposure comes from the presence of ^{210}Po contamination in Ni CVD-1. The tubes were etched at least an order of magnitude deeper than before to thoroughly remove any contaminants which may have come from the mandrel. Additionally a tin/silver solder was used to attach the central wire as it was consid-

ered possible that the Po had 'boiled off' from the lead based solder used in Det #1 when it was melted and plated onto the counter walls. Finally, one half of one detector was exposed to air whose Rn levels were measured under the assumption that perhaps the Po contamination was airborne. Unfortunately Stage 2b was not without its problems:

Ni CVD 3 showed a marked rise in its data rate shortly after being installed. This was not due to any problems with the high voltage and the pre-amps but to a small slow gas leak from the detector. As the pressure inside decreased the gas gain increased (Equation 3.1). This was effectively the same as lowering the trigger threshold and resulted in an increase in the rate due to the predominant ^{40}K Compton activity at low energies. The detector was returned to Los Alamos where a small leak was located at the junction between the feed-thru and the body of the endcap. It was sealed using Torr-Seal epoxy, refilled and returned to WIPP.

Once Ni CVD 3 had been returned to WIPP, there was an increased number of counts in NI CVD 2. On this occasion the increased rate was caused by the central wire slipping inside the feed-thru which eventually broke. It too was returned to LANL for repair. This lead to another R&D effort to determine the optimum wire parameters which would not result in breakage whilst allowing for minimal wire droop when the detectors were running in a horizontal mode during the cool down phase[38].

For most of December the experiment was offline. This was due to MSHA (Mine Safety and Health Administration) inspections at the WIPP. The power cables to G Shed were sufficiently old that they had to be replaced, resulting in no power to G shed over this period.

One of the digitizers began behaving erratically. One of the digitizers developed an intermittent fault which was not diagnosed from LANL. As a result parts of the low gain data from Stage 2b were rendered useless as no position information was recorded. The data from these periods has been filtered and corrected for the effective live time. The results of this and of the other two stages are expanded upon in the following Chapter.

Chapter 5

Physics Results from WIPP

5.1 Stage 1 2 m Stainless Steel Detectors

Although very little can be said quantitatively about the first stage of the WIPP experiments, at least with respect to levels of U and Th in the detectors or the thermal neutron flux, a great deal of qualitative and semi-quantitative information resulted from the analysis of this stage. As was explained in Chapter 4 it was designed to be the shake-down system for the nickel detectors. The detectors used were thin walled stainless steel which were not radioactively clean.

Only after the electronics problems mentioned in Chapter 4 had been corrected, could data taking begin in earnest. Over the period August 11^{th} 1993 to February 28^{th} 1994 a large amount of data were recorded. Over this time period the analysis software was continuously developed and modified as new pulse topologies were discovered following analysis of the resulting data sets. Because of Stage 1's extremely long running time pulses which would not have ordinarily been seen in the laboratory environment appeared. Initially, there was not always an explanation for these pulses, but they were significantly different from normal gas like pulses that it could be concluded that they were not caused by ionizing radiation in the gas. It was during this stage that many of the pulses shown in Chapter 3 were identified. Figure 5.1 is an example of a non-gas pulse discovered during Stage 1 which could be identified. It is a result of a high voltage discharge, the charge signal showing the characteristic exponential fall associated with the time constant of the pre-amplifier. In contrast, Figure 5.2 is an example of a pulse whose origin was not initially understood, but nonetheless can easily be removed from the rest of the data by its characteristic shape. Eventually it was determined that this pulse originated from the input capacitor of the pre-amplifier.

Similarly, it was during this Stage that the initial ionization first mentioned in Chapter 3 was noticed. This was a result of attempting to combine the high and low gain pulses into one consistent pulse (the low gain part of the pulse would be used when the high gain pulse had saturated the digitizer). Only when analysing the higher energy α pulses was this effect

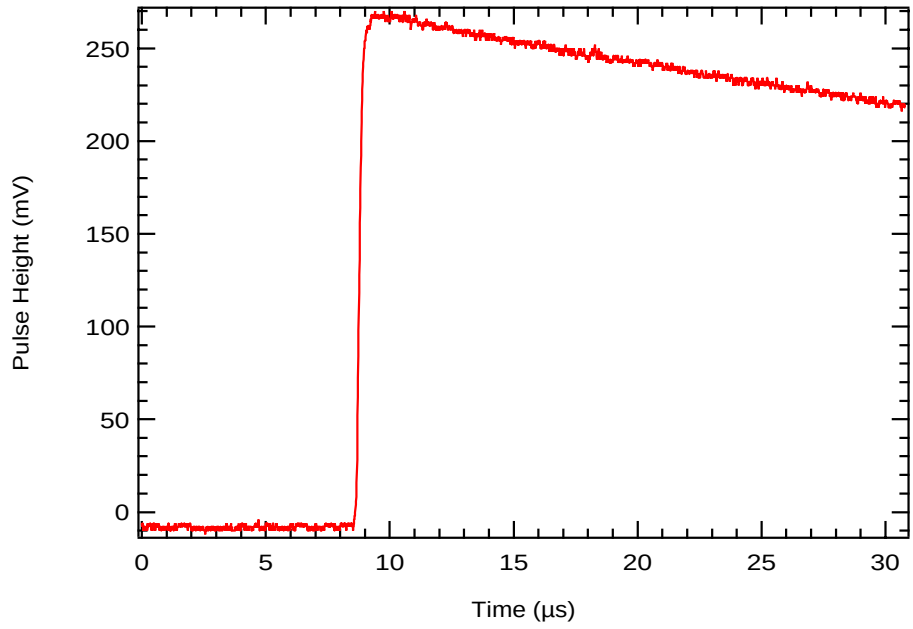

Figure 5.1: A high voltage discharge pulse distinguished by its fast rise time and decay time characteristic of the decay time of the pre-amp.

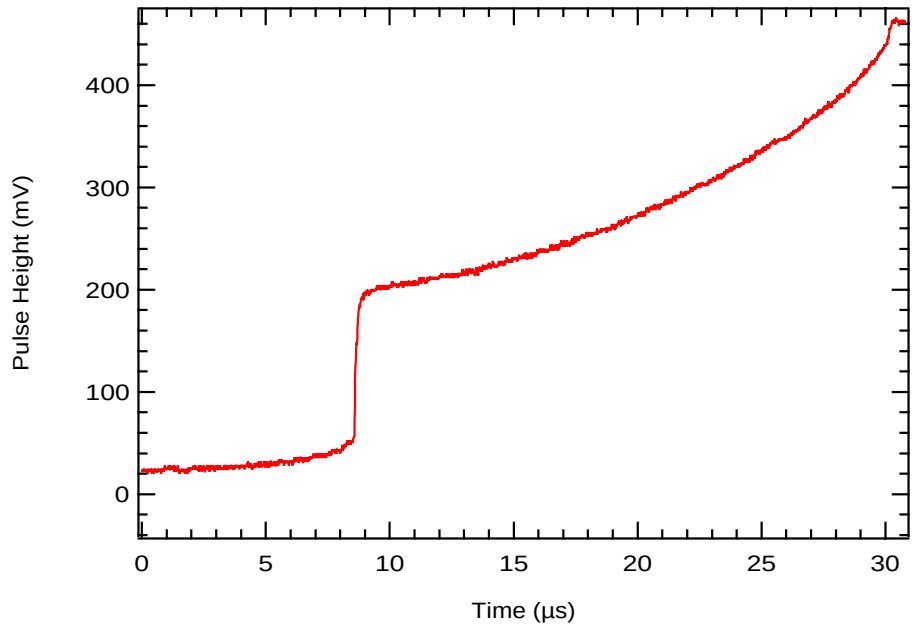

Figure 5.2: A pulse of unknown origin. It can easily be separated by the high end point of the pulse relative to its small initial height.

noticed. The effect of the initial rise was to radically alter the analysis code's ability to determine the start of the pulse as it was significantly above the level of the noise.

5.1.1 End Effects

The main driving force behind the detailed pulse shape analysis was the rise time *vs* energy plots produced. At LANL these were simpler and thoroughly understood. Any deviations were associated with cosmic activity, and in addition the shorter run times did not allow for many of the spurious pulses to become numerous enough to notice. With WIPP Stage 1 the run times were considerably longer, the cosmic background significantly reduced and the resulting long duration plots showed some strange characteristics. Figure 5.3 shows the results of 38.3 days of data taken using the long stainless steel detector #3 from August 11^{th} onwards. For comparison the calibration data is shown in Figure 5.4. In contrast with the calibration data, the extended run shows a much increased Compton band (due to ^{40}K in the salt walls) as well as another strange band over the neutron window marked "End Effects". Examination of these pulses did not show that they were caused by problems with the electronics and that they did resemble gas like pulses. Figure 5.5 shows one of these pulses. This was initially a concern. There was no way that an α particle in this energy regime or neutron could have a track with such a long rise time. Additionally, a Compton electron could not deposit sufficient energy in the gas to cause such a track. There was no significant cosmic ray flux, though the possibility remained that this could be associated with a nuclear collision resulting in a high energy proton.

Analysis of the 1–10 MeV region gave a better idea of what caused this band. Figure 5.6 shows the low gain data taken over the period August 11^{th} to September 23^{rd} 1993. The neutron peak can just be seen at around 0.8 MeV above that and curving down to lower rise times at higher energies is the band. In addition there is a significant peak around 5.3 MeV and the shape of the t_f vs energy plot is consistent with α data taken at LANL using at 5.4 Mev ^{241}Am source. The source of this peak will be discussed in Section 5.1.3. The band's continuance into the α region suggests that it is also the result of α activity in the detector. This is not unreasonable considering the considerable presence of α particles inside the detector. It then remained to determine how an α particle could create such an extended track.

The assumption was that the band was a result of α activity in the region of the detector end-caps. The reasoning behind this is that the endcap region has very odd electric fields (there was no attempt made at field shaping in Stage 1) and that the extended track might well be due to electrons created in this region arriving later at the wire than would normally be expected for this operating voltage and gas mixture. Additionally, the band must be the result of a surface contaminant as it is not a continuum. As a result a calculation was carried

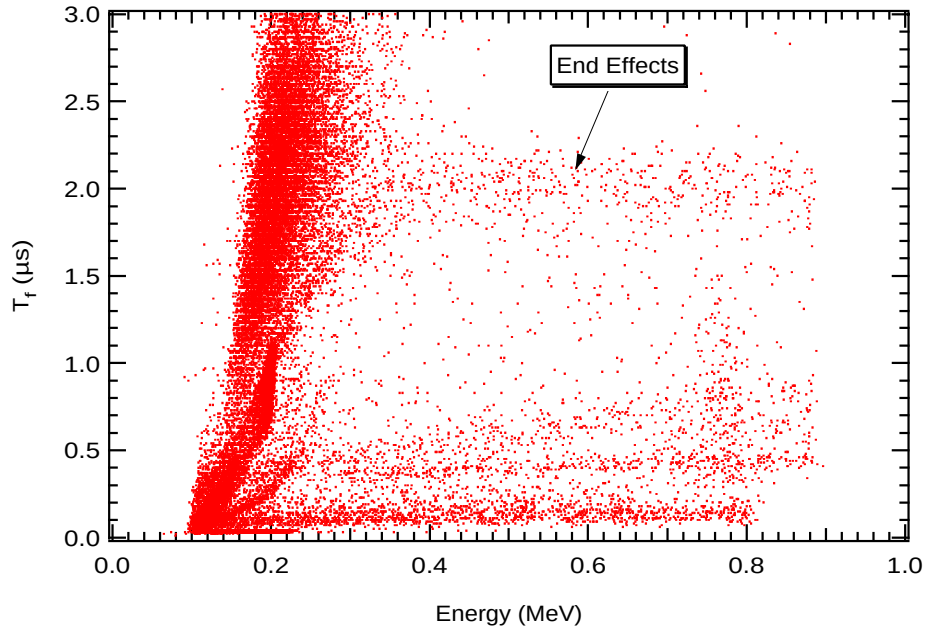

Figure 5.3: Data taken using stainless steel detector #3. The detector was operated at 1400 V between August 11$^{\text{th}}$ and September 29$^{\text{th}}$ for a total live time of 38.3 days. The resulting high gain data were analysed to produce a rise time (t_f) *vs* energy plot.

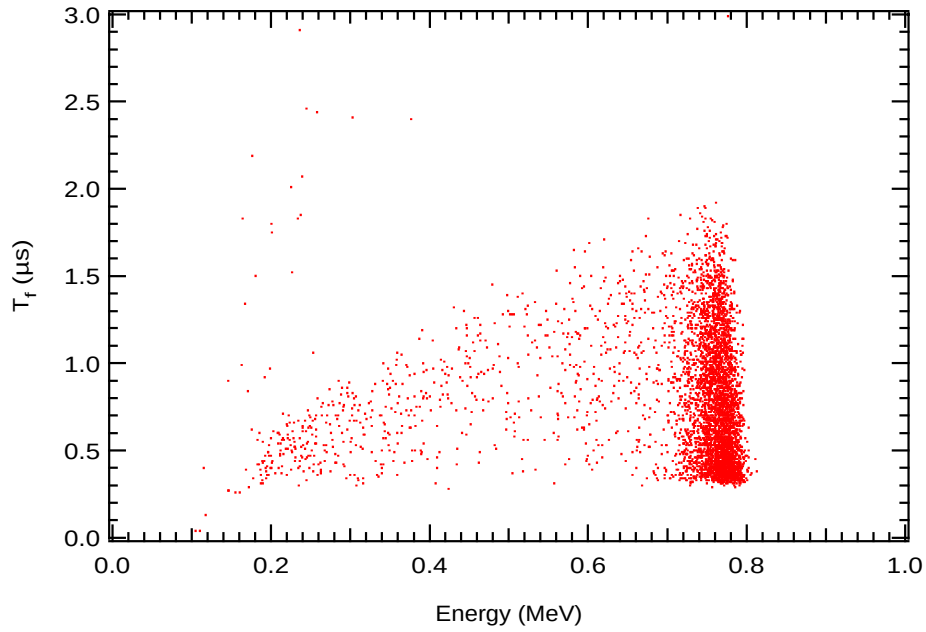

Figure 5.4: Data taken using stainless steel detector #3 with a moderated ^{252}Cf neutron source for 90 minutes. The resulting high gain data were analysed to produce a rise time (t_f) *vs* energy plot.

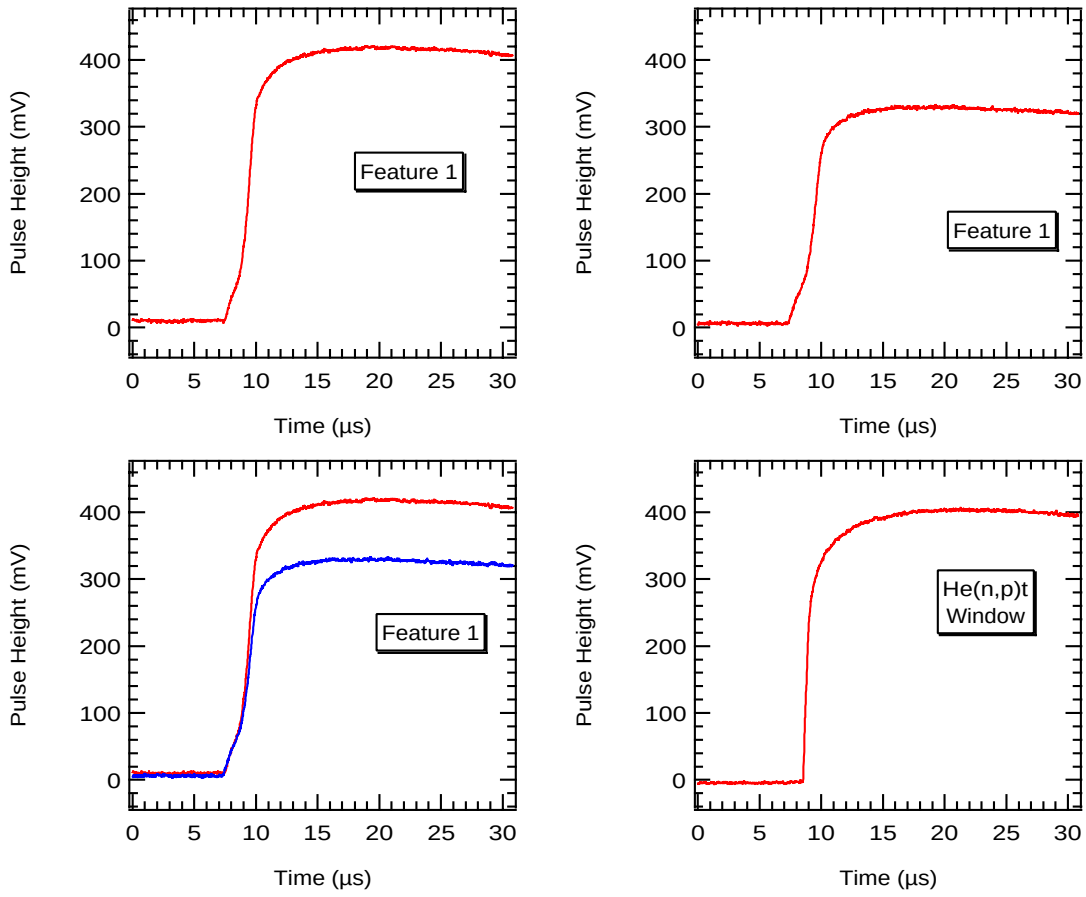

Figure 5.5: The top two pulses are taken from the end effects band with slightly different energies. The lower pulses consist of the two end effect pulses superimposed to demonstrate the similarity of their initial rises despite their differences in final energies and a normal 'fast' neutron pulse for comparison.

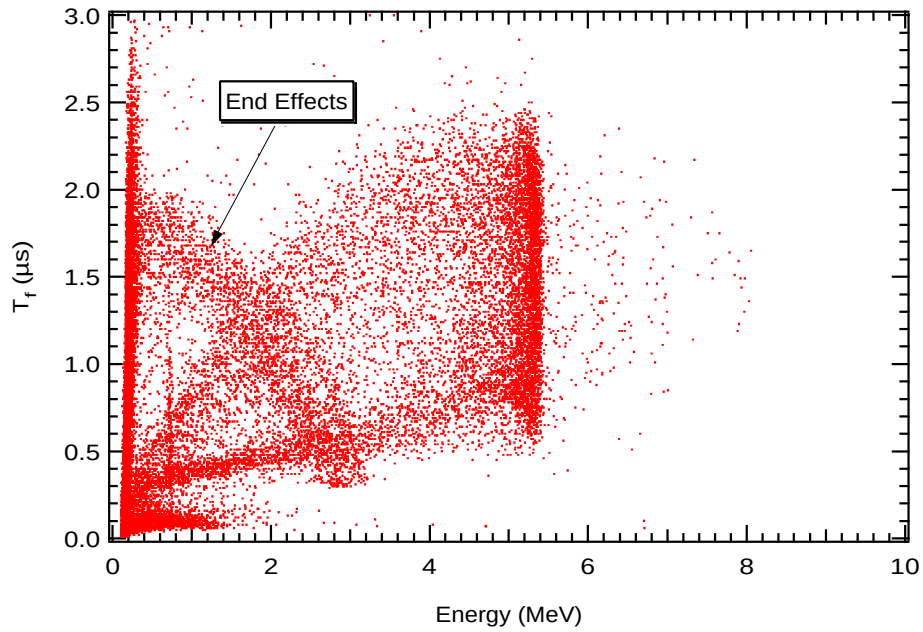

Figure 5.6: Data taken using stainless steel detector #3. The detector was operated at 1400 V between August 11^{th} and September 29^{th} for a total live time of 38.3 days. The resulting low gain data were analysed to produce a rise time (t_f) *vs* energy plot.

out on the density of points in the end effects band in comparison to the rest of the α band. Under the assumption that the fields in the first 5 cm of the detector were affected then the density of α's in vicinity of the endcaps needed to be only a factor of 5 high than that present in the stainless steel. This is realistic given not only that the feed-thru used was made from ceramic, a material which is notoriously dirty with respect to U and Th and their daughters, but also because lead based solder used in the mounting of the end-caps and the central wire.

This claim was supported by a later experiment in which the operating voltage of the detector was lowered to 1300V from its norm of 1400V corresponding to a change in the gas gain of a factor of 2. If the end effects band was truly caused by end effects in the detector the effect of lowering the operating voltage should not affect the first part of the pulse (which occurs near the endcap) as there was already no multiplication in that region. However, it would reduce the amplitude of any part of the track which entered into a region of the detector where multiplication could occur. Figure 5.7 shows pulses taken at both voltages with exactly the same rise characteristics.

For this reason it was decided to use position encoding in Stage 2 to identify the effects of pulses originating in the endcaps. Additionally, some measure of field shaping was introduced to ensure that the ionization resulting from particles emitted from the endcaps was unable to be multiplied and collected.

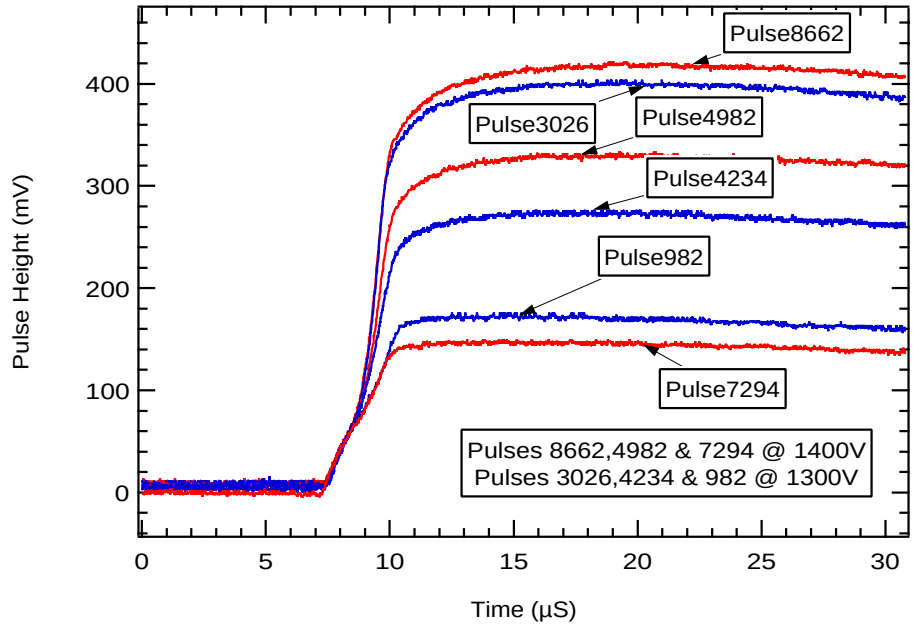

Figure 5.7: Pulse from the end effects band at 1300V and 1400 V. Note that the initial part of the pulses are exactly the same regardless of the initial voltage suggesting that the initial part of the pulse is not gas gain dependent.

5.1.2 Introduction of the δ parameter

During the analysis of the data from Stage 1 it was necessary to produce further parameters based on pulse shape as a means to identify spurious pulses. The two parameters t_f and energy were no longer sufficient to describe the full range of possible pulses. As can be seen in Figures 5.1 and 5.2 there were many examples of pulses which were not a result of ionization in the proportional counter gas. It became necessary to define a new parameter, δ, which would separate ionization from spurious pulses. Appendix B shows how this and other parameters are defined. Figure 5.8 shows this parameter plotted against energy for detector #3. Comparison between pulses in the rise time *vs* energy plots and the δ *vs* energy plots along with examination of the individual pulses allows the Figure 5.9 to be separated into several distinct bands, which represent various different pulses sources, *i.e.* HV discharges, Compton event and 'normal' gas like pulses in additional to the end effects band. As can be seen this parameter is well suited for the discrimination of non-gaseous pulses. However the effects of the endcaps reduces the separation ability of this parameter and pulse separation and identification only becomes truly successful in Stage 2 where the endcaps can be removed by position cuts.

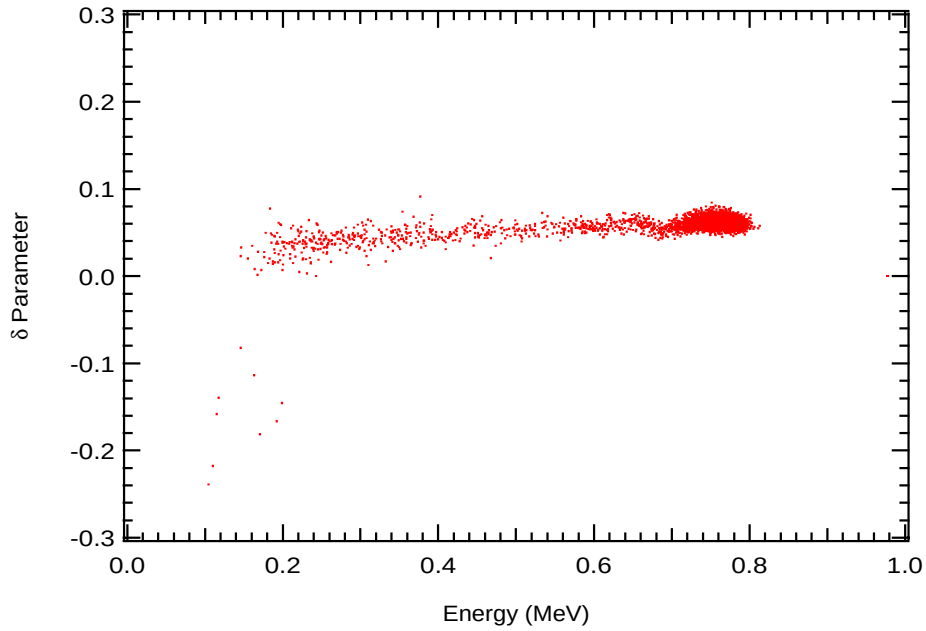

Figure 5.8: A plot of δ *vs* energy for thermal neutron calibration data taken with stainless steel detector #3. The few events at negative δ can be associated with HV discharges during calibration.

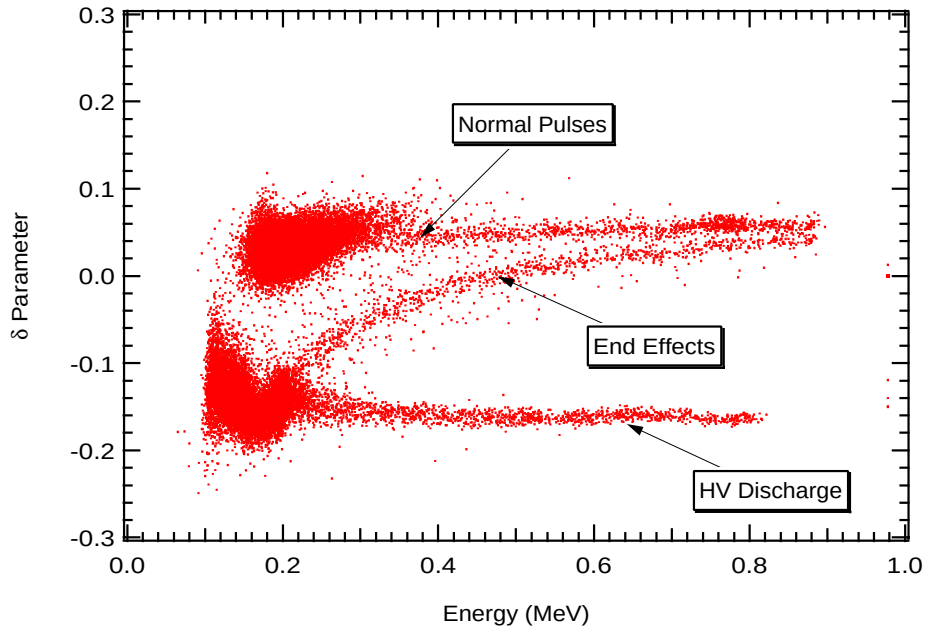

Figure 5.9: A plot of δ *vs* energy for stainless steel detector #3. The data were taken over the period August 11^{th} to September 29^{th} 1994.

5.1.3 Surface ^{210}Po Contamination

If the data from Figure 5.6 is histogrammed then it can clearly be seen that the data are consistent with a single peak at 5.3 MeV which is inconsistent with the continuum spectra expected from U and Th daughters and contamination in the bulk of the detector. The peak suggests that the source of the ionization is on the surface of the detector. A suitable isotope with a 5.3 MeV Q value is ^{210}Po produced by the decay of 22 year ^{210}Pb. If the α particle was to be emitted only from the surface of the detector the only method by which the collected ionization would be less than 5.3 MeV would be if the particle collided with the wall of the detector (the wall effect). Section 3.2.2 gives further information on the wall effect and the expected distributions.

Although ^{210}Po is not the only α emitter with a Q value in the region of 5.3 MeV it is the only one which has a 138 day halflife. Fortunately detector #3 was a long term test detector which remained sealed for over a year (it was also used to prove the stability of the gas over an extended period of time; the energy resolution did not change over this period). A data set was created using the number of counts in the peak region over this time period. Figure 5.10 shows the data along with the best fit when the data is constrained to a 138 day halflife. The fit is of the form

$$\text{decays} = a_0 + a_1 e^{\frac{-(\ln 2)t}{t_{1/2}}} \tag{5.1}$$

where a_0 corresponds to the levels of U and Th (considered constant over the period of this experiment), a_1 the level of the decaying isotope and $t_{1/2}$ its halflife.

The interesting fact remains that ^{210}Po is decaying at all when if it were part of the U and Th chain then it should be in equilibrium wit its parent ^{210}Pb which has a half-life of 22 years. Given its volatility and mobility it is not inconceivable that it would be not be in equilibrium with its parent nucleus and as such would be decaying away.

(Dis)advantages of ^{210}Po Contamination

Initially it may appear that the presence of ^{210}Po is a significant problem but on closer inspection it appears that there are certain advantages to a *small* amount being present in the detector. The major advantage concerns experiments later in this Chapter where the detectors are filled without ^{3}He to determine the effect of α particles on the neutron window. During this period it is impossible to calibrate the detectors with neutrons but the presence of the surface ^{210}Po allows the monitoring of the detector. In final production, if trace amounts of ^{210}Po were present in the detector it would provide a second calibration point (in addition to the 764 keV neutron peak). It would have no effect on the SNO vessel as it emits only an α particle to become the stable ^{206}Pb (although there is a small branch which produces a

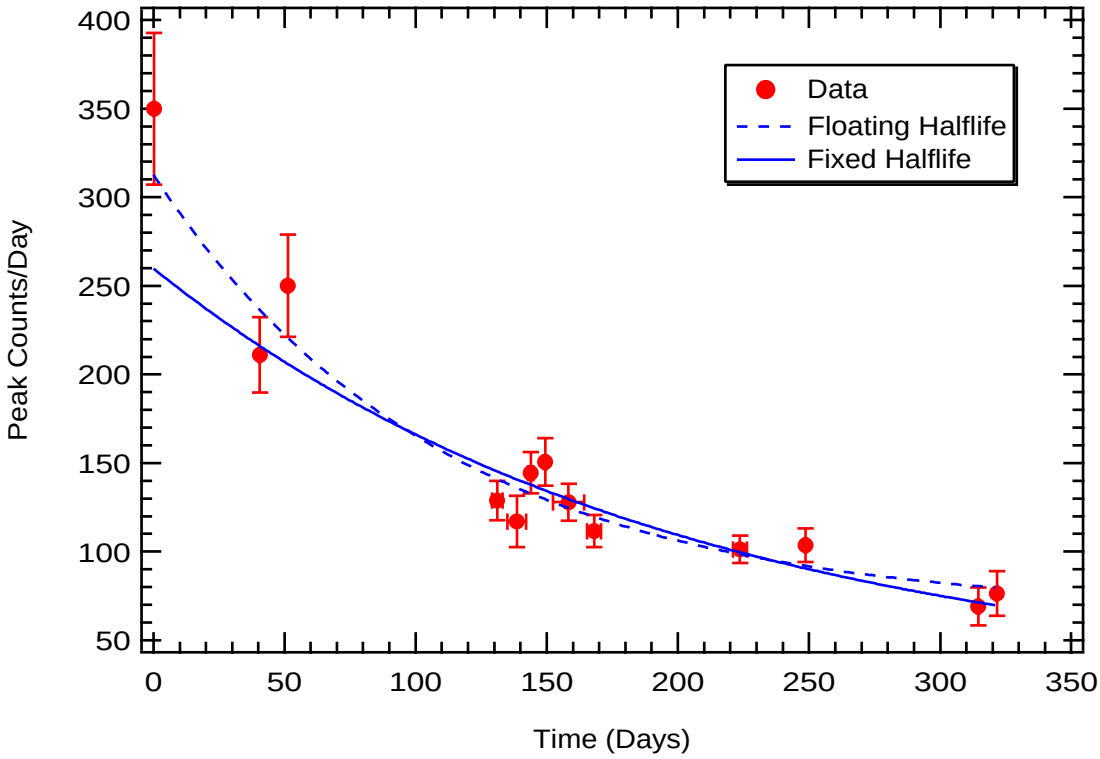

a_0	a_1	$t_{1/2}$	χ^2
22.4 ± 9.8	237.4 ± 23.3	138.0	18.0
66.5 ± 13.2	246.1 ± 25.8	76.0 ± 15	13.5

Figure 5.10: The number of decays per day over the region 5.0 to 5.6 MeV in the stainless steel detector #3. The data is shown fitted with both a fixed 138 day halflife and with the halflife allowed to float.

100 keV γ ray.)

It should be noted however, that approximately 20% of the decays from ^{210}Po lie in the tail of the distribution and overlay the neutron window. Their effect is less of a problem than bulk U and Th as they occupy a smaller region of the t_f *vs* energy plot.

5.1.4 Detector Longevity

During the operation of Stage 1, stainless steel detector #4's energy resolution degraded markedly, whilst that in detector #3 remained the same. To determine the cause of this change in resolution a neutron calibration was taken and the resulting t_f *vs* energy spectrum is shown in Figure 5.11 along with the corresponding energy spectrum. The degradation of the signal can be seen in the spread in the neutron "peak". The resolution appears worst at the lower values of t_f but apparently improves with increasing t_f. This result is consistent with a poisoned gas or more specifically that trace amounts of an electronegative gas are present. This is a significant spread in energies at lower values of t_f, which corresponds to neutron capture events where the proton-triton track is parallel to the wire. The energy degradation for these track is determined from the radial position of the neutron capture; if it captured close to the wire the resulting ionization travels through less of the contaminated gas in comparison to a capture event near the detector wall. Accordingly, less electrons are captured by the electronegative molecules and the event appears to contain more energy. At higher t_f's the track is oriented perpendicular to the wire and the difference between the number of electrons captured between a track which ends at the wire and one which ends at the wall is substantially smaller.

The result does not correspond to a bad initial fill (neutron spectra from earlier calibrations are consistent with spectra taken from detector #3). As the gas fill pressure is above the local atmospheric pressure it was impossible for some external gas to enter the detector. The only possibility that remains is that the electronegative gas was released from the walls of the detector. There are two obvious possibilities; either water vapour escaping from the stainless steel (which is known to retain water in trace quantities), or outgassing from an organic contaminant on the surface of the detector. As a result of this it was decided that all future detectors would be cleaned to remove any organic surface contaminants.

5.2 Stage 2 Double-Ended Readout

Due to the problems with the production of ultrapure endcaps, the interest generated by the α band in the rise time *vs* energy plots of Stage 1, and the desire to test the effect of surface etching, a double ended readout system which could simultaneously record the pulse shape and the position of the event was developed based upon the standard charge-division

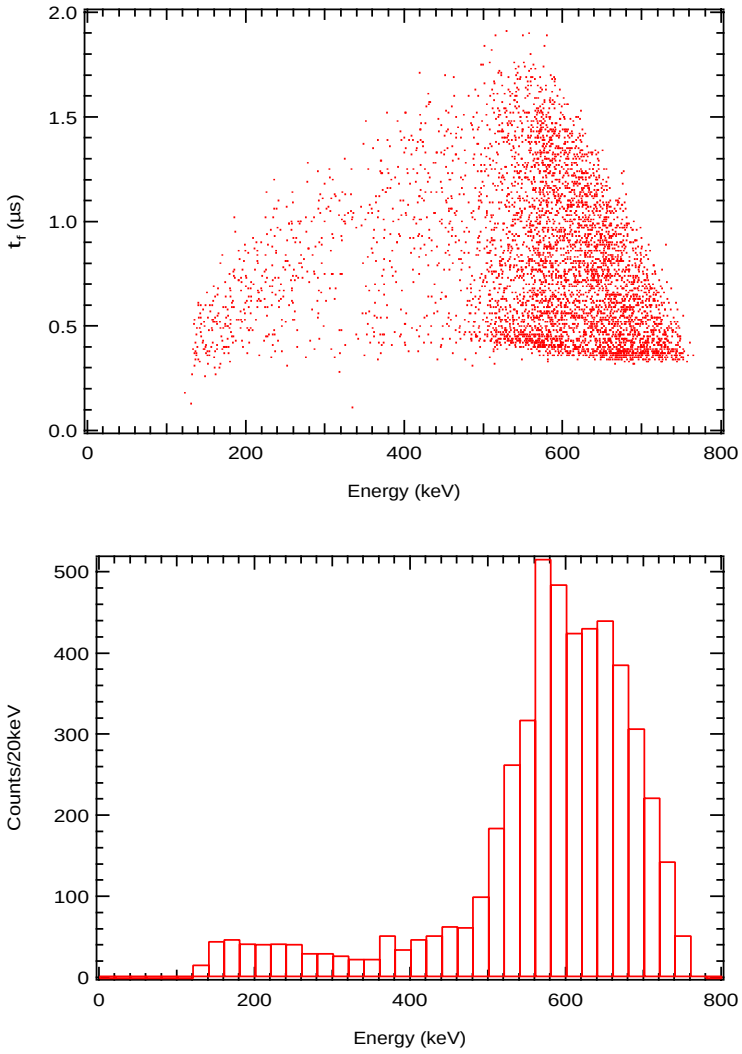

Figure 5.11: A t_f vs Energy plot for a neutron calibration of stainless steel detector number 4, demonstrating the topology of events characteristic of a 'poisoned' gas.

technique [35]. During testing at LANL the intrinsic resolution of such a system was shown to be 1 inch, in a 36 inch test detector for full energy He$(n,p)t$ events. Figure 4.8 shows the results of this experiment.

5.2.1 An explanation of the electronics

Before any discussion can start on the analysis of the data from this Stage it is necessary to re-examine the electronics layout in Figure 4.7. The main difference between Stage 1 and Stage 2 is the use of an extra pre-amplifier at the remote end of the detector. The use of charge division in proportional counters to determine the position of an event is well known [35]. The distance from one end can be determined from the ratio of the two signals from each pre-amp. Essentially,

$$\text{position} \propto \frac{Q_B}{Q_A + Q_B} \tag{5.2}$$

in the case that the wire used in the detector is resistive and that the impedance of the pre-amps is negligible. Due to the non-negligible impedance of the pre-amplifiers, the endcaps of the detector corresponded to ratios of approximately 0.2 and 0.8 instead of the expected 0 and 1.

The signals collected from each of the pre-amps is amplified through two channels of a 777 fast amplifier (one for the range 0.1–1.0 MeV and the other for 0.1–10 MeV). There are two outputs on each of the 777 channels for the B channel. One of which is fed directly into the digitizer (creating the B High and B Low signals) and the other is summed using a P/S 744 Fan-In/Fan-Out with the A output. There are three reasons for summing the signals. Firstly, the A+B output is the almost identical to the output of a single preamplifier system (strictly its the same as two preamplifiers in parallel) and was required for the event trigger. Secondly, the ratio that is required is $\frac{Q_B}{Q_A+Q_B}$ and it is nonsensical to record A and B signals and then sum them in software. Finally, summing A and B removes a source of noise, the series noise of the preamplifiers. The noise is 180° out of phase between the two amplifiers and hence cancels exactly. (More simply this can be viewed as a series noise voltage pulling charge from one pre-amplifier whilst pushing it into the other.) There is an intrinsic drawback to digitizing the summed signal; should a problem occur with the A part of the electronics the resulting summed signal may not be able to reproduce the A pulse. The combined output $A+B$ is then digitized resulting in $A+B$ High and $A+B$ Low signals. It should be noted for completeness that it is possible to record A, B and $A+B$ signal but that this would require 6 digitizers per channel (and hence 18 digitizers for Stage 2, more than were available at that time.)

To obtain the appropriate physics these four distinct channels are analysed in pairs; $A+B$ High with B High and $A+B$ Low with B Low.

Detector	Total Counts	Counts < 1 MeV	Counts > 1 MeV	Live Time < 1 MeV	Live Time > 1 MeV
Ni CVD#1	142421	3852	2157	149.9 d	149.9 d
Ni CVD#2	44222	16082	671	135.6 d	121.6 d
Ni CVD#3	72688	19720	273	98.0 d	76.8 d

Table 5.1: The number of counts in each detector following the position cuts. For completeness the total number of events is also recorded. The difference in live times between high and low gain channels can be attributed to electronic failures.

5.2.2 Multiple Series

During the approximately 18 months that Stage 2 was in operation, several problems were encountered associated with electronic and mechanical failures. For this reason the entirety of Stage 2 was split into several distinct series. Within a series all the electronic and detector configurations remained unchanged. Whenever a detector, preamplifier or digitizer or another electronic module failed, the fault was corrected and a new series was started. Additionally, if the configuration of detectors was altered a new series was started. The logic behind the change of series with even a minor change in the configuration is illustrated in Appendix F. The reduction of the data relies upon several coefficients, each of which may be altered by a change in the electronics. For each series these coefficients must be recalculated.

Each series consists of multiple data runs. The duration of each run is random and corresponds to experimental down time caused by down time or periodic maintenance, such as compressing and copying of data to a removable disk for shipment to Los Alamos. As the time of each event was an important parameter, it was necessary to define a time zero. (The computer clock contains its own time zero but is set for the number of seconds which have passed since midnight 1/1/1904 and was considered impractical). The time zero for all series was defined to be Tuesday March 15^{th} 1994 at 15:39:16.

5.3 Stage 2 Analysis

The previous two sections have described the workings of the electronic systems and the necessity of amalgamating the various data sets produced into different 'Series'. Appendix F should now be consulted for an explanation of the data reduction process required to reduce the total data set from Stage 2 into a subset of physically interesting pulses. Table 5.1 shows for each of the three Ni CVD detectors the total number of pulses, the number remaining after data reduction and the appropriate live time. There is a difference between the live times for high and low gain channels due to an error with one of the digitizers (strictly the digitizer in CAMAC crate 2 slot 12, associated with the B Low signal of the third detector set). This

digitizer occasionally recorded the entire pulse as overflowing whereas the corresponding $A+B$ Low appeared to be perfectly normal. For this reason entire time blocks were removed from the data whenever this occurred. There is an exception to this practice of removing all the data from a time block. In the final data sets of Ni CVD detector #2 (`Fri-Jul-21-13/53/27-1995` defined as Series 853 and corresponding to data taken between 490 and 510 days) the digitizer in the low gain B channel again had sporadic problems resulting in occasional pulses not being correctly recorded. As these data were the last data taken with this detector it was decided to remove these bad pulses and correct for live time by considering the number of pulses marked as overflows in comparison to the number expected over that time period. This makes the assumption that the overflows recorded in the digitizer are truly random. Indeed, the high gain channel pulses which were correctly recorded over this time period showed no statistically significant difference from earlier data sets.

5.3.1 Anomalous Pulses

Although the data reduction outlined in Appendix F is sufficient to reduce the entire data set to a more manageable distribution it is insufficient simply to remove the majority of the pulses without examining some of the pulses which failed the appropriate cuts.

Some of these pulses were removed as the signal in the B channel overflowed whilst the $A+B$ channel did not. Similarly it can be seen in some of the data sets that some of the pulse ratios are substantially greater than one. Extraction of these pulses shows that the B pulse is indeed larger than the $A+B$ pulse and that this is not a result of some analysis glitch. This is completely unphysical and can not be the result of an ionization event in the counter. Instead, it must be associated with some electronic problem. Figure 5.12 shows one of these pulses where B is greater than $A+B$ and the corresponding reconstructed A pulse. It is most likely that this pulse is caused by a capacitor glitch in one of the preamplifiers, producing a positive transient in the B preamplifier and a corresponding negative transient in the A preamplifier.

To determine the source of these pulses two new configurations of electronics and detectors was tried; the swapping of pre-amplifiers and rotation of the detector such that remote and near ends were reversed. The production of these pulses can be compared with the strange pulses of Stage 1 in that these types of pulses can not be seen in the laboratory but are visible after considerable time underground. It should also be noted that these pulses are not produced in the initial Stage 2 data sets which presents the possibility that they may be a result of the salt atmosphere on the pre-amplifiers, detectors and cables which were contained in the the external tank outside of the shed.

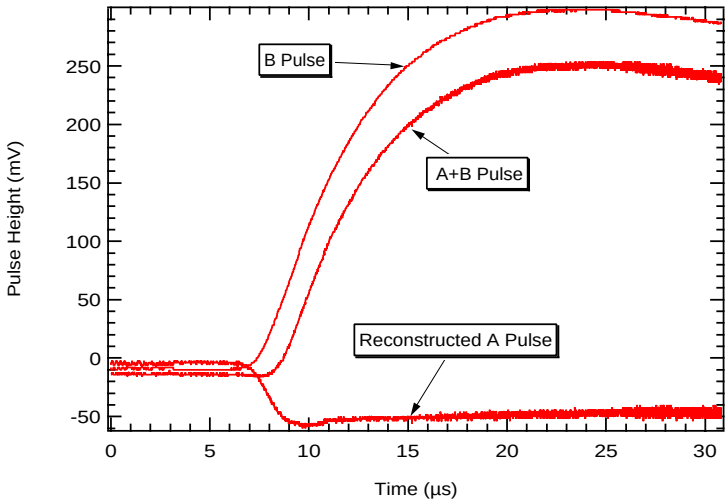

Figure 5.12: An anomalous pulse from WIPP Stage 2. Both the $A + B$, B and reconstructed A pulse are shown.

a_0	a_1	$t_{1/2}$	χ^2_{dof}
25.1 ± 10.3	27.4 ± 11.6	138.0	1.897
40.3 ± 11.7	13.1 ± 10.8	40.8 ± 66.5	1.628

Table 5.2: The results of χ^2 fits to the rate of pulses above 1 MeV in short stainless steel detector #2. The parameters a_0, a_1 and $t_{1/2}$ are defined in Equation 5.1.

5.4 Short Stainless Steel Detector #2

The stainless steel detectors were operational for only a short period of Stage 2 as their primary use was to debug the underground systems prior to the installation of prototype nickel CVD detectors. However, even after the production of the first prototype CVD nickel detector they were kept operational for a short period of time. They were not operational continuously as, being significantly more radioactive than the newer nickel detector, they dominated the data taken. However, detector#2 was kept operational for a total live time of 30.7 days. The live time was spread (unevenly) over a period of 100 days. The accumulated data after the appropriate cuts from this detector is shown in Figures 5.13 and 5.14. The ^{210}Po peak seen in Stage 1 is clearly visible in both Figures. By applying a cut to the data over the energy region 4.9–6.0 MeV the decay of the ^{210}Po can clearly be seen (Figure 5.15). The results of χ^2 fits to these data are given in Table 5.2.

The two fits are with and without a constraint on the half-life. Both fits are shown in Figure 5.15. As with Stage 1 the important characteristic of detector#2 is that it demonstrates the disequilibrium of ^{210}Po with its parent ^{210}Pb and that the majority of this ^{210}Po is on the

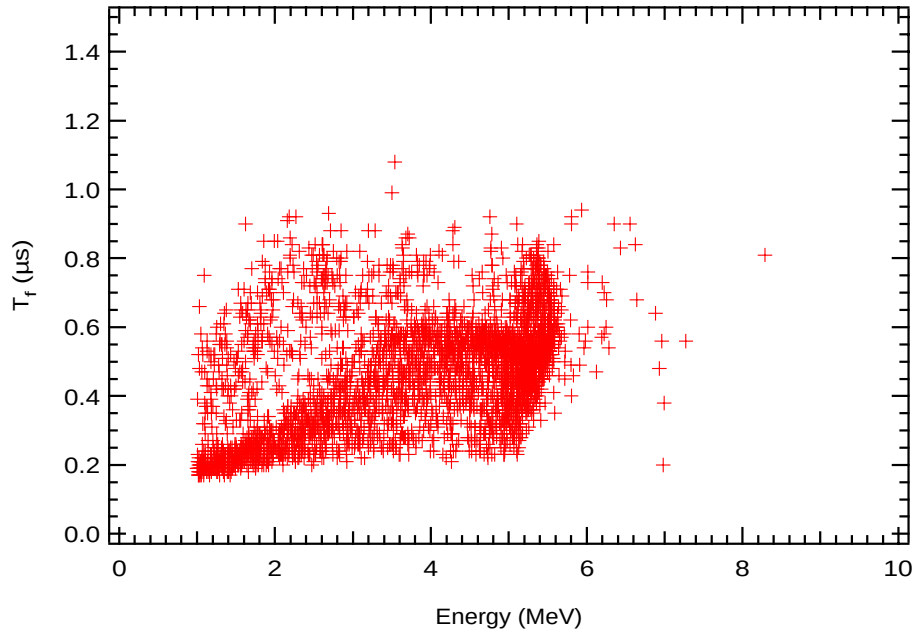

Figure 5.13: Data taken from short stainless steel detector #2 in the form of a t_f vs. Energy plot. The 5.3 MeV ^{210}Po peak can clearly be seen.

surface of the detector. In additional, it is an extremely good demonstration of the cleanliness of CVD nickel. As will be seen in later sections the quantity of data obtained from the short prototype nickel detector is very much reduced in comparison to the 25.1 counts per day above 1 MeV attributed to the non-decaying component.

5.5 Nickel CVD Detector #1

The first of the short nickel CVD prototypes used end-caps manufactured from an electro-forming method rather than the CVD method which was to be used in final production. In addition there were other problems associated with the assembly of this prototype; the initial laser welds of the two detector halves failed to hold vacuum and the detector was eventually sealed by using Torr Seal, the wire was soldered in using a lead based solder instead of a cleaner tin silver based one.

Initial tests of this detector underground revealed one very important fact. The endcaps had been designed to reduce the measured activity by extending the quartz feed-thru into the gas. The inside of the quart tube was metalized and kept at the same potential as the anode wire. The feed-thru's diameter was significantly larger than the wire's which resulted in a lower field at it's surface. Accordingly, no gas multiplication could occur in this region. However, as can be seen in the initial neutron calibration (Figure 5.16) there were some problems. The "smilely face" results from two separate effects. The turned up edges are caused by

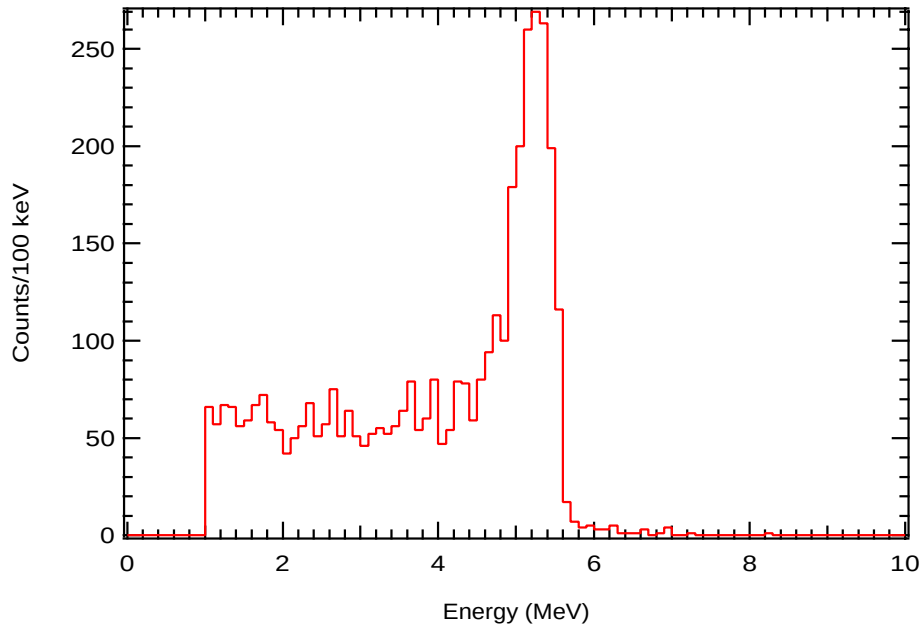

Figure 5.14: Data taken from short stainless steel detector #2 in the form of a energy histogram. The 5.3 MeV ^{210}Po peak can clearly be seen along with significant α activity which can be attributed to bulk contamination.

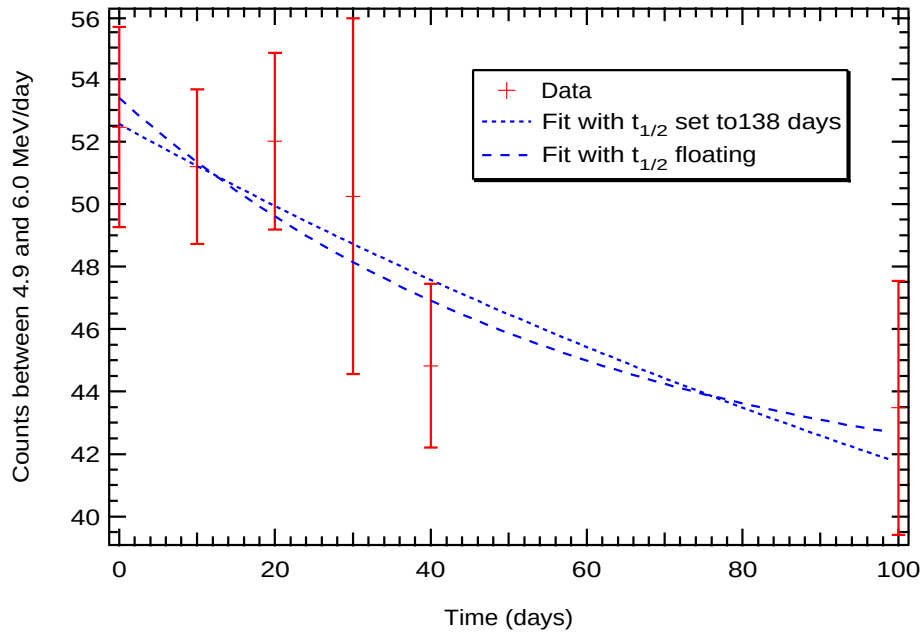

Figure 5.15: A plot of the rate of counts in the energy region 4.9–6.0 MeV as a function of time.

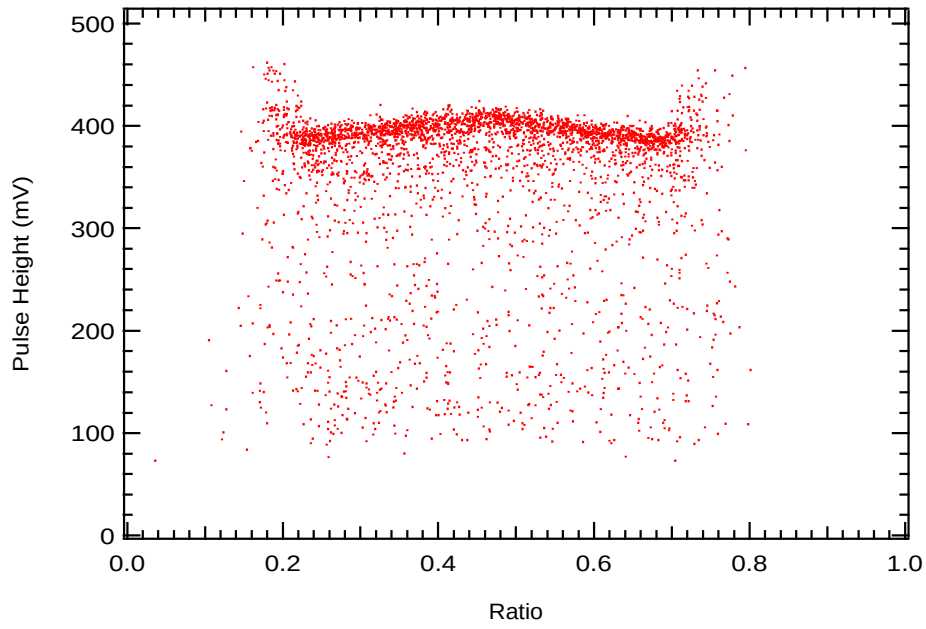

Figure 5.16: The first neutron calibration of short nickel CVD detector #1. The data has only had saturation and HV discharge pulses removed and has not been position cut.

insufficiently long feed-thrus. As a result the gain close to the endcap region is slightly higher than that of the rest of the detector (due to the decreased detector diameter at the end cap). The increase in gain towards the centre of the detector is a result of the tube taper, the gas gain being a function of the ratio b/a. Fortunately the end effects are removed by the position cut and the taper of the tube can be removed by a position dependent energy correction.

5.5.1 Effects of Etching

As was previously noted in Chapter 4 the two halves of the detector were treated differently. The left hand side of the detector was etched to an approximate depth of 0.15 μm whilst the right hand side was only cleaned with a solvent to remove organic deposits. Figure 5.17 shows the energy of individual pulses as a function of their position inside the detector. It can clearly be seen that the right hand side of the detector was significantly dirtier than the left hand side suggesting that some contamination occurred either as a result of manufacturing or during construction but that the contamination could be removed with a light etch. Several scenarios are possible:

- The contamination is the result of the manufacturing process. The tubes are produced by depositing nickel on a stainless steel mandrel. This mandrel could be a possible source of contamination and would explain why it is present on only the surface of the detector.
- The contamination is deposited on the surface after manufacturing after exposure to air.

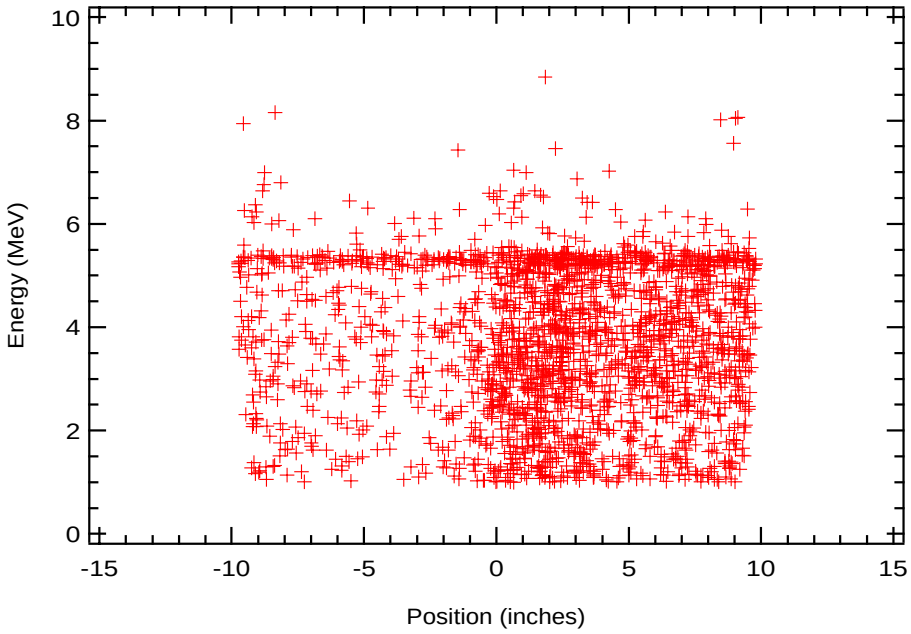

Figure 5.17: The accumulated data from short nickel CVD detector #1. Displayed as pulse energy in MeV verses position from the centre of the detector in inches.

- It is deposited during construction of the detector.

To examine these possibilities further studies were carried out in Stage 2b with the second and third prototype detectors to determine the effects of etching and exposure to air.

For analysis purposes it is necessary to separate the two halves of the detector with a position cut as their surfaces were treated differently and can not be expected to have similar levels or types of surface contamination. However, this should not exclude them exhibiting similar levels of bulk contamination. Figure 5.18 is a t_f *vs.* energy plot of the two sides of the detector. Obviously the LHS has a significantly reduced activity, though it appears that the RHS has significantly more bulk contamination. This is not consistent with the hypothesis that the etch of the LHS removed only the surface contamination. If this were correct then the bulk levels would be consistent between left and right hand sides. The correct solution is that the etch, which removed the inner most 0.15 μm, not only removed any surface contamination but also the layer of nickel which was deposited directly on the stainless steel mandrel. It is this initial layer that contains the majority of the so-called bulk activity (possibly due to diffusion of material from the mandrel). This information implies that not only must etching be performed with the next series of prototypes but also that the depth of etching must be increased. In addition, the next series should be etched to at least two different depths to determine the optimimum level. It is for this reason that NiCVD#2 and NiCVD#3 were etched to a depth of 1 or 2 μm.

Futhermore, although NiCVD#1 was eteched, Figure 5.18 indicates that there is still surface contamination on the LHS. The event rate for the detector and its left and right hand sides is shown in Figure 5.19. The decay of the surface ^{210}Po is more visible when the event rate between 4.9 and 6.0 MeV only is displayed (Figure 5.20).

5.5.2 Lead Shielding

The not unreasonable assumption has always been made that the low energy part of the spectrum is a result of Compton events. This is not unreasonable considering that this spectrum can be reproduced using a γ source such as ^{60}Co. Figure 5.21 shows a γ irradiation of detector #1. The only remaining concern is the source of the γ activity. The assumption was that the measured activity was a result of the ^{40}K present in the salt at WIPP. As a test of this hypothesis, the detector was surrounded by two inches of lead. If the source of the γ rays was indeed from the 1.464 MeV ^{40}K line then the rate would be expected to be reduced by an order of magnitude by the lead shield. Figure 5.22 shows the resulting data set taken over $\sim$ 22 days. Two points should be noted:

a There is a significant reduction in the rate of Compton's observed in agreement with that expected.

b The data was taken approximately 560 days after the start of Stage 2 which corresponds to approximately 4 half-lives of ^{210}Po. The once prevalent line at 5.3 MeV has disappeared. However, the right hand side of the detector is still significantly dirtier suggesting that the contamination was not caused solely by ^{210}Po.

5.6 Nickel CVD Detectors #2 & #3

Both short nickel detectors 2 & 3 were produced at the same time using the same components and as a result can be analysed in parallel. This is not to say that all the parameters used in the data reduction processes are the same, as the electronic components differed, but the final pulse sets after the position cut and energy recalibration are comparable. It should be noted at this time from the experiences with the first detector that these two were assembled in a clean room environment. The wire was attached using tin/silver solder instead of the more standard lead based solder and the two detector halves were successfully laser welded together. Additionally new nickel CVD end-caps were used with the long field tubes to remove the non-linear end-cap region.

For informational purposes, problems occurred with one of the tubes used to manufacture NiCVD#3. The tube contained a small pinhole leak which could not be sealed by the usual technique of applying a short laser pulse (from the laser welder which was normally used to weld

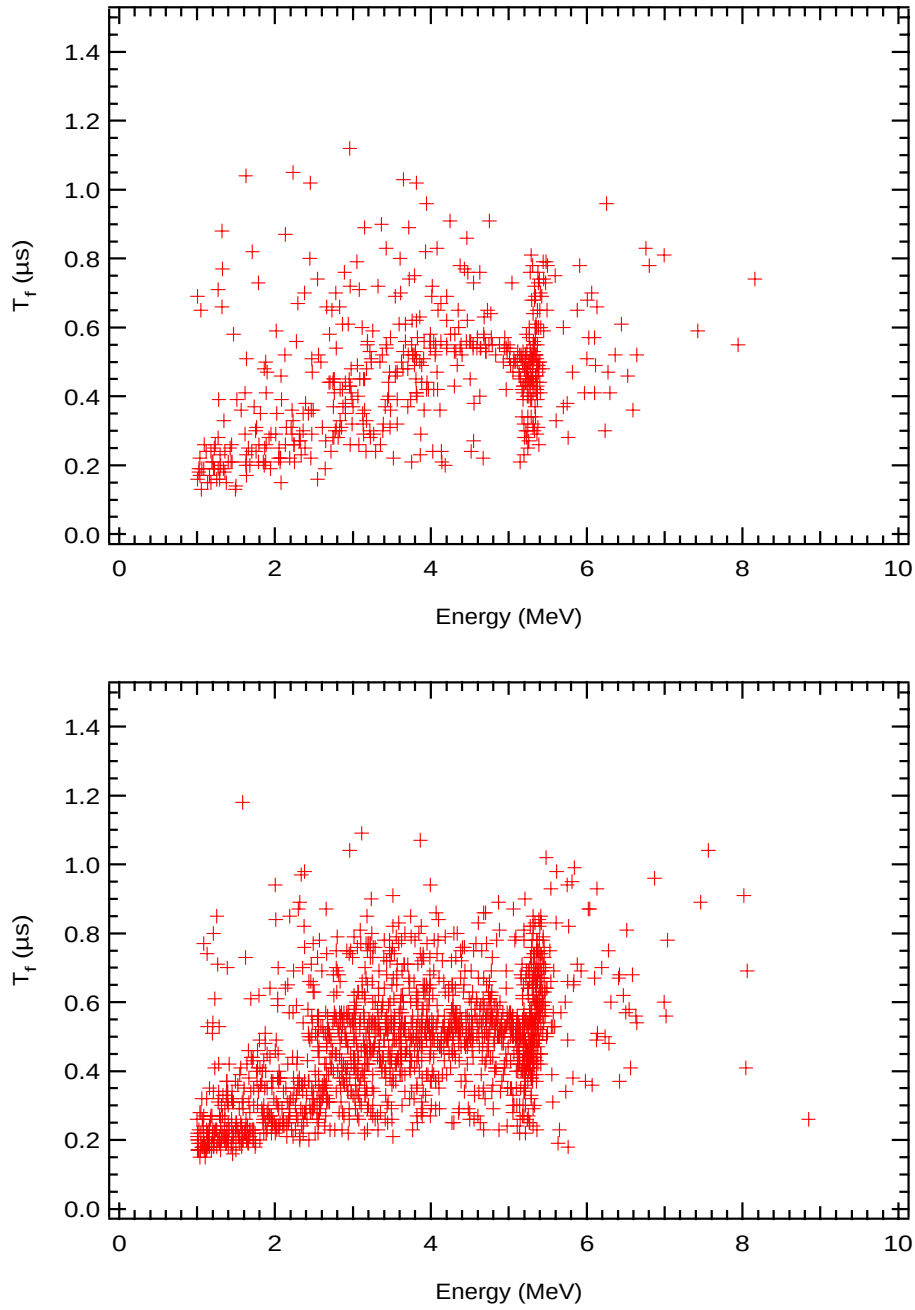

Figure 5.18: The t_f *vs.* energy plots for the left (upper) and right (lower) hand sides of NiCVD#1. Both clearly exhibit a peak at 5.3 MeV due to contamination with ^{210}Po.

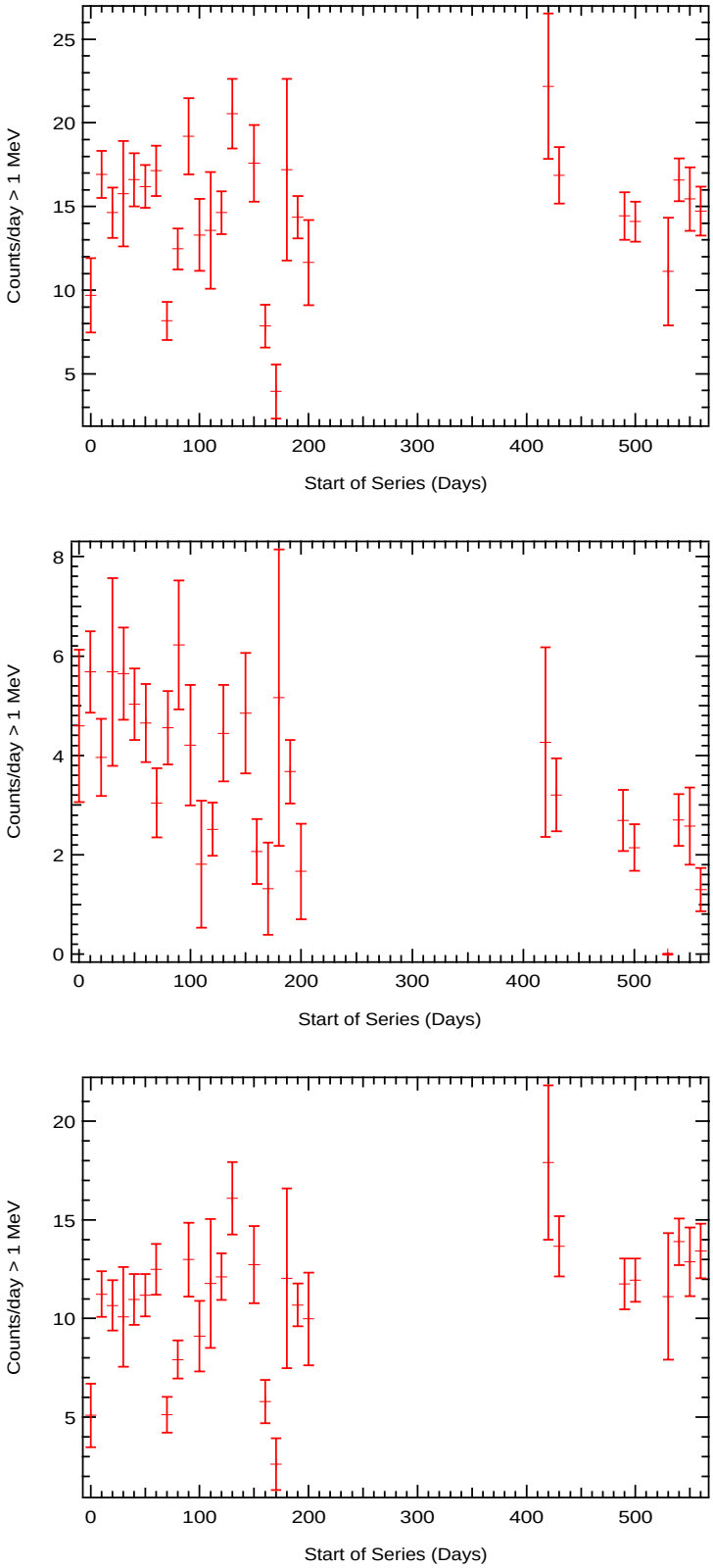

Figure 5.19: The rate in counts per day above 1 MeV for nickel CVD detector#1. The rate is calculated by summing the number of counts over a ten day period and dividing by the total live time over that period. The three graphs are, from top to bottom, total data set, left-hand side only and right-hand side only.

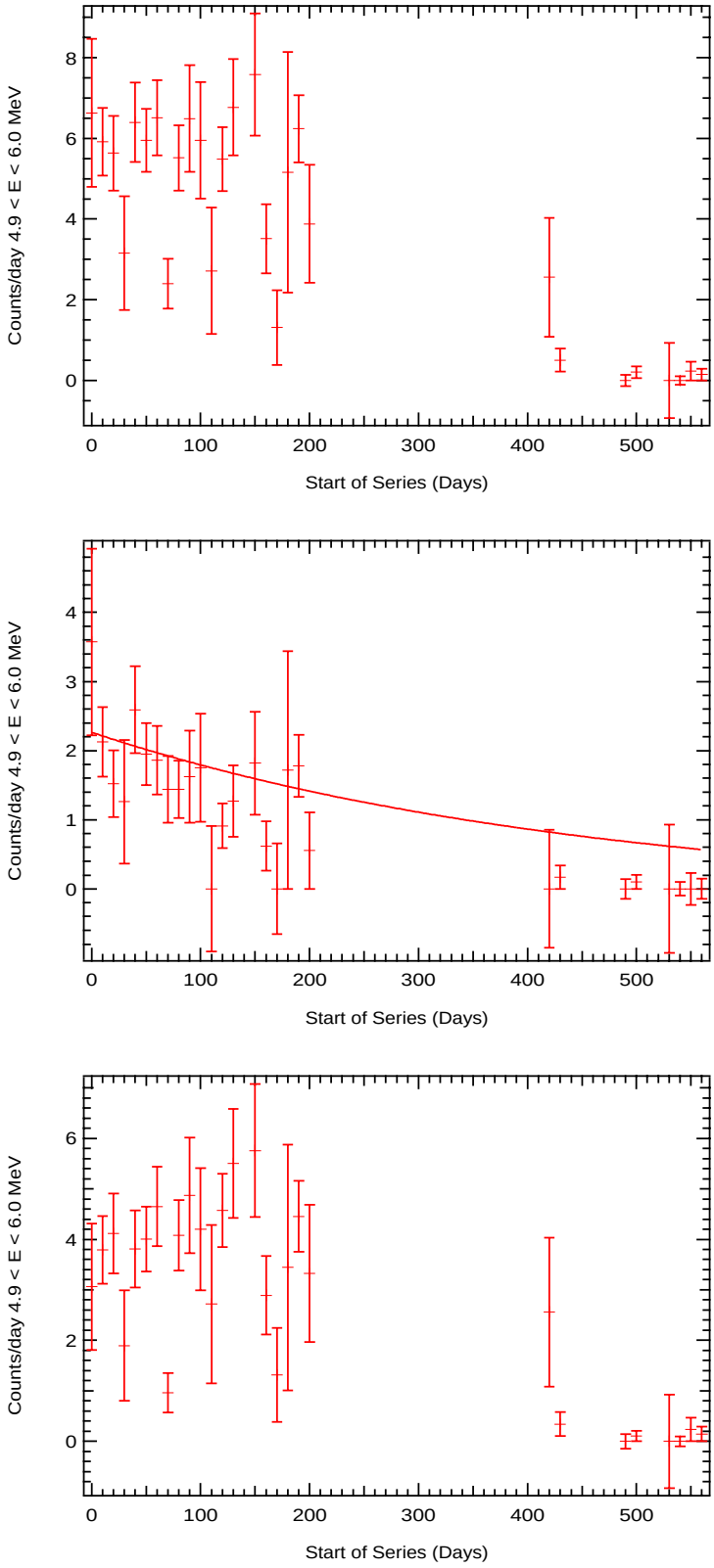

Figure 5.20: The rate in counts per day between 4.9 and 6.0 MeV for nickel CVD detector#1. The rate is calculated by summing the number of counts over a ten day period and dividing by the total live time over that period. The three graphs are, from top to bottom, total data set, left-hand side only and right-hand side only. For reference the best fit curve for a 138 half-life is plotted for the LHS data.

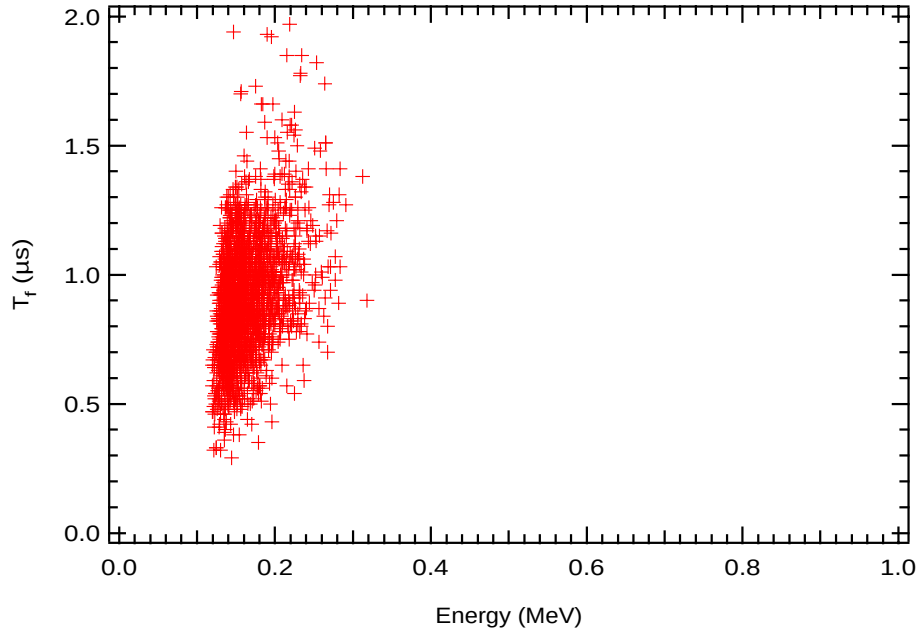

Figure 5.21: The t_f verses energy spectrum from short nickel CVD #1 as a result of irradiation with an external ^{60}Co source. Data taken Wed August 17$^{\text{th}}$ at WIPP.

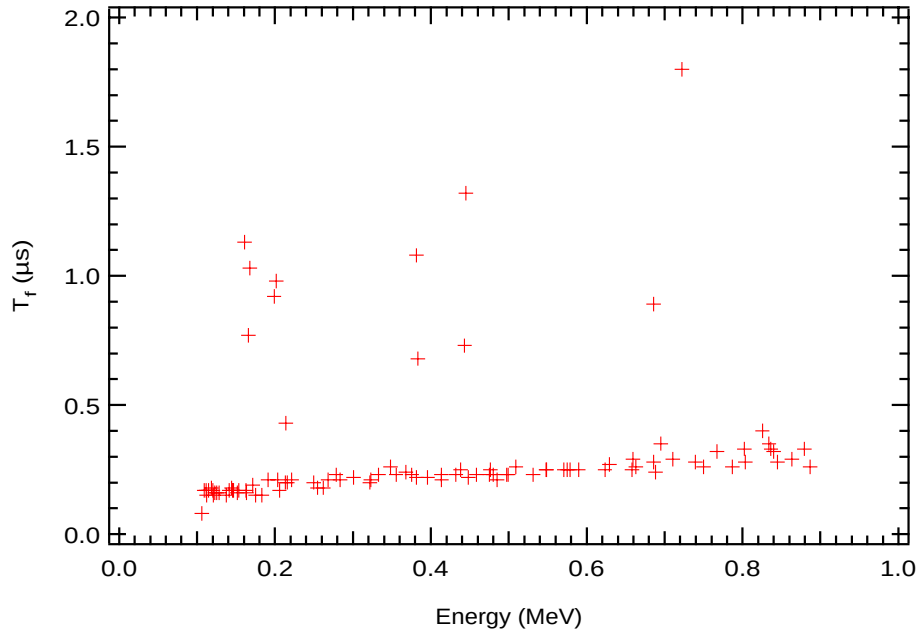

Figure 5.22: The t_f verses energy spectrum from short nickel CVD #1 resulting from a background determination over 22 days. The detector was shielded all around by 2 inches of lead and was filled with a mixture of ^{4}He and CF_4. The band of events at low t_f are the result of α activity. The low energy, high t_f band attributed to Compton events is almost completely absent.

detector halves together) to the affected area. Eventually this small section of the tube was removed and the resulting detector was shorter than the others. As a result of this problem, this half of NiCVD#3 received significantly more exposure to air than its counterpart. It must be noted that both the counters were etched prior to assembly to remove any surface contaminants.

5.6.1 Elimination of Radon

Both detectors at one point during the measurements experienced an excess of counts which can be attributed to the presence of some short lived radioactivity. This was attributed to Radon (and it daughters) in the detector. This excess of counts can clearly be seen in both detectors when attempting to fit the resulting number of counts above 1 MeV. For NiCVD#2 the excess is visible in the time period 300–310 whilst for NiCVD#3 it is visible in the first two data sets 170–190. The rate expressed as counts per day above 1 MeV are shown for NiCVD#2 and NiCVD#3 in Figures 5.23 and 5.24 respectively.

There are two questions which arise from the above statement; firstly that this assumption of Radon to account for the excess of counts appears to be a convenient excuse and secondly why Radon and not some other radio-isotope. The answer to these questions is interlinked. From examination of both detectors it can be seen that the excess decays away in a matter of days and the underlying distributions remain unchanged. ^{222}Rn has a half-life of 4.2 days and decays into daughters which have much shorter half-lives. The decay chains are shown in Appendix G. The decay effectively terminates at ^{210}Pb which has a 22 year half-life. As the Rn chain is not in equilibrium the final α decay of ^{210}Po from the original Rn source is dependent on this 22 year half-life. In addition when considering the rate above 6 MeV there is no increase in the two specified time periods, consistent with the source of additional counts having an endpoint below this level. Finally, the coincidence in time and position between the initial Rn decay and the decay of one or two of its subsequent daughters can be seen in the detectors. The decays have the correct energies and time distributions as well as emanating from the same position on the wall of the detector (to within the position resolution).

The final matter concerns the methods by which the Rn entered the detector. For NiCVD#3 the method appears obvious, as this was the initial data from the detector it could be assumed that the detector was contaminated just before being sent to WIPP. Indeed, the detectors were filled just prior to being sent to WIPP (the time delay between final gas fill and the first data set was of the order of 5 days). However, if this were the case then why only detector #3 and in addition why only the left hand side of that detector. As both the detectors were filled simultaneously, this removes the gas handling system as a possible source of the contamination. The remaining possibility is that the LHS of the detector was exposed during some part of

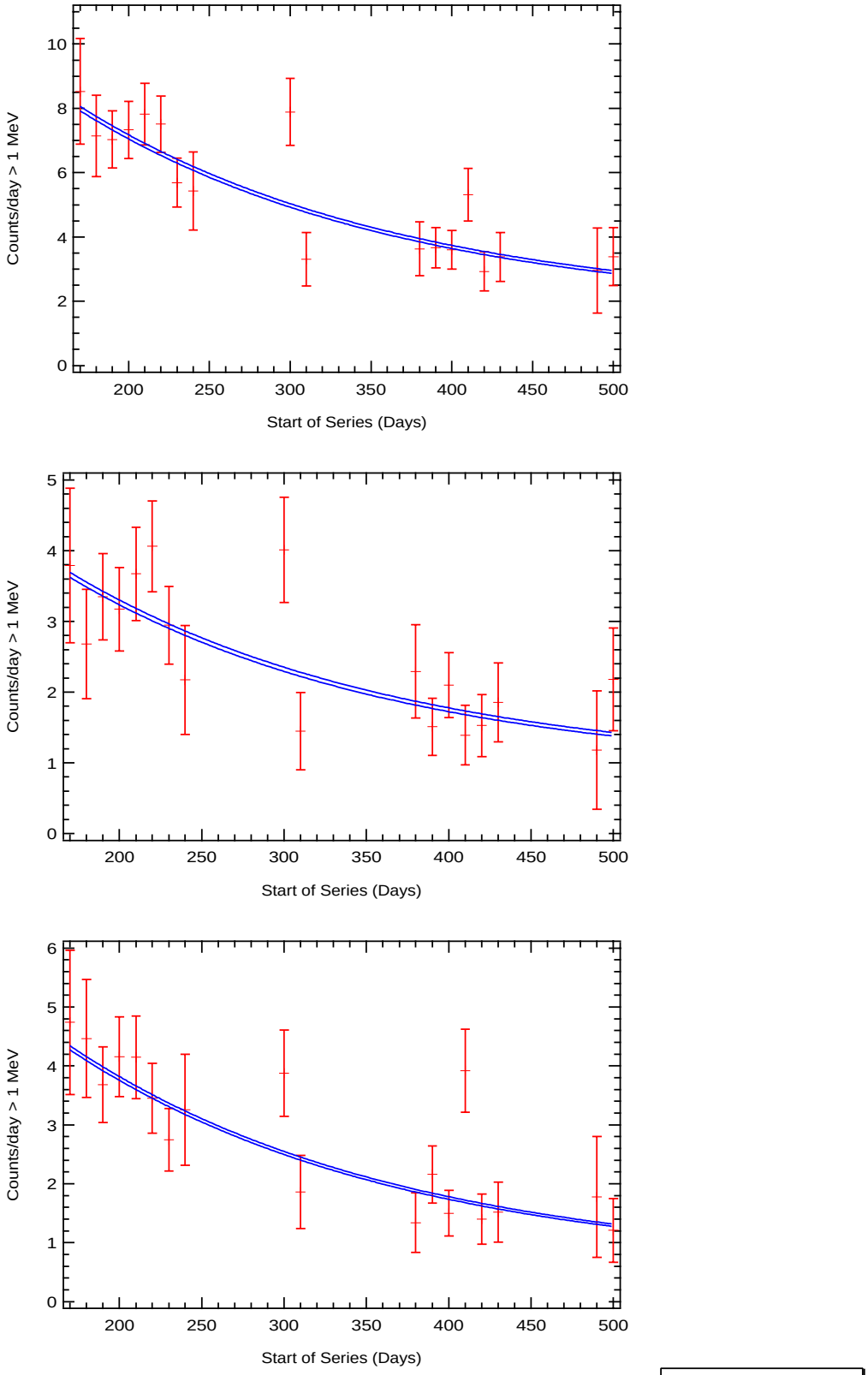

Figure 5.23: The rate in counts per day above 1 MeV for nickel CVD detector #2. The rate is calculated by summing the number of counts over a ten day period and dividing by the total live time over that period. The three graphs are, from top to bottom, total data set, left-hand side only and right-hand side only.

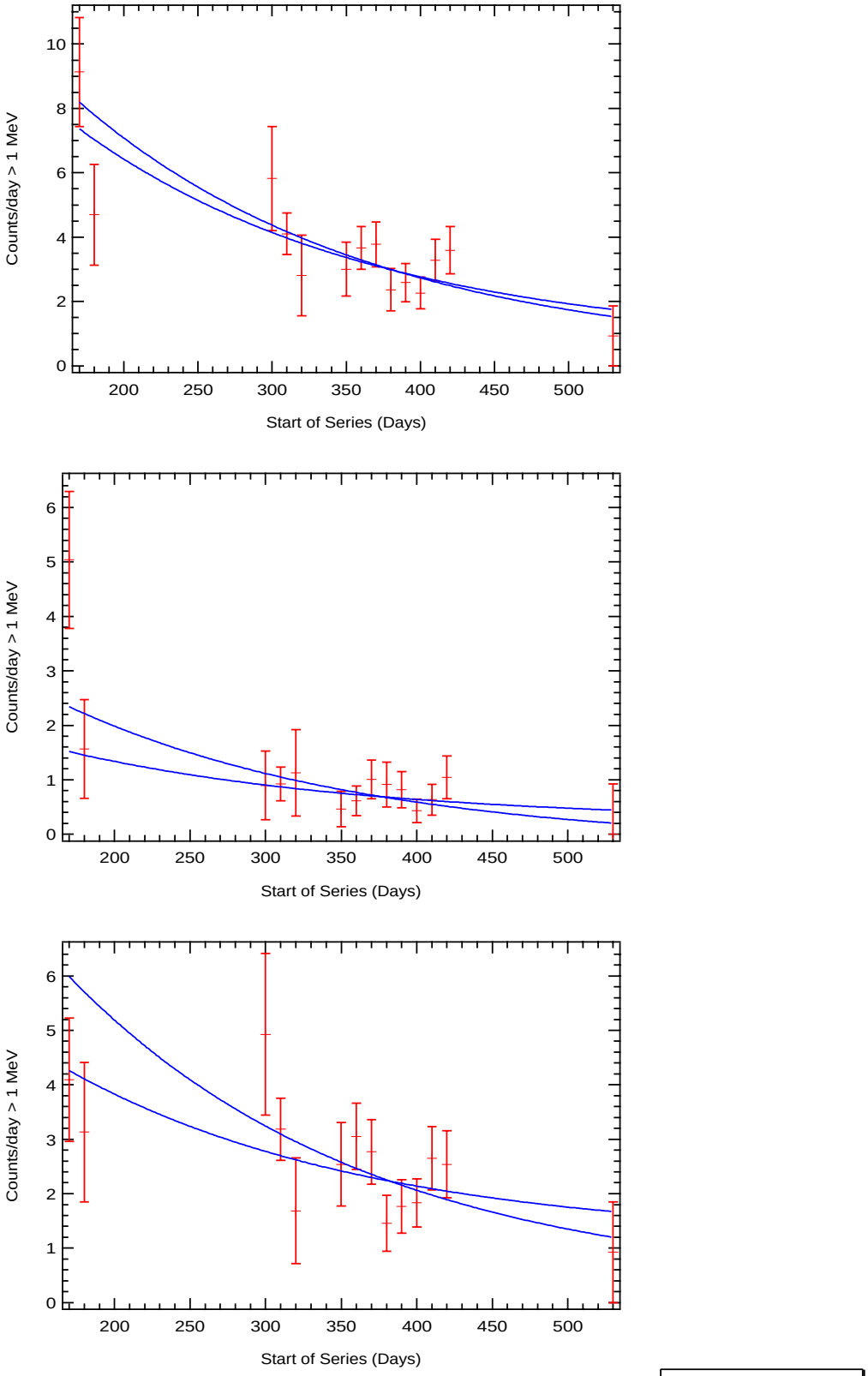

Figure 5.24: The rate in counts per day above 1 MeV for nickel CVD detector #3. The rate is calculated by summing the number of counts over a ten day period and dividing by the total live time over that period. The three graphs are, from top to bottom, total data set, left-hand side only and right-hand side only.

		a_0	a_1	$t_{1/2}$	χ^2_{dof}
All Data	Fixed $t_{1/2}$	1.75 ± 0.44	6.31 ± 0.80	138.0 ± 0.0	1.28
	Floating $t_{1/2}$	2.13 ± 1.98	6.02 ± 1.61	120.5 ± 91.0	1.36
	Straight Line	4.83 ± 0.20	—	—	4.88
LHS Only	Fixed $t_{1/2}$	0.90 ± 0.30	2.80 ± 0.54	138.0 ± 0.0	1.00
	Floating $t_{1/2}$	0.82 ± 1.99	2.86 ± 1.72	145.6 ± 200.7	1.07
	Straight Line	2.28 ± 0.14	—	—	2.49
RHS Only	Fixed $t_{1/2}$	0.60 ± 0.30	3.73 ± 0.57	138.0 ± 0.0	1.21
	Floating $t_{1/2}$	0.97 ± 1.13	3.48 ± 0.88	108.8 ± 89.3	1.29
	Straight Line	2.38 ± 0.14	—	—	3.69

Table 5.3: χ^2 fits to data from Ni CVD#2 binned as total counts above 1 MeV per 10 day period. No data sets have been removed. As the LHS and RHS of the detector where etched differently they too were analysed separately.

the construction phase. It should be noted from Chapter 4 that this half of the detector was manufactured from two pieces of tubing due to problems with pinhole leaks. It is conceivable that it received its contamination over this time period though it is not easy to explain why any surface contamination was not removed by the etching process just prior to final assembly.

For detector #2 the same reasoning does not initially appear to apply. The excess of counts appears in the middle of the data run at the start of series 700 instead of immediately after assembly. However, problems occurred with this detector which were associated with the wire. It appeared that the wire had slipped from its endcap. The detector was returned to Los Alamos, its wire was replaced and subsequently returned to WIPP. The time between the gas fill and the start of Series 700 was of the order of 4 days. Again sufficient time for a small amount of Rn present in the detector to still be visible over the following few days.

Tables 5.3 through 5.6 show the results of fits to the data sets using the model in Equation 5.1 from both detectors both with and without the time periods contaminated with Rn.

5.6.2 The Effects of Etching

From Chapter 4 it should be noted that the two halves of each of the detectors were etched separately. In addition the RHS of NICVD#3 was exposed to Rn loaded air ($\sim$ 1pCi/litre) for 48 hours. Figures 5.25 and 5.27 show the total data sets for NiCVD#2 and #3 respectively as energy deposited as a function of position from the centre of the detector.

First consider NiCVD#2 (Figure 5.25). As can be seen from the data in Table 5.4 the levels of decaying (^{210}Po) and non-decaying components (U and Th) are not statistically different when comparing left- and right-hand sides of the detector. The underlying assumption is that there is a statistical difference between a 1 μm and a 2 μm etch. Both etches result in effec-

		a_0	a_1	$t_{1/2}$	χ^2_{dof}
All Data	Fixed $t_{1/2}$	1.66 ± 0.44	6.25 ± 0.80	138.0	0.85
	Floating $t_{1/2}$	3.04 ± 0.74	5.52 ± 0.70	69.6 ± 36.9	0.82
	Straight Line	4.72 ± 0.20	—	—	4.63
LHS Only	Fixed $t_{1/2}$	0.85 ± 0.30	2.77 ± 0.54	138.0	0.72
	Floating $t_{1/2}$	1.35 ± 0.73	2.45 ± 0.56	83.7 ± 79.6	0.75
	Straight Line	2.21 ± 0.14	—	—	2.30
RHS Only	Fixed $t_{1/2}$	0.57 ± 0.30	3.70 ± 0.57	138.0	1.06
	Floating $t_{1/2}$	1.45 ± 0.42	3.32 ± 0.53	62.2 ± 36.2	1.07
	Straight Line	2.32 ± 0.14	—	—	3.65

	Counts Non-Decaying	Counts Decaying
All Data	189.92 ± 50.34	400.85 ± 51.31
LHS Only	97.25 ± 34.32	177.66 ± 34.63
RHS Only	65.21 ± 34.32	237.31 ± 36.56

Table 5.4: χ^2 fits to data from Ni CVD#2 binned as total counts above 1 MeV per 10 day period. The period 300–310 has been removed from the fits as it was contaminated with Rn whose decay can clearly be seen in the data. As the LHS and RHS of the detector where etched differently they too were analysed separately. The lower table converts the a_0 and a_1 parameters calculated from the fixed half-life fit into the total number of counts from each source.

		a_0	a_1	$t_{1/2}$	χ^2_{dof}
All Data	Fixed $t_{1/2}$	0.65 ± 0.60	6.72 ± 1.54	138.0	1.04
	Floating $t_{1/2}$	—	—	—	—
	Straight Line	3.13 ± 0.20	—	—	2.42
LHS Only	Fixed $t_{1/2}$	-0.22 ± 0.36	2.56 ± 0.93	138.0	0.89
	Floating $t_{1/2}$	0.70 ± 0.10	4.34 ± 1.26	4.31 ± 2.90	0.51
	Straight Line	0.73 ± 0.10	—	—	1.41
RHS Only	Fixed $t_{1/2}$	1.16 ± 0.49	3.10 ± 1.20	138.0	1.00
	Floating $t_{1/2}$	—	—	—	—
	Straight Line	2.33 ± 0.17	—	—	1.44

Table 5.5: χ^2 fits to data from Ni CVD#3 binned as total counts above 1 MeV per 10 day period. As the LHS and RHS of the detector where etched differently they too were analysed separately.

		a_0	a_1	$t_{1/2}$	χ^2_{dof}
All Data	Fixed $t_{1/2}$	0.22 ± 0.97	7.98 ± 2.69	138.0	0.89
	Floating $t_{1/2}$	—	—	—	—
	Straight Line	3.02 ± 0.20	—	—	1.61
LHS Only	Fixed $t_{1/2}$	0.23 ± 0.53	1.28 ± 1.44	138.0	0.48
	Floating $t_{1/2}$	—	—	—	—
	Straight Line	0.70 ± 0.10	—	—	0.51
RHS Only	Fixed $t_{1/2}$	0.26 ± 0.88	5.73 ± 2.44	138.0	1.03
	Floating $t_{1/2}$	0.90 ± 2.49	6.32 ± 5.89	93.5 ± 163.3	1.14
	Straight Line	2.28 ± 0.18	—	—	1.44

	Counts Non-Decaying	Counts Decaying
All Data	15.77 ± 69.55	205.05 ± 69.12
LHS Only	16.49 ± 38.00	32.89 ± 37.00
RHS Only	18.64 ± 63.10	147.24 ± 62.70

Table 5.6: χ^2 fits to data from Ni CVD#3 binned as total counts above 1 MeV per 10 day period. The period 170–300 has been removed from the fits as it was contaminated with Rn whose decay can clearly be seen in the data. As the LHS and RHS of the detector where etched differently they too were analysed separately. The lower table converts the a_0 and a_1 parameters calculated from the fixed half-life fit into the total number of counts from each source.

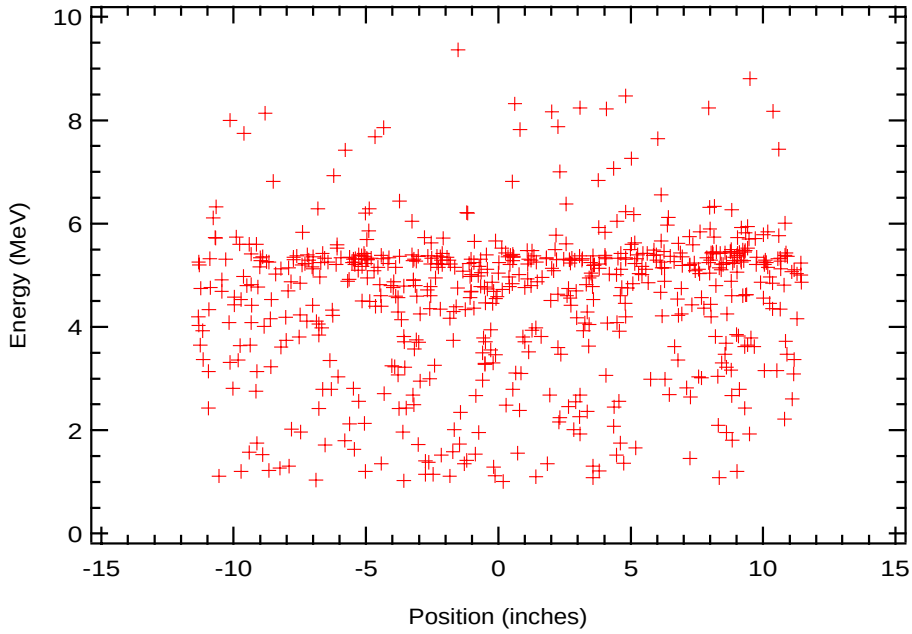

Figure 5.25: The accumulated data from NiCVD#2 displayed as pulse energy (MeV) vs pulse position (inches from the centre of the detector).

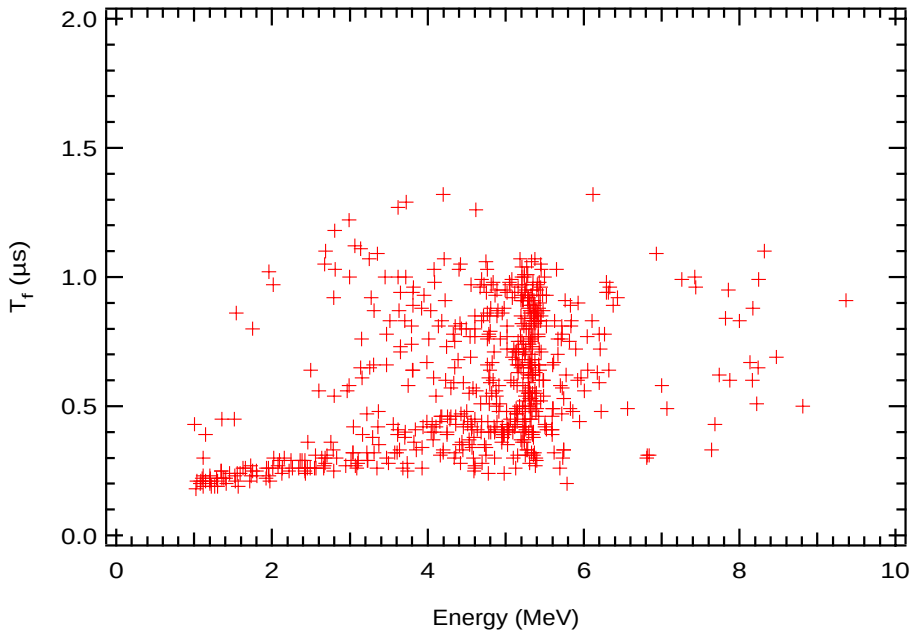

Figure 5.26: The accumulated data from NiCVD#2 displayed as a t_f *vs* energy plot.

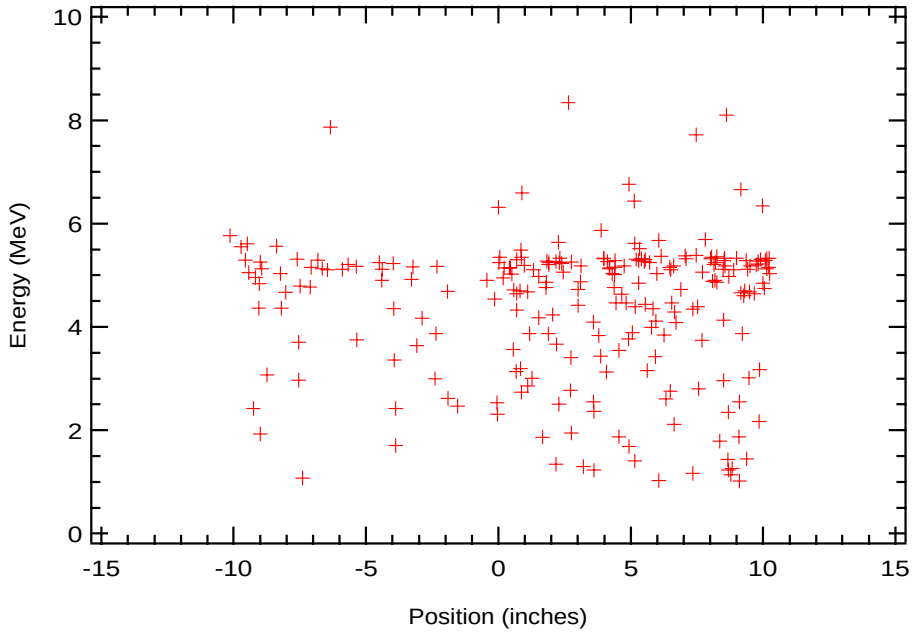

Figure 5.27: The accumulated data from NiCVD#3 displayed as pulse energy (MeV) vs pulse position (inches from the centre of the detector).

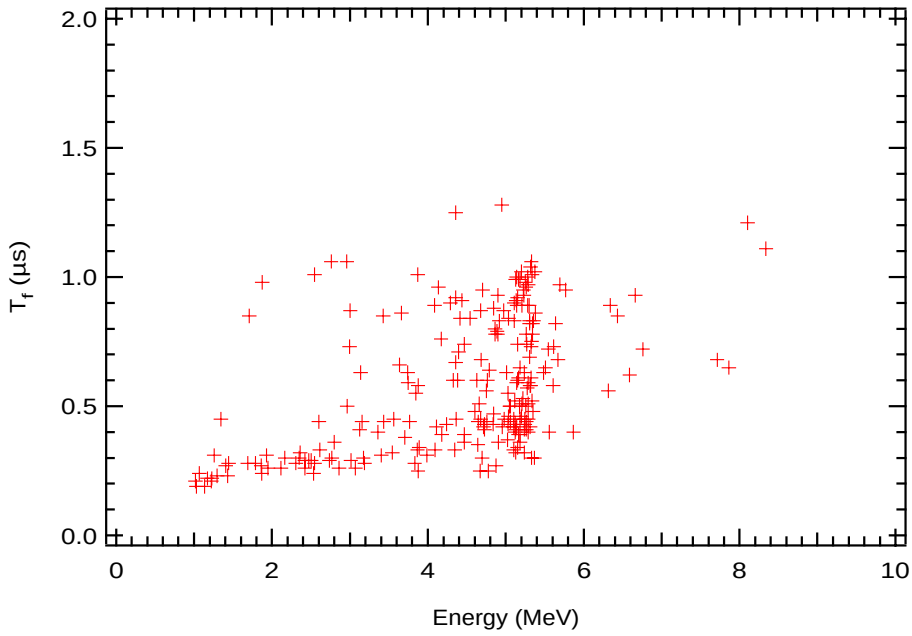

Figure 5.28: The accumulated data from NiCVD#3 displayed as a t_f *vs* energy plot.

tively the same levels of non-decaying components, emphasizing that a 1 μm etch is sufficient to remove impurities of the surface of the detector which have resulted from manufacturing processes. This assumption is incorrect if the bulk activity of the detector is the significant component of the data. If this were the case, the level of etching would not affect the levels of U and Th detected as the range of an α particle is only 10 μm (0.4 mil). This possibility is addressed in the next section.

For NiCVD#3 the data in Table 5.6 indicates that the levels of the non-decaying component are again, within statistics, the same. There is however a significant difference between the decaying components when comparing the two sides. This can be attributed to the exposure of the RHS of the detector to air and reinforces the theory that exposure to air without etching results in surface contamination with ^{210}Po. The method by which the ^{210}Po rather than any other radio-isotope is more favourably deposited on the detector walls is unknown.

5.6.3 Surface and Bulk Contamination

It has been seen from the above section that the exposure of a detector to air can result in surface contamination. This is a major concern given that at some stage, even for some short period, all components of the detectors were exposed to air. Even thought the (apparently) most abudently deposited isotope is the relatively benign ^{210}Po (benign as neither it nor its daughter is able to produce a γ ray above the 2.2 MeV threshold required for photodisintegration of the deuteron in SNO), it is not inconceivable that other long-lived isotopes are similarly deposited. The results of this hypothesis are born out in when examining the data sets from NiCVD#2 and #3 where short-lived (supposedly Rn) contamination entered the detector during repairs. It is therefore not acceptable to equate the total non-decaying component with the total activity of U and Th **in** the detector on the grounds that the data will most likely consist of both components from the bulk of the material as well as from the surface of detector walls. Figures 5.26 and 5.28 show the final results of the combined data sets as t_f *vs* energy plots. It should be noted that the plots are appear to be dominated by surface activity.

The most preferable method for separating the two (bulk and surface) components whould be to use the Maximum Likelihood technique described in Appendix C given the underlying t_f *vs* energy distributions. In fact it would be necessary to use five distributions; the surface ^{210}Po and the surface/bulk U and Th chains. In addition the use of the surface/bulk U and Th chain distributions implies that the chains are in equilibrium, which can not be verified (nor is it especially likely given the production method of the detectors). Chapter 3 has dealt with the expected distribution of bulk and surface U and Th distributions and although Monte Carlo distribution exist of these distributions, they do not include all the effects associated with the the electronics. As a result the Monte Carlo rise time and energy distributions are not

directly comparable the data and can not be used to separate the components. By inspection and comparisons of Figures 5.26 and 5.28 with 3.15 it can be noted that the majority of the activity, even when disregarding the 210Po, is surface activity.

Although, qualitatively it is possible to state that the majority of the events are a result of surface contamination, it is possible to place an upper limit to the bulk contamination. This can be determined by examining the non-decaying components of the exponential decay fits and assuming that all the activity measured is from the bulk.

Non-decaying Counts	Live Time (days)	Non-decaying Rate	Surface m^2	Counts $/m^2/day$
189.9 ± 50.3	121.6	1.56 ± 0.41	0.095	16.2 ± 4.3
15.8 ± 69.6	76.8	0.21 ± 0.91	0.085	2.5 ± 10.7

These 'upper limits' are measure in units of α events above 1 MeV per m^2 of detector surface per day. The corresponding values for bulk U and Th at 10 ppt are 1.8 and 0.5. Although upper limits of NiCVD#2 and NiCVD#3 are above these levels, it must be remembered that the limits were created without any attempt to remove any long-lived surface components. Future Ni CVD detectors will be handled inside a clean room and kept inside Rn proof bags to reduce the levels of surface contamination. Recent results of radioassays of small parts of the production phase tubes indicate that the level of U and Th is less than 2 ppt each [41].

5.6.4 Neutron Window

Previous work in Chapter 3 has commented on the use of the rise time parameter in the separation of neutron capture and alpha events. The data from both NICVD#2 and #3 have been combined in Figure 5.29. The combined data sets correspond to 233.6 days of live time or a total of 23.36 m^2·days (where a m^2·day corresponds to 1 day of data from a detector with an internal surface area of 1 m^2). It is interesting to note that the final full NCD array will have a total area of 60.65 m^2. Although this is the proof of principle that this simple analysis parameter is able to separate neutron capture and alpha events at the ~50% level in the final SNO detector the measurement was made using detectors running a different total gas pressure, a different gas gain and using a totally different type of electronics than the final NCD production system. For that reason it has been decided that it will be necessary to make some of final production counters 'dead' by filling them with ^{4}He instead of ^{3}He making them insensitive to neutron capture. These detectors will then be able to prove the neutron free region of the rise time energy spectrum in the final production system. This method and the location of these 'dead' detectors is covered more fully in Chapter 6.

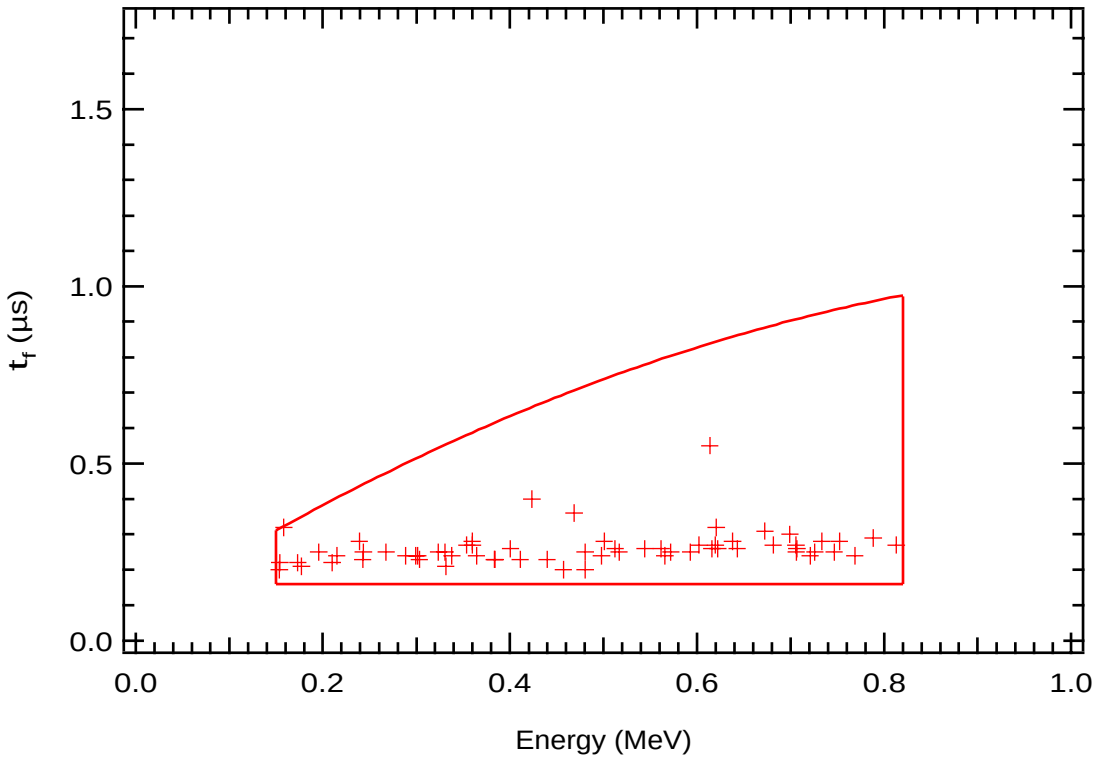

Figure 5.29: The total data between 0.1 and 1.0 MeV for NICVD#2 and NiCVD#3 displayed as a t_f *vs* energy plot.

5.6.5 High Energy Neutron Irradiation

During the WIPP experiments it was decided to determine the effect of irradiating the detector with high energy neutrons (Figure 5.30). This was performed by using an unmoderated ^{252}Cf source. This same source was usually moderated to produce the thermal neutrons used to calibrate the detectors which contained some ^{3}He. Unmoderated, the neutrons emitted have a Maxwellian energy distribution.

$$p(E) \propto \sqrt{E} e^{-\frac{E}{E_0}} \qquad E_0 \sim 1.3\,\mathrm{MeV} \tag{5.3}$$

The expect reactions of the fast neutrons on the nickel walls of the detector are (n,p) and (n,α) with the (n,α) having a higher cross section. The resulting data not only provides information of the effect of high energy neutrons but defines the α band of the detector as the α particles are produced uniformly throughout the detector wall. This corresponds to the bulk α distributions but has the advantage of not requiring at dirty detector.

It should be noted from the plot that the proton produced from the (n,p) reactions contaminate the neutron only window. This is not unexpected as the neutron capture is similarly an (n,p) reaction. However, this is not a concern for the final SNO detector for two reasons. Firstly, the expected high energy flux in the centre of the detector is expected to be extremely small and secondly the cross section for the alternative (n,α) is substantially larger.

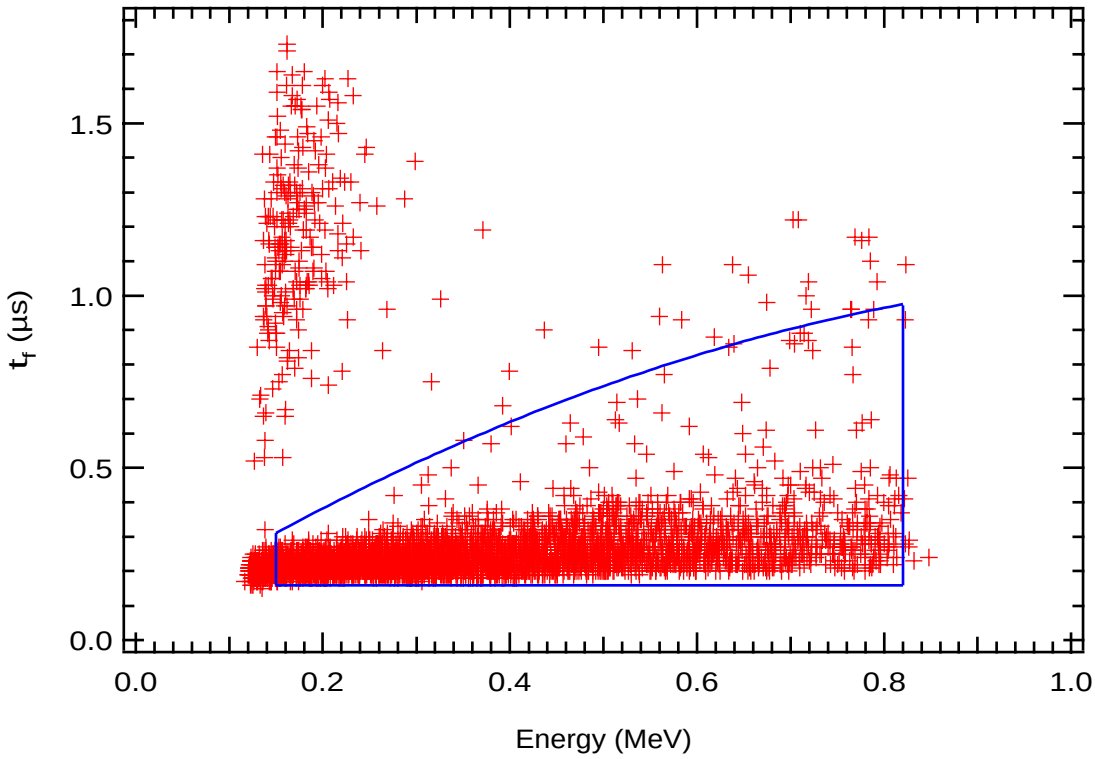

Figure 5.30: A t_f *vs* energy plot of the data resulting from irradiation of NiCVD#3 with non-thermal neutrons.

Chapter 6

Extraction of Physics from the NCD Array

6.1 Neutral Current Detectors in SNO

The results of both radioassay and WIPP experiments indicate that background levels required for the use of discrete neutral current detectors in SNO can be reached, but there still remains the question of where the detectors should be placed. Both the number of detectors and their positions must be considered. Increasing the number of detectors increases the neutron capture efficiency, but causes more interference with the Čerenkov light.[1] The studies by Wilhelmy showed that tubes with a 5 cm diameter placed on a 1 m grid was the best compromise between neutron capture efficiency and light interference. Both a square lattice grid and a hexagonal grid were considered. There was no significant difference in capture efficiency or interference. The square lattice was the preferred option as it allowed easier manipulation of sources (two orthogonal planes and the z-axis). An artist's impression of the NCD array is shown in Figure 6.1.

With this geometry, the detector strings range from almost 11 m in length for the four central detectors to 2.72 m for those on the outer edge. Due to problems manipulating 11 m long detectors underground, each detector string will be assembled above the neck of the acrylic vessel from several shorter segments. As nickel CVD tube will be produced in 2 m lengths it was decided from both a logistical and shipping point of view that the segment lengths should be 2, 2.27 and 2.72 m long. (A 2 m tube is cut into two 27 cm and two 72 cm pieces, the remaining 2 cm being used for assay purposes.) The 2.72 m corresponds to the longest tube that could be taken down the INCO hoist. The pieces are then laser welded onto other 2 m tubes to produce the required lengths. Construction of the largest detectors involves laser welding together five segments $3 \times 2\,\mathrm{m} + 1 \times 2.27\,\mathrm{m} + 1 \times 2.72\,\mathrm{m} = 10.99\,\mathrm{m}$. The full length counters are made by welding together the individual counter segments over the neck of the

[1] It should be noted that this interference results not only from the counters but also from their associated cables.

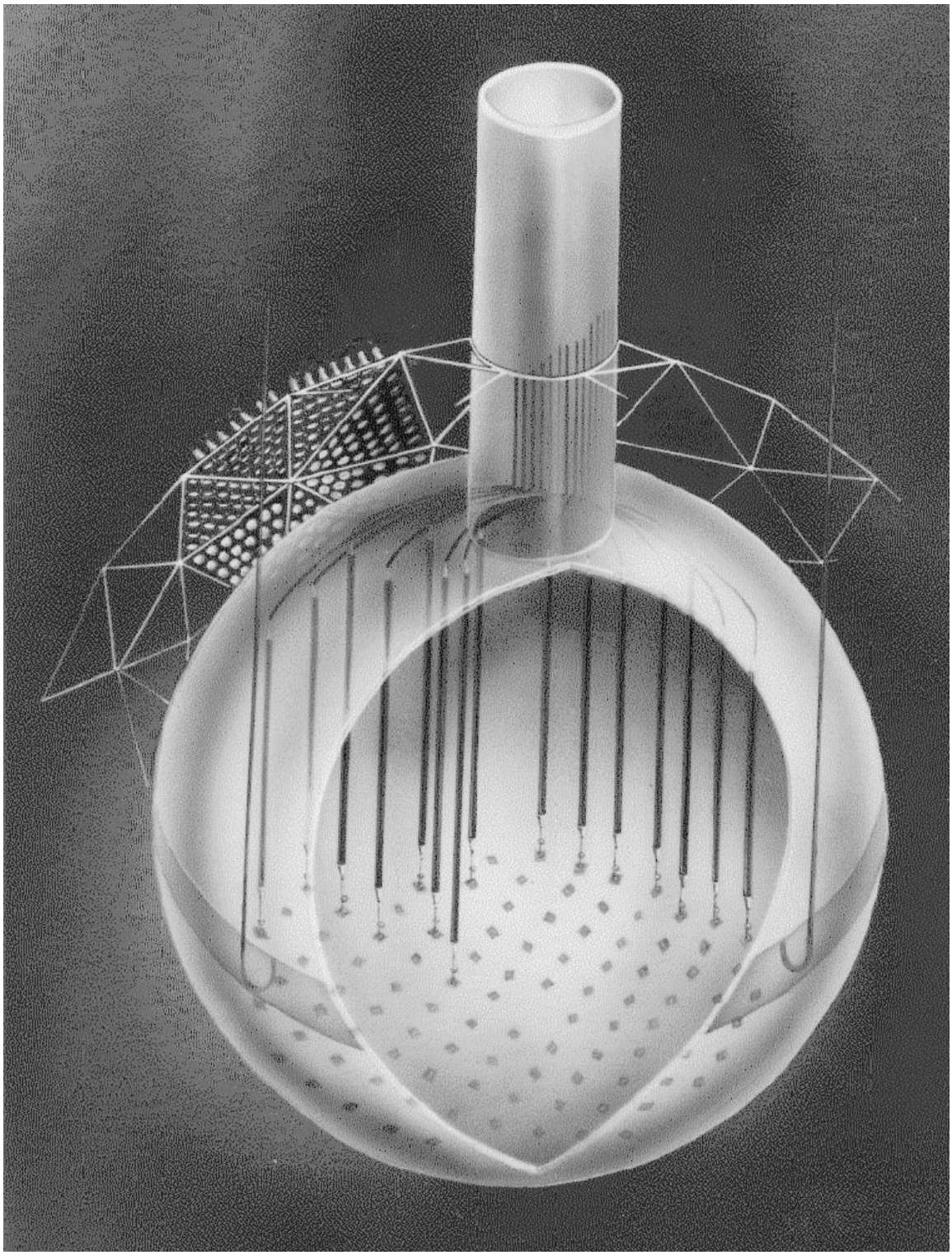

Figure 6.1: An artist's impression of neutral current detectors in SNO. Note that the detector diameters are not to scale.

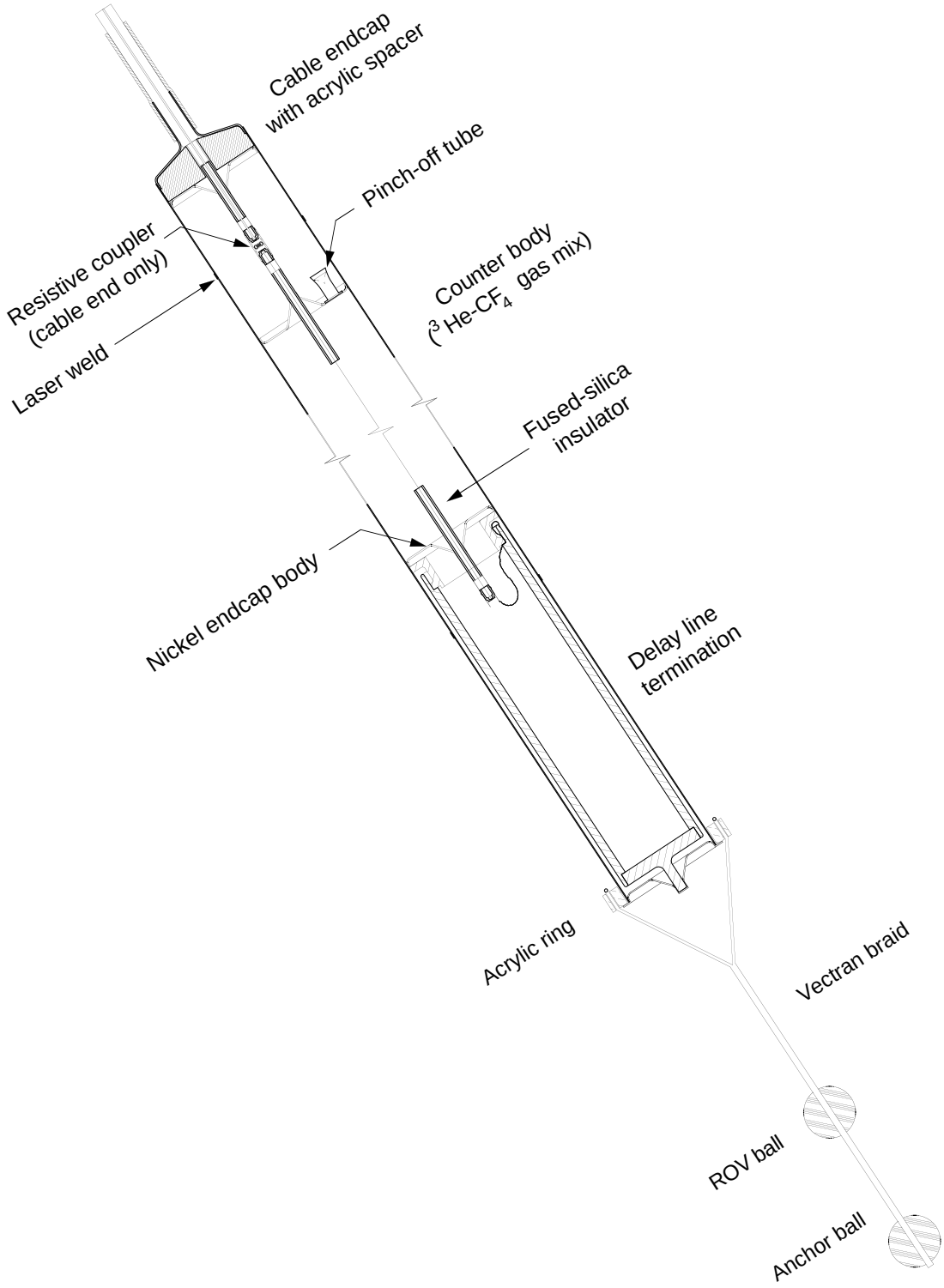

Figure 6.2: A cutaway drawing of a neutral current detector.

acrylic vessel. Once the two segments have been joined they are lowered into the SNO vessel so that the next segment may be laser welded on top. Once a string of segments has been completed it is pulled down to the bottom of the vessel using a Remotely Operated Vehicle (ROV). The ROV is essentially a sealed, remotely controlled 'toy' submarine complete with an underwater camera to aid in locating each attachment point. The details concerning the construction of individual segments, the couplings between them, the lower attachments to the acrylic vessel and the connections to the readout cable are beyond the scope of this thesis but can be found in the NCD construction document [37]. Suffice to say that a great many man-years have been and will be spent working on these problems. Figure 6.2 shows a typical neutral current detector.

6.1.1 NCD Electronics

Unlike the previous WIPP experiments, current sensitive pre-amplifiers will be used. There are several reasons for returning to current pre-amps (the first NCD experiments at Los Alamos were conducted with current sensitive preamplifiers). The first is that they produce a more comprehensible description of the original ionization profile in comparison with charge sensitive preamplifiers where the signal is integrated. Secondly, it has been shown that it is possible to extract position information by analysing the 'reflection-step' in the initial rise of the pulse. Of the current induced in the wire due to the motion of the positive ions, half travels directly towards the preamp whilst the other half travels towards the remote end of the detector where it is reflected, as this end is not terminated. This reflection from the remote end of the detector manifests itself as a kink in the initial part of the pulse. The time taken for the kink to appear after the start of the pulse is proportional to the distance from the remote end of the counter. This creates a problem with determining the position of events which are created near the remote end of the counter as the delay is almost negligible. This is solved by 'electrically' extending the counter using a delay line at the remote end. Due to cleanliness and light absorption issues it is impossible to run a second line to the bottom end of the detectors and use the normal methods of charge division or pulse timing. Operating the detectors as transmission lines requires proper termination, either by means of a matching resistor or a 415Ω, inductively wound cable to the pre-amps. Although the resistor acts as a series noise generator the result is preferable to the dispersive effects of the inductively wound cable. For these reasons and the potential benefit of position resolution, charge sensitive preamplifiers were abandoned.

Figure 6.3 shows the preliminary design for electronics. The pulses from individual strings are multiplexed into an 8 input transient digitizing oscilloscope. The individual strings are also connected to ADCs which will have a lower energy threshold than the digitizers. This

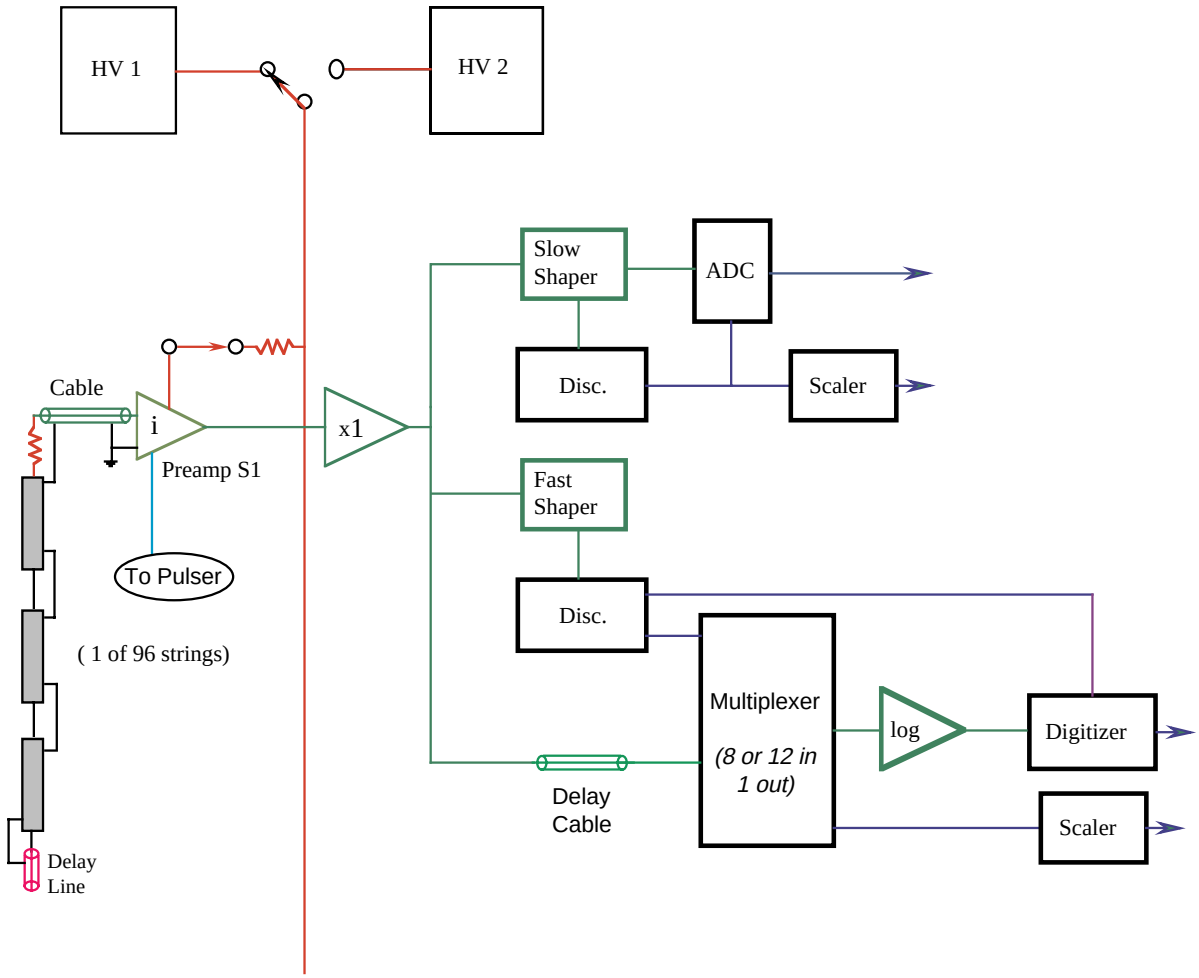

Figure 6.3: The conceptual design for NCD electronics.

will allow recording of lower energy signals at a faster rate than could be obtained using the digitizers. This is important for the case of a supernova, where the expected rate is of the order of kHz and timing on the order of milliseconds is desirable.

Due to the large number of strings and the cost of the digitizers a multiplexing system must be used. This should not be a concern as the expected neutral current rate from the entire array is of the order of tens of events per day. It does, however, create a problem with the triggering mechanism. Each string must have its own triggering circuit in order to identify which of the detectors attached to the multiplexor (MUX) fired. It requires a finite amount of time for the fast shaped pulse to reach the required threshold and therefore open the appropriate channel in the MUX. In order to perform pulse shape analysis the entire pulse and a small amount of baseline must be recorded. For previous systems which used one transient digitizer per channel this was not an issue. For SNO a delay of more than 100 ns must be

introduced between the trigger and the signal to allow sufficient time for the MUX to open and the digitizer to record all the pulse and a sufficient amount of baseline.

Logarithmic Amplifiers

There is a major disadvantage with using current sensitive as opposed to charge sensitive preamplifiers - the dynamic range of their outputs. This is not a problem associated with the amplifiers but with the electronics used to digitize the resulting signals. A charge sensitive preamplifier's minimum and maximum pulse heights are defined by the minimum and maximum energies deposited in the gas of the counter. For NCD's the interesting range is 191 keV (the proton edge) to 8.95 MeV (the top energy of the Th α chain). However, a current sensitive preamplifier's minimum and maximum pulse heights are defined by the instantaneous minimum and maximum current from the proportional counter. The largest current would be associated with a 8.95 MeV α particle arriving parallel to the wire, whilst the smallest would be a 191 keV ^{3}He(n,p)t event perpendicular to the wire. The effects of straggling, the track of the ionizing particle being not strictly a straight line due to interactions with gas molecules, reduce the effective dynamic range to of the order of 200. This corresponds to a large dynamic range, easily more than could be successfully digitized using commercial 8 bit (256 channel) digitizers whilst still retaining detailed information on all pulses. The solution is to use a logarithmic amplifier to compress the top end of the dynamic range. Unfortunately, when accompanied by discrete digitization, this results in a loss of energy resolution at the higher end of the range. With the inclusion of the ADC's, however, the true energy can be reconstructed. Tests performed at Los Alamos have shown that the logged pulse can be successfully reconstructed and used in the same manner as linear current pulses for the purposes of pulse-shape discrimination. Figure 6.4 shows the resulting rise time *vs* energy spectra for charge and current pulses from a test proportional counter at Los Alamos. It illustrates that the preliminary work with charge sensitive preamplifiers can be duplicated with current sensitive preamplifiers. The analysis of neutron events can be performed without the logarithmic amplifier as the dynamic ranges is an order of magnitude smaller and can be digitized. However, as proof of principle, pulses from a neutron calibration were simulataneously digitized as both current and logged current pulses. Figure 6.5 shows examples of fast and slow neutron pulses and the ability to reconstruct them from their logged counterparts.

6.2 Neutron Signal Separation

From previous Chapters it has been shown that it is possible to completely separate neutron and background signals with a loss of efficiency of 50% and that by using a Maximum Likelihood fitter this may be improved upon, dependent on the background of α events in the

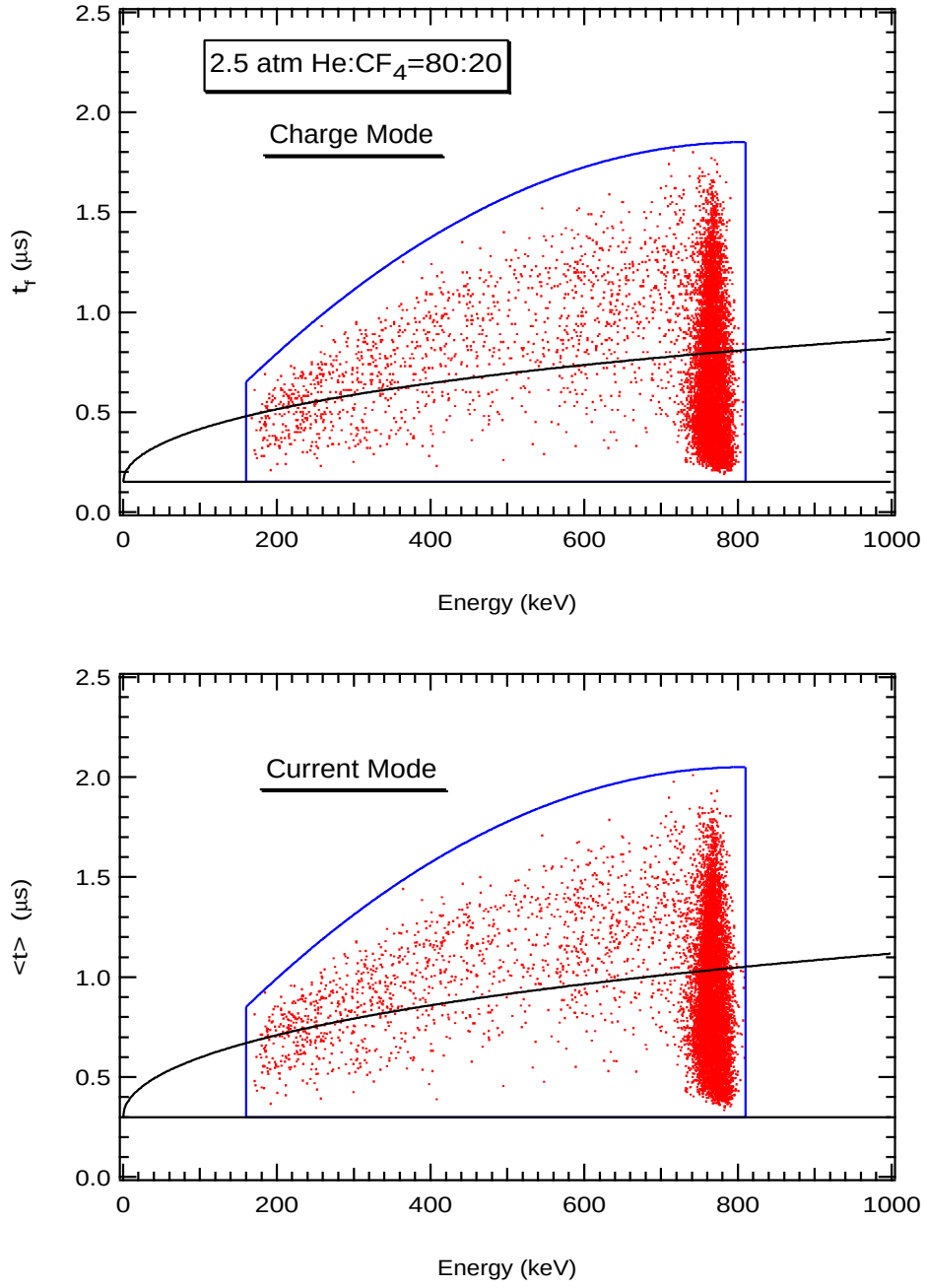

Figure 6.4: The rise time *vs* energy spectra from a test proportional counter using neutrons from ^{252}Cf as a source. The upper graph uses charged pulses whilst the lower one uses current pules.

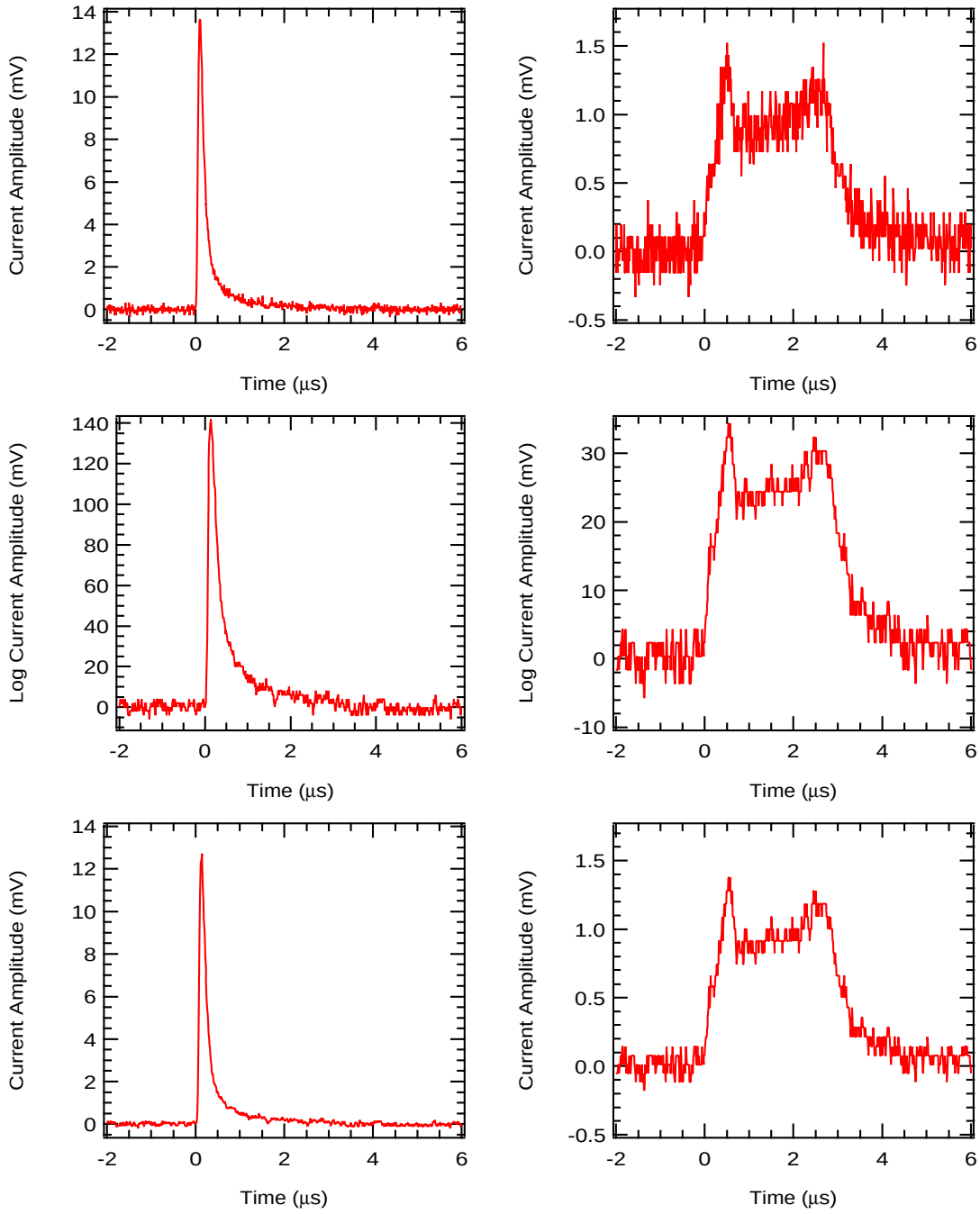

Figure 6.5: Pulses from a test proportional counter using neutrons from ^{252}Cf as a source. The graphs from top to bottom are; a non-logged current pulse, a logged current pulse, and a logged current pulse which has been antilogged.

neutron window. As a result, approximately 50% of the total number of neutrons detected come from the event-by-event analysis whilst the remainder are obtained by statistical analysis.

Further information is, however, contained in the *location* of neutron captures within the NCD array. At worst two dimensional (x, y) data is available, though the possibility remains for z information of the order of 1 m from studying the pulse and its reflection from the far end of the detector remains[42]. Even with the strict radiopurity requirements of SNO, background neutrons will still be produced by contaminants in the detector. These background sources may not necessarily have the same spatial distribution as neutrons produced by the neutral current interaction. For this reason several Monte Carlo simulations were performed for the possible sources of background neutrons to study their distributions and the ability to separate them from the true NC signal or more generally from isotropically distributed neutrons.

6.2.1 Neutron Distributions in SNO

As this is a first order analysis of the array distribution only the most important sources of backgrounds were considered. As a result, Monte Carlo simulations[43] were considered for the following six sources of neutrons;

1. The neutral current interaction producing neutrons isotropically in the heavy water. This is of the order of 5000 events/ktonne-year produced in the detector (Bahcall 1992 SSM).

2. Photo-disintegration of deuterons by γ rays from contaminants in the heavy water. As these contaminants are expected to be uniformly distributed in the heavy water, the neutron production is also expected to be isotropic. Both water assay measurements and possibly Čerenkov measurements of the emitted γ rays should give an estimate of their levels.

3. Photo-disintegration of deuterons by γ rays from U and Th daughters in individual detector strings. Given that all the detectors will contain trace amounts of U and Th and that this activity is largely attributed to the counter walls then the background generated by them is expected to appear uniform.

4. Photo-disintegration of deuterons by γ rays from U and Th uniformly distributed in the walls of the acrylic vessel. Again given a mean path length of only 18 cm for the γ ray the majority of neutrons produced are reabsorbed by the hydrogen in the vessel walls. The distribution of captures of these neutrons by neutral current detectors is highly weighted towards the walls of the vessel, in contrast to the isotropic nature of the first two distributions. If the effects of the chimney can be ignored then this distribution is

expected to the spherically symmetric. For the purpose of this simulations the chimney was ignored though later studies will include it.

5. Photo-disintegration of deuterons by γ rays from localized 'hot-spots' in the walls of the acrylic vessel. Like the previous background source the majority of neutrons will be captured in the detectors closest to the wall but in this case there will be no spherical symmetry.

6. Photo-disintegration of deuterons by γ rays from U and Th daughters in individual detector strings where there is a abnormally high concentration of U or Th in the detector. Given a mean path length of 18 cm for the γ ray most neutrons are expected to be produced near the detector which emitted the γ ray. Even with neutron thermalisation distances of the order of 1 m the majority of neutrons captures occur on the offending detector.

Examples of isotropic, hot spot and acrylic vessel distributions are shown in Figures 6.6 and 6.7. These data have been binned into radial rings and (x, y) capture co-ordinates. Radial rings correspond to all the detectors which have the same radial position. For the isotropic and acrylic vessel sources the data have been cylindrically symmetrized.

6.2.2 NCD Geometries

Not only were various simulations of the different sources of neutrons carried out, but also the simulations were performed for differing detector geometries. The initial design was that the detectors were to be arranged on a square lattice grid, spacing 1 m and that there were to be 112 strings. However, during the course of this thesis, two questions were raised.

1. Are the detectors on the farthest edge of the detector strictly necessary? Being closest to the edge of the acrylic vessel they provide the best estimate of the neutron background from this source, but they provide little information on the neutral current signal. It is possible that the PMT array will better able to extract the levels of U and Th than the NCD array due to the factor of 500 between γ and n productions. Removing them may not have a significant effect on the ability to determine the neutral current signal, but would reduce the number of strings from 112 to 96. This would also have the effect of removing 16 channels of electronics and their associated expense. There are two other reasons for not installing the final ring of detectors. Firstly, attempting to physically install these detectors may prove to be extremely difficult given the angle of the acrylic vessel at that radius. Secondly, reducing the number of cables reduces interference with the Čerenkov light (the outermost ring would contribute approximately 20% of the cables by length) especially in the area of the chimney where the density of cables is largest.

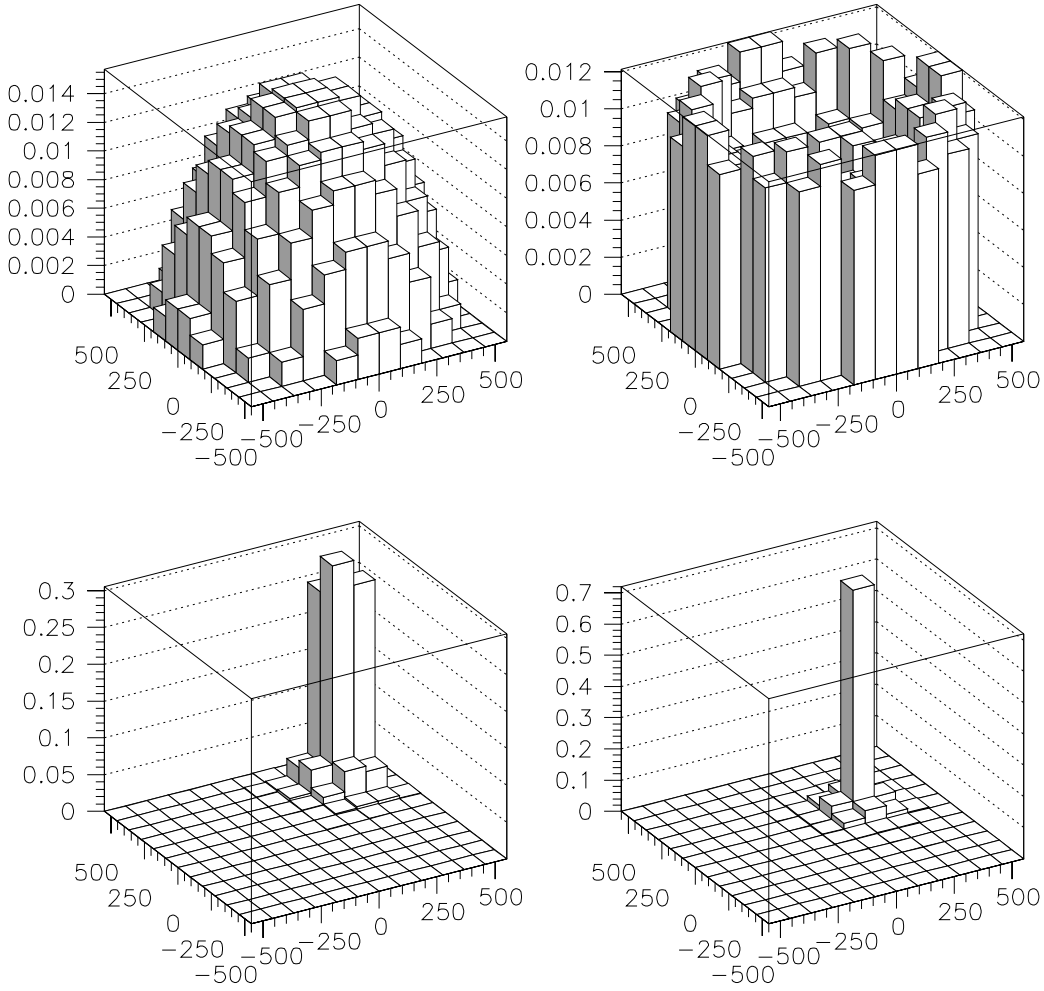

Top Left The neutral current signal.

Top Right Photodisintegration neutrons where the offending γ-ray originates in the acrylic vessel.

Bottom Left Photodisintegration neutrons where the offending γ-ray originates from a hot spot on the surface of the acrylic vessel

Bottom Right Photodisintegration neutrons where the offending γ-ray originates from a hot spot on one of the neutral current detectors.

Figure 6.6: Two dimensional histograms illustrating the normalized neutron capture distributions from a variety of sources.

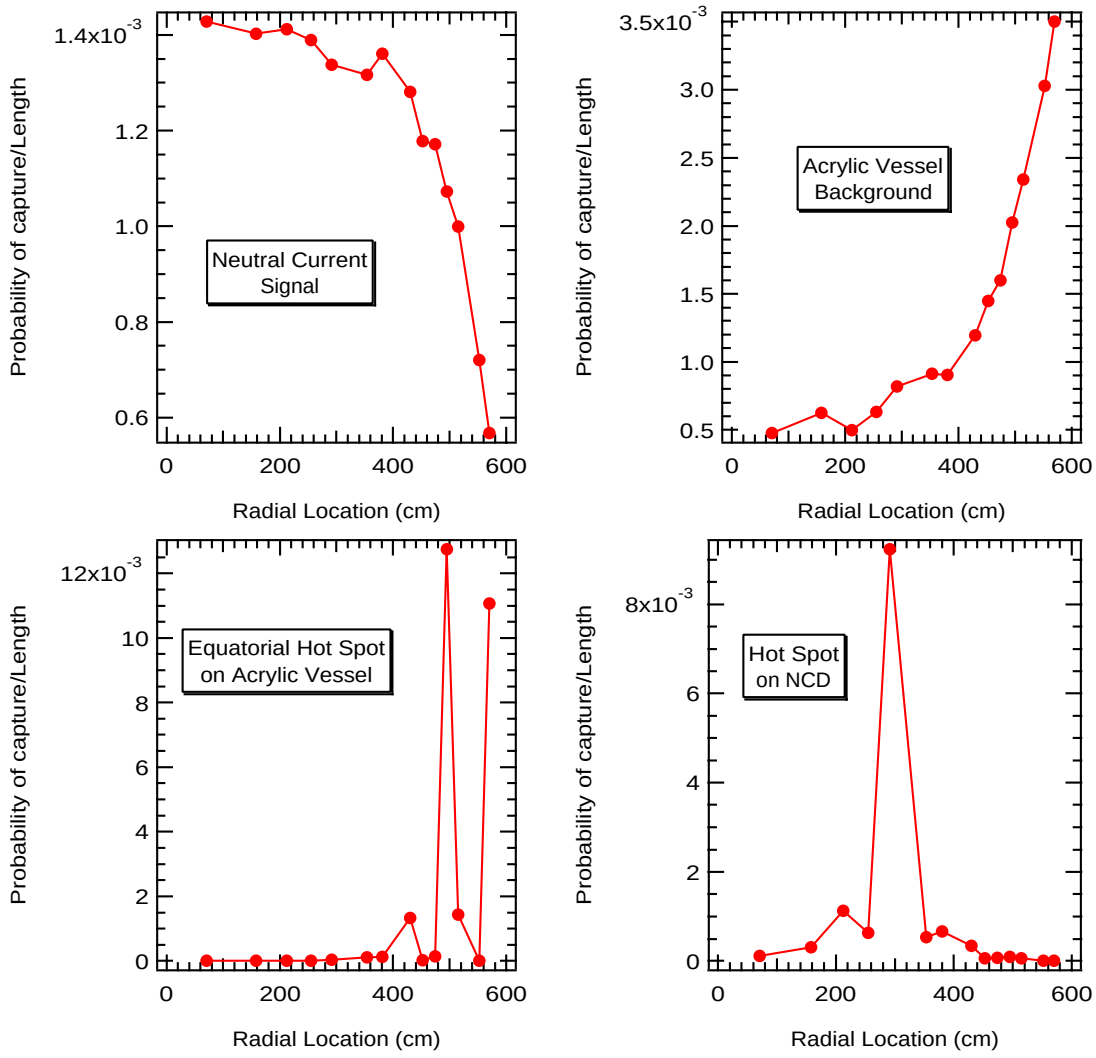

Figure 6.7: Neutron capture distributions of isotropic, hot-spot and acrylic vessel sources respectively.

2. Is it necessary that all the detectors be filled with ^{3}He? If some of the detectors were to be filled with ^{4}He they would be insensitive to neutrons and only sensitive to their own internal activity. The work at WIPP where detectors were refilled with ^{4}He was the proof of principle demonstrating that there is part ($\sim$50%) of the neutron window that is completely free from α contamination. These data were, however, taken using much smaller detectors with a different total gas pressure, and charge sensitive pre-amplifiers. Using longer detectors in a low activity environment with true NCD electronics would give greater statistics in this region. These conditions would all be met if some detectors from the NCD array were filled with ^{4}He instead of ^{3}He. The ^{4}He counters are referred to as 'dead' as they are unable to capture neutrons. If up to 5% of the array were made dead then would this significantly effect the ability to determine the NC rate? Also what would be the best location for these detectors which would maximise the separation of signal and backgrounds?

To answer these questions Monte Carlo simulations were performed and the ability to extract the neutral current signal from other signals compared to the default geometry. Table 6.1 details all the geometries simulated. Figure 6.8 should be used as an aid to determining the location of the dead counters. As the Monte Carlo code used to produce these simulations was not capable of the subtleties of neutron transport (as compared to large and complex codes such as MCNP), it must be noted that these efficiencies quoted are for informational and relative comparison purposes rather than to be used as an absolute measure of the true neutron capture. However, it is not expected that the distribution of neutron captures will change significantly with an improved neutron transport code. It should be noted that there were several suggestions as to the location of the dead counters. The choices for these locations was dependent upon the criteria that no more than 5% of the array could be made dead and that cylindrical symmetry should be preserved. Only G_6 deviates from this symmetry and was chosen because it was a compromise between losing information on the isotropic signal (by removing a central detector) and losing information of the acrylic vessel distribution (by removing an outermost detector). The arguments for and against these geometries are detailed in Section 6.4.

6.2.3 Neutron Transport and Detection

The distributions in Figure 6.7 were generated by a simple Monte Carlo which used the a fixed Fermi-length to determine the position of the next interaction [43]. This simple Monte Carlo did not include the extreme details of neutron transport as found in MCNP (Monte Carlo N-particle), which also includes photon and electron transport. The libraries and scattering routines from MCNP have now been combined into the overall SNO Monte Carlo, SNOMAN

Geometry	Description
G_0	The base geometry. It features the full 112 strings on 14 radial rings.
G_1	As G_0 but detectors at $(\pm 3.5, \pm 3.5)$ use ^{4}He.
G_2	As G_0 but detectors at $(\pm 1.5, \pm 5.5)$ and $(\pm 5.5, \pm 1.5)$ use ^{4}He.
G_3	As G_0 but all the detectors in ring 14 have been removed.
G_4	As G_3 but detectors at $(\pm 3.5, \pm 3.5)$ use ^{4}He.
G_5	As G_3 but detectors at $(\pm 2.5, \pm 2.5)$ use ^{4}He.
G_6	As G_3 but detectors at $(-2.5, -2.5)$, $(-0.5, 0.5)$ and $(0.5, 5.5)$ use ^{4}He.

Geometry	Isotropic Eff.	AV Eff.	Live	Dead
G_0	41.8%	11.4%	792	0
G_1	40.8%	11.0%	768	24
G_2	40.9%	10.6%	776	16
G_3	40.3%	9.7%	760	0
G_4	39.5%	9.2%	736	24
G_5	38.9%	9.4%	724	36
G_6	39.7%	9.5%	736	24

Table 6.1: The different geometries simulated. Efficiencies are recorded for the number of neutrons captured compared to those produced from isotropic and acrylic vessel sources. The lengths of live and "dead" detectors in each geometry are recorded in metres.

(SNO Monte-Carlo and ANalysis), though the computation time required for this much more detailed analysis is substantial. A discription of the Monte Carlo technique used to produce these data sets can be found in detail in Reference [43].

6.2.4 Binning of Neutron Data

The Maximum Likelihood fitter described in Appendix C requires that the data to be fitted be binned in some manner. In general, Maximum likelihood fitters do not require the data to be binned, but in this instance it was the preferred method. For the NCD's there are many possible options, but they can be simplified into three categories:

1D The original square lattice, G_0, features 14 distinct radial positions. Each bin is the sum of the counts from all the detectors in that ring. All other geometries can similarly be binned, with the number of radial positions ranging between 13 and 14.

2D There are two possible methods of binning; the square lattice grid, where each point on the square grid contains the number of counts associated with the string at that location (if there was no detector at that grid location then a zero was recorded), and the ring by ring array where the number of counts in each detector in a ring is recorded in the

array.[2] There is no functional difference between these two methods, they are only different representions of the same 112 data points and unsurprisingly the separation algorithms report the same results regardless of which method is used. They are used purely out of convenience. Data presented in the form of the square lattice is easier to understand on a detector by detector basis, the number of counts being easily identified with a detector at at particular (x, y) grid location. The ring by ring array is useful in hot spot searches when it is necessary to determine if a detector in a particular ring contains an excess of counts in comparison to the mean number of counts in that ring. This is only useful when the expected distributions are radially symmetric and hence the number of counts in each detector in a ring are expected to be statistically the same.

3D The same two methods as above are used, but the third dimension arises from the z information, as each detector is split vertically into one metre segments. As the current position resolution is only of the order of one metre, these methods contain the maximum amount of information that can be obtained from the array.

Figure 6.8 shows a plan view of the square detector array with radial rings marked. The table beneath shows the location of the first detector on each ring in (x, y), the radial position, the length per string of detectors and the number of strings in each ring. The final two columns show the total length of detector and the length of detector used in the Monte Carlo simulation. The difference between Total Length and Monte Carlo Length is purely historical — when the simulations were originally performed detector strings were to be made from 1,2 & 3 m segments. Finally Ring 6 was split into 6a and 6b as there are two distinct (x, y) positions with the same radial dimension (the same is true of Ring 14). The reason for separating Ring 6 is related to Geometry G_5 where 4 of the detectors (corresponding to Ring 6b) are made dead.

6.2.5 Neutron Signal Separation Efficiencies

Sample distributions were created for each of the possible sources of neutrons and for each of the possible geometries. The Monte Carlo simulations produced of the order of 40,000 events for both neutral current and acrylic vessel distributions. The large number of events was produced to reduce statistical fluctuations associated with the Monte Carlo. For comparison the typical number of neutrons generated for one year of running from these distributions was of the order of 2500 and 125 events for neutral current and acrylic vessel data sets. The data were recorded as neutron capture positions with infinite (x, y, z) resolution. They were then

[2] It can be shown statistically that for uniform isotropic distributions, one and two dimensional grids are exactly analogous. Cylindrical symmetry reduces the number of distinct points in the (x, y) grid from 112 to 14.

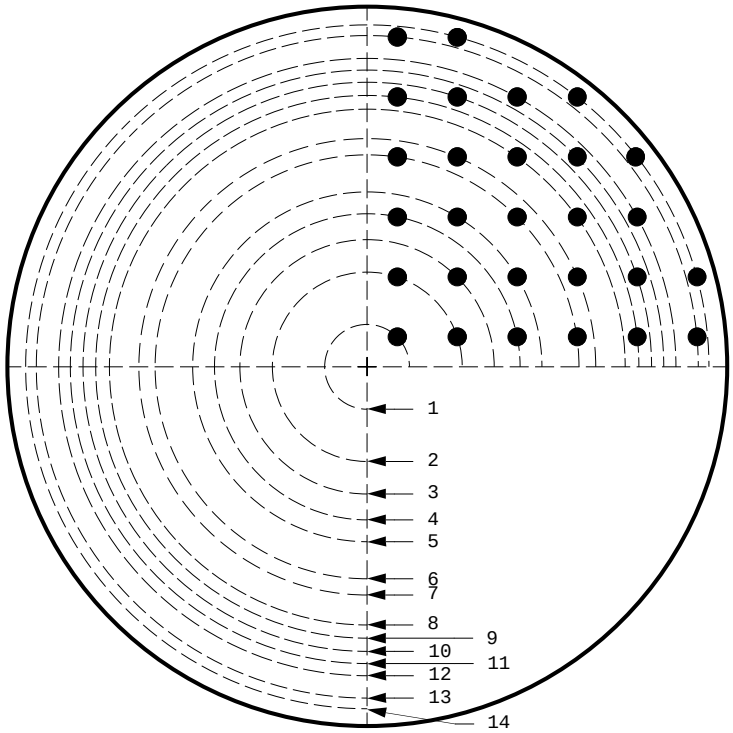

Ring	x (m)	y (m)	R (m)	Length/ String	# of Strings	Total Length	MC Length	Det.'s Per Ring	Live Length
1	0.50	0.50	0.707	10.99	4	43.96	44	20	41.12
2	0.50	1.50	1.581	10.88	8	87.04	88	32	82.49
3	1.50	1.50	2.121	10.43	4	41.72	40	16	39.44
4	0.50	2.50	2.550	10.16	8	81.28	80	32	76.73
5	1.50	2.50	2.916	9.71	8	77.68	80	32	73.13
6a	0.50	3.50	3.536	8.99	8	71.92	72	32	67.37
6b	2.50	2.50	3.536	8.99	4	35.96	36	16	33.68
7	1.50	3.50	3.808	8.54	8	68.32	64	32	63.77
8	2.50	3.50	4.301	7.44	8	59.52	56	24	56.11
9	0.50	4.50	4.528	6.99	8	55.92	56	24	52.51
10	1.50	4.50	4.743	6.54	8	52.32	48	24	48.91
11	3.50	3.50	4.945	6.00	4	24.00	24	12	22.29
12	2.50	4.50	5.148	5.44	8	43.52	40	16	41.24
13	0.50	5.50	5.523	4.00	8	32.00	32	16	29.72
14	1.50	5.50	5.701	(2.00)	(16)	(32.00)	(32)	(16)	(1.98)
					Total	775.20	760	328	728.51

Figure 6.8: A plan view of one quarter of the square detector array. The detector locations are at $(\pm x + 0.5\,\mathrm{m}, \pm y + 0.5\,\mathrm{m})$ where x and y are integers. For clarification the 14 radial rings are marked. Each detector lies on one of these rings.

converted into discrete distributions using the above binning methods. Distributions which were expected to be symmetric (all except 'hot spot' distributions) were then symmetrized using radial (for the two dimensional lattice) or radial with reflection in the z-axis (for the three dimensional lattice). These were then used as the underlying distributions, the $f_i(\underline{x})$ of Appendix C, to generate samples of data depicting one year running of SNO.

Acrylic Vessel Separation

From tests performed at the University of Washington, it has been shown that for roughly one half of the pulses (the ones with the fastest rise times) position resolution along the length of the detector of the order of 1 m can be obtained. These measurements were performed using current sensitive preamplifiers but without the log amps. In order to test sensitivity, the data from all the series of Monte Carlos were binned using both the 2D and 3D grids to determine the effects of losing z position information.

The results are shown in Table 6.2. The first table shows the average from 1000 simulations using 2730 isotropic neutrons and 125 neutrons from contaminants in the acrylic vessel. The 2730 isotropic neutrons is the expected number of neutrons captured after one year of running; 2500 from the neutral current interaction, and the remainder from contaminants in both the heavy water (at the level of 10^{-15} g/g) and the neutral current detectors (at the level of 2 ppt). At the level of 1 ppt Th the acrylic vessel is expected to produce 125 neutrons per year captured on the NCD array. The simulation was performed using the G_0 geometry. Appendix E contains the details of the Monte Carlo simulations and the methods for producing the simulations. The errors quoted reflect the rms of the 1000 fitted parameters and should be compared with the statistical limit of $\sqrt{2730} \sim 52$. The error on each parameter may also be calculated from the square root of the diagonal elements of the inverted Hessian matrix (see Appendix C). The second table shows the square root of the average value of the diagonal elements of the error matrix returned by each fit. From the similarity of the corresponding errors it can be concluded that the Monte Carlo and fitting procedures are working correctly. The final number is the average value of the correlation coefficient (see Appendix C).

From this table it can be shown that the loss of z information does not significantly alter the ability to separate isotropic and acrylic vessel distributions for the detector geometry, G_0 as the difference in errors returned by the fits is of the order of 0.2% (1D - 2.66%, 3D - 2.43%). It must be noted, however, that should position information be available it will be used not only in the separation of NC and AV distributions but possibly more importantly in the separation of non-uniform signals and hot spots. The results of separations from other geometries are listed in Table 6.3. In these geometries the difference between the errors of 1D and 3D fits ranges up to 0.75%.

Fit Results	Signal	1D Fit	2D Fit	3D Fit
Isotropic Signal	2730	2732.2 ± 72.2	2727.2 ± 71.0	2731.7 ± 65.3
AV Background	125	126.7 ± 52.7	128.1 ± 50.2	124.9 ± 38.8

Average Errors	1D Fit	2D Fit	3D Fit
Isotropic Signal	72.8	72.7	64.2
AV Background	51.9	51.9	39.0
Correlation	0.679	0.679	0.557

Table 6.2: The results from 1000 simulations of 2730 isotropic and 125 acrylic vessel neutrons using the detector geometry G_0. The table shows the average of the result of 1000 simulations where the errors are the standard deviations of these results. The lower table shows the square root of the average of the diagonal elements of the error matrix.

Finally, Table 6.4 shows the result of increasing the number of neutrons from the acrylic vessel. Even if the acrylic vessel neutrons captured increases by an order of magnitude the change in the measured isotropic number of neutrons is only of the order of 0.5%. In other words, the discrete nature of the NCD array is a robust means for separating AV background from the isotropic neutron capture signal. Furthermore, from Table 6.3 it can be seen that removing the outer ring and/or making use of ^{4}He strings does not significantly reduce the separation between isotropic and AV background signals.

It should be noted that this analysis does not attempt to determine the importance of z information when determining the position and removal of a hot spot. Nor does it examine the ability to remove the effects of the readout cables by a comparing the upper and lower hemispheres (although it was beyond the ability of the Monte Carlo program to simulate their effect). The ability to separate uniform distributions from hot spots is demonstrated in the following section.

6.3 Separation of Non-uniform Signals

The previous section dealt with the separation of isotropic and acrylic vessel distributions only, albeit with many geometries and multidimensional information. However, even with SNO's stringent purity requirements, it would be unwise to imagine that the only neutrons detected in SNO would arise from these sources. Non-uniform signals come from so-called hot spots, parts of SNO that contain more than the expected amounts of U and Th or that do not fill the D_2O volume uniformly like NCD endcaps. To reduce the levels of cosmogenically induced radioactivity the detectors will be required to 'cool down' for 6 months underground before they are placed into the SNO vessel. During this period the detectors will be tested, not only

	Geometry	Signal	1D Fit	2D Fit	3D Fit
Isotropic Signal		2730	2728.7 ± 72.5	2734.4 ± 72.6	2726.9 ± 64.2
AV Background	G_1	125	126.9 ± 51.6	124.8 ± 51.6	125.0 ± 39.0
Correlation			0.677	0.677	0.558
Isotropic Signal		2730	2731.9 ± 77.0	2729.9 ± 77.0	2730.4 ± 65.1
AV Background	G_2	125	123.9 ± 57.6	124.2 ± 57.6	124.3 ± 40.3
Correlation			0.720	0.721	0.573
Isotropic Signal		2730	2735.0 ± 85.4	2730.7 ± 85.4	2730.4 ± 66.3
AV Background	G_3	125	120.7 ± 68.4	124.1 ± 68.5	123.7 ± 42.2
Correlation			0.780	0.781	0.593
Isotropic Signal		2730	2730.5 ± 84.0	$2731.3.3 \pm 83.9$	2728.4 ± 65.6
AV Background	G_4	125	123.1 ± 66.7	122.6 ± 66.6	125.9 ± 41.3
Correlation			0.772	0.772	0.583
Isotropic Signal		2730	2728.8 ± 83.5	2727.3 ± 83.4	2732.9 ± 65.6
AV Background	G_5	125	126.9 ± 66.1	127.3 ± 66.1	123.5 ± 41.1
Correlation			0.769	0.768	0.581
Isotropic Signal		2730	2728.5 ± 87.4	2731.4 ± 87.0	2729.9 ± 65.2
AV Background	G_6	125	127.4 ± 71.0	124.0 ± 70.3	123.4 ± 40.5
Correlation			0.792	0.791	0.575

Table 6.3: The results from 1000 simulations of 2730 isotropic and 125 acrylic vessel neutrons in each of the different detector geometries.

Fit Results	Signal	1D Fit	2D Fit	3D Fit
Isotropic Signal	2730	2732.2 ± 72.2	2727.2 ± 71.0	2731.7 ± 65.3
AV Background	125	126.7 ± 52.7	128.1 ± 50.2	124.9 ± 38.8
Error	1.91%	2.64%	2.60%	2.39%
Isotropic Signal	2730	2731.0 ± 74.9	2729.1 ± 74.9	2729.4 ± 65.0
AV Background	250	248.2 ± 55.9	250.6 ± 56.0	249.8 ± 41.8
Error	1.91%	2.74%	2.74%	2.38%
Isotropic Signal	2730	2727.0 ± 78.8	2728.4 ± 78.8	2728.9 ± 66.4
AV Background	500	501.7 ± 63.1	501.1 ± 63.1	499.6 ± 46.7
Error	1.91%	2.89%	2.89%	2.43%
Isotropic Signal	2730	2726.0 ± 85.5	2730.2 ± 85.5	2734.5 ± 68.6
AV Background	1000	1001.2 ± 74.8	999.4 ± 74.7	1002.8 ± 54.1
Error	1.91%	3.13%	3.13%	2.51%

Table 6.4: The results from 1000 simulations of 2730 isotropic and differing levels of acrylic vessel neutrons in geometry G_0. The error is the percentage error of the calculated value of the isotropic signal and should be compared to the statistical limit of 1.91%.

to ensure that they survived the transportation to Sudbury but also to obtain limits on their levels of activity. This will currently involve the use of a small DAQ system separate from the main SNO electronics. Analysis of the resulting digitized data will reveal if any of the detector segments are radioactively "hot". It must again be noted that the method of self analysis only probes the first 50 μm of the detector material (the 50 μm corresponds to the range of a 9 MeV α particle in the nickel). However, as everything is radioassayed the tubes are not expected to be the source of hot spot contamination. One possible exception is the end caps which can not be assayed in this manner but again all components of the endcaps will be counted prior to assembly. Although there is a proposal to test some of the detectors in a whole body counter it will not be possible to test them all. Hence, there remains the possibility of a hot endcap which could act as a source of background neutrons. In addition, the same is true for the panels of the acrylic vessel. The individual panels are not assayed before being bonded to form the acrylic vessel. Again, there is a possibility for a hot panel.

This problem is approached from three angles. Firstly, what is the effect of a hot spot on the ability to extract the neutral current signal when only isotropic and acrylic vessel distributions are used in the fit? Secondly, is there some method to determine if a hot spot is present in the distribution? Thirdly, can the effects of the hot spot be removed during analysis and the true neutral current signal recovered?

6.3.1 The Effects of Hot Spots on Signal Extraction

To analyse the problem of hot spots, distributions were created using isotropic and acrylic vessel distributions along with differing hot spot distributions. A fit was then performed using only the first two cylindrically symmetric distributions. The results from these fits are shown in Table 6.5. The equatorial II (EQII) hot spot is a gamma emitter on the surface of the acrylic vessel, lying in the equatorial plane at 45° to the x-y axis of the NCDs. This point was chosen as it is the furthest point away from any detector in Geometry G_3. The table is shown for the geometries G_0 and G_3 to determine the effect of removing the outer ring. The four rows of the table represent the following:

1. The original distribution using only neutrons from the isotropic and AV distributions.
2. As above but with 50 neutrons included from the EQII hot spot.
3. As above but as the location of the hot spot is known *apriori* the detectors which are most sensitive to it have been excluded from the fit.
4. Finally, to determine the effect of removing a number of detectors from the fitting procedure another distribution was created using only the isotropic and AV distributions but excluding the same detectors as in row 3.

As can be seen from Table 6.5 the fitter has problems when the hot spot distribution of 50 neutrons was introduced. The effect is to approximately double the acrylic vessel contributions whilst decreasing the isotropic signal by 1σ. The 1D and 2D fitting codes are most affected as they compensate for the excess of events in the outer ring by increasing the acrylic vessel contribution and correspondingly reducing the isotropic signal. The 3D fitter is somewhat more robust having more information on the distribution of events but still overestimates the acrylic vessel contribution. An attempt was then made to exclude from the fit those detectors which were most seriously affected by the hot spot. Excluding these detectors removed 80% of the contamination and the fit was repeated. The results are more consistent with those obtained using only the expected isotropic distributions but the errors have increased consistent with reducing the number of detectors whilst still retaining of the order of 10 events from the hot spot. The increase is most radical for the 1D distribution where 2 detector rings must be excluded from the fitting procedure corresponding to the greatest removal of information. For comparison, data sets were generated using only isotropic and acrylic vessel distributions and the same detectors were excluded from the fits. The results of these fits compared favourably with the original fits using all the detectors but created with only the isotropic and AV distributions. Again there is an increase in the errors corresponding to a reduction in the available information. Given *apriori* knowledge of the location and effect of a hot spot, these results are not surprising. It is easy to remove a known hot spot and obtain the correct answer. It is more difficult to remove the effects of hot spots without *apriori* knowledge of their strengths and locations.

This exercise has shown how a hot spot containing less than 2% of the signal can significantly hijack the fit and the care that must be taken when analysing real data to first check for hot spots before attempting a fit.

6.3.2 Identification of Unknown Hot Spots

The identification of unknown hot spots is based not upon differences between the distribution of captured neutrons and those expected from Monte Carlo simulations but relies instead upon the radial symmetry of the expected isotropic and AV distributions. Obviously, this simple analysis does not hold true when the expected isotropic and AV distributions are asymmetric and as such no analysis can be performed on data from geometry G_6. In this scenario it would be necessary to rely on Monte Carlo simulations for the underlying distributions. Therefore, when considering only symmetric detector distributions and assuming that the neutron captures come from **only** isotropic and acrylic vessel distributions then the number of counts in each detector in a ring are expected to be the same within statistics. In the absence of some great conspiracy, **all** hot spot distributions are azimuthally asymmetric. The identification of

Geometry G_0	Signal	1D Fit	2D Fit	3D Fit
Isotropic Signal	Symmetric	2732.2 ± 72.2	2727.2 ± 71.0	2731.7 ± 65.3
AV Background	Only	126.7 ± 52.7	128.1 ± 50.2	124.9 ± 38.8
Isotropic Signal	EQII	2656.9 ± 73.6	2659.4 ± 73.6	2723.4 ± 64.4
AV Background	Hot Spot	247.1 ± 54.9	246.1 ± 54.8	180.2 ± 40.1
Isotropic Signal	80% of Hot	2729.9 ± 86.7	2735.8 ± 73.8	2738.4 ± 64.4
AV Background	Spot Removed	135.8 ± 83.4	129.8 ± 54.3	134.5 ± 39.6
Isotropic Signal	80% Equiv.	2730.4 ± 86.4	2729.8 ± 73.5	$2729.0.5 \pm 64.3$
AV Background	Removed	125.0 ± 82.7	123.2 ± 53.9	124.6 ± 39.4

Geometry G_3	Signal	1D Fit	2D Fit	3D Fit
Isotropic Signal	Symmetric	2735.0 ± 85.4	2730.7 ± 85.4	2730.4 ± 66.3
AV Background	Only	120.7 ± 68.4	124.1 ± 68.5	123.7 ± 42.2
Isotropic Signal	EQII	2698.7 ± 87.6	2702.3 ± 87.5	2768.8 ± 67.0
AV Background	Hot Spot	209.5 ± 72.0	204.5 ± 71.9	133.7 ± 43.1
Isotropic Signal	80% of Hot	2736.3 ± 89.8	2735.7 ± 86.4	$2742.3.5 \pm 66.8$
AV Background	Spot Removed	121.6 ± 81.2	125.8 ± 71.0	132.9 ± 42.7
Isotropic Signal	80% Equiv.	2737.5 ± 89.7	2732.7 ± 86.4	2731.0 ± 66.6
AV Background	Removed	120.9 ± 81.1	124.6 ± 71.0	125.3 ± 42.4

Table 6.5: The results from introducing a hot spot of 50 events and attempting to fit using only the isotropic and AV distributions and the effects of removing detectors with excess counts. The first rows use events from only the isotropic and AV distributions. The second set and 50 events from the EQII hot spot. The third set removes detectors (or detector segments) which contain 80% or more of the events from the hot spot. For comparison, the fourth set shows the results from removing the same detectors from a distribution of only isotropic and acrylic vessel events.

hot spots then reduces to the search for detectors within each radial ring which are statistically inconsistent with the others. The advantage of this approach is that it removes any dependence on the Monte Carlo from hot spot searches.

For locating hot spots, the neutron capture distribution is separated into radial rings (with the option of further separation along the z axis if position information is available). For each of the 14 rings, a mean must be calculated but in a manner such that if one or more of the detectors contains an excess of counts due to a hot spot then those detectors are to be excluded from the calculation. The methods employed to do this are Trimming and Winsorising.Trimming involves removing the highest and lowest values from a distribution and then calculating the geometric mean of the remaining points. Strictly, this is first order trimming, whilst n^{th} order trimming involves removing the n^{th} highest and n^{th} lowest values from the distribution. Winsorising involves replacing the highest and lowest values from a distribution by the second highest and second lowest values and then calculating the geometric mean from the new distribution. Again this is first order Winsorising, whilst n^{th} order Winsorising involves replacing the n^{th} highest and n^{th} lowest values with the $(n+1)^{th}$ highest and $(n+1)^{th}$ lowest value. Examples of these are shown in Table 6.6.

The first table represents a data set drawn from a Poisson distribution of mean 16. Winsorising and Trimming have little effect on the geometric mean. The quoted error is derived from the rms deviation from the mean. The final probability is the probability that the largest value of the original distribution (in this case 19) comes from a distribution of the calculated mean. The second table shows the same data set but with one of the members replaced with the number 29 whose probability of occurring in a distribution of mean 16 is 0.002. The final column shows the probability of 29 occurring in a data set whose mean is the calculated geometric mean of the altered distribution. The third table shows again a data set taken from a Poisson distribution of mean 16, but now with only four points. With this particular data set Winsorising and Trimming have no effect on the geometric mean. The final table shows the effect that the anomalous value 29 has on a data set of only four points. With only four data points Winsorising and Trimming have a more drastic effect. The probability that the anomalous value could occur statistically is reduced by an order of magnitude in contrast to the case of 8 data points where the probability changes by a factor of 3.

For the case of neutral current detectors the number of detectors in each ring varies between four and sixteen. Identification of a hot spot is made by examining the number of counts in each detector and calculating the probability of such a number of events having come from a distribution whose mean is defined by one of the above geometric means. Any detector with a statistically unlikely number of counts above the calculated geometric mean should be considered as containing neutron events from a hot spot and excluded from the Maximum

	Distribution	Geometric Mean	Probability
Original	$\{19, 16, 19, 12, 15, 18, 14, 13\}$	15.750 ± 3.969	0.237
Sorted	$\{12, 13, 14, 15, 16, 18, 19, 19\}$	15.750 ± 3.969	0.237
Winsorized	$\{13, 13, 14, 15, 16, 18, 19, 19\}$	15.875 ± 3.984	0.247
Trimmed	$\{13, 14, 15, 16, 18, 19\}$	15.833 ± 3.979	0.244
2^{nd} Order Winsorized	$\{14, 14, 14, 15, 16, 18, 18, 18\}$	15.875 ± 3.984	0.247
2^{nd} Order Trimmed	$\{14, 15, 16, 18\}$	15.750 ± 3.969	0.237

	Distribution	Geometric Mean	Probability
Original	$\{19, 16, \mathbf{29}, 12, 15, 18, 14, 13\}$	17.000 ± 4.123	0.0050
Sorted	$\{12, 13, 14, 15, 16, 18, 19, 29\}$	17.000 ± 4.123	0.0050
Winsorized	$\{13, 13, 14, 15, 16, 18, 19, 19\}$	15.875 ± 3.984	0.0020
Trimmed	$\{13, 14, 15, 16, 18, 19\}$	15.833 ± 3.979	0.0019
2^{nd} Order Winsorized	$\{14, 14, 14, 15, 16, 18, 18, 18\}$	15.875 ± 3.984	0.0020
2^{nd} Order Trimmed	$\{14, 15, 16, 18\}$	15.750 ± 3.969	0.0017

	Distribution	Geometric Mean	Probability
Original	$\{18, 16, 13, 15\}$	15.500 ± 3.937	0.295
Sorted	$\{13, 15, 16, 18\}$	15.500 ± 3.937	0.295
Winsorized	$\{15, 15, 16, 16\}$	15.500 ± 3.937	0.295
Trimmed	$\{15, 16\}$	15.500 ± 3.937	0.295

	Distribution	Geometric Mean	Probability
Original	$\{18, 16, \mathbf{29}, 15\}$	19.500 ± 4.415	0.0261
Sorted	$\{15, 16, 18, 29\}$	19.500 ± 4.415	0.0261
Winsorized	$\{16, 16, 18, 18\}$	17.000 ± 4.123	0.0027
Trimmed	$\{16, 18\}$	17.000 ± 4.123	0.0027

Table 6.6: Examples of Trimming and Winsorising and their effects on the mean of a distribution and. The data sets are alternately from a regular Poisson distribution of mean 16 and the same distribution but with one value replaced with the statistically unlikely number 29. The final column in each table shows the probability of the highest number in the original distribution occurring given the calculated geometric mean.

Likelihood fit. Work in the previous section has shown that the exclusion of detectors which contain hot spot events has little effect on the estimate of the true isotropic signal.

It should be noted at this stage that Winsorising and Trimming are a first approximation at determining the presence of hot spots. Further information could be obtained if the data were analysed as localized groups of detectors.

6.3.3 Analysis of Simulated Data

As an example of this technique a data set consisting of 2500 isotropic, 125 AV and 50 EQII events was created using geometry G_3. The data set was created by randomly selecting neutron capture events from the original Monte Carlo data sets which contained 40,282, 38,899 and 1,170 events respectively. The simulated data set consisted of 2675 events recorded as neutron captures at (x,y,z). Table 6.7 shows these data sorted into radial rings along with the contribution to each detector from the EQII hot spot. The hot spot can be clearly seen in the first counter in ring 11. The probability of observing 46 counts if the expected value is 21.5 counts is less than 3×10^{-6}. It should be noted, that in ring 8 the probability of observing only 6 events from a distribution with an expected value of 26 is similarly less than 3×10^{-6}. Also, in ring 10 the probability of observing 36 events is only 8×10^{-5}. Table 6.8 shows the results of fits to this data set. It should be noted, as demonstrated previously, that as a result of the weaker correlation between isotropic and AV with the 3D distributions the separation is less effected by the hot spot. As a test of the Monte Carlo another data set was generated using the same technique in which the anomalies not due to the hot spot disappeared. These data are shown on a ring by ring basis in Table 6.9. Table 6.10 calculates the several means for that particular distribution.

1. Contains the mean expected if the distribution consisted of only 2500 isotropic and 125 AV events.

2. This is the mean of the data shown in Table 6.9.

3. Represent the mean of the data set if the hot spot was not present.

4. Contains the 1^{st} order Winsorised mean of the data from Table 6.9.

This table is used to demonstrate both the effect of the hot spot and the Winsorising technique in removing it. Table 6.11 then shows the probability of the number of events registered in each detector having come from a Poisson distribution whose mean is given by the 1^{st} order Winsorised mean of Table 6.10. The hot spot is easily visible with a probability of 1.6×10^{-6}. Finally Table 6.12 shows the results of the Maximum Likelihood fits. It should be noted that there are two rows which state that the hot spot detectors have been removed. The first row

Ring	Counts Per Detector	Counts from Hot Spot
1	37 39 46 47	0 0 0 0
2	41 48 38 42 37 33 44 50	0 1 0 0 0 0 0 0
3	26 40 32 32	0 0 0 0
4	35 37 26 45 50 40 31 44	0 0 0 0 0 0 0 0
5	43 37 29 29 37 30 31 31	0 0 0 0 0 0 0 0
6	27 32 38 35 32 33 40 39 51 18 38 25	0 1 0 0 0 0 0 0 0 0 0 0
7	26 31 20 23 29 22 33 28	1 1 0 0 0 0 0 0
8	29 32 31 23 21 22 **6** 30	2 3 0 0 0 0 0 0
9	25 17 24 27 22 20 26 19	0 0 0 0 0 0 0 0
10	18 16 13 21 22 16 **36** 12	0 0 0 0 0 0 0 0
11	**46** 19 10 24	31 0 0 0
12	22 17 18 17 12 11 16 21	7 3 0 0 0 0 0 0
13	11 13 7 10 9 12 14 11	0 0 0 0 0 0 0 0

Table 6.7: Simulated data from geometry G_3 using 2500 isotropic, 125 AV and 50 EQII hot spot events. The last column shows the contribution from the EQII hot spot to each detector.

Data Set	Distribution	2D	3D
2500 Iso 125 AV	Isotropic	2437.0 ± 81.5	2480.1 ± 63.2
	Acrylic Vessel	188.0 ± 66.3	144.9 ± 40.7
2500 Iso 125 AV	Isotropic	2399.9 ± 83.6	2516.5 ± 63.9
50 EQII	Acrylic Vessel	275.1 ± 69.8	158.5 ± 41.6
2500 Iso 125 AV	Isotropic	2415.9 ± 82.3	2495.1 ± 63.8
50 EQII Removed	Acrylic Vessel	220.9 ± 67.9	157.7 ± 41.3

Table 6.8: The results of fits to the simulated data from geometry G_3 using 2500 isotropic, 125 AV and 50 EQII hot spot events. A fit has also been performed using the same data but without the contribution of the hot spot. The final fit remove the offending parts of the detector.

represents the same three detectors (2D) or six detector segments (3D) which were removed in Section 6.3.1 *i.e.* the assumption is made that the excess of counts is the result of an EQII hot spot and the appropriately contaminated detectors are removed. The second row removes only the detector or detector segments which were identified by the hot spot analysis. This makes no assumption as to the cause of the hot spot but only that an unstatistical excess of counts exists in that particular detector or segments.

So far only hot spots on the acrylic vessel have been considered. It is possible for hot spots to exist on the neutral current detectors themselves. The separation of these is simplified as the majority (more than 87%) of the neutrons captured are captured by the offending detector. The only concern that then remains involves the 'dead' detectors which are unable

Ring	Counts Per Detector	Counts from Hot Spot
1	43 40 49 44	0 0 0 0
2	41 36 41 43 51 46 45 42	0 0 0 0 0 0 0 0
3	42 34 55 37	0 0 0 0
4	27 43 40 29 33 31 36 24	0 0 0 0 0 0 0 0
5	42 37 31 36 37 23 26 31	1 0 0 0 0 0 0 0
6	28 37 36 33 28 27 27 37 33 40 18 31	0 1 0 0 0 0 0 0 0 0 0 0
7	20 33 24 32 24 30 31 24	0 2 0 0 0 0 0 0
8	30 32 30 35 22 16 23 22	2 5 0 0 0 0 0 0
9	23 24 37 24 21 21 22 26	0 0 0 0 0 0 0 0
10	22 22 20 25 19 21 14 17	0 0 0 0 0 0 0 0
11	**49** 20 18 26	32 0 0 0
12	14 18 10 13 15 17 13 9	2 5 0 0 0 0 0 0
13	10 5 12 12 17 4 10 7	0 0 0 0 0 0 0 0

Table 6.9: A second set of simulated data from geometry G_3 using 2500 isotropic, 125 AV and 50 EQII hot spot events. Again, the last column shows the contribution from the EQII hot spot to each detector.

Ring Number	Expected Mean Assuming 2500/125	Mean of Data	Mean of Data With HS Removed	Winsorized Mean 1st Order
1	42.047	44.000	44.000	43.500
2	40.300	43.125	43.125	43.000
3	37.017	42.000	42.000	39.500
4	36.426	32.875	32.875	32.667
5	35.865	32.875	32.750	33.000
6	31.397	31.250	31.167	31.700
7	28.553	27.250	27.000	27.500
8	24.280	26.250	25.375	26.500
9	23.360	24.750	24.750	23.333
10	18.994	20.000	20.000	20.167
11	18.960	28.250	20.250	23.000
12	14.938	13.625	12.750	13.667
13	9.302	9.625	9.625	9.333

Table 6.10: A second set of simulated data from geometry G_3 using 2500 isotropic, 125 AV and 50 EQII hot spot events. Again, the last column shows the contribution from the EQII hot spot to each detector.

Ring	Counts Per Detector	Probability Calculated From Winsorized Mean
1	43 40 49 44	0.510 0.332 0.221 0.490
2	41 36 41 43 51 46 45 42	0.390 0.143 0.390 0.510 0.145 0.372 0.430 0.450
3	42 34 55 37	0.366 0.216 0.011 0.384
4	27 43 40 29 33 31 36 24	0.184 0.047 0.118 0.297 0.500 0.430 0.302 0.071
5	42 37 31 36 37 23 26 31	0.074 0.265 0.408 0.323 0.265 0.043 0.127 0.408
6	28 37 36 33 28 27 27 37	0.290 0.195 0.245 0.432 0.292 0.232 0.232 0.195
-	33 40 18 31	0.432 0.087 0.006 0.498
7	20 33 24 32 24 30 31 24	0.086 0.169 0.291 0.219 0.291 0.341 0.276 0.291
8	30 32 30 35 22 16 23 22	0.273 0.165 0.273 0.065 0.222 0.020 0.287 0.222
9	23 24 37 24 21 21 22 26	0.528 0.472 0.005 0.472 0.363 0.363 0.444 0.317
10	22 22 20 25 19 21 14 17	0.370 0.370 0.544 0.166 0.456 0.456 0.099 0.285
11	**49** 20 18 26	1.6×10^{-6} 0.310 0.175 0.292
12	14 18 10 13 15 17 13 9	0.500 0.150 0.199 0.500 0.394 0.216 0.500 0.126
13	10 5 12 12 17 4 10 7	0.456 0.097 0.230 0.230 0.015 0.044 0.456 0.286

Table 6.11: The second set of simulated data from geometry G_3 using 2500 isotropic, 125 AV and 50 EQII hot spot events. The last column shows the probability of the number of counts appearing in each detector assuming that the expected number of counts is given by the 1^{st} order Winsorised mean.

Data Set	Distribution	2D	3D
2500 Iso 125 AV	Isotropic	2511.2 ± 81.7	2489.5 ± 63.2
	Acrylic Vessel	113.8 ± 65.4	135.5 ± 40.5
2500 Iso 125 AV 50 EQII	Isotropic	2480 ± 83.9	2530.8 ± 64.0
	Acrylic Vessel	195.0 ± 69.0	144.2 ± 41.4
2500 Iso 125 AV 50 EQII	Isotropic	2497.7 ± 82.3	2500.9 ± 63.8
HS Detectors Removed	Acrylic Vessel	134.1 ± 66.6	143.9 ± 41.0
2500 Iso 125 AV 50 EQII	Isotropic	2508.4 ± 82.5	2512.4 ± 63.7
HS Detector Removed	Acrylic Vessel	136.8 ± 67.1	141.0 ± 41.0

Table 6.12: The results of fits to the simulated data from geometry G_3 using a second set of 2500 isotropic, 125 AV and 50 EQII hot spot events.

Ring	Counts Per Detector	Counts from Hot Spot
1	52 38 46 46	0 0 0 0
2	51 42 45 38 53 36 37 47	0 0 0 0 0 0 0 0
3	57 37 34 44	1 0 0 0
4	49 42 38 37 31 43 37 49	0 0 0 0 0 0 0 0
5	31 36 53 41 26 51 47 38	1 1 0 0 0 0 0 0
6	29 48 39 38 36 30 50 39 37 43 35 39	0 16 2 0 0 0 0 0 0 0 0 0
7	32 29 27 29 32 41 38 24	5 2 0 0 0 0 0 0
8	**58 59** 27 30 29 26 35 27	24 39 0 0 0 0 0 0
9	32 21 21 34 27 20 20 21	0 0 0 0 0 0 0 0
10	21 22 23 21 22 22 29 27	1 1 0 0 0 0 0 0
11	– – – –	– – – –
12	19 18 13 13 17 11 17 17	1 6 0 0 0 0 0 0
13	7 7 13 13 11 12 14 12	0 0 0 0 0 0 0 0

Table 6.13: A third set of simulated data from geometry G_4 using 2730 isotropic, 125 AV and 100 HSII hot spot events. Again, the last column shows the contribution from the HSII hot spot to each detector. HSII corresponds to a hot spot at location (3.5, 3.52, -3.00) *i.e.* a hot spot at the end of one of the 'dead' detectors in Ring 11.

Ring Number	Expected Mean Assuming 2730/125	Mean of Data	Mean of Data With HS Removed	Winsorized Mean 1^{st} Order
1	46.532	45.500	45.500	46.000
2	44.978	43.625	43.625	43.333
3	41.464	43.000	42.750	40.500
4	41.355	40.750	40.750	41.000
5	40.394	40.375	40.125	40.667
6	35.065	38.583	37.083	38.400
7	31.605	31.500	30.625	31.167
8	28.267	36.375	28.500	34.300
9	25.448	24.500	24.500	24.000
10	21.056	23.375	23.125	22.833
11	0.000	0.000	0.000	0.000
12	16.939	15.625	14.750	15.833
13	10.237	11.125	11.125	11.333

Table 6.14: A third set of simulated data from geometry G_4 using 2730 isotropic, 125 AV and 100 HSII hot spot events.

Ring	Counts Per Detector	Probability Calculated From Winsorized Mean
1	52 38 46 46	0.206 0.133 0.539 0.539
2	51 42 45 38 53 36 37 47	0.139 0.460 0.363 0.235 0.065 0.149 0.189 0.258
3	57 37 34 44	0.008 0.326 0.173 0.311
4	49 42 38 37 31 43 37 49	0.122 0.459 0.356 0.299 0.064 0.398 0.299 0.122
5	31 36 53 41 26 51 47 38	0.071 0.262 0.036 0.500 0.009 0.065 0.179 0.376
6	29 48 39 38 36 30 50 39	0.071 0.075 0.483 0.517 0.389 0.098 0.041 0.483
-	37 43 35 39	0.453 0.249 0.328 0.483
7	32 29 27 29 32 41 38 24	0.464 0.393 0.261 0.393 0.464 0.052 0.098 0.113
8	**58 59** 27 30 29 26 35 27	1.4×10^{-4} 8.0×10^{-5} 0.120 0.264 0.209 0.087 0.475 0.120
9	32 21 21 34 27 20 20 21	0.068 0.314 0.314 0.031 0.296 0.243 0.243 0.314
10	21 22 23 21 22 22 29 27	0.403 0.486 0.513 0.403 0.486 0.486 0.120 0.217
11	– – – –	– – – –
12	19 18 13 13 17 11 17 17	0.244 0.325 0.288 0.288 0.418 0.135 0.418 0.418
13	7 7 13 13 11 12 14 12	0.123 0.123 0.348 0.348 0.540 0.460 0.250 0.460

Table 6.15: The third set of simulated data from geometry G_4 using 2730 isotropic, 125 AV and 100 HSII hot spot events. The last column shows the probability of the number of counts appearing in each detector assuming that the expected number of counts is given by the 1^{st} order Winsorised mean.

to capture the neutrons that they produce. For that reason worst case scenarios were simulated for geometry G_4. Two hot spots were simulated on one of the dead detectors at $z = 0$ and $z = 3.00$. Of the neutrons produced by photo-disintegration 18.2% and 7.5% were captured on the surrounding detectors.

Again, Tables 6.13 through 6.15 show the data, means and probabilities as before. The hot spot is discernible at the level of 10^{-4} with 100 neutrons captured from the HSII at (3.5, 3.52, 3.00). It should again be noted that the simple method of ring by ring analysis is not the best method for detecting this type of hot spot. If for example the data had been analysed using pairs of detectors, then the probability of 117 events occurring in the two detectors when the expected value is only 68.6 is $\sim 2 \times 10^{-8}$. This is more noticeable for the HSIII (3.5, 3.52, 0.00) hot spot where a detector-by-detector analysis based on the expected value per ring is unsuccessful at detecting the hot spot at the level of 100 neutrons captured per year, as the 100 counts are distributed about the eight nearest neighbours. However, a more elaborate search algorithm is able to detect this particular hot spot. By summing the eight nearest neighbours surrounding the 'dead' detectors, the four values obtained can be used to identify the hot spot. A data set consisting of 2730 isotropic, 125 acrylic vessel and 100 HSIII events was created. The sums of the nearest neighbours were $\{199, 119, 131, 122\}$ which when Winsorized gave a mean of 126.5. Each of the sums corresponds to $\{6.4, 0.7, 0.4, 0.4\}\sigma$ away from this mean value. For the value of 199 this corresponded to a probability of the order of

Distribution	2D	3D
Isotropic	2121.8 ± 72.6	2078.3 ± 58.0
Acrylic Vessel	15.2 ± 56.3	58.7 ± 36.6

Table 6.16: The results from performing a fit on one year's worth of simulated data with an unknown hot spot distribution using only the isotropic and acrylic vessel distributions.

	Counts	Mean	Winsorised	Trimmed
Ring 1	42 24 47 38	37.750	40.000	40.000
Ring 2	36 34 35 22 32 33 27 29	31.000	31.500	31.667
Ring 3	33 32 20 25	27.5	28.500	28.500
Ring 4	39 39 29 37 28 26 29 42	33.625	33.500	33.500
Ring 5	33 89 19 36 33 26 18 27	35.125	28.625	29.000
Ring 6	25 24 24 24 27 22 17 28 27 18 23 16	22.917	22.917	23.100
Ring 7	24 23 21 16 31 25 16 25	22.625	21.875	22.333
Ring 8	22 14 26 15 25 13 19 21	19.375	19.375	19.333
Ring 9	18 11 13 22 18 17 16 19	16.750	16.625	16.833
Ring 10	15 19 12 17 19 12 21 11	15.750	15.625	15.667
Ring 11	15 18 13 19	16.25	16.500	16.500
Ring 12	8 11 15 12 13 12 5 10	10.75	10.875	11.000
Ring 13	6 10 5 7 7 7 9 5	7.000	6.875	6.833

Table 6.17: Simulated data from one year of running including an unknown number of unknown strength hot spots. The table for each ring shows the number of counts in each ring along with the mean, Winsorised Mean and Trimmed Mean.

10^{-9}. In fact, given that hot spots on 'dead detectors' are the only possible scenario where a hot spot would be difficult to detect, a detailed analysis of the data from the surrounding detectors would certainly be required as part of a general NCD analysis.

Using this simple technique a hot spot which contributes only 2% of the neutrons expected from the SSM is separable at the 10^{-6} level. To test the robustness of the algorithms used in extracting hot spots and separating the isotropic and AV distributions, a data set was created for one year's worth of data along with an unknown number of hot spots of unknown strength. The data are shown in Figure 6.9. Initially a coarse fit using the 2D and 3D distributions was applied to the data assuming that only neutrons from isotropic and AV sources were present. It should be noted that a 1D distribution fit was also performed and that the results were exactly the same as those obtained from the 2D distribution fit as was expected. The results of the fits are shown in Table 6.16.

The data clearly show an excess of counts in one detector caused by hot spot activity. The data have been reorganized into independent rings to establish the presence of hot spots

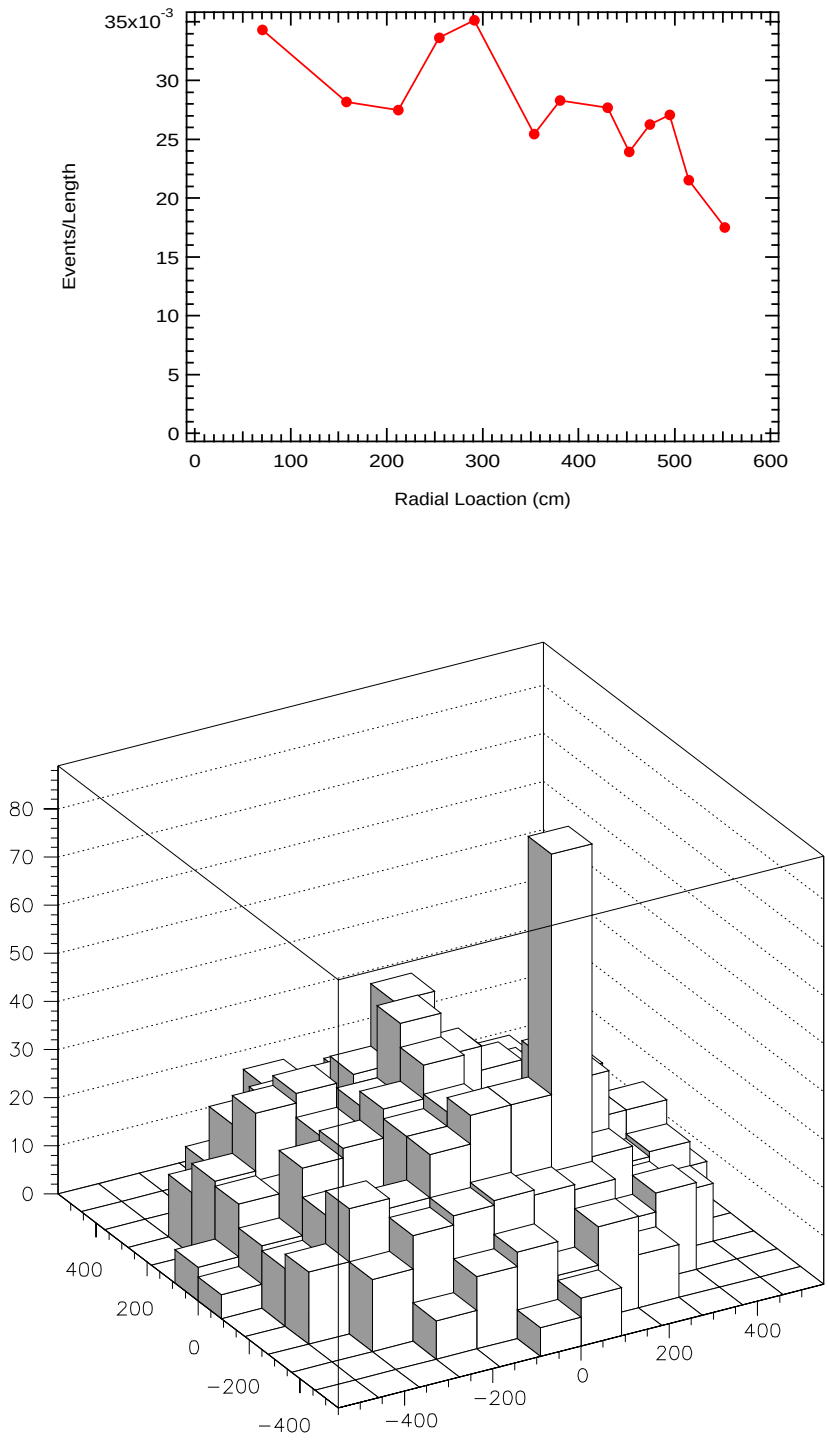

Figure 6.9: Simulated data from one year of running including an unknown number of unknown strength hot spots. The top graph shows the data sorted into radial rings whilst the lower graph is the same data display as an (x,y) grid.

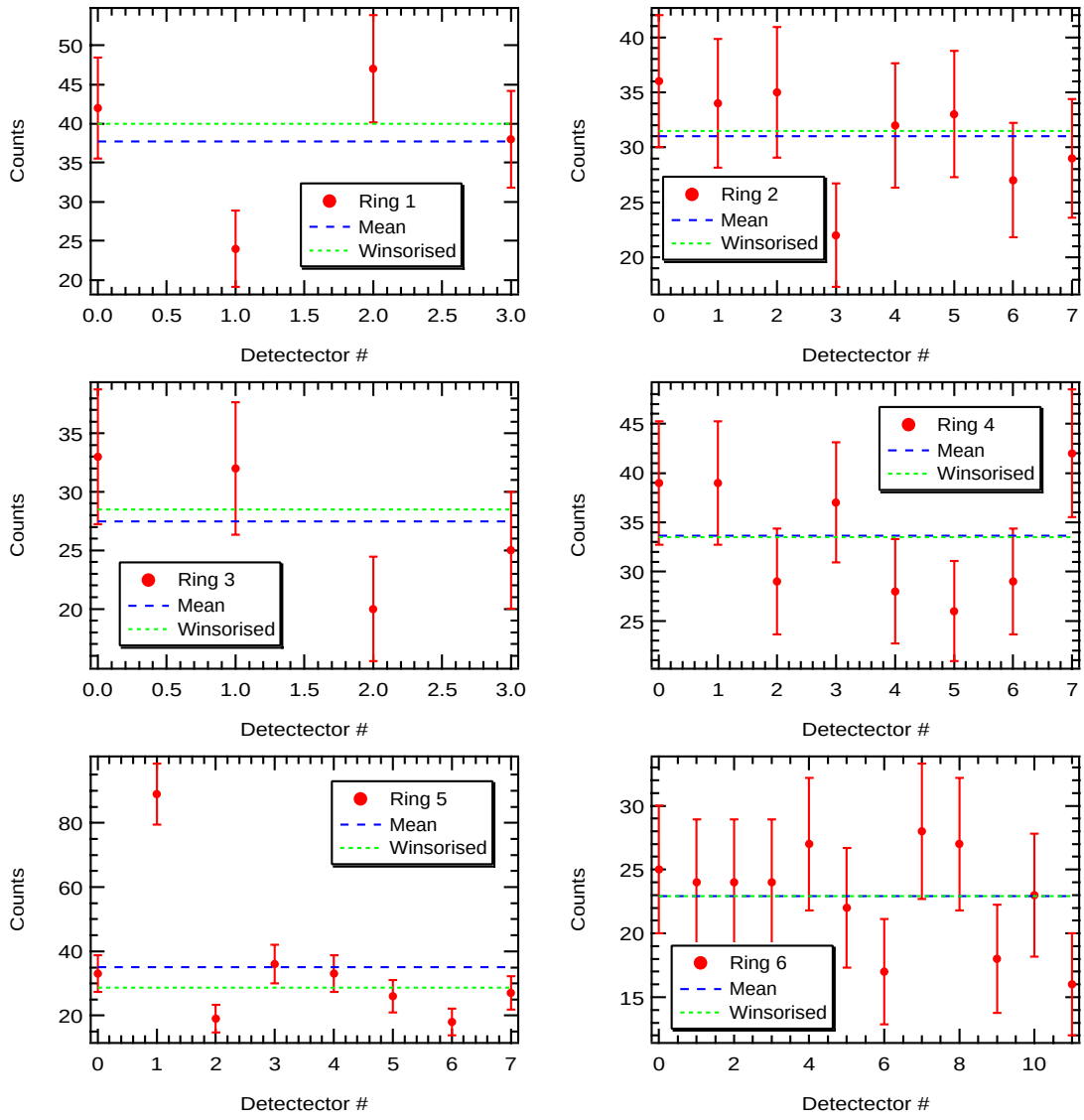

Figure 6.10: Simulated data from one year of running including an unknown number of unknown strength hot spots. The data has been sorted into independent radial rings and are shown along with both the mean and the 1st order Winsorised mean. The error bars are shown as the square root of the number of counts and should be used as an aid to viewing.

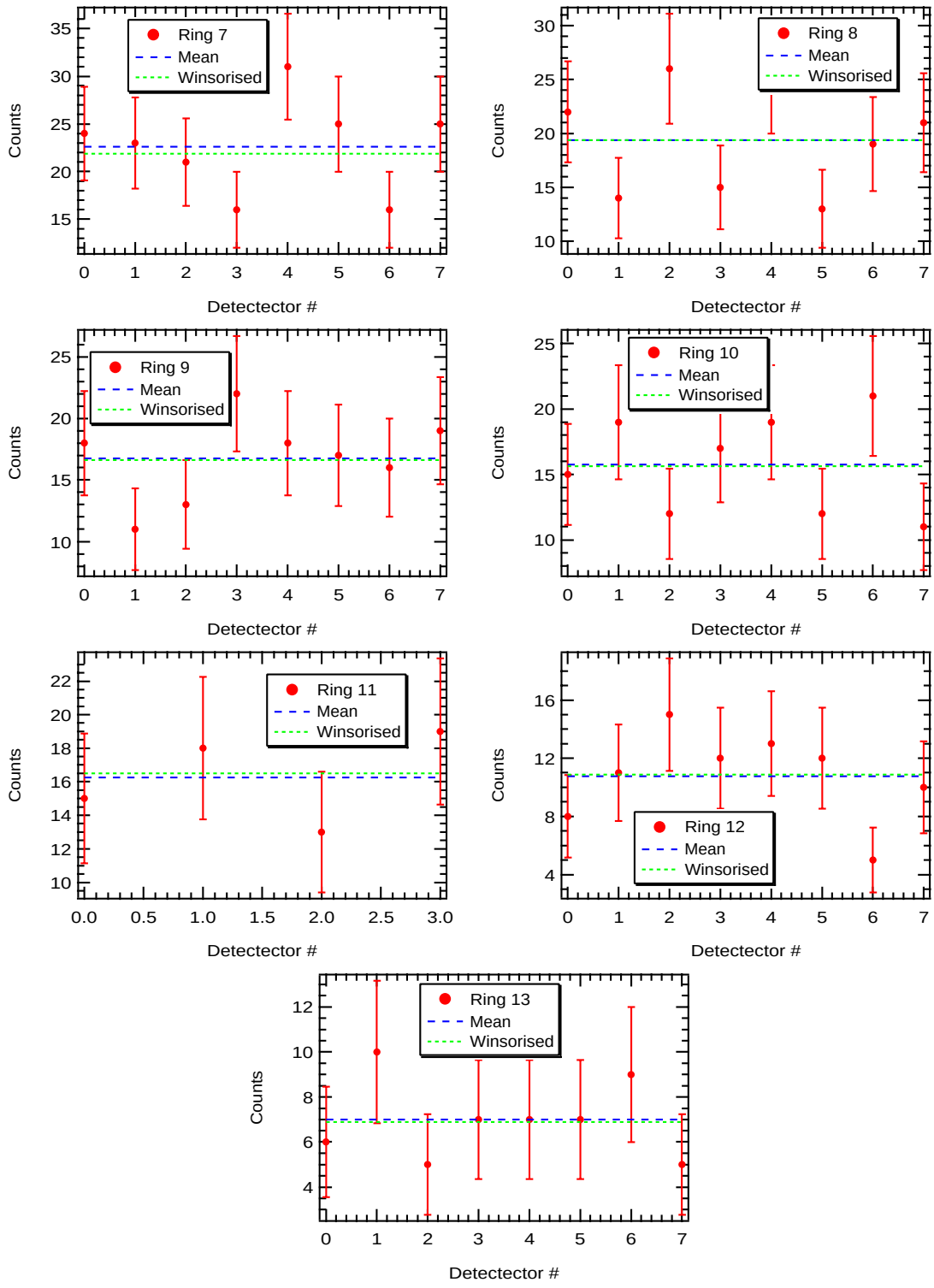

Figure 6.11: Simulated data from one year of running including an unknown number of unknown strength hot spots. The data has been sorted into independent radial rings and are shown along with both the mean and the 1st order Winsorised mean. The error bars are shown as the square root of the number of counts and should be used as an aid to viewing.

Ring 1	0.376 0.006 0.134 0.376
Ring 2	0.233 0.351 0.289 0.031 0.488 0.418 0.188 0.304
Ring 3	0.223 0.280 0.004 0.231
Ring 4	0.192 0.192 0.196 0.295 0.149 0.079 0.196 0.087
Ring 5	0.230 3×10^{-16} 0.023 0.102 0.230 0.287 0.014 0.355
Ring 6	0.359 0.438 0.438 0.438 0.222 0.396 0.085 0.168 0.222 0.126 0.479 0.054
Ring 7	0.352 0.433 0.397 0.081 0.038 0.279 0.081 0.279
Ring 8	0.304 0.085 0.086 0.131 0.124 0.052 0.436 0.386
Ring 9	0.400 0.058 0.155 0.118 0.400 0.496 0.406 0.311
Ring 10	0.403 0.227 0.147 0.397 0.227 0.147 0.112 0.091
Ring 11	0.323 0.388 0.162 0.300
Ring 12	0.151 0.475 0.137 0.406 0.298 0.406 0.016 0.354
Ring 13	0.317 0.157 0.185 0.468 0.468 0.468 0.255 0.185

Table 6.18: Simulated data from one year of running including an unknown number of unknown strength hot spots. The table for each ring shows the probability associated with each detector based on the first order Winsorised mean.

and are shown in Table 6.17 and Figure 6.10 whilst the probabilities for the number of events per detector based on the 1^{st} order Winsorised mean are shown in Table 6.18. Marked on each graph is the fitted value for that ring, the mean of all the values and the Winsorised and trimmed means. It must be noted that there is significant deviation from a Poisson distribution in ring 5. This point corresponds to a hot spot on the detector at grid location (-2.5,1.5). Further analysis of this detector is shown in Figure 6.12 and shows that the hot spot is located at $z = 3$, where $z = 0$ represents the centre of the vessel.

The effect of this hot spot is to disrupt the ability to accurately extract the radially symmetric distributions. The results of the fit after removing the hot spot are shown in Table 6.19. The number of detectors removed from the fit was varied to ascertain the effect of possibly small amounts of additional contamination. The hot spot was expected to have contributed 60.375 ± 5.350 events from analysis of the residual data.

The true distribution consisted of the following number of neutrons transported (produced but not necessarily captured). The final number captured was 2137 out of 10000 starts. The 10000 starts consisted of

- 7793 from isotropic events,
- 1426 from acrylic vessel events,
- 569 from a hot spot at (3.5, 3.5, 1.87),
- 56 from a hot spot at (-1.5, 5.5, -1.87), which corresponds to a hot spot on the AV, and

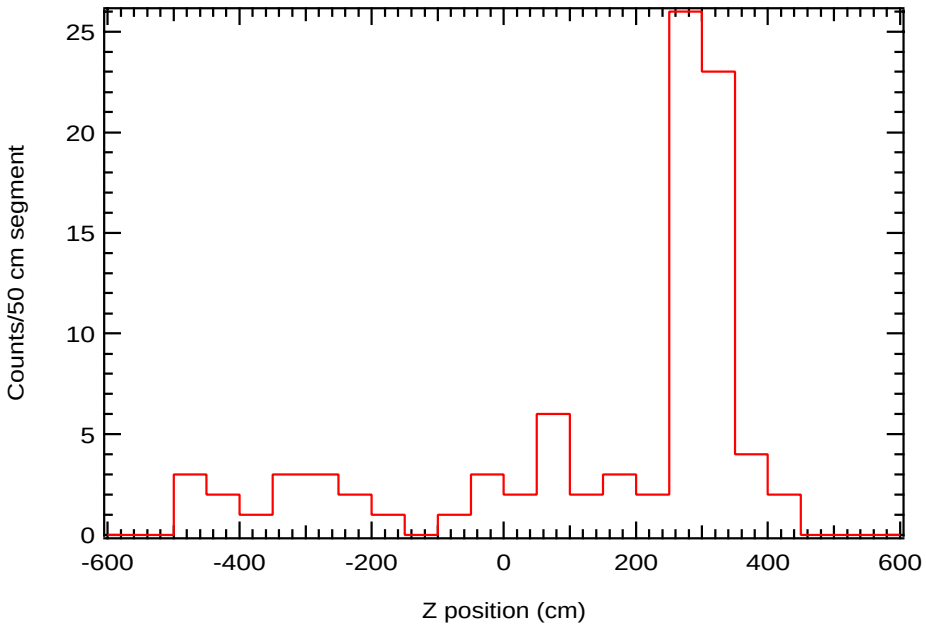

Figure 6.12: The hot spot detector at $(-2.5, 1.5)$ displayed as the number of counts per 50 cm segment.

Distribution	Cut Method	2D	3D
Isotropic	Detector Only	2032.6 ± 72.4	2013.5 ± 57.3
Acrylic Vessel		44.0 ± 56.5	74.5 ± 36.6
Isotropic	Detector and four	2010.9 ± 74.4	2002.4 ± 57.5
Acrylic Vessel	nearest neighbors	53.3 ± 57.2	78.0 ± 36.7
Isotropic	Detector and eight	2000.3 ± 76.3	2003.4 ± 57.9
Acrylic Vessel	nearest neighbors	59.5 ± 57.7	79.8 ± 36.8

Table 6.19: The results from performing a fit on one year's worth of simulated data using only the isotropic and acrylic vessel distributions but removing the effects of the hot spot. For the 3D distribution fits only the segments with $2 < z < 4$ were removed.

xy	-5.5	-4.5	-3.5	-2.5	-1.5	-0.5	0.5	1.5	2.5	3.5	4.5	5.5
-5.5						0.446	0.067					
-4.5				0.184	0.363	0.469	0.032	0.098	0.456			
-3.5			0.363	0.232	0.314	0.394	0.473	0.389	0.117	0.143		
-2.5		0.118	0.0646	0.473	0.170	0.055	0.055	–	0.473	0.181	0.347	
-1.5		0.318	0.442	0.031	0.220	0.252	0.366	0.274	0.091	0.089	0.201	
-0.5	0.384	0.110	0.256	0.475	0.306	0.082	0.047	0.026	0.094	0.363	0.169	0.301
0.5	0.301	0.469	0.063	0.450	0.476	0.021	0.209	0.408	0.303	0.200	0.436	0.301
1.5		0.098	0.038	0.170	0.034	0.191	0.312	0.237	0.373	0.247	0.318	
2.5		0.252	0.092	0.256	0.017	0.475	0.022	0.449	0.101	0.070	0.347	
3.5			0.427	0.469	0.089	0.445	0.037	0.247	0.302	0.098		
4.5				0.014	0.043	0.341	0.378	0.219	0.417			
5.5						0.116	0.384					

Table 6.20: The probability of the number of events in each detector. The expected value for each detector is calculated by from performing a fit on one year's worth of data after removing the hot spot.

- 156 events from a hot spot at (-2.5, 1.525, 3.0).

The algorithm is unable to locate the smaller hot spots as their number of counts is insufficient to make any increase statistically anomalous as can be seen in Table 6.20.

6.4 Identification of Dead Counters

The analysis carried out in previous sections has made no definitive statements on the best position for 'dead' counters. It has already been decided that the outer ring is to be removed leaving only Geometries G_3 through G_6. Geometry G_3 has no dead detectors and was the default option until it was decided that the only way to satisfy the scientific community and the collaboration that 50% of the neutron window was indeed background free was to operate detectors in SNO using SNO electronics but without ^{3}He. This leaves only Geometries G_4 through G_6 as the only possibilities that have so far been analysed.

It is possible to extract both the isotropic and AV distribution regardless of the position of the dead counters. However, it must be stated that if the positioning of detectors is asymmetric then the ability to perform hot spot searches by examining the radial distribution of counts within a ring would be lost. Hot spot searches would then have to be performed by comparison to the expected number of counts predicted by Monte Carlo clearly a more difficult and complex procedure.

The main advantages that the asymmetric option offers is that it does not leave any parts of the detector insensitive to neutrons. If central detectors were made dead it would significantly

reduce the ability to detect neutrons from the neutral current signal. Conversely, if detectors were removed from the outer edges of the vessel it would reduce the ability to separate AV and isotropic neutron signals as they are most dissimilar in this region. From Tables 6.3 and 6.1 it can be seen that there is no significant advantage to be gained from using G_6 from the point of both neutron capture and separation efficiencies. Given this information it would seem that of the possibilities so far considered either G_4 or G_5 will be the preferred NCD geometry.

Chapter 7

Conclusions

7.1 Final Conclusions

This thesis has focused on several aspects of the neutral current detectors intended for use in the Sudbury Neutrino Observatory. Chapter 3 has shown that by using simple analysis parameters derived from a digitized proportional counter pulse that ^{3}He(n,p)t events can be separated on an event by event basis from other sources of ionizing radiation at the 50% level. Chapters 4 and 5 focused on the WIPP experiment, used to determine the levels of U and Th present in the first prototype series of short CVD nickel detectors as well as to make general measurements made with stainless steel detectors and also to develop the pulse shape discrimination techniques. Finally, Chapter 6 focused on the final neutral current detectors and their possible geometries in the SNO detector with the emphasis on the ability to extract the isotropic signal from other backgrounds.

However, this thesis would not be complete without some mention of the ability to extract the final and most important signal, the number of neutral current events. The following arguments are taken from [40].

The total number of neutron captures, N_T, is composed of three components; N_I, the number of captures from isotropic sources, N_R, the number of captures from the radial dependent sources and N_A, the number of captures from non-symmetric sources. Isotropic sources are the neutral current signal, photodisintegrations caused by U and Th daughters dissolved in the heavy water and those resulting from uniform levels of U and Th in the NCDs. Radially symmetric sources are photodisintegrations caused by activity in the acrylic vessel, the detector cables and delay lines and the surrounding light water. Finally, the non-isotropic sources are hot spots either on the NCDs or the acrylic vessel. As seen in Chapter 6, N_I, N_R and N_A components are separable.

The isotropic signal must be further reduced to obtain the neutral current signal.

$$N_I = \epsilon(N_{\rm NC} + N_I^{\gamma,n} \equiv S + B \tag{7.1}$$

$$N_{\mathrm{NC}} = \frac{1}{\epsilon} N_I - N_I^{\gamma,n} \tag{7.2}$$

where ϵ represents the NCD detector array's efficiency for capturing neutrons and $N_I^{\gamma,n}$ is the total of events from sources of isotropic photodisintegration neutrons. The value of ϵ can be determined from both Monte Carlo and calibration information, whilst the levels of $N_I^{\gamma,n}$ must be deduced from *insitu* measurements. Accordingly, the error on the neutral current signal can be expressed in terms of the error if the other quantities mentioned in Equation 7.2

$$\sigma_{\mathrm{NC}}^2 = \left(\sigma_\epsilon^2 + \sigma_I^2\right) \cdot \left(1 + \frac{B}{S}\right)^2 + \left(\frac{B}{S}\right)^2 \cdot \left(\sigma_I^{\gamma,n}\right)^2 \tag{7.3}$$

where the σ's represent the relative error of each contribution. Hime [40] examines in detail the expected signals, both from neutral and charged currents, and their associated errors for the cases of the SSM, sterile neutrinos and both vacuum and MSW oscillations. Figure 7.1 gives the expected ranges of values for the ratios of neutral and charge current in comparison to the expected values from the SSM for these particular cases. It should be noted that this method of comparing the ratios is not able to distinguish adequately between MSW and vacuum oscillation solutions. Instead, these solutions can be separated by examination of the shape of the charge current spectrum.

7.2 Current State of the NCD Project

Much progress has been made in the production of the Neutral Current Detectors. At this time, a total of 115 m of detectors (out of a total of 770 m) are "cooling down" underground in special racks inside the clean room at SNO. Slight variations have been made to the construction methods to reduce further the possible source of contamination. In addition other design changes have taken place to alleviate problems with construction itself.

Individual tubes are cut in segments of 50, 100 and 200,*cm*. Each end is then flared to allow the eventual joining (welding) of the individual segments. It has been found that polonium is still highly volatile and as a result the simple etching procedures used in the initial counter construction were not adequate. The polonium, once dissolved from the surface of the detector would attempt to replate itself on the surface by displacing a nickel atom. As a result the new method of production use electropolishing in addition to acid etching to remove polonium from the surface, as well as aluminium deposits from the mandrel used in production. Following etching the tubes are rinsed and vacuum backed to remove any remaining acid and moisture.

Following construction and filling of the detectors (which involves a fast fill to alleviate problems associated with gas fractionization) each string must be tested to determine the quality of the fill and to ensure that there are no high voltage issues (such as breakdown). However, as has been shown earlier in this thesis , HV breakdown do not interfere with the

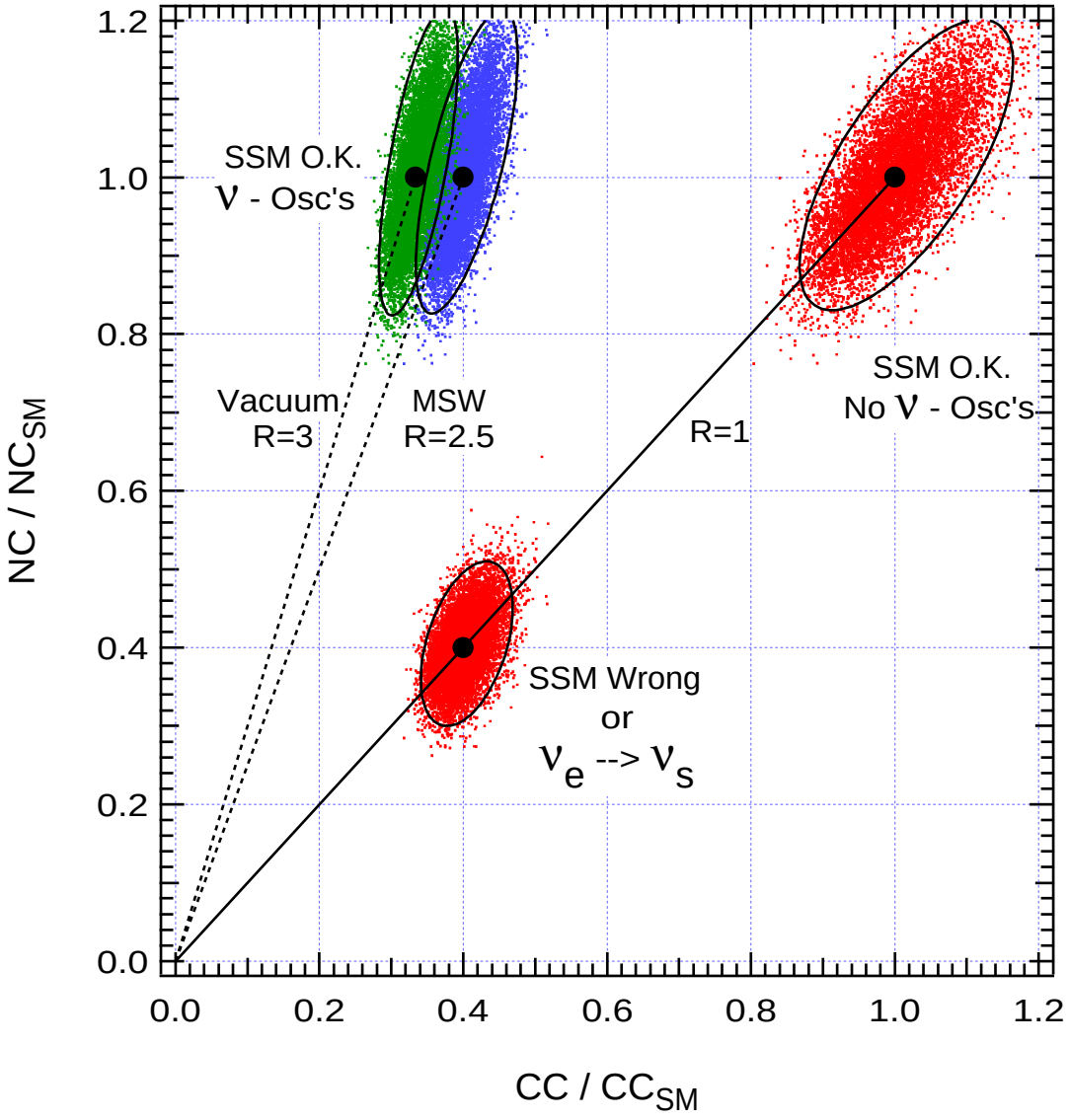

Figure 7.1: The project ratios of observed and calculated charge and neutral current signals for the cases of he SSM, sterile neutrinos and both vacuum and MSW oscillations.

neutron signal but can drastically increase the data rate. Inspite of this, the counters are over-voltaged to 2400 V (the nominal operating voltage is 1835 V) and any counter which exhibits more than 3 breakdown events in a 12 hour period is disassembled and repaired.

After filling and HV tests have been completed counters must then be characterised. Their gain and resolution are measured using a thermal neutron flux. The requirement is that all counters have the same gain within $\pm 2\%$. In addition the resolution can be used to determine the quality of the fill (a wide peak implies an impure gas mixture). Again any counter which fails these test must be purged and refilled.

As a result of these new techniques, current measurements at SNO indicate that the ^{210}Po rate is less than 6 counts/m^2/day and is decaying away, as expected, with a 138 day half-life whilst the bulk U/Th levels have an upper limit of 9.12 ± 3.1ppt.

7.3 CHIME

CHIME stands for *C*ounter *H*ardware *I*n-situ *M*easurement *E*xperiment. The experiment uses seven $1.14\,m$ neutral current detectors fastened together into a hexagonal arrangement (Figure 7.2). This collection of tubes will then be placed at the centre of SNO, in the heavy water, though the possibility remains of moving the CHIME vertically. The tubes themselves will have been through the entire production process and will be of the same quality as the final NCD detectors. However, these tubes will not be connected to any read out electronics. Their sole purpose is to be observed by the PMT array. This will allow a estimation of the additional photo-disintegration background caused by the NCD array. In addition a measurement of the activity from these counters will indicate if there have been any problems during construction.

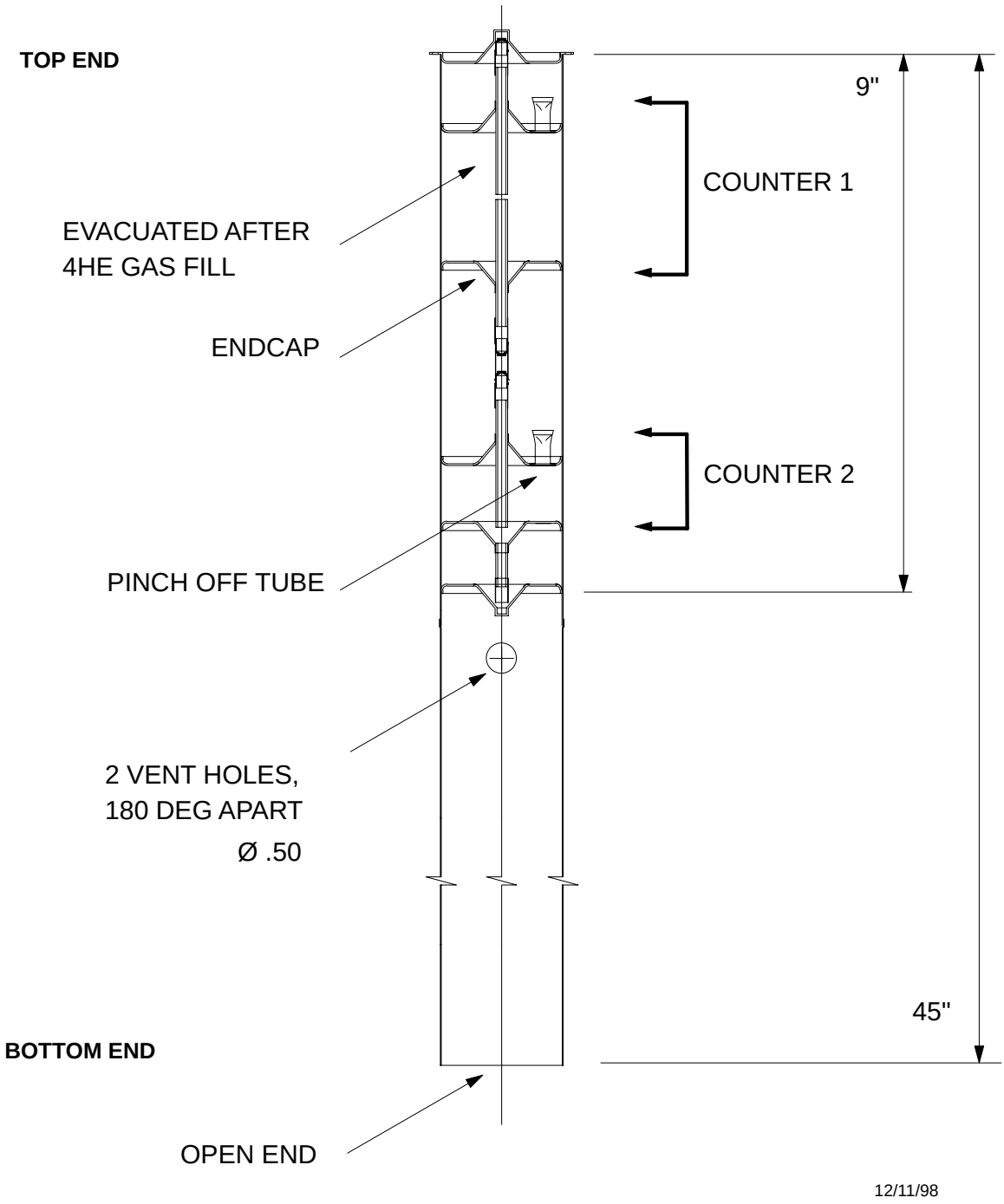

Figure 7.2: One of the seven segments from the CHIME detector. The counter is designed to mock up a real detector with a welded join in the middle of the detector. The vent holes are to allow the bottom of the counter to fill with D_2O and become negatively buoyant.

Appendix A

The MSW Effect

From Section 1.5.2 the basic principles of oscillations between weak eigenstates when mass and weak eigenstates are not the same has been demonstrated. In the presence of matter however, the Hamiltonian is changed for the electron type neutrino. An additional term must be added to account for the interaction between electron neutrino and the surrounding matter.

$$i\frac{\partial}{\partial t}\begin{pmatrix}\nu_e\\ \nu_f\end{pmatrix} = \frac{1}{2}\begin{pmatrix}\frac{-\Delta m^2}{2E}\cos 2\theta + \sqrt{2}G_F n & \frac{\Delta m^2}{2E}\sin^2\theta\\ \frac{\Delta m^2}{2E}\sin^2\theta & \frac{\Delta m^2}{2E}\cos 2\theta - \sqrt{2}G_F n\end{pmatrix}\begin{pmatrix}\nu_e\\ \nu_f\end{pmatrix} \tag{A.1}$$

where the Fermi constant $G_F \sim 1.2 \times 10^{-5}\,\mathrm{GeV}^{-2}$ and

$$n = \begin{cases} n_e, & \text{for } \nu_e \longrightarrow \nu_\mu \text{ or } \nu_\tau \\ n_e - \frac{1}{2}n_n, & \text{for } \nu_e \longrightarrow \nu_s \end{cases} \tag{A.2}$$

where $n_e(n_n)$ is the density of electrons (neutrons). The sterile neutrino's lack of neutral current interaction accounts for the extra term. In the absence of matter Equation A.1 reproduces the vacuum equation 1.11. In the presence of matter the MSW resonance occurs at a density of

$$n = \frac{\Delta m^2 \cos 2\theta}{2\sqrt{2}G_F E} \tag{A.3}$$

when the diagonal terms become equal and even a small vacuum mixing angle can lead to a large mixing between states.

If there were a constant density of matter then the resonance would again require fine tuning. However, the neutrino is created near the centre of the Sun where the densities are extremely high and as it moves outwards the density decreases. For a range of energies (for a given value of Δm^2 and θ) a neutrino will encounter a layer of just the right density for MSW resonance. As it passes through this layer the two energy eigenvalues will cross. If the density varies slowly enough (adiabatically) then there will be an almost certainty of conversion. If the crossing is non-adiabatic, the conversion probability will be smaller [44]. The important result is that the suppression of the neutrino flux is now very much energy dependent. This will result in a distortion of the solar neutrino energy spectrum. Figure1.9 shows the survival probabilities for two possible sets of values of θ and Δm^2 which provide a solution for the solar neutrino problem.

Appendix B

Standard Analysis Techniques

B.1 Charge Pulses

The majority of the data taken and analyzed throughout the course of this thesis were charge pulses. The pulse analysis can be split into two sections; position information and pulse shape information. The position information is available only in the situation where two amplifiers were used, one at each end of the detector. The analysis is relatively simple, and is the software version of a technique that has been used for many years.

B.1.1 Charge Pulse Analysis

The procedure for the analysis of charge pulses can be applied to both the singled-ended (WIPP Stage 1) and double-ended (WIPP Stage 2) data sets. For the double-ended system two pulses were produced; $A + B$ and B. Only the $A + B$ is required for the pulse shape analysis.

1. Calculate the d.c. offset, V_0, and the r.m.s. noise, V_{rms} of the first n_{av} points of the pulse, where n_{av} is typically 400 points (4μs). The d.c. offset is then subtracted from the pulse.

2. Calculate the start of the pulse by finding the first point which is above $n_\sigma(V_{rms} + dig)$, and then backtracking to the first point which is not above $(V_{rms} + dig)$. This is the start time t_0. The value of n_σ is dependent on the noise levels, but was typically 1.5–3.0 and dig is the digit bin size (typically 2 mV for the WIPP system).

3. Calculate the energy of the pulse, V_{int} as the average of n_E points $t_{\text{int}}\,\mu$s after the start of the pulse. ($n_e \sim 40\,\text{pts}/400\,\text{ns}$, $t_{\text{int}} \sim 10\,\mu$s.)

4. Calculate the time taken, t_f, relative to the start time t_0, to reach a certain fraction, f, of the pulse's energy, ($f \sim 0.5$). This value, t_f, is taken to be the rise-time of the pulse.

5. Calculate δ as the ratio $(V_{end} - V_t)/V_t$ where V_{end} is the pulse height at the end of the pulse (approximately 20μs after t_0) and V_t is the pulse height $t\,\mu$s after the start of the

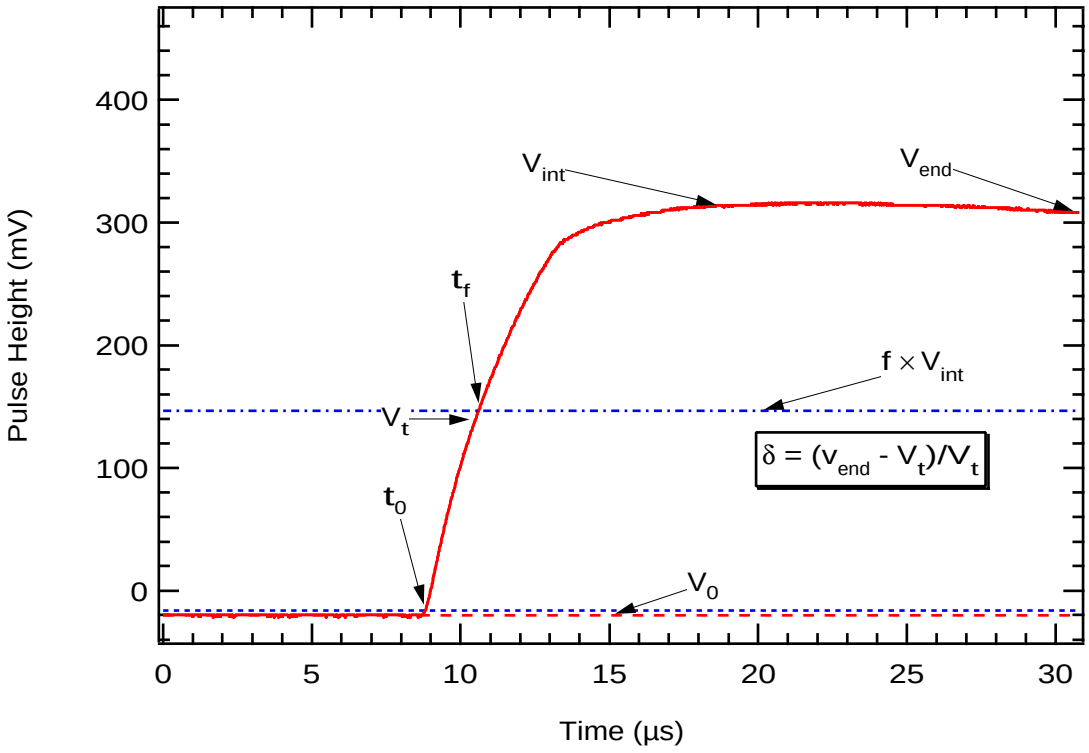

Figure B.1: A typical charge pulse with analysis parameters plotted.

pulse (typically $t \sim 2\,\mu$s).

This was the end of the first pass analysis. There were other passes which refine the values of t_0, V_{int} and t_f to remove the effects of digitization. Figure B.1 shows these parameters plotted on a typical pulse.

B.1.2 Charge Pulse Analysis with Position

The position analysis used was only relevant for double-ended charge pulses, where both the $A+B$ and B signals were recorded. The method relied on the same technique used in the previous section to remove the baseline from the $A+B$ pulses and determine the start time t_0. The baseline offset was then removed from the B pulse by averaging over all the points from the beginning of the data up to $t_0 - 0.5\,\mu$s. The position is then determined from the ratio of these two pulses. Strictly this ratio could be taken at any time after the start of the pulse, but due to the response of the pre-amplifiers it was determined that the best method of calculating this ratio was to average a number of points n_{position} (typically 10) t_{position} (typically $2\,\mu$s) after the start of the pulse (t_0). Figure B.2 shows a typical charge pulse ($A+B$) and the corresponding B pulse.

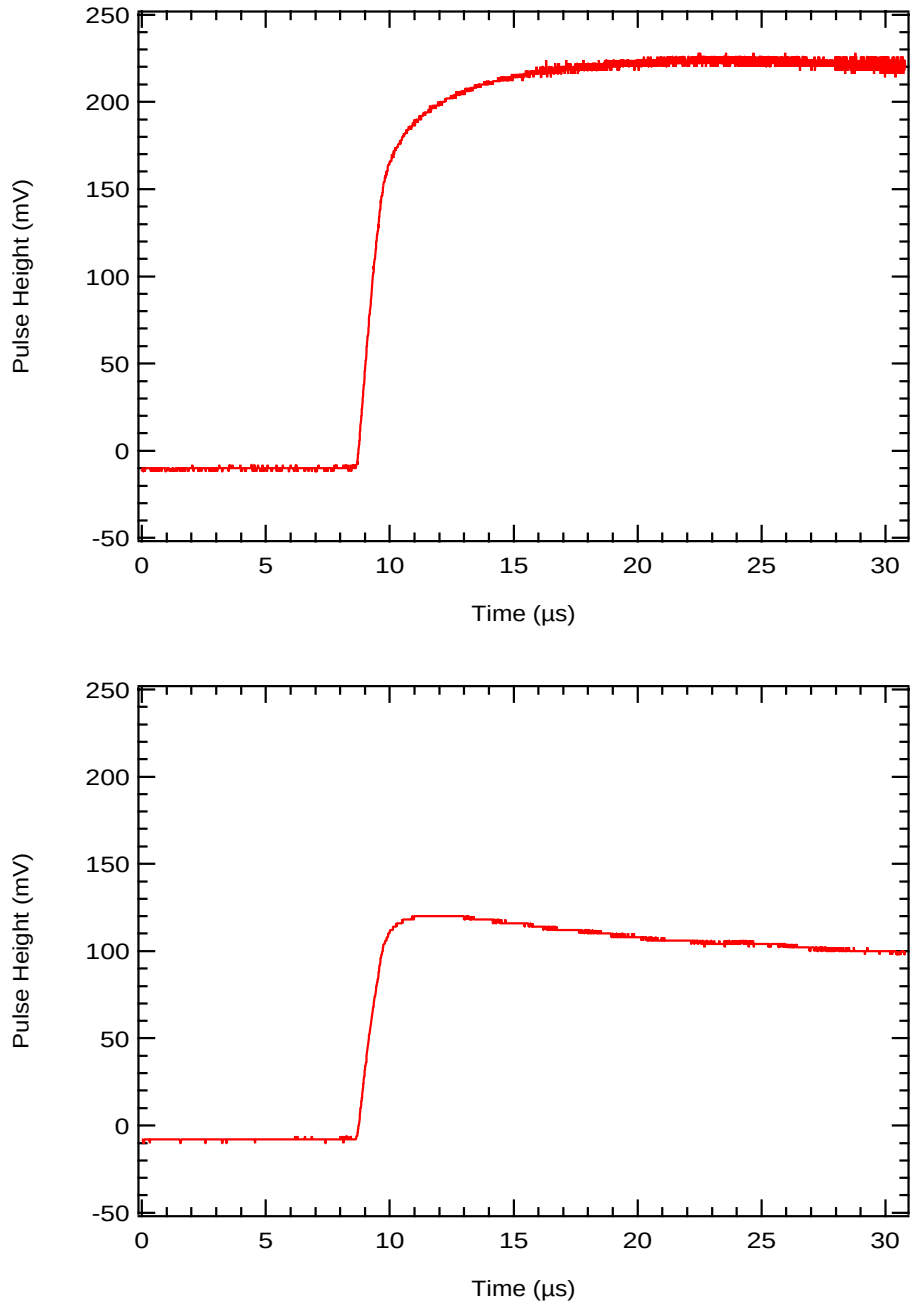

Figure B.2: A typical charge pulse $A + B$ (upper diagram) from a double-ended system with its corresponding B pulse (lower diagram).

B.2 Parameter Choices

The previous sections have given some idea of the typical values for each of the input analysis parameters. The values (and indeed some of the output parameters) were determined empirically throughout the course of this thesis. There is little reason not to use 10.1μs instead of 10μs for the integration time for charge pulses. However, it was determined that 10μs resulted in a better energy resolution than either 9 or 11μs. More detail are available in reference [34].

Appendix C

Maximum Likelihood Fitters

C.1 The Maximum Likelihood Fitter

The theory behind the Maximum Likelihood fit is well known. It is employed in situations where the data is multidimensional. Here it is employed as an estimator for the number of counts in the two dimensional distributions is t_F vs. E plots or the one, two or three dimensional data sets used when separating neutral current from acrylic vessel background distributions, where the number of counts is small and the Poisson distribution is valid (as opposed to the Gaussian distribution, valid at high counts).

The probability for finding a number of counts, n, at vector $\underline{x}$ is

$$P\Big(n(\underline{x})\Big) = \frac{e^{-\mu(\underline{x};\underline{A})}\mu(\underline{x};\underline{A})^{n(\underline{x})}}{n(\underline{x})!} \tag{C.1}$$

where the expected value μ is given by the sum of, m known functions, $f_i(\underline{x})$, and A_i, the weight of each function,

$$\mu(\underline{x}) = \sum_{i=1}^{m} A_i f_i(\underline{x}) \tag{C.2}$$

Maximum likelihood function is then defined by

$$\mathcal{L} = \prod_{\underline{x}} P\Big(n(\underline{x})\Big) \tag{C.3}$$

$$\log \mathcal{L} = \sum_{\underline{x}} \log P\Big(n(\underline{x})\Big) \tag{C.4}$$

The log function is the one that is usually maximized. One way of doing this is to solve the differential equal to zero, remembering that the only free parameters are A_i, the contribution of each distribution.

$$\frac{\partial \log \mathcal{L}}{\partial A_i} = \sum_{\underline{x}} \Big(\frac{n(\underline{x})}{\mu(\underline{x};\underline{A})} - 1 \Big) f_i(\underline{x}) = 0 \tag{C.5}$$

This can be solved via Newton–Raphson if the Hessian matrix is known,

$$H_{ij} = \frac{\partial^2 \log \mathcal{L}}{\partial A_i \partial A_j} = -\sum_{\underline{x}} \frac{n(\underline{x})}{\mu(\underline{x};\underline{A})^2} f_i(\underline{x}) f_j(\underline{x}) \tag{C.6}$$

After the fit has been completed the Hessian matrix can be inverted to provide the error matrix.

$$\mathrm{Err}_{ij} = H_{ij}^{-1} \tag{C.7}$$

The diagonal terms of this matrix provide an estimate of the error on each of the fitted parameters whilst the off-diagonal elements give a measure of the correlations between different distributions.

$$\sigma_i = \sqrt{\mathrm{Err}_{ii}} \tag{C.8}$$

$$\mathrm{correlation}_{ij} = \frac{\mathrm{Err}_{ij}}{\sqrt{\mathrm{Err}_{ii}\mathrm{Err}_{jj}}} \tag{C.9}$$

The remaining problem lies with determining the appropriate functions, f_i, for the fit. These, for the case of pulse shape analysis, can be measured via experiment or for the neutron capture distributions from Monte Carlo.

C.2 Comparison To χ^2 Fit

This section is to be used for comparison with the χ^2 fitter which is used in situations where the error on every point fitted is Gaussian distributed.

$$\chi^2 = \sum_{\underline{x}} \Big(\frac{\mu(\underline{x};\underline{A}) - n(\underline{x})}{\sigma(\underline{x})} \Big)^2 \tag{C.10}$$

where $\sigma(\underline{x})$ is the error at $\underline{x}$ and other variables are as previously defined. Again minimization of this function is performed by differentiating with respect to $\underline{A}$.

$$\frac{\partial \chi^2}{\partial A_i} = \sum_{\underline{x}} \Big(\frac{\mu(\underline{x};\underline{A}) - n(\underline{x})}{\sigma(\underline{x})} \Big) \frac{f_i(\underline{x}}{\sigma(\underline{x})} = 0 \tag{C.11}$$

If the number of counts is sufficiently large that the Gaussian errors can be used then $\sigma(\underline{x})^2 = n(\underline{x})$, and the chi-squared fit becomes

$$\frac{\partial \chi^2}{\partial A_i} = \sum_{\underline{x}} \Big(\frac{\mu(\underline{x};\underline{A})}{n(\underline{x})} - 1 \Big) f_i(\underline{x}) = 0 \tag{C.12}$$

The resulting formula used in the χ^2 fit bears remarkable similarity to the formula used in the Maximum Likelihood analysis.

Appendix D

Cosmogenic Production of Radio-Isotopes in Nickel

D.1 Introduction

The ^{3}He proportional counters are made by the chemical vapor deposition of nickel from nickel carbonyl, $Ni(CO)_4$. This produces almost pure nickel with almost no Uranium or Thorium. However, although the counters can be produced with very low activity any exposure to cosmic ray neutrons produces activity from spallation products.

D.2 Cosmogenic Probabilities

The only radio-nuclides that are of concern are those which are capable of photodisintegration of the deuteron and which have a half-life of greater than ten days. A list was compiled of all the possible isotopes which had half-lives of greater than ten days and these were examined in detail to determine if the photons given off after the decay had an energy of greater than 2.224 MeV. From all the isotopes only ^{56}Co emitted an appreciable number of photons. Figure D.1 shows the gamma ray spectrum. A calculation shows that 31% of ^{56}Co decays result in gamma rays with energy greater then 2.224 MeV.

Unfortunately ^{56}Co can be formed as a spallation product of nickel with cosmic ray neutrons.

$$^{58}\mathrm{Ni(n, p2n)}^{56}\mathrm{Co} \qquad ^{60}\mathrm{Ni(n, p4n)}^{56}\mathrm{Co} \tag{D.1}$$

So, even if the nickel is ultra-pure, any exposure to cosmic rays will produce this energetic and comparatively long-lived contaminant.

D.3 Photodisintegration of the Deuteron

Since there appears no way to remove all the ^{56}Co it is necessary to calculate the effect that it will have upon the detector so that a limit may be specified. The ^{56}Co nucleus decays to an

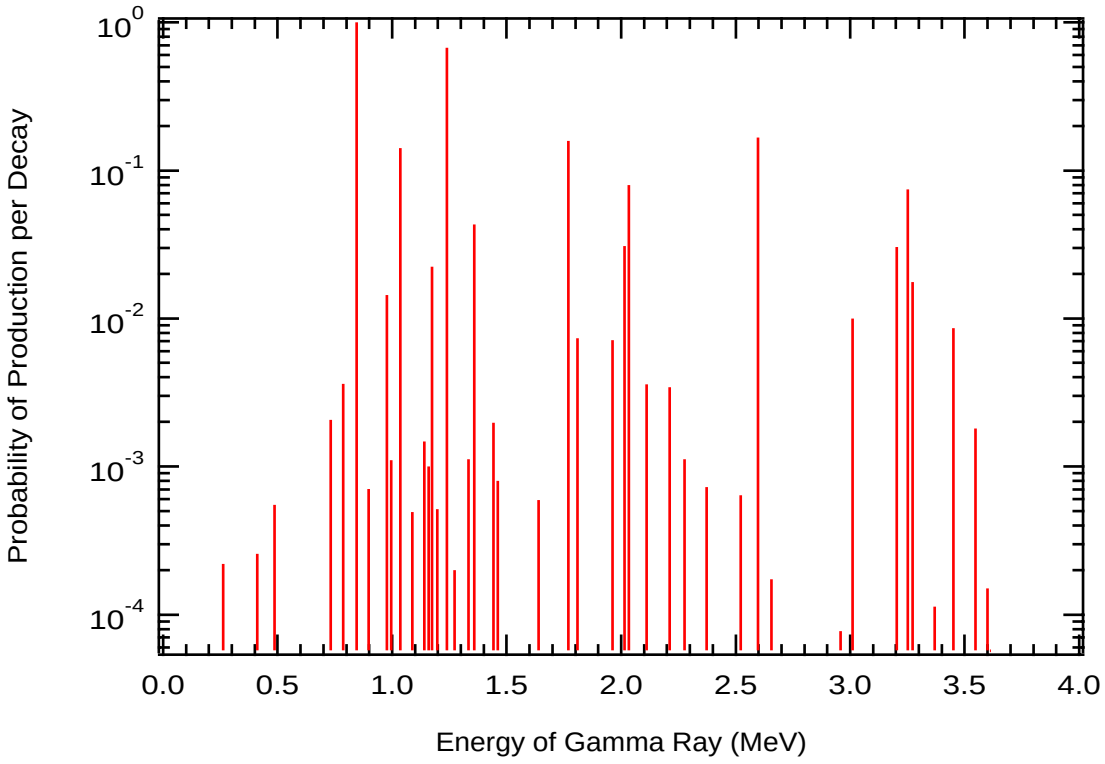

Figure D.1: The gamma ray spectrum for ^{56}Co.

excited state of ^{56}Fe which then de-excites by gamma cascade to its ground state. The energy distribution of the significant (> 2.0MeV) gammas is shown in Table D.1.

Once the photon has been produced it can interact with the heavy water inside the detector in two[1] manners:

1. Photodisintegrate a deuteron, or

2. Compton scatter from an electron.

The probability of the photon causing photodisintegration can be calculated by comparing the cross-sectional areas for photodisintegration and Compton scattering and taking into account the number of deuterons and electrons per D_2O molecule.

$$p(D \rightarrow np) = \frac{2 \times \sigma_{pd}}{10 \times \sigma_{Comp} + 2 \times \sigma_{pd}}$$

The cross-section for the photodisintegration of the deuteron is given to a good approximation by $\sigma_{pd} = \sigma_{E1} + \sigma_{M1}$ with $E1$ and $M1$ being the electric and magnetic cross-sections

[1]The cross-sections for the photoelectric effect and pair production are so small that their contributions can be ignored.

Table D.1: The Decay of ^{56}Co

Photon Energy MeV	Probability per Decay
2.2763	1.1176×10^{-3}
2.3736	7.7220×10^{-4}
2.5229	6.3780×10^{-4}
2.5984	0.16634
2.6574	1.7300×10^{-4}
2.9598	7.2200×10^{-5}
3.0102	9.9988×10^{-3}
3.2023	3.0400×10^{-2}
3.2536	7.4300×10^{-2}
3.2733	1.7600×10^{-2}
3.3696	1.1260×10^{-4}
3.4516	8.5750×10^{-3}
3.5480	1.8000×10^{-4}
3.6006	1.5000×10^{-4}
3.6116	5.7000×10^{-5}

(higher terms $E2$ etc. can be ignored for the purposes of this calculation).

$$\sigma_{E1} = \frac{8\pi}{3}\frac{\alpha\hbar}{M\omega_0}\left[\frac{\omega_0(\omega-\omega_0)}{\omega^2}\right]^{\frac{3}{2}}$$

$$\sigma_{M1} = \frac{2\pi}{3}\frac{\alpha\hbar^2}{M^2c^2}(\mu_p-\mu_n)^2\frac{\omega_0^{1/2}(\omega-\omega_0)^{1/2}[\omega_0^{1/2}+W_0^{1/2}]^2}{\omega(\omega-\omega_0+W_0)}$$

Evaluating all the constants gives the cross-sections as

$$\sigma_{E1} = 17.17\left[\frac{\omega_0(\omega-\omega_0)}{\omega^2}\right]^{\frac{3}{2}} \quad \text{mb}$$

$$\sigma_{M1} = 0.1282\frac{\omega_0^{1/2}(\omega-\omega_0)^{1/2}[\omega_0^{1/2}+W_0^{1/2}]^2}{\omega(\omega-\omega_0+W_0)} \quad \text{mb}$$

with ω is the energy of the photon, ω_0 is the binding energy of the deuteron and W_0 is a constant, equal to 0.037 MeV. Figure D.2 shows the total cross-section against photon energy.

The Compton scattering cross-section is given by

$$\sigma_{Comp} = 2\pi r_0^2\left\{\frac{1+\omega}{\omega^3}\left[\frac{2\omega(1+\omega)}{1+2\omega}-\ln(1+2\omega)\right]+\frac{\ln(1+2\omega)}{2\omega}-\frac{1+3\omega}{(1+2\omega)^2}\right\} \tag{D.2}$$

where r_0 is the classical radius of the electron and ω is given in terms of the photon's energy divided by the mass of the electron. The numerical factor $2\pi r_0^2$ simplifies to 492 mb and Figure D.3 shows the Compton cross-section verses photon energy.

As can be seen, the two cross-sections are highly energy dependent, and hence calculation of the number of neutrons produced per ^{56}Co decay requires knowing the exact energy spectrum of the emitted gammas.

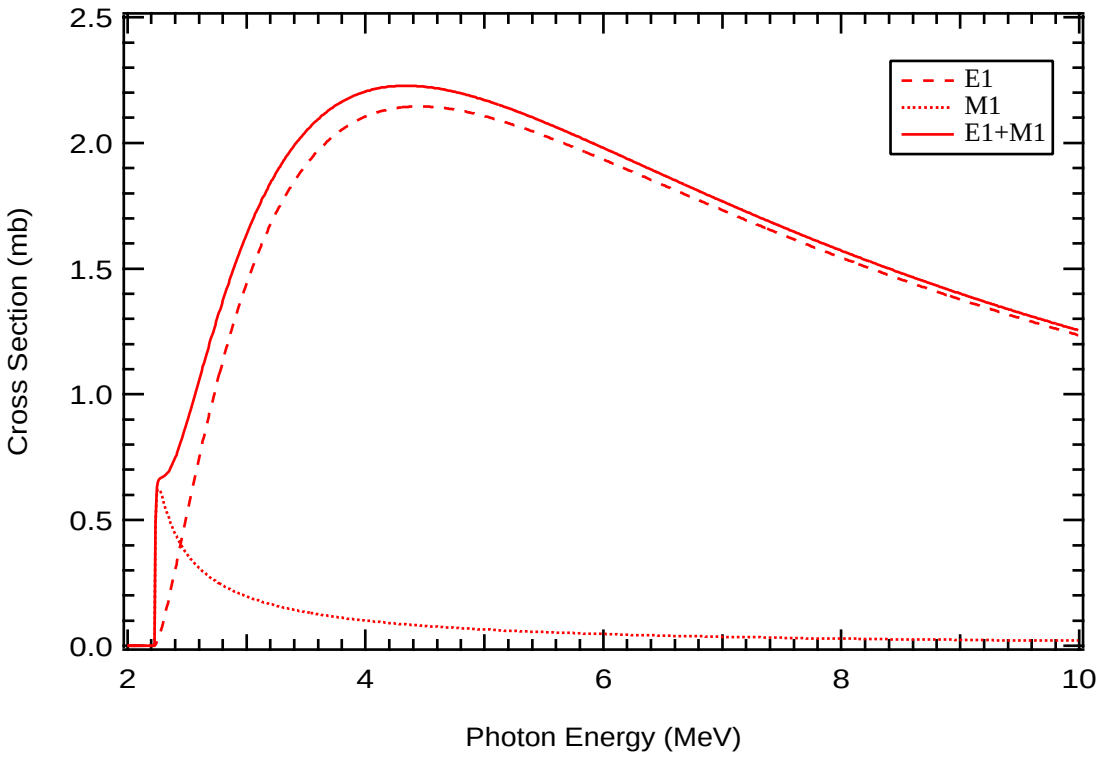

Figure D.2: The photodisintegration cross-section for the deuteron.

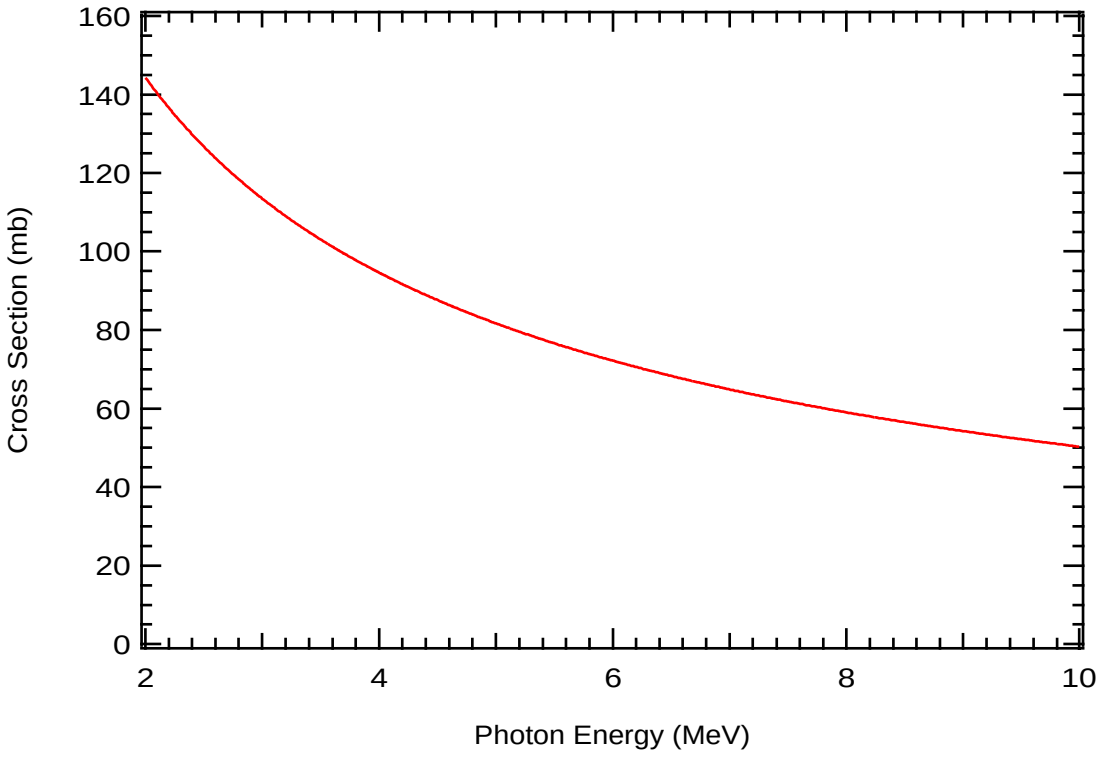

Figure D.3: The Compton scattering cross-section for electrons.

A very naïve way of calculating the effect of a gamma ray of a particular energy would simply be to compare the cross-sections of the average energy gamma ray: Of the gammas greater than 2.224 MeV the average energy is 2.88 MeV. At this energy the cross-sections are σ_{Comp} =116.4 mb and σ_{pd} =1.5 mb which implies that probability of causing photodisintegration is 2.57×10^{-3} or one neutron per 389 decays. As only 31% of ^{56}Co nuclei emit these higher energy gamma rays when they decay then the number of decays per neutron becomes 1255.

However, this assumes that the Compton scattered photon no longer has enough energy to cause photodisintegration, which is not always the case. A more precise calculation must take this effect into account and a Monte-Carlo must be employed to calculate the energy of the scattered photon.

The probability that the photon is scattered into the angular range $\theta \rightarrow \theta + \delta\theta$ is given by

$$p(\theta) = \frac{\pi r_0^2}{\omega_\theta^2}(\omega_\theta + \frac{1}{\omega_\theta} - \sin^2\theta)\sin\theta d\theta/\sigma \tag{D.3}$$

with $\omega_\theta = 1 + \omega(1 - \cos\theta)$. Using Monte-Carlo techniques it is then possible to select the angle through which the photon is scattered taking into account the non-isotropic nature of the scattering. The energy of the scattered photon is then given by

$$\omega' = \frac{\omega}{1 + \omega/m(1 - \cos\theta)} \tag{D.4}$$

If the new energy is less than that required to cause photodisintegration then the photon can be ignored, otherwise the comparison of cross-sections must be repeated to see if this new, lower energy, scattered photon could cause photodisintegration.

This more precise measure of the number of photodisintegrations has to be performed by Monte-Carlo analysis due to the continuous distribution in the scattered photon's energy.

D.4 Levels of ^{56}Co Produced by Cosmic Rays

As the CVD process ensures that no ^{56}Co is present in the nickel at the time of manufacture, then the decay rate for an isotope which has a half-life of $t_{1/2}$ and in material which has been exposed to cosmic rays for a period t_e, is given by

$$R(t_e) = R_0(1 - e^{-t_e \ln 2/t_{1/2}}) \tag{D.5}$$

where R_0 is the equilibrium decay rate ($R_0 = 24.22$ decays/day/kg).

If the nickel is then stored under ground, away from cosmic rays, for a time t_u then the decay rate is reduced by the normal decay factor, *ie*

$$R(t_e, t_u) = R_0(1 - e^{-t_e \ln 2/t_{1/2}})e^{-t_u \ln 2/t_{1/2}} \tag{D.6}$$

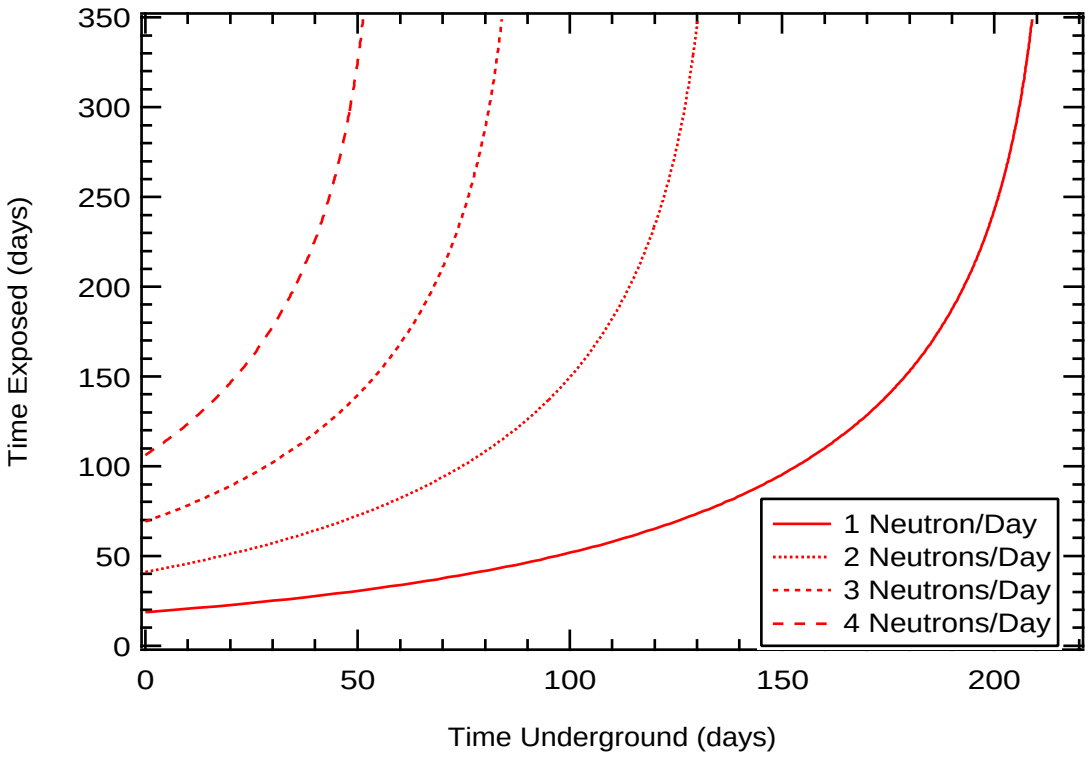

Figure D.4: Contour plot for the number of neutrons produced per day by all the neutral current detectors.

The results from the Monte-Carlo show that one neutron is emitted per 1140 ^{56}Co decays[2]. Assuming that the detectors contains 310 kg of nickel, then the expected number of neutrons produced per day is

$$R(D \to np) = \frac{310}{1140} R_0 (1 - e^{-t_e \ln 2/t_{1/2}}) e^{-t_u \ln 2/t_{1/2}} \tag{D.7}$$

The number of neutrons produced per day from the decays of U and Th chains in the D_2O is one. This is 10% of the neutron flux from solar neutrinos (the standard solar model predicts 13 neutrons/day/ktonne D_2O). The same standard of purity is required for NCD's and places a limit on the exposure and decay times. The allowed region is shown in Figure D.4.

D.5 Conclusions

Although it is possible to produce nickel free of ^{56}Co by the CVD process, spallation by cosmic rays will eventually produce significant levels. This level can be reduced by either,

1. Short exposure time to cosmic rays, or,

[2]A check was performed on the Monte-Carlo by running the code with the data for ^{208}Tl. The result obtained agrees with the White Book's value.

2. Long storage underground,

the ratio of which are shown in figure D.4.

Another factor which must be taken into consideration is the altitude at which the counters are assembled. Los Alamos is 7200 ft above sea-level and the cosmic ray fast neutron component is 6.3 times stronger than at sea level. Given the large mass, activity levels and a reasonable time scale for manufacture of detectors from nickel tubes, the nickel must be stored underground prior to its insertion into the SNO vessel.

Appendix E

Monte Carlo Techniques

E.1 Production of Distributions

The Maximum Likelihood analyses of Chapter 6 required the production of various underlying neutron capture distributions both as a total neutron capture distribution (*e.g.* typically a distribution of 2730 neutrons from an isotropic distribution and 125 neutrons from an acrylic vessel distribution) and the underlying probability distributions, the $f_i(\underline{x})$ of Appendix C.

E.2 Probability Distributions

The underlying probability distributions were created from neutron capture data produced by Monte Carlo simulations. For each geometry G_0 through G_6, Monte Carlo neutron capture events were generated for both isotropic and acrylic vessel neutron sources. In addition, for certain geometries neutron capture events were generated for other possible sources *e.g.* hot spots on the acrylic vessel and hot spots on various detectors. The data sets generated were typically of the order of 40,000 points, though the number of starts required to produce this many events varied between the different simulated sources. Each data set consists of (x, y, z) capture locations with 'infinite' precision *i.e.* the z resolution of the detectors was not taken into consideration. These data were then binned into the one, two or three dimensional distributions required by the fitter.

1D For the one dimensional distributions the binning required determining the corresponding ring number from the (x, y) capture location.

2D For the two dimensional distributions the binning required determining the appropriate detector corresponding to the (x, y) capture location. For the case of a distribution which is expected to be symmetric *i.e.* isotropic and acrylic vessel sources, the distribution is symmetrized on a ring by ring basis. This involves setting the number of counts in each detector to the average number of counts in that ring.

3D For the three dimensional distributions the binning required determining not only the appropriate detector but also the position along that detector. For binning purposes the z resolution was limited to 1 m, the same as the inter-detector spacing. This was considered a reasonable resolution given preliminary tests from the University of Washington. Similarly, for distributions which are expected to be symmetric the data were symmetrized. For the three dimensional case, the symmetrization occurs not only around individual rings but also about the $z = 0$ plane.

To produce the appropriate probability distributions all of the above distributions were normalized.

E.3 Neutron Capture Distributions

There were two methods used to create the neutron capture distributions, one for the multiple Monte Carlo simulation to determine the extraction efficiencies and the other when only a single data set was required to demonstrate the effects of hot spots with respect to a specific distribution.

E.3.1 Multiple Monte Carlo Simulations

During the course of Chapter 6 there have been references to the results of 1000 Monte Carlo simulations. The data for these simulations were obtained by using the probability distributions derived in Section E.2. As an example consider a simulated distribution which is supposed to consist of 2730 events from isotropic sources and 125 from acrylic vessel sources. The two probability distributions are $f_{NC}(\underline{x})$ and $f_{AV}(\underline{x})$ respectively, where $\underline{x}$ is the radial ring number or 2D/3D grid location depending on the number of dimensions used. The Monte Carlo simulations can then be generated by

$$n(\underline{x}) = \mathcal{P}\Big(2730 f_{NC}(\underline{x}) + 125 f_{AV}(\underline{x})\Big) \tag{E.1}$$

where $n(\underline{x})$ is the number of simulated events at location $\underline{x}$ and $\mathcal{P}(\mu)$ is a random number obtained from a Poisson distribution of mean μ. These data were then used as the raw input data for the Maximum Likelihood fitter. The 1000 runs are an attempt to remove statistical fluctuations in the data.

E.3.2 Single Monte Carlo Simulations

In demonstrations of hot spot searches it was necessary to produce a single example data set which contained an exact number of counts from each source with the ability to remove one or more of the sources from the data set to demonstrate its effect on the fitting algorithm. For these reasons the data set was generated in a different manner to the Multiple Monte

Carlo data sets. Instead, the required number of events were obtained directly from the original Monte Carlo simulations. For example if 2500 isotropic source neutron capture event were required then 2500 events were extracted at random from the 40,000 (x, y, z) simulated captures. This same method was used for any other neutron capture distributions that were required. These data sets were then amalgamated as required, *e.g.* 2500 isotropic + 125 acrylic vessel or the same 2500 isotropic + 125 acrylic vessel with an additional 50 hot spot events, and the resulting (x, y, z) data sets were binned into 1D, 2D and 3D distributions. These distributions were then used as the input data sources for the Maximum Likelihood fitter.

Appendix F

WIPP Stage 2 Data Reduction

With the experience gained during Stage 1, it was decided that the data from Stage 2 should be reduced further after initial pulse shape analysis with the emphasis on removing invalid data (*e.g.* pulses which had overloaded the digitizers). Furthermore, pulses which did not originate from ionization in the gas were also excluded. From the remaining data set a position cut was then applied to remove the effects of the endcaps and any associated activity in that region. The resulting data set contained only pulses which resulted from ionization in the central part of the detector. At each stage the number of pulses which passed or failed was recorded. In addition individual series were separated into 10 day periods to aid in determining any time dependent effects. The entire procedure is detailed below:

1. All pulses which saturate either of the digitizers ($A+B$ or B) either because of overflow or underflow are removed. The number of each type is recorded. In addition if a pulse overflows the B channel but does not overflow the $A+B$ channel it is marked as a spurious pulse.

2. All pulses which have a bad t_0 (start time) are excluded. A bad t_0 implies that the analysis code could not find any part of the pulse sufficiently above the baseline noise which could be considered, as a first approximation, as the start of the pulse.

3. All pulses which have a bad t_f are excluded. A bad t_f is associated with small energy pulses where the scanning algorithm finds a point which meets the $f\times$energy criteria before the start time of the pulse. This occurs most often with Compton pulses analysed using the low gain data set.

4. Similarly all pulses which fail the second guess at t_0 and t_f are recorded but not excluded from the fit as these parameters are not required as part of the standard analysis procedure.

5. The total number of events which have passed this stage are recorded. This represents the set of pulses which passed through the entire analysis and contain all the parameters

High Gain	Counts	Rate	Counts	Rate
Series	170–180		180–190	
Live Time	3.166		4.479	
Counts	537	169.6	851	190.0
Saturation etc.	97	30.6	167	37.3
$A + B$ Overflow	62	19.6	118	26.3
B Overflow	36	11.4	80	17.9
$A + B$ Underflow	0	0.0	5	1.1
B Underflow	59	18.6	77	17.2
Spurious	2	0.6	9	2.0
Bad T_0	0	0.0	0	0.0
Bad T_f	0	0.0	0	0.0
Bad T_0'	0	0.0	0	0.0
Bad T_f'	0	0.0	0	0.0
Events	440	139.0	684	152.7
HV Cut	19	6.0	28	6.3
Events	421	133.0	656	146.5
Position Cut	205	64.8	314	70.1
Final Events	216	68.2	342	76.4

Low Gain	Counts	Rate	Counts	Rate
Series	170–180		180–190	
Live Time	3.166		4.479	
Counts	537	169.6	851	190.0
Saturation etc.	48	15.2	78	17.4
$A + B$ Overflow	0	0.0	2	0.4
B Overflow	0	0.0	2	0.4
$A + B$ Underflow	0	0.0	5	1.1
B Underflow	48	15.2	67	15.0
Spurious	0	0.0	0	0.0
Bad T_0	0	0.0	0	0.0
Bad T_f	219	69.2	371	82.8
Bad T_0'	6	1.9	8	1.8
Bad T_f'	0	0.0	1	0.2
Events	270	85.3	402	89.8
HV Cut (High)	14	4.4	20	4.5
Events	256	80.9	382	85.3
HV Cut (Low)	1	0.3	3	0.7
Events	255	80.5	379	84.6
Position Cut	227	71.7	343	76.6
Final Events	28	8.8	36	8.0

Table F.1: Data from Ni CVD #2 from Series 500. Only the first two ten day periods are shown.

which can be used in the characterization of the pulse.

6. All high voltage discharge pulses are removed. As the majority of HV discharge pulses are equivalent in pulse height to low energy ionization events it is difficult to remove them from the low gain data sets as the pulses are often too small to be analysed correctly (usually the t_f parameter is not correctly interpreted). For this reason the removal of HV events from the low gain data sets is performed in two stages. First, all the events which were classified as HV discharge in the high gain data set are removed (as all events are encoded with an event number) and second, a slightly different δ and V_{int} cut is applied. Again the numbers of events which pass or fail this section are noted. For high gain data sets a simple cut using the t_f and δ parameters can be used to remove all HV discharges.

7. A position cut is applied to the data to leave only the data from the central part of the detector. It must be noted that the position resolution worsens with decreasing pulse energy as the pulse height decreases but the noise on the signal remains the same. As a result the position cut is pulse height/energy dependent and is an inverse function of the pulse height. Following the position cut the pulse height is converted from its mV scale to an MeV energy scale. Additional any dependence of the energy of the pulse based on its position along the length of the detector is removed. (This is a result of the tapered manufacturing process for the three nickel detectors and does not affect the short stainless steel detectors.)

8. Lastly and for only one of the detectors a δ and t_f cut was applied to the data to exclude events which could not have been produced by ionization in the detector.

Throughout the filtering the data are separated into two files corresponding to those pulses which passed the appropriate tests and those which failed. Table F.1 shows the number of pulses which pass or fail each filtering stage and the appropriate rate per day and Figures F.1 and F.2 show a data before and after the filtering process.

In order to remove both high voltage discharge pulses, perform the position cut and convert pulses heights to energies a set of parameters is required for each detector in each of the electronic configurations. Tables F.3 through F.6 show the parameters used for each of the detectors in each of the series. It should be noted that these parameters change from series to series with changing electronics. Each table the lists the following parameters:

R_0 The ratio which corresponds to the remote (B) end of the detector.

R_L The ratio which corresponds to the near (A) end of the detector.

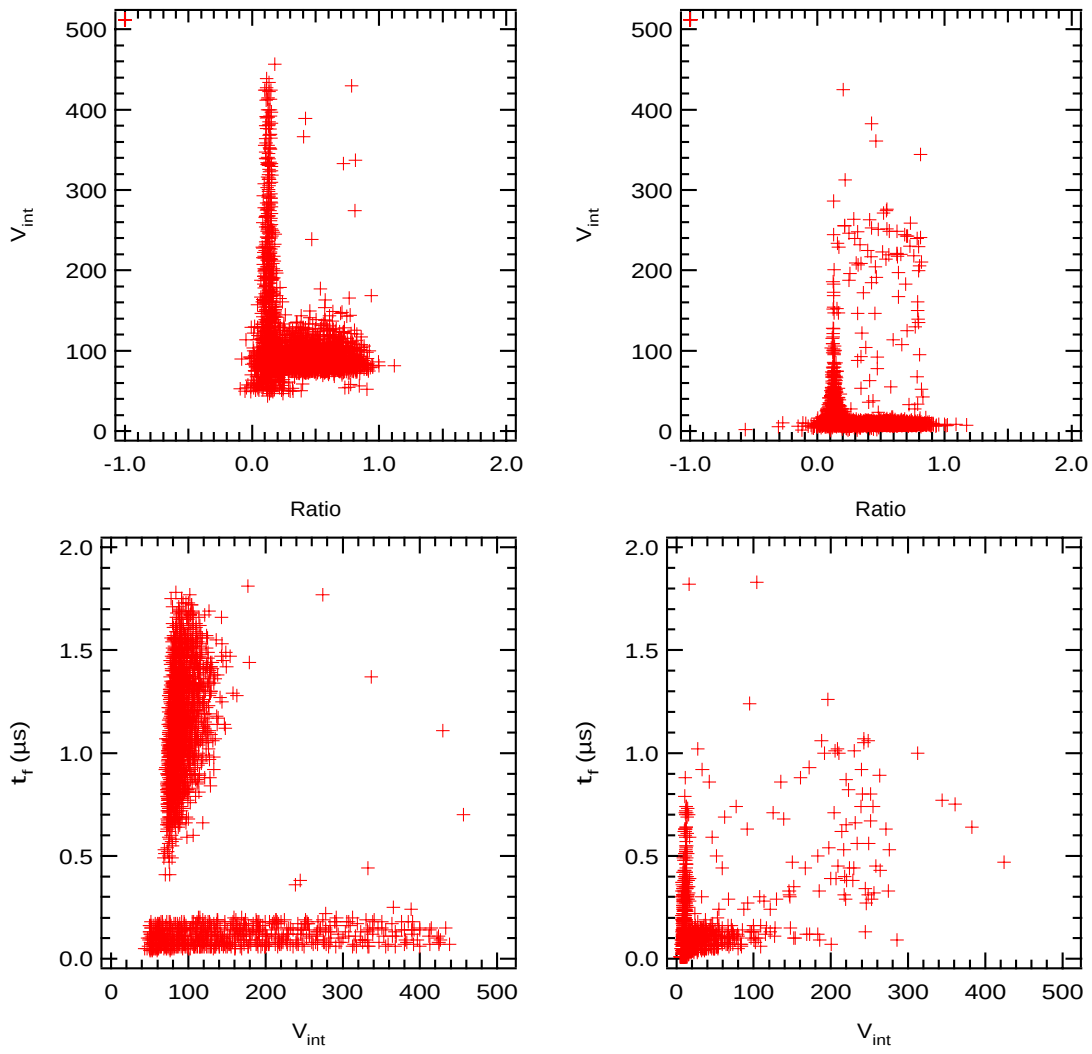

Figure F.1: The raw data from Ni CVD#2 data over the period 300–310 days (7.225 live days). As no fitering/conversion has yet been performed the pulse heights are recorded in mV, the actual ouput of the digitizers. Similarly, the position is recorded in terms of the actual pulse height ratios.

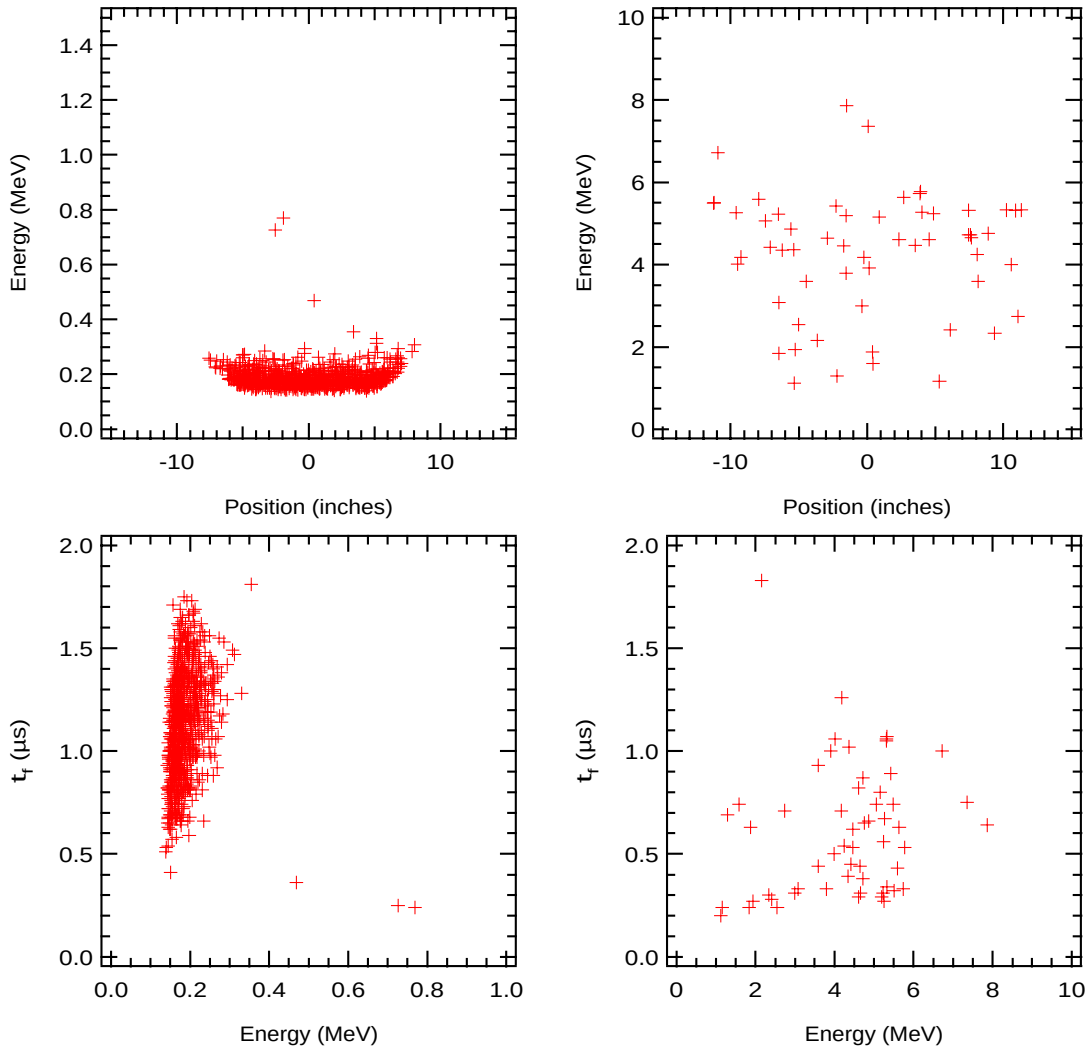

Figure F.2: The final position cut data from Ni CVD#2 data over the period 300–310 days (7.225 live days). Following the conversion and filtering processes pulse energies and positions are displayed in their natural units.

Peak The peak position in mV corresponding to 0.764 MeV (neutron capture) and 5.3 MeV (^{210}Po)for the high and low gain channels respectively. Values in parentheses are estimated values. For the high gain neutron capture peak this is derived from the ^{210}Po peak and the relative gain of the high and low data sets.

Gain The gain difference between the high and low gain channels.

Delta Cut The two parameters used to separate HV discharge pulses from the rest of the data set. For the high gain data the pulse is classified as a high voltage discharge if

$$\delta < P_1 + \frac{P_2}{t_f} \tag{F.1}$$

where P_1 and P_2 are the two parameters listed, t_f is the pulse's rise-time parameter and δ is the pulse's δ parameter. Refer to Appendix B for the definition of these parameters. For low gain data the pulse is classified as discharge if

$$\delta < P_1 \quad \text{and} \quad V_{\text{int}} > P_2 \tag{F.2}$$

where V_{int} is the pulse's energy measured in mV.

Duration The total live time of the series in days.

In addition the length of each detector is supplied. For the short nickel CVD detectors which where produced from tapered tubes, there is a position dependent energy correction. This correction is listed below in the corresponding table.

F.1 Series Numbers and Their Meaning

As has been mentioned earlier any change in the electronic/detector configuration defined the start of a new series. For reference, a list has been included detailing the changed made between different series For the purposes of book keeping and easy of reference three idenitical electronics channels were used during Stage 2, one for each of the detectors and were labelled 1 through 3. Table F.2 lists the typical information kept for each of the channels. Whenever an electronics module was replace or altered a new series was started

Series 000 The initial test of Stage 2a which utilized three short stainless steel detectors filled with a 65:35 mixture of He:CF_4. Each of the three detectors (SS#1, SS#2 and SS#3) and in the appropriate electronics channel.

Series 100 The first prototype nickel detector is installed in electronics channel 3, whilst SS#3 is moved into electronics channel 1 and SS#1 is returned to Los Alamos (as SS#1 had the highest background rate of the three stainless steel detectors). Additional

changes are made to the electonics (preamplifiers and fast amplifiers are exchanged for ones calibrated at LANL).

Series 200 The HV for the two stainless steel detectors is removed as they dominate the data rate.

Series 250 The HV for the two stainless steel detectors is restored for a short period, whilst that for the nickel detector is removed.

Series 300 Problems occur with discharge in the preamplifiers used for the nickel detector. The detector is reinstalled in electronics channel 2.

Series 400 NiCVD#1 is removed to LANL where it is refilled without ^{3}He. Problems occur with discharge in the preamplifiers used for the nickel detector. The detector is reinstalled in electronics channel 1.

Series 500 The second and third prototype detectors are installed and all faulty electonics are replaced. Each of the nickel detector is placed in the corresponding electronics channel. During this run the HV is removed from NiCVD#1 as it is now the dominant component in the data rate. Additionally, problems are found with NiCVD#3 (it has a pinhole leak) and it is returned to LANL. Finally, problems are found with NiCVD#2 which, when it is reopened at LANL, were found to caused by the central wire slipping from its solder joint.

Series 600 NiCVD#3 is reinstalled and NiCVD#2 is returned to LANL. However, during this series there are significant power outages due to mine safety inspections and little data is recovered. In addition, the digitizer is Crate 2 Slot 21 reports constant overflows and the resulting data can not be analysed over the energy region 1–10 MeV.

Series 700 NiCVD#2 is reinstalled and the faulty digitizer is replaced. Currently NICVD#2 and NiCVD#3 are operating in electronics channels 1 and 2 respectively. At the end of the data set the new UPS (uniterruptable power suppply) is delivered to WIPP. Data taking is halted until it is installed. During this period an intermitant problem occurs with the digitizer is Crate 2 Slot 21. This problem is not diagnosed until after the completion for Stage 2b.

Series 750 The two detectors are switched to determine is supurious pulses were the result of problems associated with teh design of the end-caps or if they were related to problems with the preamplifiers.

Series 800 The two detectors are returned to their original configurations.

	Channel 1	Channel 2	Channel 3
Side A Preamp	Preamp 1	Preamp 5	Preamp 6
Side B Preamp	Preamp 2	Preamp 7	Preamp 8
Preamp Power	Box 1 (A-1, B-3)	Box 2 (A-5, B-7)	Box 3 (A-6, B-8)
HV Power	Box 1 Channel A	Box 1 Channel B	Box 2 Channel A
HV Power DAC	Channel 12	Channel 13	Channel 14
Channel A High	FAMP-1 Block 1	FAMP-2 Block 1	FAMP-2 Block 5
Channel A Low	FAMP-1 Block 2	FAMP-2 Block 2	FAMP-2 Block 6
Channel B High	FAMP-1 Block 3	FAMP-2 Block 3	FAMP-2 Block 7
Channel B Low	FAMP-1 Block 4	FAMP-2 Block 4	FAMP-2 Block 8
Signal (A+B) High	FAN-2 Block 1	FAN-1 Block 1	FAN-1 Block 3
Signal (A+B) Low	FAN-2 Block 2	FAN-1 Block 2	FAN-1 Block 4
Shaping Amplifier	SAMP-1	SAMP-2	SAMP-3
Inverter	FAN-3 Block 1	FAN-3 Block 2	FAN-3 Block 4
Discriminator	DISC-1 Block 1	DISC-1 Block 3	DISC-1 Block 5
Trigger Out	FAN-4 Block 1	FAN-4 Block 2	FAN-4 Block 3
Digitizer $(A+B)$ High	Crate 1 Slot 2	Crate 1 Slot 16	Crate 2 Slot 12
Digitizer B High	Crate 1 Slot 5	Crate 1 Slot 19	Crate 2 Slot 15
Digitizer $(A+B)$ Low	Crate 1 Slot 8	Crate 2 Slot 2	Crate 2 Slot 18
Digitizer B Low	Crate 1 Slot 11	Crate 2 Slot 5	Crate 2 Slot 21

Table F.2: The three 'idenitical electronic channels used in Stage 2. Abbreviation used; FAMP - fast amplifier (P/S 777), FAN - fan in-fan out (P/S 744), SAMP - shaping amplifier (Tenelec 242), DISC - discriminator (P/S 705).

Series 850 The two detectors are again switched from their original configurations. Additionally, NiCVD#3 is later replaced in electronics channel 2 by NiCVD#1. The prupose was to measure the final levels of U and Th in the detector (most of the ^{210}Po having already decayed away .

Series 900 NiCVD#1 is shield by a 'tube' of lead bricks in an attempt to deduce the source of the Compton band in the data.

Short Stainless Steel Detector #1						
Series	R_0	R_L	Peak	Gain	Delta Cut	Duration
000Hi	0.11	0.77	424	10.15	-0.05, 0.005	3.217
000Lo	0.14	0.77	308	n/a	-0,40	
100Hi	n/a	n/a	n/a	n/a	n/a	n/a
100Lo	n/a	n/a	n/a	n/a	n/a	

Short Stainless Steel Detector #2						
Series	R_0	R_L	Peak	Gain	Delta Cut	Duration
000Hi	0.12	0.78	404	10.45	-0.05, 0.005	3.217
000Lo	0.13	0.80	288	n/a	0,40	
100Hi	0.11	0.78	(428)	10.45	-0.05, 0.005	28.837
100Lo	0.13	0.79	284	n/a	0,40	
250Hi	0.11	0.78	(428)	10.45	-0.05, 0.005	2.6342
250Lo	0.13	0.79	284	n/a	0,40	

Short Stainless Steel Detector #3						
Series	R_0	R_L	Peak	Gain	Delta Cut	Duration
000Hi	0.13	0.81	384	10.15	-0.05, 0.005	3.217
000Lo	0.13	0.77	280	n/a	-0,40	
100Hi	0.13	0.77	(418)	10.15	-0.15,0.005	28.837
100Lo	0.15	0.75	284	n/a	-0.075,40	
250Hi	0.13	0.77	(418)	10.15	-0.15,0.005	2.6342
250Lo	0.15	0.75	284	n/a	-0.075,40	

Table F.3: The parameters used in the filtering of data from the three short stainless steel detectors used in Stage 2a. It should be noted that the parameters vary from series to series corresponding to the changes with the electronics. All detectors were 30" long.

Series	R_0	R_L	Peak	Gain	Delta Cut	Duration
100Hi	0.18	0.75	404	10.15	-0.15,0.005	28.837
100Lo	0.17	0.72	300	n/a	-0.1,40	
200Hi	0.18	0.76	396	10.15	-0.17,0.005	36.371
200Lo	0.18	0.73	292	n/a	-0.1,40	
300Hi	0.16	0.77	460	10.5	-0.1,0.005	17.456
300Lo	0.16	0.79	336	n/a	-0.1,40	
400Hi	0.18	0.79	(390)	9.8	-0.15,0.005	9.669
400Lo	0.18	0.78	276	n/a	-0.1,40	
500Hi	0.19	0.81	(370)	9.8	-0.15,0.005	11.364
500Lo	0.18	0.79	262	n/a	0,40	
600Hi	n/a	n/a	n/a	n/a	n/a	
600Lo	n/a	n/a	n/a	n/a	n/a	
700Hi	n/a	n/a	n/a	n/a	n/a	
700Lo	n/a	n/a	n/a	n/a	n/a	
750Hi	n/a	n/a	n/a	n/a	n/a	
750Lo	n/a	n/a	n/a	n/a	n/a	
800Hi	n/a	n/a	n/a	n/a	n/a	
800Lo	n/a	n/a	n/a	n/a	n/a	
850Hi	0.22	0.79	((414))	10.19	-0.10,0.005	23.954
850Lo	0.23	0.81	(282)	n/a	-0.075,40	
900Hi	0.16	0.77	((406))	10.0	-0.15,0.005	22.280
900Lo	0.16	0.79	(282)	n/a	-0.075,40	

Detector Length 26.5”

Energy Correction for Tube Taper

$$\begin{aligned} \text{Energy} &= \text{Energy} \times (1 - 4.447 \times 10^{-3} \times X_{\text{position}}) \\ \text{Energy} &= \text{Energy} \times (1 + 4.447 \times 10^{-3} \times X_{\text{position}}) \end{aligned}$$

Table F.4: The parameters used with short Ni CVD detector #1.

Series	R_0	R_L	Peak	Gain	Delta Cut	Duration
500Hi	0.13	0.79	(367)	10.60	-0.15,0.005	57.560
500Lo	0.13	0.80	240	n/a	0,40	
600Hi	n/a	n/a	n/a	n/a	n/a	n/a
600Lo	n/a	n/a	n/a	n/a	n/a	
700Hi	0.13	0.79	(390)	10.40	-0.05,0.005	12.063
700Lo	0.13	0.79	260	n/a	0,40	
750Hi	0.14	0.74	(383)	10.22	-0.05,0.005	9.771
750Lo	0.15	0.74	260	n/a	0,40	6.898
800Hi	0.13	0.77	(374)	10.47	-0.05,0.005	26.296
800Lo	0.15	0.80	248	n/a	0,40	
850Hi	0.15	0.77	(422)	10.46	-0.05,0.005	29.863
850Lo	0.15	0.75	280	n/a	0,40	18.820
900Hi	n/a	n/a	n/a	n/a	n/a	n/a
900Lo	n/a	n/a	n/a	n/a	n/a	

Detector Length 29.9”

Energy Correction for Tube Taper

$$\begin{aligned} \text{Energy} &= \text{Energy} \times (1 - 4.982 \times 10^{-3} \times X_{\text{position}}) \\ \text{Energy} &= \text{Energy} \times (1 + 6.726 \times 10^{-3} \times X_{\text{position}}) \end{aligned}$$

Table F.5: The parameters used with short Ni CVD detector #2.

Series	R_0	R_L	Peak	Gain	Delta Cut	Duration
500Hi	0.17	0.82	(429)	10.63	-0.00,0.005	5.093
500Lo	0.16	0.80	280	n/a	0,40	
600Hi	0.16	0.74	n/a		-0.05,0.005	19.780
600Lo	n/a	n/a	n/a	n/a	n/a	0.000
700Hi	0.16	0.73	(455)	10.12	-0.02,0.005	34.962
700Lo	0.16	0.74	312	n/a	0,40	34.539
750Hi	0.13	0.79	(404)	10.29	-0.05,0.005	4.821
750Lo	0.14	0.80	272	n/a	0,40	
800Hi	0.15	0.73	(465)	10.33	-0.05,0.005	26.322
800Lo	0.16	0.73	312	n/a	0,40	25.351
850Hi	0.14	0.79	(398)	10.16	-0.05,0.005	5.900
850Lo	0.14	0.81	272	n/a	0,40	
900Hi	0.12	0.72	((406))	10.86	-0.05,0.005	1.078
900Lo	0.11	0.73	(272)	n/a	0,40	

Detector Length 27.4”

Energy Correction for Tube Taper

$$\begin{aligned} \text{Energy} &= \text{Energy} \times (1 - 5.156 \times 10^{-3} \times X_{\text{position}}) \\ \text{Energy} &= \text{Energy} \times (1 + 6.540 \times 10^{-3} \times X_{\text{position}}) \end{aligned}$$

Table F.6: The parameters used with short Ni CVD detector #3.

Short Stainless Steel Detectors #2 & #3			
Series	Period	High Gain	Low Gain
000	0	3.211	
100	0	1.960	
	10	8.452	
	20	6.568	
	30	1.585	
	40	6.550	
250	100	2.637	

Table F.7: Series, periods and live times for Short Stainless Steel Detectors #2 & #3.

Short CVD Detector #1			
Series	Period	High Gain	Low Gain
100	0	1.960	
	10	8.450	
	20	6.565	
	30	1.585	
	40	6.540	
200	40	0.021	
	50	9.748	
	60	7.528	
	70	6.244	
	80	8.337	
	90	3.698	
300	100	2.856	
	110	1.105	
	120	8.753	
	130	4.724	
400	150	3.299	
	160	4.838	
	170	1.522	
500	180	0.581	
	190	8.980	
	200	1.803	
850	420	1.172	
	430	5.927	
	490	7.064	
	500	9.790	
900	530	1.079	
	540	10.000	
	550	4.267	
	560	6.929	

Table F.8: Series, periods and live times for Short NiCVD#1.

Short CVD Detector #2			
Series	Period	High Gain	Low Gain
500	170	3.166	
	180	4.479	
	190	8.957	
	200	9.144	
	210	8.442	
	220	9.850	
	230	9.839	
	240	3.683	
700	300	7.225	
	310	4.838	
750	380	8.106	5.233
	390	1.665	
800	390	7.607	
	400	9.992	
	410	7.907	
	420	0.790	
850	420	7.072	
	430	5.929	
	490	7.073	1.690
	500	9.788	4.129

Table F.9: Series, periods and live times for Short NiCVD#2. Differences between high and low gain channels are noted in the Low Gain column. The differences are associated with electronic problems in one of the digitizers.

Short CVD Detector #3			
Series	Period	High Gain	Low Gain
500	170	3.176	
	180	1.917	
600	250	1.208	0.000
	260	0.874	0.000
	270	1.762	0.000
	280	5.842	0.000
	290	8.501	0.000
	300	1.593	0.000
700	300	2.233	
	310	9.740	
	320	1.780	
	350	4.676	4.330
	360	8.183	
	370	7.949	
	380	0.745	0.669
750	380	4.821	
800	390	7.624	7.360
	400	9.992	9.285
	410	7.918	
	420	0.790	
850	420	5.900	
900	430	1.078	

Table F.10: Series, periods and live times for Short NiCVD#3. Difference between high and low gain channels are noted in the Low Gain column. The differences are associated with electronic problems in one of the digitizers.

Appendix G

^{232}Th and ^{238}U decay schemes

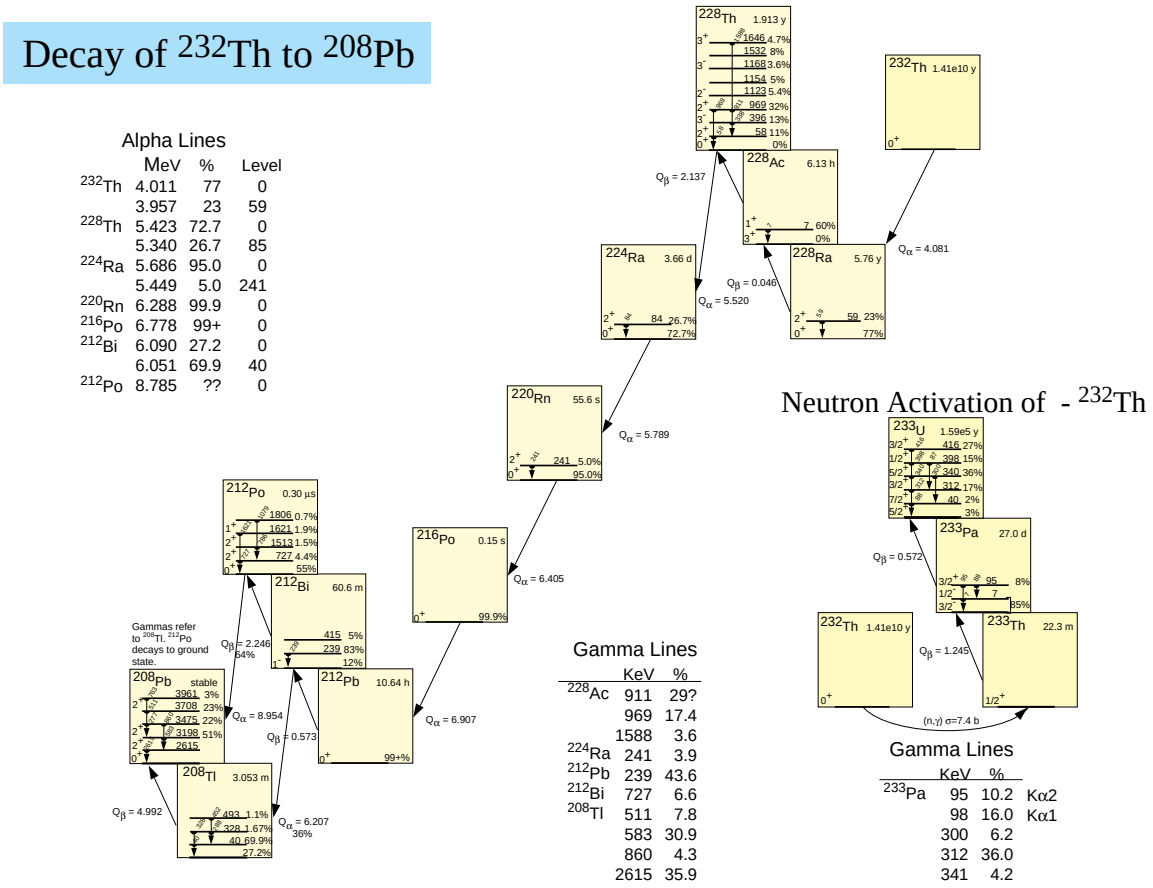

Figure G.1: The decay chain for ^{232}Th.

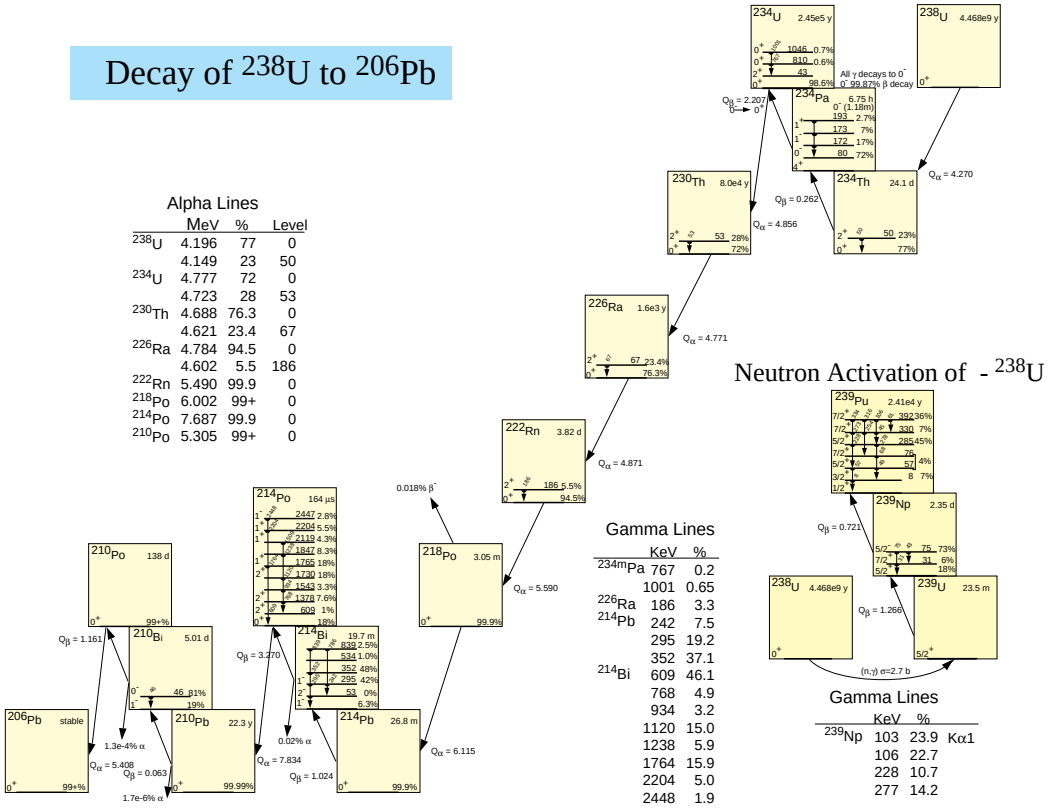

Figure G.2: The decay chain for ^{238}U.

Bibliography

[1] C.L. Cowan Jr., F. Reines, F.B. Harrison, H.W. Kruse, A.D. McGuire, Science, 124, 103, (1956).

[2] L.Montanet *et al.*, *Reviews of Particle Properties*, Phys. Rev. D, 50, 1180 (1994).

[3] J.N. Bahcall, *Neutrino Astrophysics*, Cambridge University Press (1989).

[4] J.N. Bahcall and M.H. Pinsonneault, Rev. Mod. Phys. **64** 885 (1992).

[5] J. N. Bahcall, M. H. Pinsonneault, S. Basu, and J. Christensen-Dalsgaard, *Are Standard Solar Models Reliable?* Phys. Rev. Lett. **78** 171 (1997).

[6] J.N. Bahcall and A. Ulmer, Phys. Rev. D **53** 4202 (1996).

[7] K.M. Heeger and R.G.H. Robertson, Phys. Rev. Lett. **77** 3720-3723 (1996).

[8] P. Langacker, Invited talk presented at *32nd International Scholl of Subnuclear Physics*, Erice 1994.

[9] T.J. Bowles and V.N. Gavrin, *the Status of the Solar Neutrino Problem*, Annu. Rev. Nucl. Sci. 1993.43:117-64.

[10] A. Cumming and W.C. Haxton, Phys. Rev. Lett. **77** 4286-4289 (1996).

[11] B.T. Cleveland *et al.*, Preprint, 1996.

[12] Kamiokande II Collaboration, K.S. Hirata *et al.*, Phys. Rev. Lett. **65**, 1297 (1990); **65**, 1301 (1990); **66**, 9 (1991); Phys. Rev. D **44**, 2241 (1991); Kamiokande III Collaboration, Y. Fukuda *et al.*, Phys. Rev. Lett. **77**, 1683 (1996).

[13] Y. Totsuka, to be published in *Proceedings for Texas Conference*, December 1996.

[14] SAGE Collaboration, A.I. Abazov, *et al.*, Phys. Rev. Lett. **67**, 3332 (1991); J.N. Abdurashitov *et al.*, Phys. Lett. B **328**, 234 (1994); Phys. Rev. Lett. **77**, 4708 (1996).

[15] GALLEX Collaboration, P. Anselmann *et al.*, Phys. Lett. B **285**, 376 (1992); **285**, 390 (1992); **314**, 445 (1993); **327**, 337 (1994); **357**, 237 (1995); W. Hampel *et al.*, Phys. Lett. B **388**, 384 (1996).

[16] S.L. Glashow and L.M. Krauss, Phys. Lett., **B190**, 199 (1987).

[17] L. Wolfenstein, *Neutrino Oscillations in Matter*, Phys. Rev. D, **17** 9, 2369 (1978).

[18] The SNO Collaboration, *The Sudbury Neutrino Observatory Proposal*, SNO-STR-87-12 (1987).

[19] R.B. Leighton, R.W. Noyes and G.W. Simon, Ap. J., **135** 474 (1962).

[20] T.J. Bowles *et al.*, *Neutral-Current Detection in the Sudbury Neutrino Observatory (SNO)*, FIN-94-ER-E324 (1992).

[21] S.P. Mikheev and A.Yu. Smirnov, *Resonance enhancement of oscillations in matter and solar neutrino spectroscopy*, Sov. J. Nuc. Phys. **42** (6) 913 (1986).

[22] M.D. Lay, D.Phil thesis (Oxford 1994).

[23] A. Burrows, D. Klein and R. Gandhi, *Supernova Neutrino Bursts, the SNO Detector, and Neutrino Oscillations*, Nucl. Phys. B (Proc. Suppl.) 31 (1993) 408-412.

[24] W.R. Leo, *Techniques for Nuclear and Particle Physics Experiments*, Springer-Verlag (1987).

[25] D.H. Wilkinson, *Ionization Chambers and Counters*, Cambridge University Press (1950).

[26] C.K. Hargrove, *Use of Gd in Gas Counters as a Neutral Current Detector in SNO*, SNO-STR-025-94 (1994).

[27] M.M. Fowler and J.B. Wilhelmy, *Removal of Tritium from Gaseous Helium-3*, SNO-STR-017-94 (1994).

[28] T.J. Bowles and V.N. Gavrin, *The Status of the Solar Neutrino Problem*, Annu. Rev. Nucl. Part. Sci. 117 (1993).

[29] G.G. Miller, J.A. Olivares and J.B. Wilhelmy, *Determination of Th and U in High Purity Ni*, SNO-STR-93-054 (1993).

[30] N. Hata, S. Bludman, and P. Langacker, *Astrophysical solutions are incompatible with the solar neutrino data*, Phys. Rev. D,49, 3622 (1994).

[31] M.G. Bowler it et al.,*Some Monte Carlo Studies of the Added Salt Option*, (1996).

[32] S.J. Brice, *Monte Carlo and Analysis Techniques for the Sudbury Neutrino Observatory*, D.Phil Thesis, Oxford (1996).

[33] G.F. Knoll, *Radiation Detection and Measurement*, Wiley (1979).

[34] A. Hime and P.M. Thornewell, *Event Topology and Pulse-Shape Discrimination in ^3He Proportional Counters*, work in progress.

[35] W.R. Kuhlmann, K.H. Lauterjung, B. Schimmer and K. Sistemich, Nucl. Inst. & Meth. **40** 118-120 (1966).

[36] A. Goldschmidt, private communications.

[37] P.J. Doe *et al.*, *Contruction of an Array of Neutral-Current Detectors for the Sudbury Neutrino Observatory*, SNO-STR-95-023.

[38] A. Hime, *Operating Constraints and Performance of a ^3He Neutral Current Detector Array in SNO*

[39] A. Hime, private communications.

[40] A. Hime, *Extracting the NC-Signal from D_2O + NCD's*, SNO Collaboration Meeting, May 2-4, 1997.

[41] R.G.H Robertson and G.M. Miller, private communications.

[42] J.V. Germani, University of Washington, private communications.

[43] J. Wilhelmy, *New Monte Carlo Calculations for Neutron Detection in SNO*, LA-UR-92-2447 (1992), J. Wilhelmy and M.M. Fowler, SNO-STR 90-92 (1990), J. Wilhelmy and M.M. Fowler, SNO-STR 91-035 (1991).

[44] T.K. Kuo and J. Pantaleone, Rev. Mod. Phys. **61** (1989).